Nonlocal Regularisation of Anisotropic Sand Models

Xin Li

Submitted in fulfilment of the requirement for the degree of

Doctor of Philosophy

James Watt School of Engineering

College of Science and Engineering

University of Glasgow

February 2024

Abstract

Nonlocal regularisation is frequently used to resolve the mesh-dependency issue caused by strain softening in finite element (FE) simulations. Nonlocal methods are proposed based on the hypothesis that the response of materials depends on the deformation field of a local material point and a weighted average of its neighbouring points. The nonlocal regularisation of an anisotropic critical state sand model which can capture the strain-softening and state-dependent dilatancy response of sand is presented. The evolution of the void ratio is assumed nonlocal in this method. The regularisation method has been implemented using the explicit stress integration method.

A comprehensive comparison of three weighting functions (including the Gaussian distribution (GD), Galavi and Schweiger (G&S) and over-nonlocal (ON) functions) has been investigated in different boundary value problems (BVPs). All functions give mesh-independent force-displacement relationships in drained and undrained plane strain compression tests. The shear band thickness shows a slight variation when the mesh size is smaller than the internal length. None of them can eliminate the mesh dependency of shear band orientation. The G&S method is the most efficient in eliminating the mesh dependency, especially in the strip footing problem. The ON method can give excessive overprediction of volume expansion around strip footings, leading to unrealistic low reaction forces on strip footings at large deformation. All three weight functions give mesh-independent results for the earth pressure acting on a retaining wall.

A more in-depth investigation of the G&S method is presented. The plane strain compression tests with rough boundary conditions under both drained and undrained conditions are simulated. Mesh-independent predictions of force-displacement relationship curves, shear band orientation and shear band thickness are given. After applying nonlocal regularisation, the evolution of state variables obtained from selected elements and cross-sections reduces the fluctuation in their changes and significantly diminishes the differences in peak values observed across various mesh sizes in the local model. The effectiveness of reducing mesh dependency in the nonlocal method increases when the void ratio is higher or when the confining pressure increases.

Table of Contents

List of Tables

List of Figures

Acknowledgement

First and foremost, I would like to express my deepest gratitude and utmost respect to my first supervisor, Dr. Zhiwei Gao. Throughout the journey of completing this thesis, my supervisor has provided me with invaluable guidance, support, and inspiration both academically and personally. Firstly, in terms of academics, my supervisor has taught me many study methods, such as how to practice oral skills, how to write papers, and how to search for and analyse the literature. Secondly, in my life, my supervisor has shown me how to approach problems with the right mindset, and his way of dealing with people has also had a significant impact on me. Finally, my supervisor's dedication to academic excellence and passion for research has deeply influenced and inspired me, enabling me to walk firmly on the academic path. I would also like to express my deepest gratitude to my second supervisor, Dr. Peter Grassl.

Furthermore, I would like to thank my beloved family for their support, understanding and encouragement. Firstly, my family have provided me with a warm and safe home environment, giving me the energy and emotional support to pursue my dreams. Whether during busy academic times or when facing challenges and difficulties, my family have always stood by me, supporting me, and giving me the courage and confidence to face the various challenges of the future. Secondly, my family have never tired of listening to my complaints or sharing my joys, providing me with endless comfort and encouragement. When I feel lost and confused, my family always provide guidance and advice, helping me regain my confidence and motivation.

Lastly, I would like to thank everyone who has helped, encouraged, and accompanied me during my academic journey.

Author's Declaration

I declare that this thesis is an original report of my research has been composed by myself and this work has not been submitted for any other degree or professional qualification. I confirm that the work submitted is my own except where explicitly stated otherwise in the text. My contribution to this work has been explicitly indicated below.

I acknowledge that this work was conducted under my supervisor, Dr. Zhiwei Gao. I specifically acknowledge that the method used in this thesis was initially proposed by Dr. Zhiwei Gao and successfully implemented. I have expanded the implementation of this method and extended this method upon the work conducted by Dr. Zhiwei Gao.

The following publications are based on this thesis:

Gao, Z.W., Zhao, J.D. and Li, X. (2021). The deformation and failure of strip footings on anisotropic cohesionless sloping grounds. *International Journal for Numerical and Analytical Methods in Geomechanics*, 45(10), pp. 1526-1545. (doi: 10.1002/nag.3212)

Gao, Z.W., Li, X. and Lu, D.C. (2022). Nonlocal regularization of an anisotropic critical state model for sand. *Acta Geotechnica*, 17(2), pp. 427-439. (doi: 10.1007/s11440-021-01236-3)

Li, X. and Gao, Z.W. (2023). Evaluation of Nonlocal Regularisation Methods for Sand Models. *In: UK Association for Computational Mechanics 2023 (UKACM 2023)*, The University of Warwick, Coventry, UK, 19-21 April 2023, (Accepted for Publication)

Gao, Z.W., Li, X. and Lu, D.C. (2023). Nonlocal Regularization of an Anisotropic Critical State Model for Sand. *In: 10th European Conference on Numerical Methods in Geotechnical Engineering*, London, 26-28 June 2023, (doi: 10.53243/NUMGE2023-123)

Li, X. and Gao, Z.W. (2024). Evaluation of three weight functions for nonlocal regularisation of sand models. *International Journal of Geomechanics*, (Accepted for Publication)

Symbols/Abbreviations

l_c	Internal length scale
η_v	The viscosity
E	Young's modulus
ρ	The mass density
f	The yield function
κ	Hardening parameter
∇^2	The second order of Laplacian
n_{ij}	The gradient to the yield function
h^p	The hardening modulus
$\dot{\lambda}$	The plastic multiplier
g^p	The gradient influence variable
D^{ep}	The tangential stiffness matrix
ω_{ij}	The overall rotation
ω_{ij}^c	The Cosserat rotation
u_x, u_y	The translational degrees
ω_z	The rotational degree
k_{xz}, k_{yz}	The micro curvatures
μ_{xz}, μ_{yz}	The couple stress tensor
$\varepsilon_{xy}, \varepsilon_{yx}$	The strain components
σ	Stress vector
ε	Strain vector
u	Displacement vector
$[\sigma]_{sym}, [\varepsilon]_{sym}$	The symmetric tensors
$[\sigma]_{skw}, [\varepsilon]_{skw}$	The skew-symmetric tensors
ε_{ij}	Strain tensor

u_i	The component of the displacement vector
e_{ijk}	Ricci permutation tensor
k_{ij}	Micro-curvature tensor
σ_{ij}	Stress tensor
μ_{ij}	The couple stress tensor
l_t	The internal length related to bending couple stress
$\bar{\sigma}_{ij}(x)$	Nonlocal stresses
$\bar{\varepsilon}_{ij}(x)$	Nonlocal strains
ξ	Local coordinate
x	The global coordinate
ω	The weight function of the nonlocal method
v	The weighted volume
h	Hardening function
k	The scalar softening variable
c'	Cohesion of soil
φ'	Friction angle of soil
m	Over-nonlocal parameter
p	The mean effective stress
δ_{ij}	The Kronecker delta
r_{ij}	The stress ratio tensor
$g(\theta)$	Interpolation function
θ	Lode angle
M_c, M_e	The critical state stress ratio
c	Material constant
H	The hardening parameter
L	The loading index

K_p	The plastic modulus
$h_1, h_2, n, e_A, e_\Gamma, \lambda_c, \xi_c, d_1, m_1, k_f$	Model parameters
G	Elastic shear modulus
A	Anisotropic variable
r_H	The function of the stress and internal variable
ζ	The dilatancy state parameter
e	The void ratio
ψ	State parameter
p_a	Atmospheric pressure
F_{ij}	The fabric tensor
F_0	The initial degree of anisotropy
n_{ij}	The loading direction tensor
g	The plastic potential function
k_h	A non-negative anisotropy constant
de_{ij}^p	Plastic deviatoric strain increment
m_{ij}	A unit-norm deviatoric tensor
$d\varepsilon_{ij}^p$	The total plastic strain increment
D	Dilatancy
G	Elastic shear modulus
K	Elastic bulk modulus
G_0	A material constant
ν	Poisson's ratio
de_{ij}^e	Elastic deviatoric strain increment
$d\varepsilon_v^e$	Elastic volumetric strain increment
E_{ijkl}	Elastic stiffness tensor
$d\varepsilon_{ij}$	Total strain increment

df	The condition of consistency of the yield function
Λ_{ijkl}	The elastoplastic stiffness tensor
$h(L)$	The Heaviside step function
e_{min}	The minimum void ratio
e_{max}	The maximum void ratio
e_0	Initial void ratios
q	Deviatoric stress
ε_{a}	Axial strain
ε_v	Volumetric strain
r_i	The distance between the current integration point and the $i-$th integration point
X^{IP}	The integration point
$d\varepsilon_{vn}$	The nonlocal volumetric strain increment.
de	The increment of void ratio
$d\varepsilon_{vl}^{s}$	The local volumetric strain increment
de^{s}	The nonlocal void ratio increment for the sub-increment
t_s^{sand}	The physical shear band thickness of sand
t_s^{num}	The numerical shear band thickness
h^{sand}	The physical softening stiffness
h^{num}	The numerical softening stiffness
γ'	The effective weight of Toyoura sand
h_w	The height of retaining wall
σ_h	The lateral earth pressure
l	Normalised shear band thickness
λB	The distance between the footing and slope crest

β	The orientation of the shear band, slope angle
R_v	Vertical reaction force
R_{pv}	Peak vertical reaction force
s/B	Normalised vertical settlement
s/H	Normalised vertical displacement
u/h_w	Normalised wall displacement
B	Width of strip footing
F	Degree of anisotropy
K_0	The initial lateral earth pressure coefficient
h	Mesh size
Q	Vertical load
d_{50}	The mean particle size
t_s, t_{s1}, t_{s2}	The shear band thickness
α	Bedding plane orientation
r_v	Scaling variable
D_r	Relative density
p_0	Confining pressure

FEM	Finite element method
BVPs	Boundary value problems
GD	Gaussian distribution function
G&S	Galavi and Schweiger (2010) distribution function
ON	Over-nonlocal method
2D problem	Two-dimensional problem
3D problem	Three-dimensional problem
PDE	Partial differential equation

DP model	The Drucker-Prager model
SYM	Two lines of symmetry
IP	Integration point
UMAT	User-defined materials
USDFLD	User-defined field variables
ENCD, VOLINT	Common block array
NEL	The total number of elements
NIP	The number of integration points in each element
IVOL, NPT	The volume of each integration point
GETVRM	The utility routine
CPE8R	Eight-nodded plane strain quadratic elements with reduced integration

Chapter 1: Introduction

1.1 Background

Strain localisation refers to the phenomenon in which materials experience significant deformation concentration in localised areas when subjected to loading (Weidner and Biermann, 2021). This phenomenon typically occurs in certain sections or specific locations of the materials. Strain localisation can occur in various geotechnical engineering problems, such as failure of slopes or retaining walls, excavations, and tunnelling (Lambe and Whitman, 1979; Terzaghi et al., 1996; Peck et al., 2008; Coduto et al., 2018).

The strain localisation in geomaterials such as sand and clay is caused by their mechanical behaviour at the element level and external loading conditions (Song and Khalili, 2018; Oka and Kimoto, 2021). Strain localisation in geomaterials has been found to be influenced by confining pressure, density, boundary conditions, sample size, fabric anisotropy and drainage conditions (Chu et al., 1996; Desrues and Viggiani, 2004; Gao et al., 2012). Strain localisation in geomaterials, such as soils and rocks, is significantly influenced by confining pressure, density, and boundary conditions. Increased confining pressure generally enhances the material's strength and ductility, delaying the onset of strain localisation and resulting in more diffuse deformation (Wood, 2004). Conversely, lower confining pressures reduce strength and ductility, leading to earlier and more pronounced strain localisation (Muir Wood, 1990). Density also plays a crucial role, with higher density materials exhibiting greater strength and stiffness, thus delaying localisation (Vardoulakis & Sulem, 1995). Lower density materials, on the other hand, tend to localise strain earlier due to their lower strength and stiffness (Terzaghi et al., 1996). Boundary conditions further modulate strain localisation, where fixed boundaries can increase stress concentrations and promote localisation along specific planes, while flexible boundaries allow for more uniform deformation, thus delaying localisation (Desrues & Viggiani, 2004; Vardoulakis, 1980). The interplay between these factors is complex: high confining pressure combined with high density generally leads to more stable, diffuse deformation, whereas low confining pressure and low density encourage early and pronounced strain localisation (Schofield & Wroth, 1968; Vermeer & de Borst,

1984). Understanding these interactions is crucial for predicting material behaviour under stress and is essential for designing stable geotechnical structures

Experimental evidence indicates that localised deformation is a primarily plastic strain (Alshibli et al., 2003; Desrues and Viggiani, 2004; Antolovich and Armstrong, 2014). Mathematically, strain localisation is a bifurcation problem from a continuous deformation to a discontinuous one (Borja and Aydin, 2004). Therefore, the occurrence and development of deformation bands resulting from strain localisation are precursors to the failure of geomaterials and geotechnical structures.

Deformation bands which describe the strain localisation in soils can be categorised based on their kinematic properties (Aydin et al., 2006) into three main types: (i) shear bands, (ii) compaction bands, and (iii) dilation bands.

(1) Shear bands are characterised by a dominant shear displacement gradient, often accompanied by a reduction in porosity (compaction). In some cases, they can also result in an increase in porosity (dilation) (Antonellini et al., 1994). Shear bands are typically associated with compaction caused by grain sliding, grain rotation, and/or grain fracturing (Aydin, 1978).

(2) Compaction bands refer to tabular bands where localised porosity reduction or compaction occurs without a macroscopic shear offset (Mollema and Antonellini, 1996).

(3) Dilation bands are localized zones of deformation within geomaterials characterised by volumetric expansion, occurring perpendicular to the maximum compressive stress direction and significantly influencing geomaterial behaviour. Unlike shear bands, which exhibit shear deformation, or compaction bands, which show volumetric contraction, dilation bands involve an increase in volume within the affected zone (Desrues & Viggiani, 2004). The formation of dilation bands can enhance permeability by creating fluid flow pathways, impacting hydrogeology and petroleum engineering (Alshibli & Roussel, 2006). Additionally, these bands influence stress redistribution, potentially stabilising localised stress concentrations but possibly leading to extensive deformation under persistent stress conditions (Holcomb & Rudnicki, 2001). Dilation bands also alter failure mechanisms in geomaterials, preceding or accompanying other deformation bands and contributing to complex failure processes, essential for predicting and mitigating structural

failures in geotechnical engineering (Vardoulakis, 1980). Recognising and understanding dilation bands are crucial for assessing the stability and integrity of geological and engineered structures, ensuring safety margins in design and analysis (Vermeer & de Borst, 1984).

These bands are characterised by two discrete surfaces and are often observed in consolidated, low-porosity brittle rock. Deformation bands can also be classified based on the dominant deformation mechanism (Fossen et al., 2007). This classification depends on various factors such as grain size, shape, sorting, cementation, mineralogy, porosity of the host sediment, and the stress conditions during band formation. Following Fossen et al. (2007), four main types can be recognised:

(1) Disaggregation bands are commonly observed in the deformation of soft sediments (e.g., Maltman, 1988, 1994; Fossen et al., 2011; Brandes and Tanner, 2012) and have also been reported in deltaic gravels (Exner and Grassemann, 2010). Sometimes referred to as microfaults or shear bands in geotechnical engineering literature (e.g., Davis and Selvadurai, 2002), these bands accommodate slippage of soft, water-saturated, or unconsolidated sediments along shear surfaces with minimal volumetric strain. These thin bands are typically porosity-neutral, making them transparent to fluid flow in rocks containing these structures.

(2) Phyllosilicate bands are common in mudrocks and shales, recognized as thin tabular zones filled with material resembling fault gouge. These bands may impede fluid flow and contribute to anisotropy in the host-rock permeability. They often form in grain-supported mudrocks (i.e., clay content less than ~35-40%); in higher clay content mudrocks, matrix-supported shearing may produce clay-smear zones, associated with reduced frictional strength and stable, creep-like frictional stability (Sone and Zoback, 2014).

(3) Cataclastic bands are similar to cataclastic compactional shear bands. The textures within a cataclastic deformation band show the importance of the deformation mechanism (i.e., grain crushing during band formation) and factors such as displacement magnitude. Grain-size reduction, shape change (i.e., increased grain angularity), and interlocking can lead to strain hardening of cataclastic compactional shear bands (e.g., Katsman et al., 2004; Kaproth et al., 2010; Wong and Baud, 2012), even at shallow depths (<1 km), eventually stopping displacement accumulation. Recognizing cataclastic deformation

bands is crucial as they may indicate a shift from strain-hardening banding to strain-softening faulting in sedimentary sequences.

(4) Solution and cementation bands record the interaction between grain properties, fluid composition, diagenesis, and pre-existing deformation bands. These secondary structures have been studied by several researchers (e.g., Antonellini et al., 1994; Parnell et al., 2004; Fossen et al., 2007; Exner et al., 2013). Grain dissolution and mineral precipitation or aggregation, such as pyrite, calcite, silica, and various clays, can either strengthen or reduce the permeability of deformation bands through secondary diagenetic alteration (Exner et al., 2013). Notable exposures of deformation-band arrays, such as at Devils Wall in the Harz Mountains of Germany, are examples of cementation bands formed during or after cataclastic deformation bands (Klimczak and Schultz, 2013).

The development of strain localisation is usually accompanied by a reduction in the overall strength of the materials, thus significantly affecting the behaviour of both the geomaterials and geotechnical structures. The phenomenon of strain localisation in geomaterials is of paramount importance for the study and prediction of geotechnical engineering and geological hazards, as it directly relates to the stability and safety of geotechnical structures. To prevent and control the adverse effects of strain localisation, engineers need to fully consider the properties of the materials and loading conditions and take appropriate measures during the design and construction processes. In the analysis and design of geomaterials and geotechnical structures, a good predictive computational model should be able to fully account for the localisation of deformation and the formation and development of shear bands in geomaterials.

Over the past decades, numerous studies of shear banding have been focused on fluid-saturated geomaterials. For instance, Rudnicki (2002) used a transversely isotropic constitutive relation to observe the occurrence of compaction bands in a porous rock, Borja and Aydin (2004) adopted the rate‐independent constitutive model to analyse the tabular bands based on shear and volumetric deformations in granular rocks, Jefferies (1993) developed Nor-Sand critical state model to model sand by the density, or void ratio, Oka et al. (2000) studied the development of shear bands in water‐saturated clay under quasi‐static deformations, Zhang et al. (2000) conducted a dynamic strain localisation analysis and simulated the shear banding in fully saturated and partially saturated sand samples by elastoplastic model. In recent years, there has been significant interest in the phenomenon of strain localisation in unsaturated soils. This interest arises

from its relevance to practical engineering applications, such as the failure of unsaturated soil slopes (Gens, 2010) and the production and storage of geothermal energy (Brandl, 2006). Unsaturated soils are three-phase porous media consisting of a deformable solid skeleton, pore water, and pore air (Ng and Menzies, 2014). Strain localisation in unsaturated soils involves the coupled solid deformation and unsaturated fluid flow process. For example, Borja (2004) used the Cam-Clay plasticity model to simulate strain localisation of partially saturated porous media, Oka et al. (2018) developed an elasto-viscoplastic model for dynamic strain localisation in unsaturated soils, Wang and Song (2020) implemented a mesoscale constitutive model to analysis the thermal unsaturated soils. Research on dry sand has extensively explored its mechanical properties and deformation behaviours under various conditions, revealing that it exhibits critical state behaviour where it deforms without changes in stress or volume, an insight crucial for predicting failure in sandy slopes and foundations (Schofield and Wroth, 1968). Studies have demonstrated that dry sand shows peak strength followed by a reduction in residual strength, which is important for structures involving large deformations (Lambe and Whitman, 1979). Triaxial testing indicates that higher confining pressures enhance shear strength and stiffness, vital for structures under high lateral pressures (Wood, 1990), while understanding lateral earth pressure is essential for designing retaining walls and earth dams (Terzaghi et al., 1996). Research by Tatsuoka et al. (1990) on the effect of loading rate has shown that the strength and stiffness of dry sand can be rate-dependent, with faster loading rates generally resulting in higher apparent strength and stiffness. This finding is crucial for understanding the behaviour of sand in dynamic loading conditions, such as traffic loads and seismic events.

In computational modelling, capturing strain localisation accurately is crucial for obtaining realistic and reliable predictions of material behaviour and structural response under various loading conditions (Sanavia et al., 2005). Advanced numerical methods, such as the finite element method (FEM), can help simulate and analyse the phenomenon of strain localisation and its effects on structures and materials. The FEM, as a numerical technique, considers the material's constitutive relationship, allowing it to predict the entire process of deformation localisation, the formation and development of deformation bands, and ultimately the failure of materials and structures. Its results can serve as a supplement to the design process or directly be used for design purposes. For complex loading conditions and important structures with intricate geometric boundaries, finite element analysis is indispensable (Zienkiewicz et al., 1999; Hughes, 2000).

Furthermore, simulating the entire process of strain localisation using the FEM helps understand the failure mechanism of geomaterials and geotechnical structures.

However, the response of the FEM continuum after it has reached its peak is inherently dependent on the mesh used, as noted by Bažant and Jirasek (2002). Mathematically, this mesh dependency is linked to the transformation of the governing partial differential equations from elliptic to hyperbolic, which occurs when the material behaviour transitions from hardening to softening. Previous research has also highlighted this issue (e.g., Mühlhaus, 1986; Galavi and Schweiger, 2010; Guo and Stolle, 2013; Lu et al., 2019; Cui et al., 2023). Alsaleh et al. (2006) have pointed out that the FE simulation of strain localisation is subject to mesh dependency due to the use of classical continuum models that do not account for micro-structural factors, such as particle size and associated voids. Different methods have been proposed to resolve the mesh-dependency issue, including, the strain-gradient enhanced approaches (e.g., Aifantis, 1984; de Borst and Mühlhaus, 1992; Dorgan and Voyiadjis, 2003), micro-polar plasticity approach (e.g., Mühlhaus, 1986; Alshibli et al., 2006; Tang et al., 2013), nonlocal regularisation method (e.g., Eringen, 1972; Lü et al., 2009; Galavi and Schweiger, 2010; Guo and Stolle, 2013; Lazari et al., 2015; Summersgill et al., 2017; Mallikarachchi and Soga, 2020; Singh et al., 2021; Gao et al., 2022; Cui et al., 2023) and viscous plasticity theory (e.g., Oka et al., 1995; Wang et al., 1997; Higo, 2004; Yin et al. 2010). An internal length scale is introduced to the constitutive model formulation in these methods, which controls the degree of deformation localisation and preserves the well-posedness of the governing partial differential equations irrespective of the refinement of the mesh (de Borst et al., 1993).

Among these methods, nonlocal regularisation is the most widely used for advanced soil models. In the study of strain localisation, nonlocal regularisation is often favoured over methods such as viscosity regularisation, strain-gradient enhanced approaches, and the micro-polar continuum approach due to several key advantages. Firstly, nonlocal regularisation methods effectively mitigate the issue of mesh dependency that often arises in numerical simulations of strain localisation, leading to the improvement of the credibility of numerical simulations. Secondly, compared to strain-gradient enhanced approaches and micro-polar continuum theories, nonlocal regularisation is easier to implement within existing finite element frameworks. This is because it does not necessarily require significant modifications to the constitutive equations or additional

degrees of freedom. This simplicity allows researchers to apply nonlocal regularisation methods more quickly, reducing technical barriers to implementation. Finally, although nonlocal regularisation introduces some computational overhead, it is often less demanding than the highly complex formulations required by micro-polar continuum theories or the additional gradients and higher-order terms in strain-gradient methods. The improvement in computational efficiency makes nonlocal regularisation methods practical for large-scale engineering projects and complex material analyses.

Nonlocal methods are proposed based on the hypothesis that the response of materials depends on the deformation field of a local material point and a weighted average of its neighbouring points (Mallikarachchi, 2019). All stress, strain, and state variables are considered nonlocal variables in fully nonlocal constitutive models. However, employing a fully nonlocal model often leads to complex constitutive equations. As a result, in most cases, a partially nonlocal approach is preferred. In a partially nonlocal model, only certain state variables (e.g., void ratio, plastic shear strain, or yield surface size) are assumed to be nonlocal (Galavi and Schweiger, 2010). When selecting state variables for the partially nonlocal approach, several key factors must be considered Firstly, the primary consideration should be whether the state variable can influence the strain-softening results predicted by the model. Secondly, the complexity of the model itself must be taken into account. Some state variables in more complex models can be challenging to treat as nonlocal due to the intricate physical processes and interactions they involve, increasing the difficulty of their nonlocal transformation. Numerical implementation complexity is another crucial factor. Even if a state variable has a significant impact on strain-softening, if treating it as a nonlocal variable greatly increases computational complexity and numerical implementation difficulty, a balanced approach must be sought. This might involve simplifying the model or identifying alternative variables. Numerical stability and convergence are also critical factors. The handling of nonlocal variables must consider their impact on the numerical stability of simulations. Some nonlocal variables might introduce additional computational complexity and potential numerical instability, necessitating the design of appropriate numerical algorithms to ensure stable simulations.

This approach has proven effective in regularising most soil models with strain softening. For example, researchers like Galavi and Schweiger (2010) and Summersgill et al. (2017) have assumed that strain softening is governed by the nonlocal plastic shear strain.

Additionally, Lu et al. (2011) have proposed the use of a nonlocal plastic multiplier to control the increment of plastic strain and regularise soil models exhibiting strain-softening behaviour.

1.2 Objective

The nonlocal method has mainly been used in soil models that have simple strain-softening rules. In studies conducted by Galavi and Schweiger (2010) and Summersgill et al. (2017), the variable that governs strain softening is solely a function of plastic shear strain. In such cases, the model can be readily regularised by assuming that the strain-softening variable depends on the nonlocal plastic shear strain. However, natural sand exhibits strain softening influenced by several variables, including void ratio, mean effective stress, fabric anisotropy, and plastic strain. The hardening parameter in an advanced sand model, which describes strain softening, cannot be explicitly expressed in terms of these variables. This complexity poses challenges when applying nonlocal regularisation to these models. Instead, the increment of the hardening parameter is described in relation to these variables.

Mallikarachchi and Soga (2020) were among the first to propose a nonlocal regularisation method for an advanced sand model, accounting for the influence of void ratio and mean effective stress on soil behaviour. Specifically, they assumed that the void ratio increment depends on the void ratio increment at both local and neighbouring integration points. This approach effectively reduces the mesh dependency of model predictions for drained and undrained plane strain compression tests. However, this method has not yet been applied to practical geotechnical problems; meanwhile, the impact of weighting functions has not been investigated. Furthermore, the integration of this regularisation method with explicit/implicit stress integration methods has not been addressed. Hence, this thesis builds upon the work of Mallikarachchi and Soga (2020) by implementing an advanced sand model that considers anisotropy and fabric characteristics within the framework of nonlocal theory.

1.3 Thesis Outline

The outline of this thesis is as follows:

In Chapter 2, an introduction and comparison of four mainstream regularisation methodologies were presented. Following that, a detailed exploration of the evolution and development of fully nonlocal theory to partially nonlocal theory within the nonlocal method is provided, along with a review of their previous applications.

In Chapter 3, an anisotropic critical state sand model used in this thesis was introduced, and the validation of the model using experimental tests was presented.

In Chapter 4, three different weight functions: (1) Gaussian distribution (GD) function, (2) GandS distribution function (G&S), and (3) Over-nonlocal (ON) method were compared and introduced. Then, the nonlocal formulation of the constitutive model and implementation in Abaqus was discussed.

In Chapter 5, a comprehensive comparison of three different weight functions was carried out by various BVPs, including drained and undrained plane strain compression tests, the strip footing problems on level ground and near a slope, and retaining wall problems under both passive and active conditions.

In Chapter 6, plane strain compression tests with rough boundary under both drained and undrained analysis are simulated. The effect of initial density and confining pressure on the nonlocal regularisation method is discussed. Furthermore, the evolution of state variables within the shear band under smooth boundary conditions is investigated by cross-sections and selected elements (inside and outside the shear band). Additionally, the effect of anisotropy on strain localisation is investigated using soil samples with various bedding plane orientations. Finally, this chapter also investigated the nonlocal method in three-dimensional boundary value problems.

Chapter 7 summarises the conclusions and perspectives reached in the previous chapters.

Chapter 2：Literature review

2.1 Introduction

When a sand model with strain-softening is used in boundary value problems such as plane strain compression problems and footing problems, the solution can become unreliable due to the mesh-dependency. For example, the shear band thickness, shear band orientation and stress-strain relationship are affected by mesh size. The mesh-dependency is caused by the assumption used in standard elastoplastic models that the stress–strain relationship at an integration point is dependent on the local stress, strain and state variables only. Mathematically, this mesh dependency is associated with the change in the governing partial differential equations from elliptic to hyperbolic, which happens when the material behavior shifts from hardening to softening.

Different methods have been proposed to resolve the mesh-dependency issue, including viscous plasticity theory (e.g., Oka et al., 1995; Wang et al., 1997; Higo, 2004; Yin et al., 2010), strain-gradient enhanced approach (e.g., Aifantis, 1984; de Borst and Mühlhaus, 1992; Dorgan and Voyiadjis, 2003), micro-polar plasticity approach (e.g., Mühlhaus, 1986; Alshibli et al., 2006; Tang et al., 2013) and nonlocal regularisation method (e.g., Eringen, 1972; Lü et al., 2009; Galavi and Schweiger, 2010; Guo and Stolle, 2013; Lazari et al., 2015; Summersgill et al., 2017; Mallikarachchi and Soga, 2020; Singh et al., 2021; Gao et al., 2022; Cui et al., 2023). The mesh-dependency issue can be addressed by incorporating the internal length scale in the constitutive models or regularisation methods.

This Chapter mainly focuses on introducing four different regularisation methodologies, including the viscosity regularisation method, strain-gradient enhanced approach, micro-polar continuum approach and nonlocal method.

2.2 Viscosity regularisation method

Visco-plasticity is a theory within continuum mechanics that characterises the rate-dependent inelastic behaviour of solids. In one-dimensional representation, the elastic response of visco-plastic materials can be modelled using Hookean spring elements. The rate-dependence can be represented by nonlinear dashpot elements, similar to viscoelastic

materials, as for plasticity, which can be described by adding sliding frictional elements, as shown in Figure 2.1.

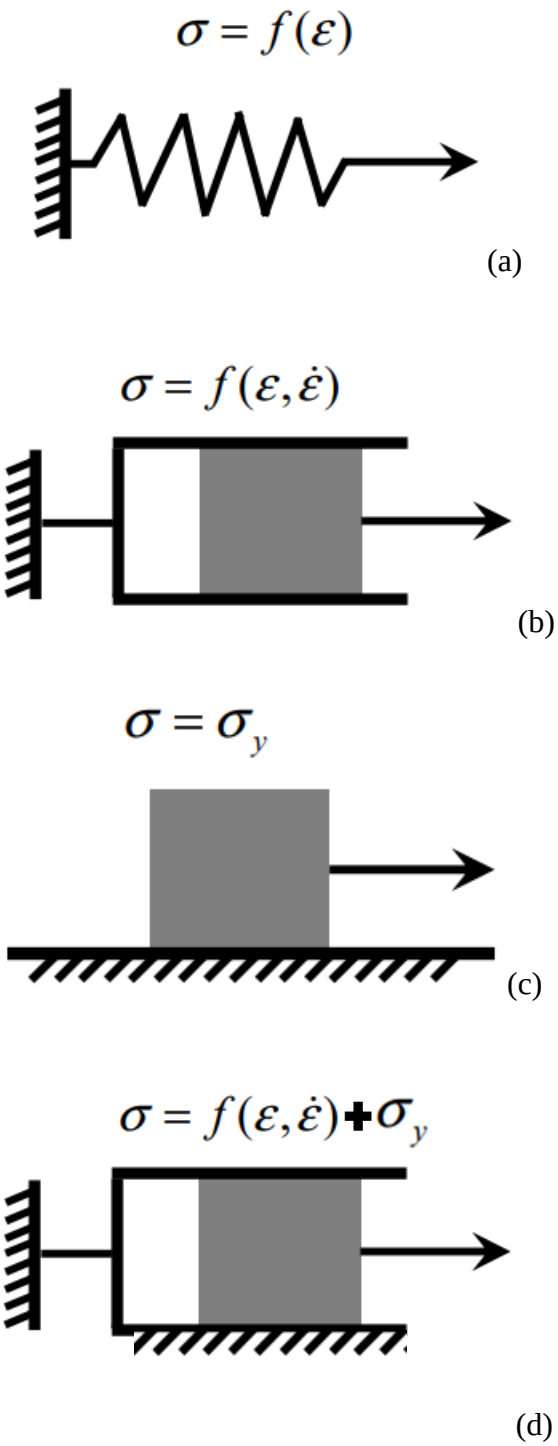

Figure 2.1 Demonstration of visco-plastic model: (a) Spring element; (b) Dashpot; (c) Sliding friction element; (d) Visco-plastic model

Viscosity regularisation relies on reducing and distributing high deformation rates in the localised region within the finite element mesh using viscosity. This utilisation of visco-plasticity as a regularisation method is primarily linked to rate-dependent behaviour. The rate-dependency was used to describe mesh sensitivity for localisation problems in metal (Needleman, 1988; Shawki and Clifton, 1989), rock and concrete fracture (Sluys and de Borst, 1991), saturated porous media (Loret and Prevost, 1991), dilatant materials and clay (Oka et al., 2002; Yin and Hicher, 2008; Yin and Karstunen, 2011). In many cases, materials behave differently under different strain rates. For example, metals may exhibit strain rate sensitivity. When using visco-plasticity, the model takes into account the rate at which deformation occurs, and this can help in reducing the mesh dependency because it considers the local deformation rates. However, adding an artificial feature, such as internal length, to the material behaviour is necessary when visco-plasticity does not display rate dependence (Dias da Silva, 2004). Needleman (1988) also pointed out that even though the dimensions of internal length in the classical visco-plastic model are unclear, rate-dependent constitutive models inherently introduce an internal length scale into the governing equations.

Various factors such as the shear wave speed, shear modulus, softening parameter, and viscosity parameter are considered influential in determining the thickness of the shear band (Dias da Silva, 2004). These factors can be connected to the cutoff value of the strain rate at the boundary of the shear band through an implicit parameter with an internal characteristic length scale. This length scale is defined in terms of the viscosity η_v, Young's modulus E and the mass density ρ as below：

$$l_c = \frac{\eta_v}{\sqrt{E\rho}} \tag{2.1}$$

Meanwhile, the viscosity regularisation technique does not need any additional global discretisation since it only requires operations at the constitutive model level, whose implementation in common non-linear finite element packages is well-established (Dias da Silva, 2004).

Wang et al. (1997) proposed a visco-plastic model for one-dimensional element analysis. The strain rate distribution along the element was implicitly expressed by the internal length scale, and this improvement has facilitated better prediction of shear band thickness. Wang et al. (1997) found that the thickness of strain localisation increases when the absolute value of the softening parameter decreases or the viscosity parameter increase. The determination of the thickness of the strain localisation also depends on the minimum value between the

internal length scale and the imperfection size. It has been observed that when the imperfection size is smaller than the material length scale, it dominates the shear band thickness. However, if the imperfection size exceeds the material length scale, the influence of the imperfection diminishes, and the shear band thickness is primarily determined by the material length scale. In essence, the relative sizes of the imperfection and the material length scale dictate their respective contributions to the shear band thickness (Wang et al., 1997).

Furthermore, visco-plasticity is commonly modelled in two dimensions using the overstress theory proposed by Perzyna (1963) and Duvaut and Lions (1972). These theories provide frameworks for capturing the complex rate-dependent behaviour and inelastic response of materials under two-dimensional loading conditions. In the Perzyna and Duvaut-Lions visco-plastic theories, an important distinction from the inviscid plasticity theory stems from the fact that the current stress states can be outside the yield surface and that the yield function may have a value larger than zero. However, when the viscosity goes to zero, the model proposed by Perzyna may not converge to the inviscid solution (Simo et al., 1988). The Duvaut-Lions model also has the limitation that it must be used in conjunction with an integration algorithm for the inviscid elastoplastic rate equations, in which the initial stress is used only to compute the trial stress since it may be outside the yield surface. Thus, Dias da Silva (2004) proposed an elastoplastic rheological model (Figure 2.2 and 2.3) for viscous regularisation that combines a Maxwell-type visco-elastic behaviour to avoid the limitations in Perzyna and Duvaut-Lions models.

The mesh sensitivity results, illustrated in Figure 2.2, demonstrate varying directions and thicknesses of the shear bands observed in the two different meshes. However, Figure 2.3 shows the results obtained when the viscosity is introduced employing the rheological model. It can be observed that the results obtained are more similar, with shear bands with the same directions in both meshes.

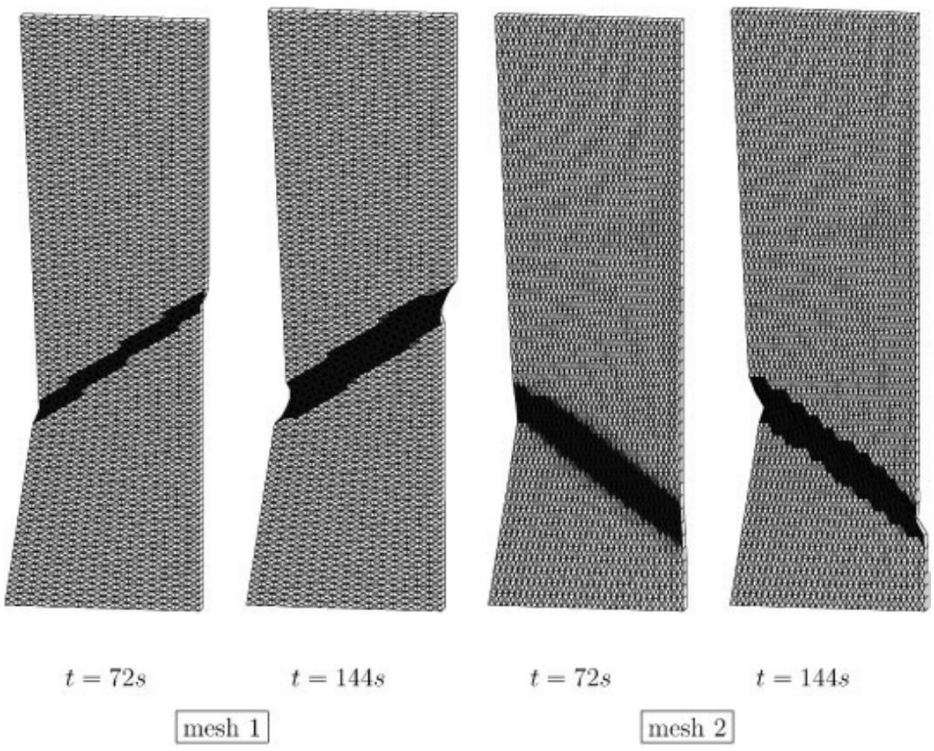

Figure 2.2 Shear bands in a von Mises specimen using two different meshes: computation with low viscosity using the rheological model (Dias da Silva, 2004)

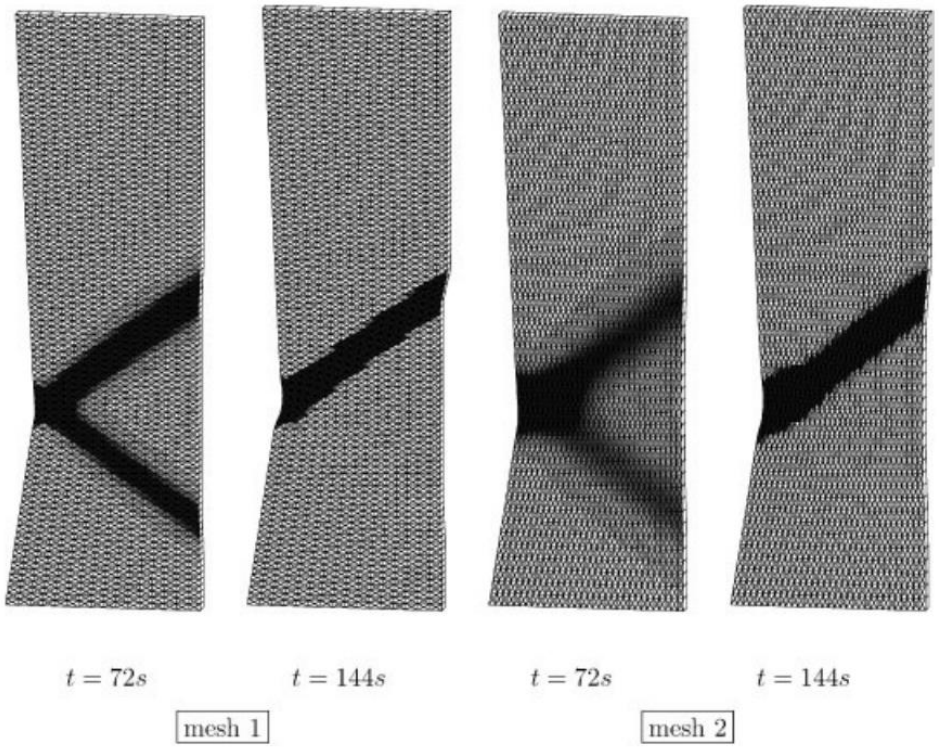

Figure 2.3 Shear bands in a von Mises specimen using two different meshes and the rheological model (Dias da Silva, 2004)

Moreover, the primary advantage of viscosity regularisation is that it does not necessitate additional global discretisation. Instead, it only requires supplementary operations at the local level within constitutive models. This makes its implementation straightforward in common nonlinear finite element packages. Additionally, viscosity regularisation is effective for both the de-cohesion failure mechanism and the slip-driven softening failure mechanism (Wang et al.,1997; Dias da Silva, 2004). However, there are certain disadvantages associated with viscosity regularisation. It needs to introduce the viscosity to describe material behaviour, even when the material does not exhibit rate dependence. This limits its applicability to transient loading conditions. Furthermore, the regularising effect of viscosity regularisation diminishes rapidly for slow loading rates or when approaching the rate-independent limit.

2.3 Strain-gradient enhanced approaches

The strain-gradient theory and nonlocal theory belong to a common theoretical category. Strain-gradient models can be derived from nonlocal models by expanding the kernel of the integral employed in the averaging procedure for the plastic strains (Liu, 2018). In the beginning, second and higher-order elasticity gradient theory was introduced and applied in the constitutive modelling to describe the effect of the microstructure on material behaviour (Toupin, 1962; Mindlin, 1965; Eringen, 1966). Kröner (1967) and Eringen and Edelen (1972) extended the implementation of strain-gradient enhanced approaches based on elasticity gradients theory. Then, the elasticity gradient theory was developed for plasticity by some researchers. The plasticity gradient theory was first used to analyse persistent slip bands (Aifantis, 1984) and shear bands in metals (Coleman and Hodgdon, 1985). The higher-order gradient theory was combined with the flow rule and the yield function by Vardoulakis and Aifantis (1989, 1991). The plasticity gradient theory was also implemented in water-saturated soils, and the strain localisation exhibits a strong dependence on the strain gradient, which was shown by Chikazawa et al. (2001) via a gradient-dependent visco-plastic constitutive model.

Both elastic and plastic strain-gradient models consist of higher-order gradient terms (Laplacian) in governing equations. These terms integrate a length scale and can regularise the strain softening. According to the governing equations, the strain-gradient theories can be divided into explicit and implicit strain-gradient theories. In explicit strain-gradient

theories, higher-order deformation gradients enter the equilibrium equations explicitly. In implicit strain-gradient theories, the gradient influences more implicitly from an additional partial differential equation.

Based on the direct use of higher-order derivatives of the local plastic strain in the yield condition, the explicit gradient theory, which utilises higher-order derivatives of the local plastic strain in the yield condition, was developed by Aifantis (1987) for modelling strain localisation in metals. However, it is important to note that the explicit gradient formulations are only valid in the plastic domain. The implicit gradient theory was developed to address the numerical challenge caused by explicit gradient theory. It involves formulating a Helmholtz-type partial differential equation (PDE) with appropriate boundary conditions. This approach is applicable in both the elastic and plastic domains. By using the Helmholtz-type PDE, the newly introduced nonstandard variable becomes connected to the local internal variable either throughout the entire body or, at the very least, exhibits long-range interactions. As a result, this preserves a significant nonlocal feature (Xue et al., 2022). de Borst et al. (1991, 1992, 1996) introduced implicit gradient plasticity formulations (Equation 2.2) that imposed limitations on the yield function, specifically restricting it to second-order derivatives. This restriction enabled the yield function to depend not only on the hardening parameter itself but also on the Laplacian of the hardening parameter. The work of de Borst and Mühlhaus (1991), de Borst et al. (1993), Pamin (1994), and de Borst and Pamin (1996) further explored and developed these formulations.

The gradient dependence is included solely in the definition of the yield function f：

$$f\left(\sigma_{ij}, \kappa, \nabla^2\kappa\right) = 0 \tag{2.2}$$

where κ is the hardening parameter and ∇^2 is the second order of Laplacian.

Gradient plasticity offers a notable advantage over nonlocal theory in that the consistency condition results in a partial differential equation instead of an integral differential equation.

$$\dot{f} = n_{ij}^T \dot{\sigma}_{ij} - h^p \dot{\lambda} + g^p \nabla^2 \dot{\lambda} = 0 \tag{2.3}$$

where n_{ij}, h^p and g^p are given by,

$$n_{ij} = \frac{\partial f}{\partial \sigma_{ij}} \tag{2.4}$$

$$h^p(\kappa, \nabla^2\kappa) = -\frac{\dot{\kappa}}{\dot{\lambda}}\frac{\partial f}{\partial \kappa} \tag{2.5}$$

$$g^p(\kappa) = \frac{\dot{\kappa}}{\dot{\lambda}}\frac{\partial f}{\partial \nabla^2 \kappa} \tag{2.6}$$

in which n_{ij} is the gradient to the yield function; h^p is the hardening modulus; $\dot{\lambda}$ is a plastic multiplier and g^p is a gradient influence variable. For strain softening, the hardening modulus h^p is negative and the additional variable g^p must be positive. When $g^p = 0$, the theory reverts to the classical plastic flow theory. However, when $h^p < 0$ the tangential stiffness matrix D^{ep} becomes non-symmetric, leading to a tendency towards instability. The objective of the strain-gradient enhanced approaches is to maintain the well-posedness of the governing equations for materials that do not meet the material stability requirement. The gradient term present in Equation (2.6) can act as a stabiliser when $h^p < 0$ which ensures that the governing partial differential equation (Equation 2.3) maintains ellipticity even after the onset of strain localisation. Moreover, when addressing mesh dependency issues in finite element analysis, the strain-gradient theory is also implemented by introducing the concept of an internal length. The gradient influence variable g^p can be expressed as $g^p = -h^p l_c^2$ （Pamin, 1994), and the mesh-independent result of strain-gradient theory under the biaxial compression test is shown in Figure 2.4.

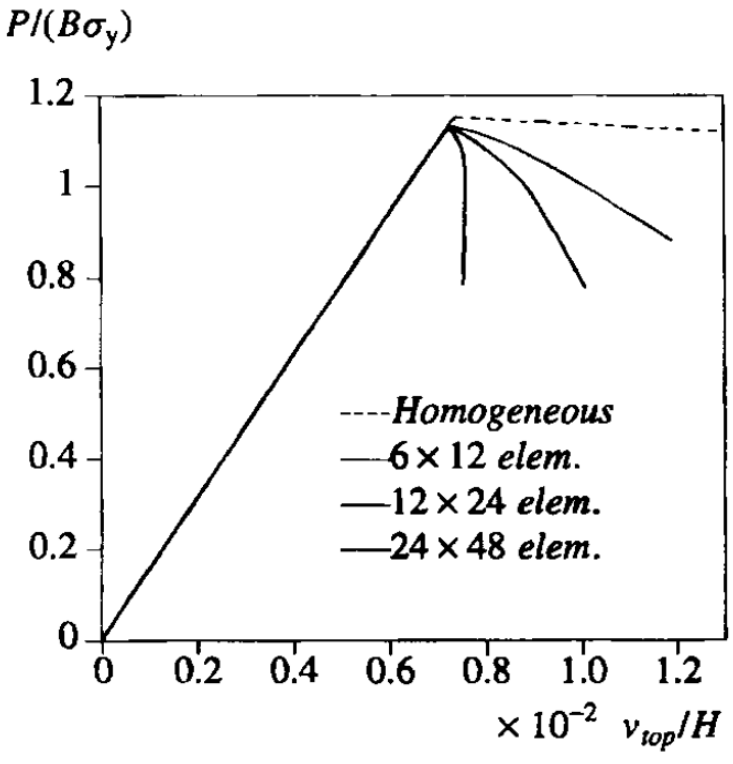

(a)

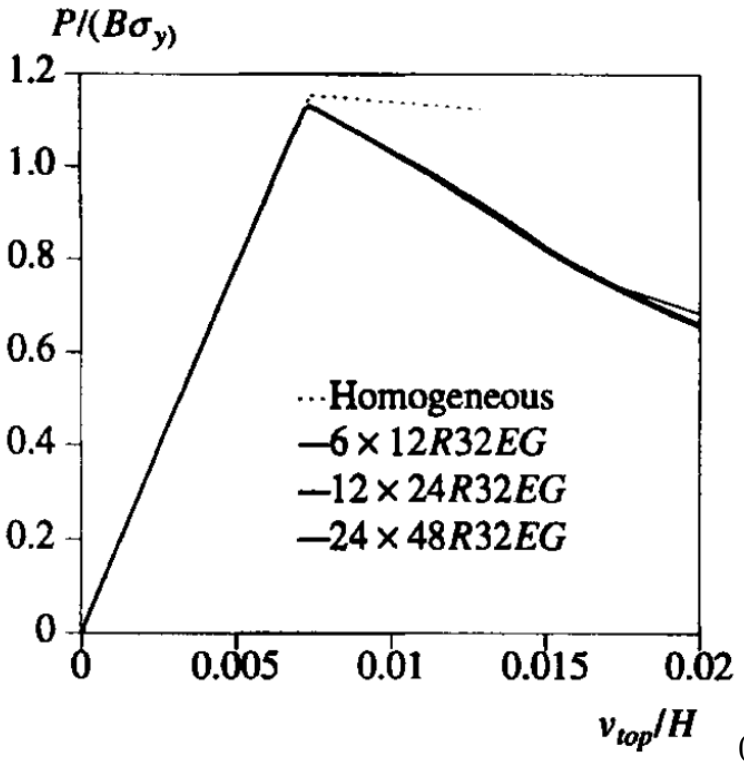

(b)

Figure 2.4 Load-displacement diagrams for (a) Classical continuum and (b) Strain-gradient model (de Borst and Pamin, 1996)

The nonlocal implicit gradient theory, utilising the Helmholtz-type PDE, has been effectively combined with various models to regularise ill-posed boundary value problems (BVPs) in the context of concrete and soils. These combinations include plasticity models (Miehe et al., 2013), damage models (Zreid and Kaliske, 2016), and a mesh-adaption framework (Na et al., 2019). More recently, within a thermodynamics framework (Forest, 2009), several classes of high-order continuum approaches have been proposed. Examples of these include the tensorial gradient plasticity model (Poh et al., 2011), large-deformation gradient plasticity model (Anand et al., 2012), and non-associative pressure-dependent gradient plasticity model (Lü et al., 2020). Thus, the implicit gradient theory has enabled the natural derivation of the generalised balance equation and nonlinear constitutive relations between generalised stresses and strains through the additional micro-variable and the conjugate generalised stresses.

Moreover, there are still some differences between explicit and implicit gradient-enhanced approaches. Firstly, in the implicit gradient-enhanced softening model, spatial interactions extend across the entire domain, similar to the nonlocal model (Peerlings et al. 2001). This

means that the effects of deformation at any point can influence other points throughout the domain. On the other hand, the explicit gradient-enhanced softening formulation is considered local in a mathematical sense. This means that the nonlocal strain at a particular point depends solely on the local strain and its gradients at that same point. In this situation, spatial interactions are limited to an infinitesimal neighbourhood around each point. As a result, the influence of deformation is confined to a localised region rather than spanning the entire domain. Secondly, fourth-order displacement derivatives in the equilibrium equations were introduced by an explicit gradient-enhanced approach. Stronger continuity requirements were imposed on displacements by the explicit gradient-enhanced softening formulation compared to the implicit gradient-enhanced softening and nonlocal approaches. These stronger continuity requirements can pose challenges under some specific circumstances, for stance, singular deformation fields or strongly localised. Meeting these requirements may be difficult, and it can significantly impact the predicted response of the material.

2.4 Micro-polar continuum approach

Cosserat brothers first proposed the Cosserat theory, also known as the micro-polar theory (Cosserat and Cosserat, 1909). The Cosserat theory enables us to describe the rotational and translational deformations of grains at the particle level by introducing three additional degrees of freedom of a single grain. Micro-rotations are related to micro-curvatures and couple stresses. A rotational degree of freedom is defined with the rotation axis orthogonal to the 2D plane, the micro-curvatures are spatial derivatives of the rotational degree of freedom, and the coupled stresses energetically conjugate to the micro-curvatures. The moment stresses (moment per area) are provided by the rotational degree of freedom. Therefore, the material may then oppose a couple stress to the development of curvature (Khoei et al. 2007). The introduction of the couple stress leads to a non-symmetric stress tensor (Ebrahimian et al. 2012). Moreover, the internal length scale relates a couple stress to micro-curvature. This internal length scale can be introduced to the constitutive model to control the shear band thickness and regularise the strain softening.

In the beginning, the fundamental linear equations of Cosserat elasticity were derived based on the Cosserat theory, and the solution was obtained by Mindlinin (1965). Then, Neuber (1965) applied this theory to distribute the surrounding stress of a circular hole under

uniaxial tension. The Cosserat continuum theory became popular in geomechanics in the mid-1970s. The finite element method with independent rotations began with Mülhaus et al. (1987). The thickness of shear bands in granular materials was analysed by Cosserat kinematics continuum theory in a two-dimensional problem. This is a significant implementation of the Cosserat continuum in strain localisation. The overall rotation (ω_{ij}) was used in the continuum equations of their work, which is different from the grain or the Cosserat rotation (ω_{ij}^{c}). Thus, non-symmetric stain and stress tensors were caused by the deviation in the rotation (couple stress), which differs from classical tensors.

The classic strain tensors can be divided into an antisymmetric (spin tensor) and a symmetric component (stretch tensor). Due to the differences in displacement gradients, the spin tensor is generally related to micro-rotation (Liu, 2018). However, the classic strain tensors of conventional continuum mechanics only consider macro-rotation, which fails to capture the real kinematics, such as micro-rotation in granular materials. Thus, Cosserat theory (micro-polar theory) is proposed by independent micro-rotations of material points, as seen in Figure 2.5 (an element having four material points):

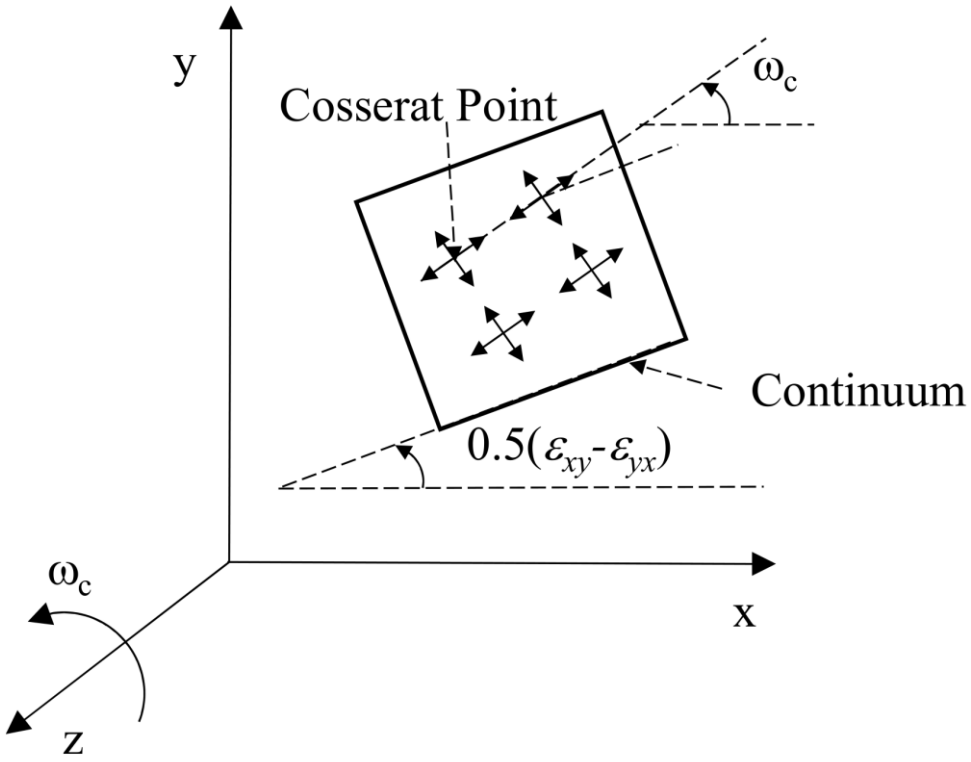

Figure 2.5 Separation between micro-rotation and macro-rotation in 2D space and their effect on the kinematics (Liu, 2018)

In the two-dimensional Cosserat continuum, each material point possesses three degrees of freedom. These degrees of freedom consist of two translational degrees (u_x, u_y) and one rotational degree (ω_z). This configuration aligns with the representation of rotation for particles with a rotational axis perpendicular to the two-dimensional plane. The displacement vector u can be expressed as follows:

$$u = [u_x, u_y, \omega_z]^T \tag{2.7}$$

During deformation, the displacement of each element is displaced by (u_x, u_y) while it is rotated by the angle ω_z around the z-axis.

The corresponding strain vector is defined as:

$$\varepsilon = [\varepsilon_{xx}, \varepsilon_{yy}, \varepsilon_{zz}, \varepsilon_{xy}, \varepsilon_{yx}, k_{xz}l_c, k_{yz}l_c\ ]^T \tag{2.8}$$

where l_c is defined as the internal length scale, taken into the strain tensor to make all components dimensionless. k_{xz} and k_{yz} are the micro curvatures.

The k_{xz} and k_{yz} are introduced in the Cosserat continuum and are defined as:

$$k_{xz} = \frac{\partial \omega_z}{\partial x},\ k_{yz} = \frac{\partial \omega_z}{\partial y} \tag{2.9}$$

The strain components in the Cosserat continuum are defined as:

$$\varepsilon_{xx} = \frac{\partial u_x}{\partial x}\ ,\ \varepsilon_{yy} = \frac{\partial u_y}{\partial y} \tag{2.10}$$

$$\varepsilon_{xy} = \frac{\partial u_y}{\partial x} - \omega_z,\ \varepsilon_{yx} = \frac{\partial u_x}{\partial y} + \omega_z \tag{2.11}$$

The corresponding stress vector is defined as:

$$\sigma = [\sigma_{xx}, \sigma_{yy}, \sigma_{zz}, \sigma_{xy}, \sigma_{yx}, \mu_{xz}l_c, \mu_{yz}l_c\ ]^T \tag{2.12}$$

where μ_{xz} and μ_{yz} are the couple stress tensor.

As Figure 2.6 shows, the stress distribution becomes unsymmetric when additional rotational degrees of freedom are applied to two-dimensional problems. This is caused by the existence of a rotational degree of freedom and couple stresses.

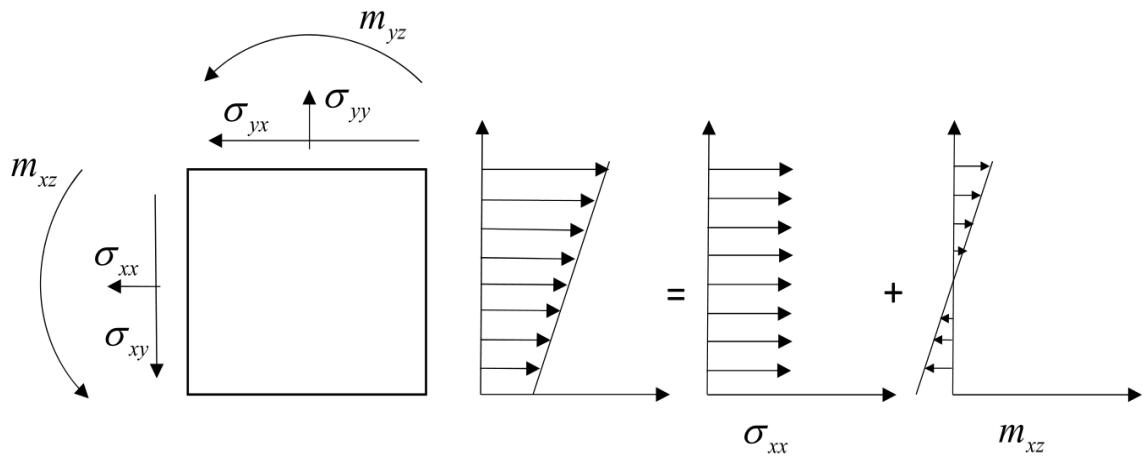

Figure 2.6 Asymmetry stress distribution in micro polar theory (Liu,2018)

The stress and strain tensors can be decomposed into the symmetric and skew-symmetric parts, in which the symmetric tensors $[\sigma]_{sym}$ and $[\varepsilon]_{sym}$ introduce the stress and strain tensors in the classical continuum and the skew-symmetric tensors $[\sigma]_{skw}$ and $[\varepsilon]_{skw}$ indicate the effects of couple stress and rotation in the Cosserat continuum.

The strain tensor can be rewritten as:

$$\varepsilon_{ij} = \frac{\partial u_i}{\partial x_i} - e_{ijk}\omega_z \tag{2.13}$$

where u_i is the component of the displacement vector, and e_{ijk} is Ricci permutation tensor which is defined as a completely antisymmetric tensor in three dimensions. $e_{ijk} = 1$ if (i, j, k) is an even permutation of (1, 2, 3), $e_{ijk} = -1$ if (i, j, k) is an odd permutation, and $e_{ijk} = 0$ if any index (i, j, k) is repeated. In three dimensions only, the cyclic permutations of (1, 2, 3) are all even permutations, similarly the anticyclic permutations are all odd permutations. This means in three dimensions, it is sufficient to take cyclic or anticyclic permutations of (1, 2, 3) and easily obtain all the even or odd permutations. From Equation (2.13), it is clear that the strain tensor is not symmetric. The gradient of the micro-rotation vector is known as the micro-curvature tensor and is defined in the form of:

$$k_{ij} = \frac{\partial \omega_i}{\partial x_i} \tag{2.14}$$

while the strain tensor ε_{ij} is work conjugate to the stress tensor σ_{ij}, the curvature tensor k_{ij} is work conjugate to the couple stress tensor μ_{ij}.

The constitutive equations governing an elastic Cosserat medium can be expressed as:

$$\sigma_{ij} = E_{ijkl}\varepsilon_{kl} \tag{2.15}$$

$$\mu_{ij} = M_{ijkl}k_{kl} \tag{2.16}$$

As for the three-dimensional condition, the displacement vector u defined as follows:

$$u = [u_x, u_y, u_z, \omega_x, \omega_y, \omega_z]^T \tag{2.17}$$

The corresponding strain vector is defined as:

$$\varepsilon = [\varepsilon_{xx}, \varepsilon_{yy}, \varepsilon_{zz}, \varepsilon_{xy}, \varepsilon_{yx}, \ \varepsilon_{yz}, \ \varepsilon_{zy}, \varepsilon_{zx}, \varepsilon_{xz}, \ \frac{k_{xx}}{l_t}, \frac{k_{yy}}{l_t}, \frac{k_{zz}}{l_t}, \frac{k_{xy}}{l_c}, \frac{k_{xz}}{l_c}, \frac{k_{yx}}{l_c}, \frac{k_{yz}}{l_c}, \frac{k_{zy}}{l_c}, \frac{k_{xz}}{l_c}]^T \tag{2.18}$$

where l_t is the internal length related to bending couple stress.

The corresponding stress vector is defined as:

$$\sigma = [\sigma_{xx}, \sigma_{yy}, \sigma_{zz}, \sigma_{xy}, \sigma_{yx}, \sigma_{yz}, \sigma_{zy}, \sigma_{zx}, \sigma_{xz}, \mu_{xx}l_t, \mu_{yy}l_t, \mu_{zz}l_t, \mu_{xy}l_c, \mu_{xz}l_c, \mu_{yx}l_c, \mu_{yz}l_c, \mu_{zx}l_c, \mu_{zy}l_c]^T \tag{2.19}$$

The pioneering research of combining finite element code with Cosserat theory was done by de Boest (1993). The internal length was used in strain localisation at failure conditions, laying the foundation for the regularisation technique. After work by de Boest, the Cosserat continuum model was established as the regularisation approach to investigate strain localisation problems (Tejchman and Wu, 1993). The efficiency of the Cosserat theory as a regularisation technique was also investigated by Ristinmaa and Vecchi (1996). Moreover, higher grade micro-polar materials that exhibit an internal length scale were introduced by Iordache and Willam (1998). In their work, the micro-polar Cosserat continua was used to examine the regularisation properties of discontinuous bifurcation problems. Researchers have recently extended the use of the Cosseart micro-polar continuum theory as a regularisation approach in some two-dimensional problems to model strain localisation. Alsaleh and Alshibli, respectively, have enriched the theoretical research and implantation of the micro-polar method. The mesh-independent results of strain localisation in granular materials came up by their enhanced Lade's single hardening model (Alsaleh et al., 2006; Alshibli et al., 2006). In addition, Liu (2018) presented a mesh-independent result of a micro-polar model under the biaxial compression test shown in Figures 2.7-2.9.

The micro-polar models show mesh-independent results for load-displacement curves (Figure 2.7) and equivalent plastic strain distribution plots (Figures 2.8 and 2.9). In Figure 2.7(a), the strain hardening part is insensitive to the mesh size until the peak and becomes mesh-dependent in the strain softening part. Coarse mesh displays more stiff behaviours in the softening regime than in a fine mesh. In Figure 2.7(b), the load-displacement curves of the other three fine meshes coincide with each other. Moreover, as illustrated in Figure 2.8, the shear band becomes thicker when the element size becomes coarse for the classical models. In contrast, for the micro-polar model shown in Figure 2.9, the shear band thickness is almost the same for the models with different mesh sizes.

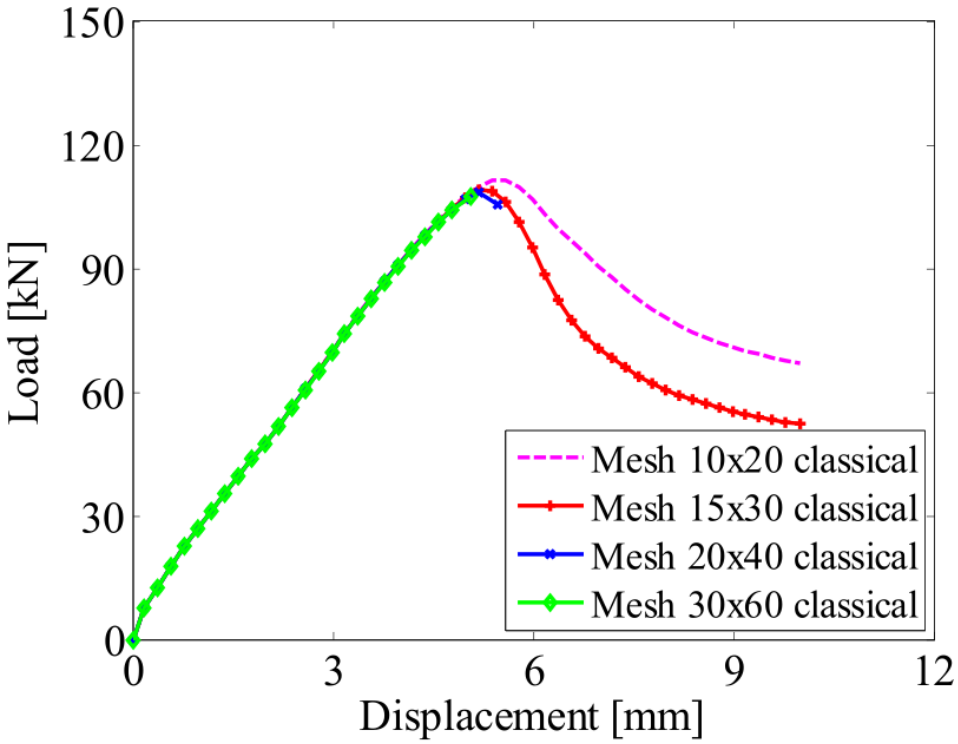

(a)

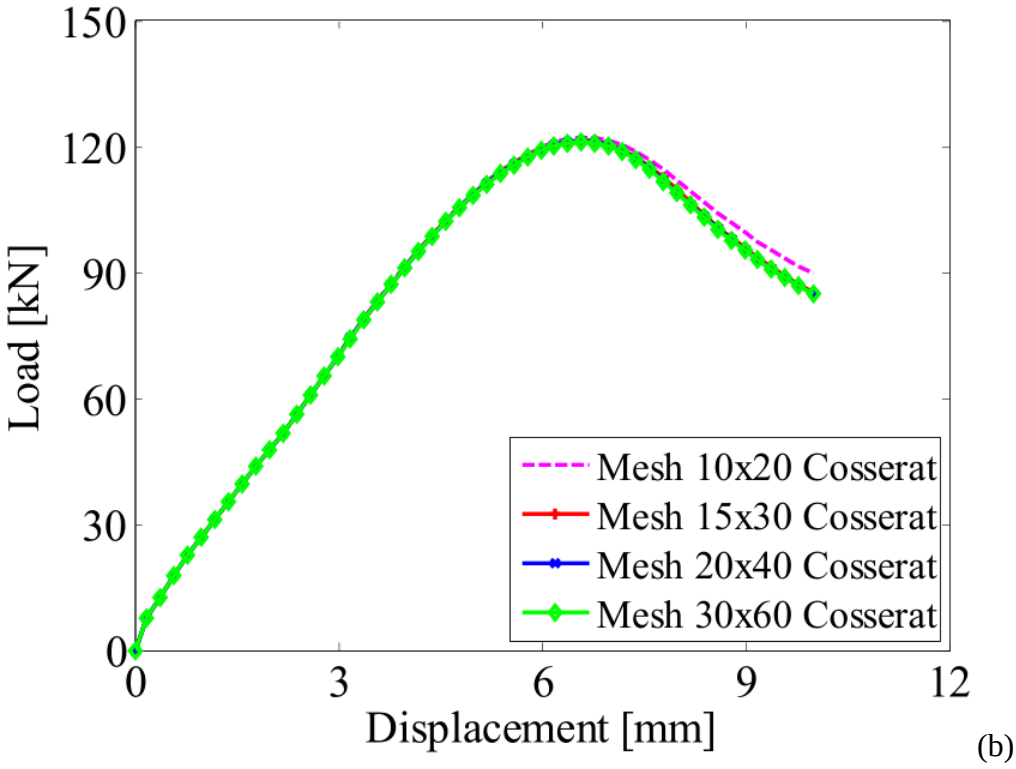

Figure 2.7 Load-displacement curve for (a) Classical continuum and (b) Micro-polar model (Liu, 2018)

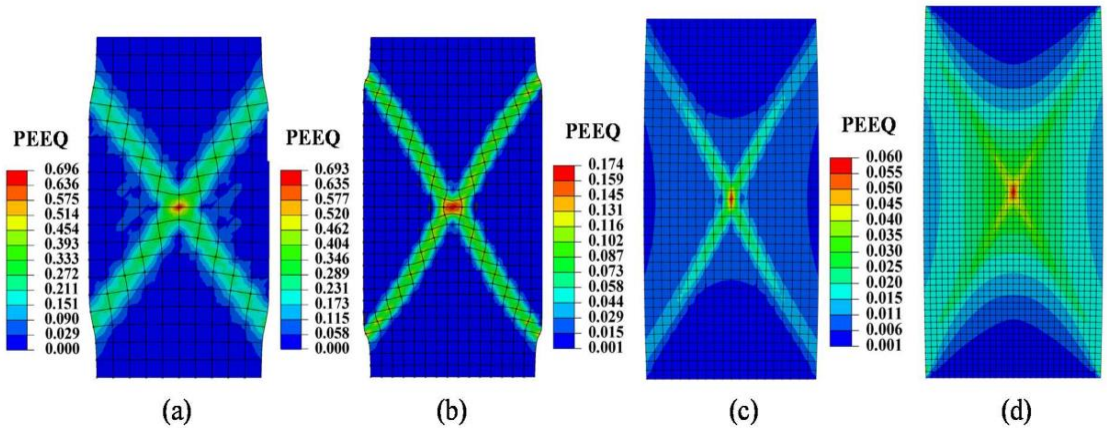

Figure 2.8 Shear bands of four different mesh sizes using the classical model: (a) mesh 10×20; (b) mesh 15×30; (c) mesh 20×40; (d) mesh 30×60 (Liu, 2018)

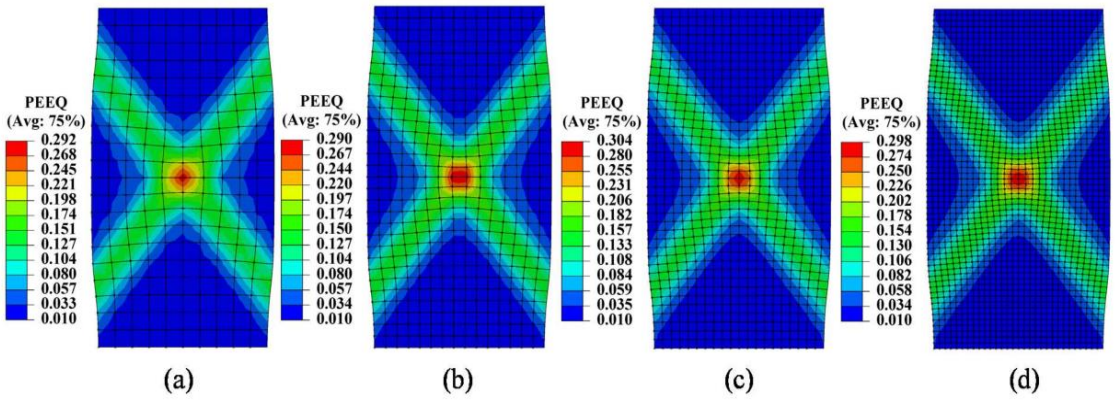

Figure 2.9 Shear bands of four different mesh sizes using the micro-polar model: (a) mesh 10×20; (b) mesh 15×30; (c) mesh 20×40; (d) mesh 30×60 (Liu, 2018)

In addition, Khoei et al. (2010) and Tang et al. (2013) presented a Cosserat micro-polar continuum model for three-dimensional problems to model strain localisation. For example, in a 3D tensile strip problem, the results indicate that Cosserat analyses regularise the localisation zone, whereas the classical solution exhibits a sudden jump at the edge of the localised region. (Figures 2.10-2.12).

For a classical model in Figure 2.10, the shear band thickness of the fine mesh is much smaller than the one obtained from the coarse mesh, and the mesh distortion can be observed. Meanwhile, the maximum value of effective plastic strain for a classical solution with fine mesh is almost twice the coarse mesh. On the contrary, the maximum values of effective plastic strain obtained by the Cosserat model from Figure 2.11 (b) are similar to one obtained from the coarse mesh in Figure 2.11 (a). Furthermore, the variations with displacement of predicted reaction are plotted in Figure 2.12 for the Cosserat and classical models using different meshes. The mesh objectivity of the Cosserat model is obvious in this figure, particularly when the internal length $l_c = 2 \text{ and } 3 \text{ mm}$. The decrease of l_c increases the mesh dependency of the solution. However, these results are much better than the classical ones.

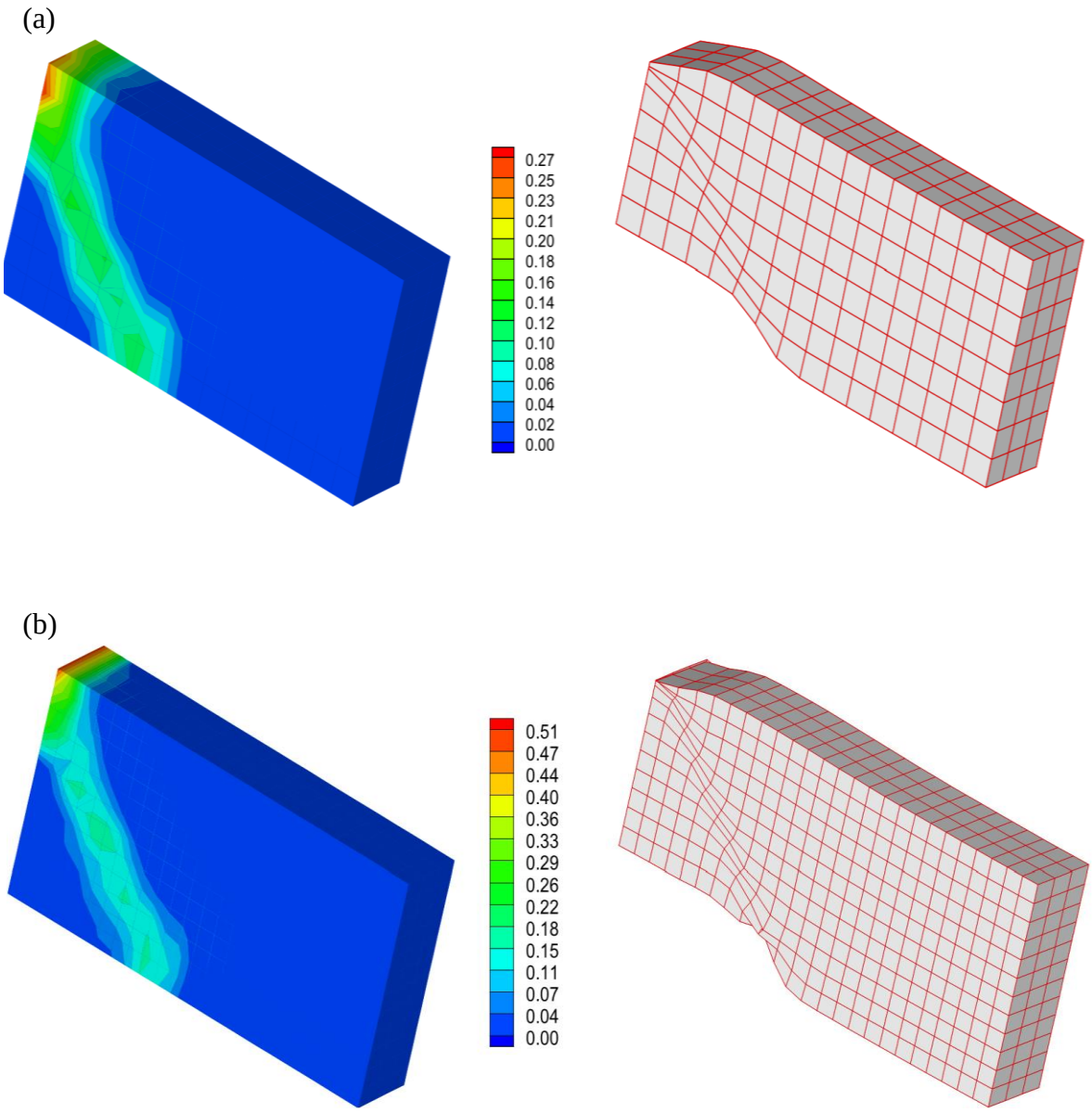

Figure 2.10 The effective plastic strain contours and deformed meshes for a strip in tensile using Classical theory: (a) coarse mesh; (b) fine mesh size (Khoei et al., 2010)

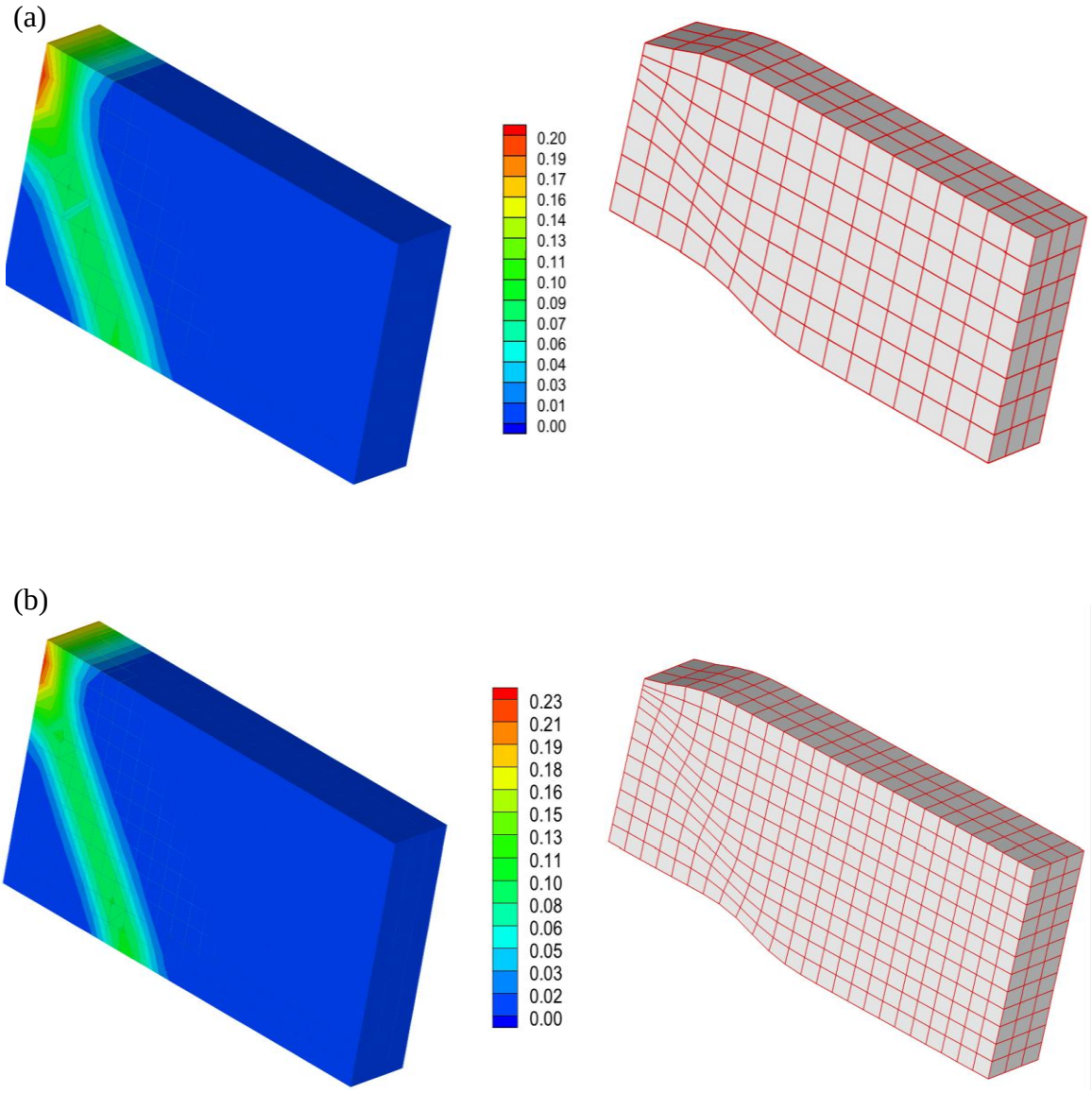

Figure 2.11 The effective plastic strain contours and deformed meshes for a strip in tensile using Cosserat theory: (a) coarse mesh; (b) fine mesh size (Khoei et al., 2010)

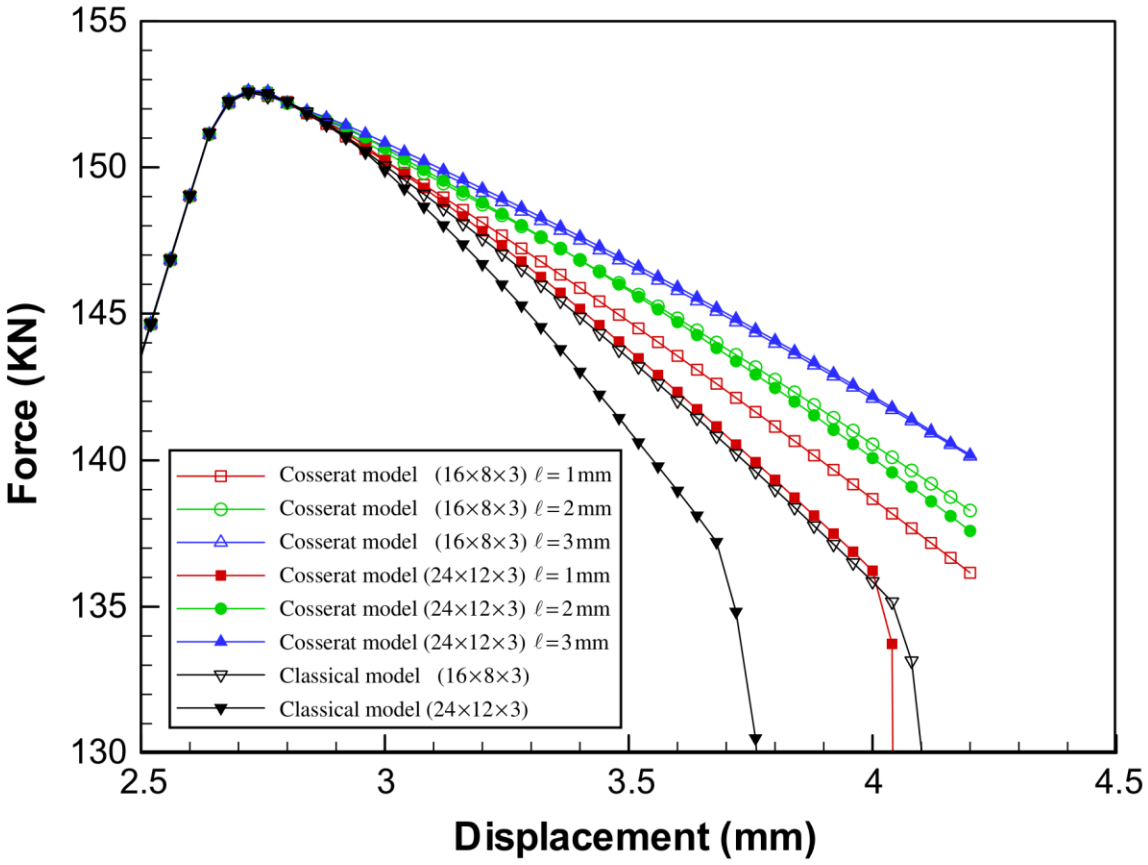

Figure 2.12 The load-displacement curves for a strip in tension; a comparison between the classical and Cosserat models at various internal length parameters **(**Khoei et al., 2010)

In summary, the micropolar approach considers the rotations of individual grains and the resulting couple stresses during shearing, even though these effects may remain negligible during homogeneous deformation. This consideration of grain rotations and couple stresses aligns with the physical behaviour observed in experiments. Therefore, the micropolar approach is believed to provide a more appropriate representation of shear zones in granular materials.

2.5 Nonlocal method

The nonlocal method is proposed based on the hypothesis that material responses should depend on the deformation field of a local material point and its neighbourhood points (Mallikarachchi, 2019). In the nonlocal approach, the softening rules of local variables usually depend on nonlocal variables (spatial averaging value of surrounding points) within a representative volume of the material (Galavi and Schweiger, 2010). The internal

characteristic length scale defines the representative volume's diameter and controls the shear band thickness and location.

At first, the nonlocal methods were implemented in various branches of physical sciences, e.g., in the optimisation of slider bearings (Rayleigh, 1918), the modelling of liquid crystals (Oseen, 1933), radiative transfer (Chandrasekhar, 1950), and electric wave phenomena in the cortex (Hodgkin, 1964). Rogula (1965) proposed a nonlocal form of the constitutive law for elastic materials. Nonlocal elasticity was subsequently refined by Eringen and Edelen (1972). All these early studies, frequently motivated by homogenisation of the atomic theory of Bravais lattices, aimed to provide a more accurate description of phenomena occurring in crystals on a scale comparable to the range of interatomic forces. They showed that nonlocal continuum models can approximate the dispersion of short elastic waves and improve the description of interactions between crystal defects such as vacancies, interstitial atoms, and dislocations (Bažant and Jirasek, 2002).

Subsequently, Eringen (1981, 1983) was the first to extend nonlocal theory from elasticity to plasticity as a way of describing the stress field at a fracture front. The nonlocal formulations of isotropic hardening plasticity in strain space were developed by Eringen (1981). After this, nonlocal theories of plasticity were formulated in stress space by Eringen (1983). According to the flow theory, Eringen (1983) considered only perfect von Mises plasticity with an associated flow rule. However, Eringen's formulation was not meant to serve as a localisation limiter. The first nonlocal formulation of softening plasticity was proposed by Bažant and Lin (1988) and was initially introduced to describe strain localisation phenomena of softening materials. They successfully implemented the plasticity nonlocal theory in their subway project, a finite element analysis of the stability of unlined excavation of grouted soil.

Recently, a great variety of nonlocal models have been introduced and developed in a significant number of studies (Lü et al., 2009; Galavi and Schweiger, 2010; Guo and Stolle, 2013; Lazari et al., 2015; Summersgill et al., 2017; Mallikarachchi and Soga, 2020; Singh et al., 2021; Gao et al., 2022; Cui et al., 2023). In these models, the selected softening variable varied with the adopted constitutive model. However, choosing the appropriate nonlocal variable can be a challenging task, as it relies on factors such as the type of material being modelled and the specific characteristics of the problem that need to be addressed.

Moreover, nonlocal methods are effective in addressing de-cohesion and slip failure mechanisms. Specificity, when considering the total stress-strain relationship without decomposing them into elastic and plastic components, nonlocal approaches prove to be more computationally efficient compared to strain-gradient models. However, the nonlocal softening approach is only efficient for weak and no discontinuity, which is related to softening with dilatant behaviour. Therefore, the dilatant granular particles such as dense sand or over-consolidated clays can be successfully modelled in the nonlocal method (Summersgill et al., 2017; Mallikarachchi and Soga, 2020; Gao et al., 2022; Cui et al., 2023). However, it is not suitable for problems involving the development of fractures and de-cohesion (Galavi and Schweige, 2010).

2.5.1 Development of nonlocal method

The original philosophy was introducing the nonlocal character to both stress and strain, which was later termed the fully nonlocal theory (Eringen and Kim, 1974; Bažant and Chang, 1984; Bažant and Jirasek, 2002). They were too complicated to be implemented in finite element formulations (Bažant and Jirasek, 2002). Eringen and Kim (1974) simplified the theory, considering only the constitutive relationship as nonlocal while equilibrium equations remain unaltered. Due to excessive computational demand, later the nonlocal treatment was applied only to the softening parameter which drives the yield stress degradation. This kind of approach was termed the partially nonlocal theory (Bažant and Pijaudier, 1988; Mallikarachchi and Soga, 2020; Singh et al., 2021; Gao et al., 2022). The selected softening variable varied with the adopted constitutive model.

(1) Fully nonlocal theory

Generally, full nonlocal softening treats both stresses and strains as nonlocal parameters. The average stress and strain in point x are defined respectively by：

$$\bar{\sigma}_{ij}(x) = \frac{1}{v}\int_{v} \omega(x,\xi)\,\sigma_{ij}(\xi)d\xi \tag{2.20}$$

$$\bar{\varepsilon}_{ij}(x) = \frac{1}{v}\int_{v} \omega(x,\xi)\,\varepsilon_{ij}(\xi)d\xi \tag{2.21}$$

where σ_{ij} and ε_{ij} are local stresses and local strains of referenced locations, respectively; x is the global coordinate which needs to be used to calculate nonlocal stresses $\bar{\sigma}_{ij}(x)$ and nonlocal strains $\bar{\varepsilon}_{ij}(x)$; ξ is the local coordinate which is a point that refers to the locations of all surrounding points and ω is the weight function of the nonlocal method, the profile of macro and micro average strain along the representative volume with the centre point x is shown in Figure 2.13.

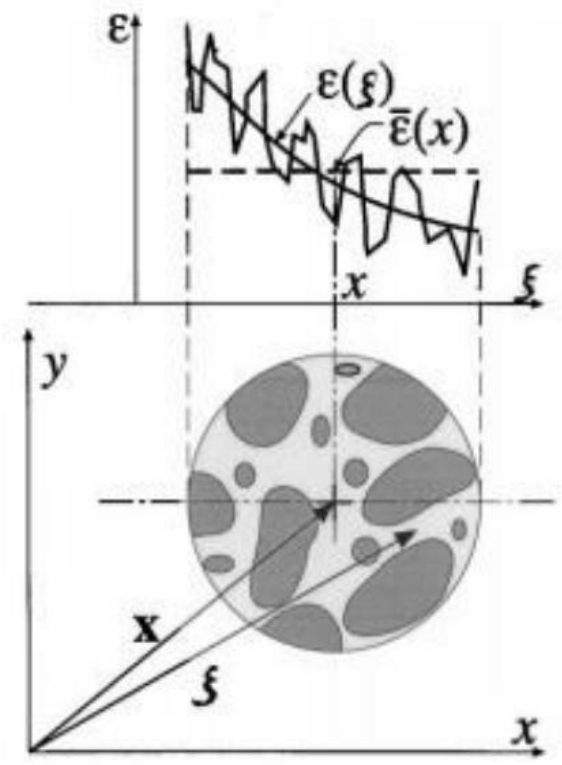

Figure 2.13 Profile of macro and micro average strain along the representative volume with the centre point x (Bažant and Jirasek, 2002)

The weighted volume v can be expressed in the following:

$$v = \int_v \omega(x, \xi)\, d\xi \tag{2.22}$$

The weighted volume is introduced to normalise the computation of the nonlocal stress and strain.

(2) Partial nonlocal theory

Fully nonlocal models are hard to implement because of the computation cost required. To overcome this difficulty, nonlocal plasticity with nonlocal hardening parameters has been developed (Bažant and Jirasek, 2002). The nonlocal softening plasticity is to treat only the scalar softening variable k as nonlocal. This method is known as partial nonlocal theory. The hardening parameter for these models can be expressed below:

$$h = h_0 + h(\bar{k}) \tag{2.23}$$

$$\bar{k}(x) = \frac{1}{v}\int_v \omega(x,\xi)\, k(\xi) d\xi \tag{2.24}$$

where h is a hardening function, k is the scalar softening variable. Partial nonlocal theory has been used to simulate the shear localisation of soils. The softening parameter, which drives the yield stress evolution, was treated nonlocal (Mallikarachchi, 2019).

2.5.2 Previous application of the nonlocal method

The nonlocal regularisation has been successfully used in various types of analyses, such as extension element tests, simple shear tests, biaxial compression tests, and for addressing boundary value problems like slopes, strip footing, and tunnel excavation (Lü et al., 2009; Galavi and Schweiger, 2010; Guo and Stolle, 2013; Lazari et al., 2015; Summersgill et al., 2017; Mallikarachchi and Soga, 2020; Singh et al., 2021; Gao et al., 2022; Cui et al., 2023).

In the beginning, several studies applied the over-nonlocal (ON) method for nonlocal regularisation.

$$\bar{\varepsilon}_{ij}(x) = (1 - \mathrm{m})\varepsilon_{ij}(\xi) + \frac{\mathrm{m}}{v}\int_v \omega(x,\xi)\, \varepsilon_{ij}(\xi) d\xi \tag{2.25}$$

where m is the over-nonlocal parameter.

Vermeer and Brinkgreve (1994) first used this method in a one-dimensional problem. An analysis was conducted on the deformation of a steel tension bar, specifically focusing on necking. The study involved applying prescribed displacements at both ends of a 100mm bar and introducing a 0.1% reduction in the tensile strength of the central Gaussian integration point. This simulation aimed to simulate an imperfection and trigger softening in

the material. Various meshes with different numbers and sizes of elements were utilised to evaluate the mesh dependence. Two sets of values for ON method parameter m and internal length (l_c) were examined: $m = 2.0$ with $l_c = 8.326mm$, and $m = 6.763$ with $l_c = 4.0mm$ These sets were chosen to ensure that the shear band or necking width remained consistent for a given local plastic strain distribution when combined with the ON method equations. The results demonstrate the validity of the ON method under these conditions.

Brinkgreve (1994) expanded the study on the ON method to two-dimensional analysis. The Drucker-Prager (DP) model, incorporating cohesion softening, was employed to simulate biaxial compression tests on drained clay samples. The softening variable chosen was the total volumetric strain, which was averaged using the ON method formulation. By selecting an appropriate value for the ON method parameter m, Brinkgreve successfully obtained force-displacement curves and the thickness of the shear band with different mesh sizes. Based on their findings, Brinkgreve (1994) recommended a parameter value of 2.0 for the ON method. Using total strain instead of plastic strain proved to be computationally efficient in this case. Fig. 2.14 shows the results from this study. It is evident that the nonlocal DP model produced mesh-independent results.

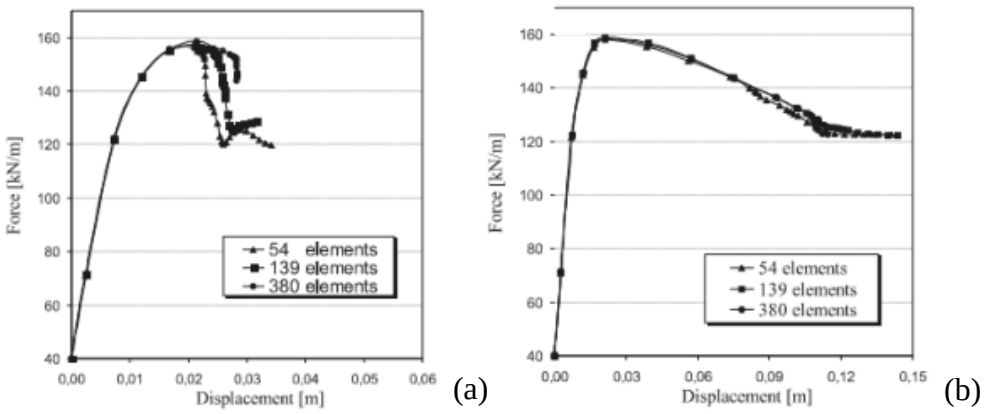

Figure 2.14 Force-displacement curves of (a) local and (b) nonlocal Drucker-Prager models (Vermeer and Marcher, 2000)

Galavi and Schweiger (2010) proposed a new weight function (G&S function) based on the Gaussian distribution (GD) method. A drained sand sample with a height of 1m and a width of 0.5m was tested using biaxial compression tests. The nonlocal regularisation is implemented in two different materials, one with $c' = 0$ and φ'softening (friction softening)

and the other one with constant φ' and c' softening (cohesion softening). The softening depends on the damage strain, which is a function of the plastic volumetric and shear strains. The damage strain is assumed nonlocal for the regularisation.

Figure 2.15 and 2.16 demonstrates the force-displacement curves and shear strain contours for friction softening and cohesion softening, respectively. In the case of friction softening (Figure 2.15), the method reduces the mesh dependency significantly, but a slight discrepancy in curves near the residual state can be observed. Galavi and Schweiger (2010) have attributed this discrepancy to a decrease in dilation near the residual state because the reduction in dilation angle changes the type of problem from a weak or no discontinuity problem to an almost strong discontinuity problem. In cohesion softening analysis (Figure 2.16), the dilation angle is fixed at 10°, and the difference in results is smaller. The shear band thickness for both friction softening and cohesion softening analyses are almost similar for four different mesh sizes.

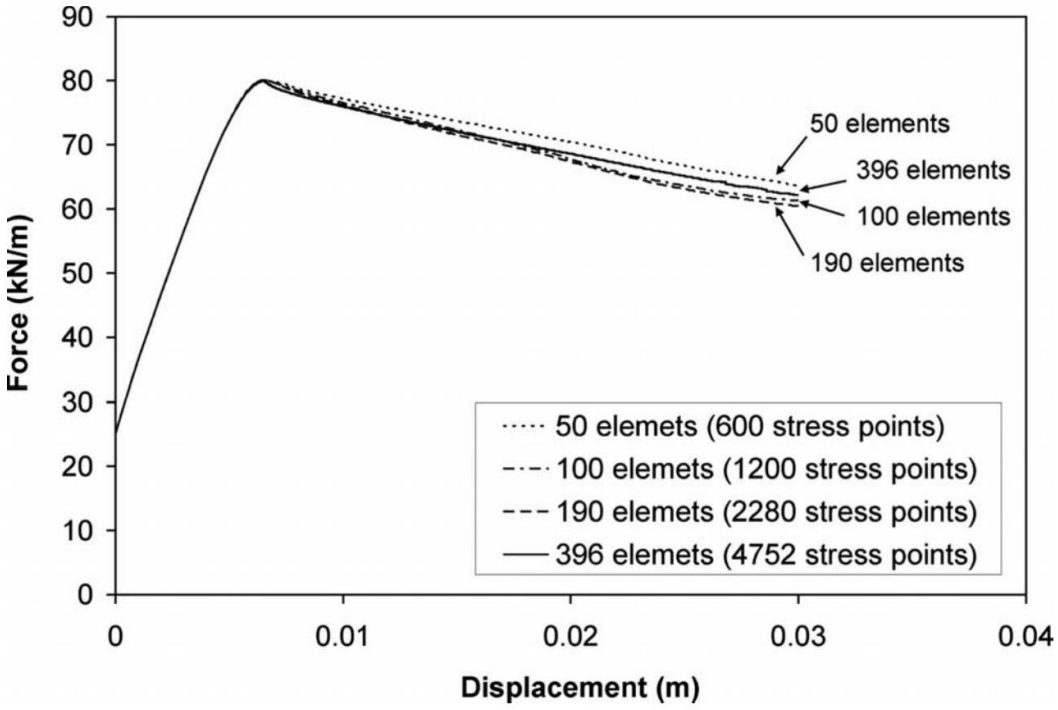

(a)

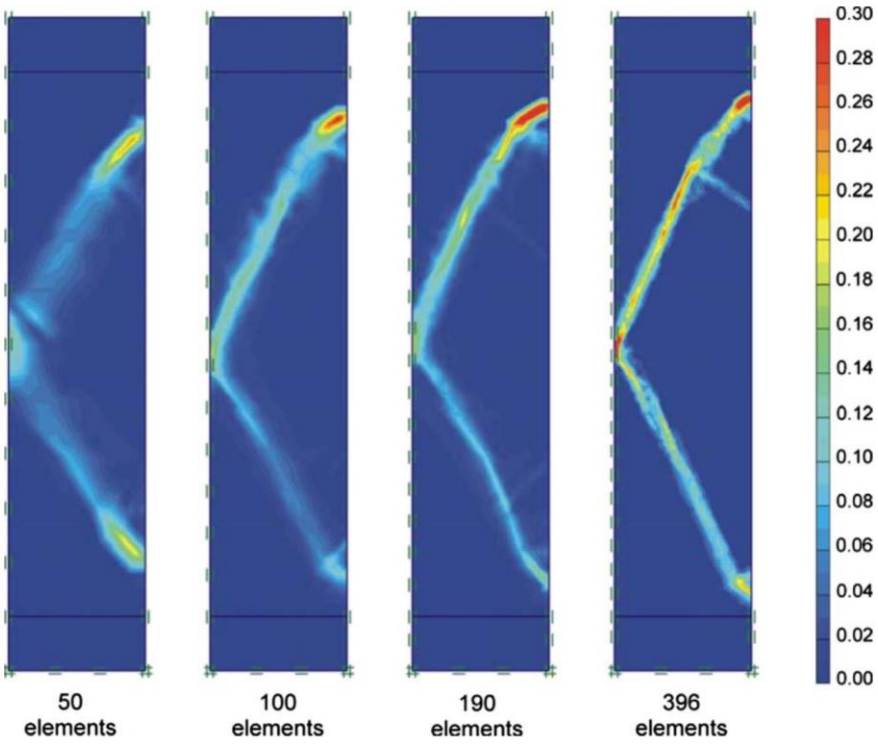

(b)

Figure 2.15 Results of the nonlocal multilaminate model with friction softening: (a) force-displacement curves and (b) contours of shear strain (Galavi and Schweiger,2010)

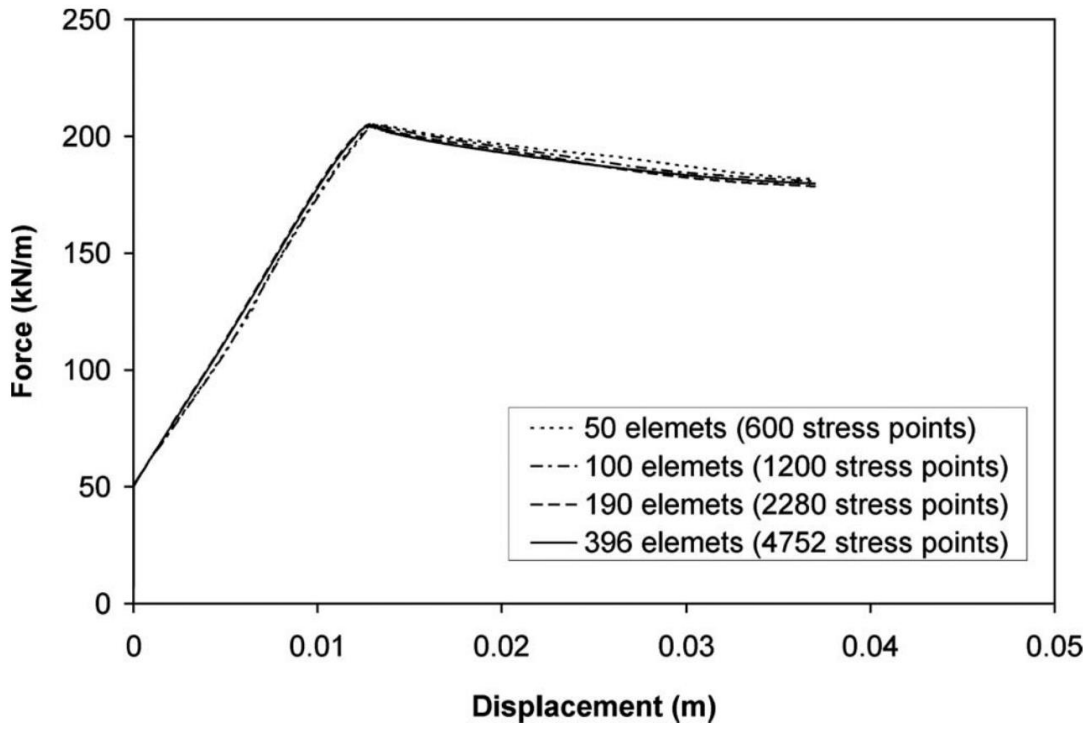

(a)

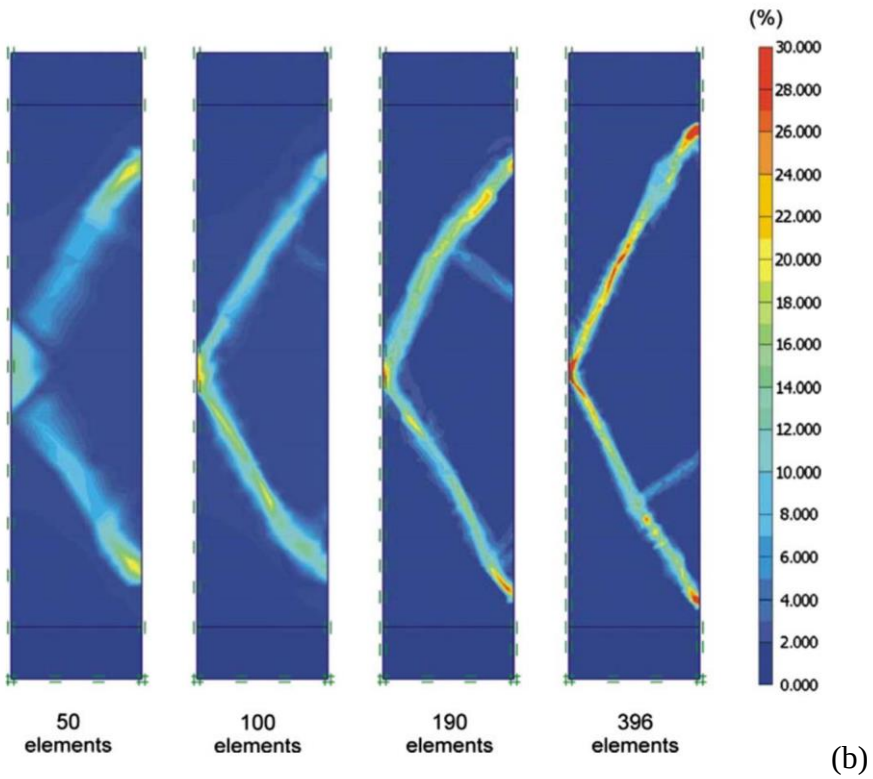

Figure 2.16 Results of the nonlocal multilaminate model with cohesion softening: (a) force-displacement curves and (b) contours of shear strain. (Galavi and Schweiger,2010)

According to Galavi and Schweigher (2010), the nonlocal method is ineffective when the mobilised dilation ceases near the residual state. Thus, further research on the nonlocal method for the dilation of dense sand was done by Mallikarachchi and Soga (2020) based on the state-dependent sand model. To validate the nonlocal method, a specimen 25 cm wide and 50 cm high was simulated in both drained and undrained biaxial compression tests. In addition, the bottom boundary conditions are such that the leftmost node is pinned, and other nodes are roller-supported. Top or side boundaries are not restrained. In this study, the G&S weight function is implemented. Since the total void ratio is a function of the rate of strain hardening and strain softening. Hence, the void ratio is treated as a nonlocal variable and regularises the strain softening.

Figure 2.17 shows the force-displacement curves predicted by the local model and nonlocal model. In the local model, the strain hardening part remains insensitive to the mesh size until reaching the peak, after which it becomes mesh-dependent in the strain softening part. Meanwhile, the softening rate decreases when the mesh size becomes coarse. In Figure 2.14(b), the nonlocal method using the G&S weight function sufficiently generates mesh-

independent force-displacement responses in the state-dependent sand model. Additionally, nonlocal averaging reduces the softening rate and delays the critical state (Mallikarachchi and Soga, 2020).

Figure 2.18 illustrates that shear band thickness for the local model is sensitive to the mesh size. The thickness of the shear band becomes wider when the mesh size is coarse. However, employing the G&S weight function can regularise the shear band thickness, ensuring mesh independence. The nonlocal model predicts nearly the same shear band thickness for different mesh sizes.

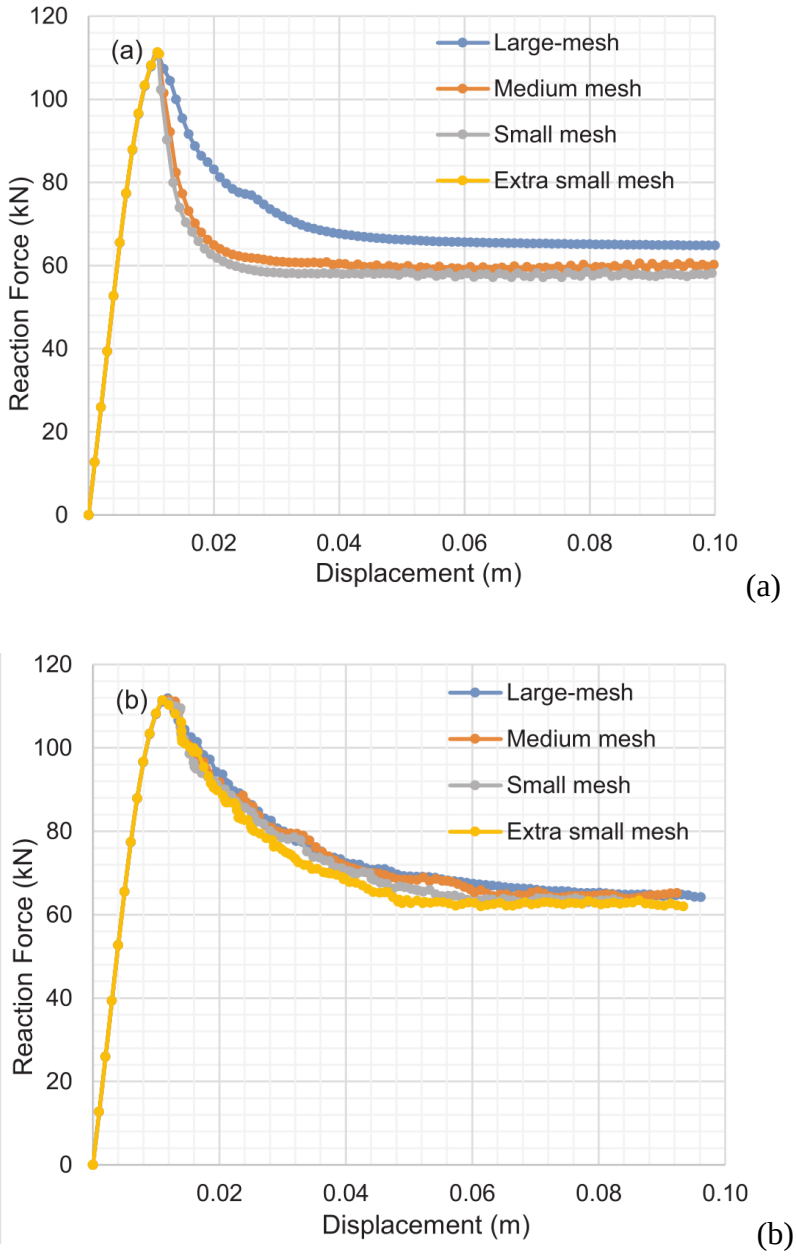

Figure 2.17 The force-displacement curves of drained dense sand were predicted with (a) the Local NS model and (b) the Nonlocal NS model. (Mallikarachchi and Soga, 2020)

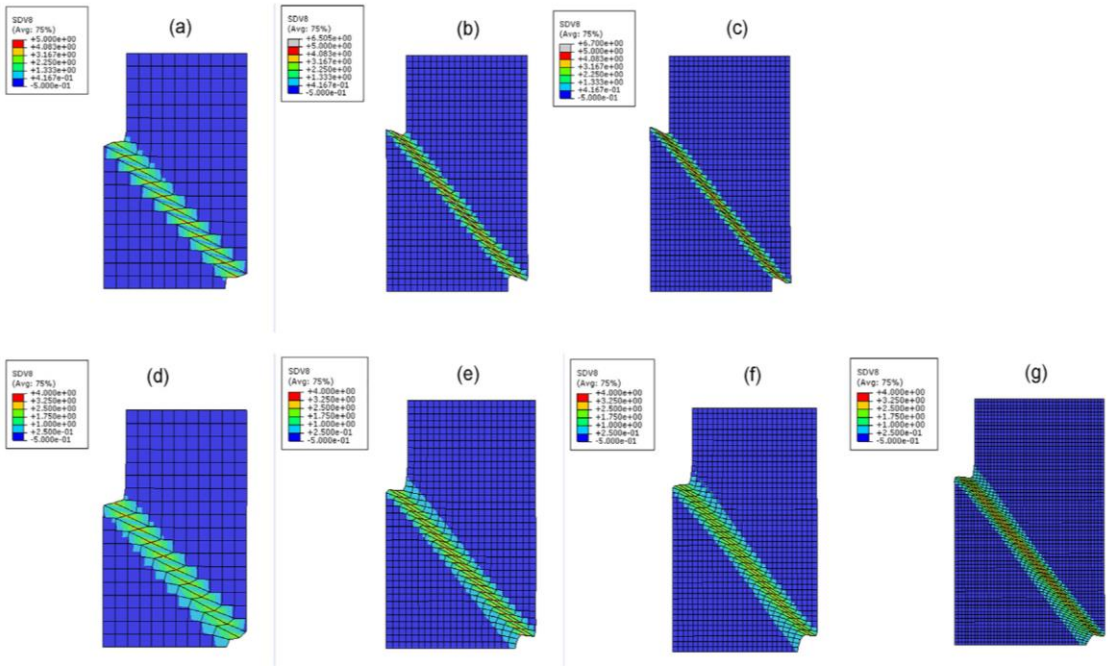

Figure 2.18 Contour plots of the deviatoric strain of drained dense sand predicted by local NS model (upper) and nonlocal model (lower) for: (a)(d) large; (b)(e) medium; (c)(f) small; (g) extra-small meshes (Mallikarachchi and Soga, 2020)

According to Figure 2.19(a) for the local model, there is an increase in the peak reaction force as the mesh becomes larger. In Figure 2.19(b), the nonlocal method utilising the G&S weight function demonstrates sufficient mesh-independent force-displacement responses under undrained conditions. The peak reaction force is almost the same for different meshes.

Regarding the contour plots of excess pore water pressure in Figure 2.20, it is observed that the shear band sucks the pore fluid, leading to an increase in negative pore pressure outside the band and a decrease inside it. In the local model, the distribution of pore water pressure appears to be mesh-dependent. Notably, the model with a coarse mesh size delays the onset of the shear band, resulting in prolonged dilative hardening. Conversely, the nonlocal model exhibits higher suction compared to the local model and maintains mesh independence.

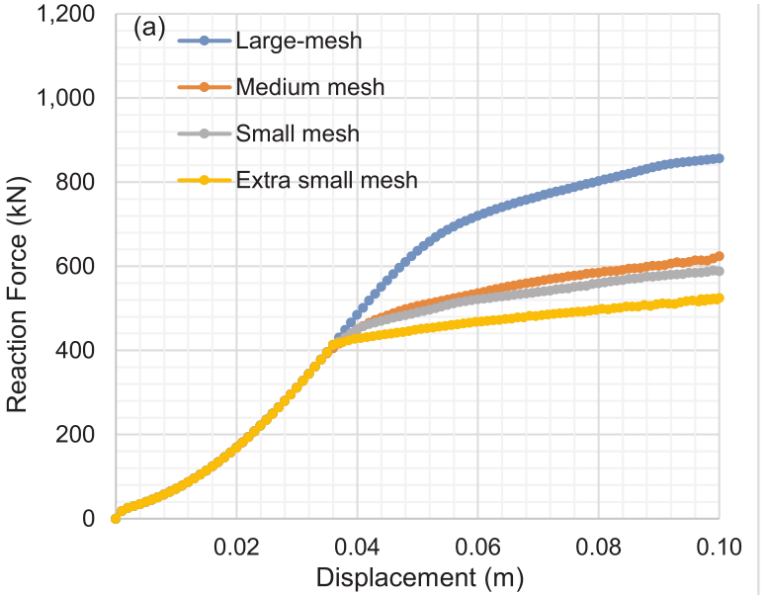

(a)

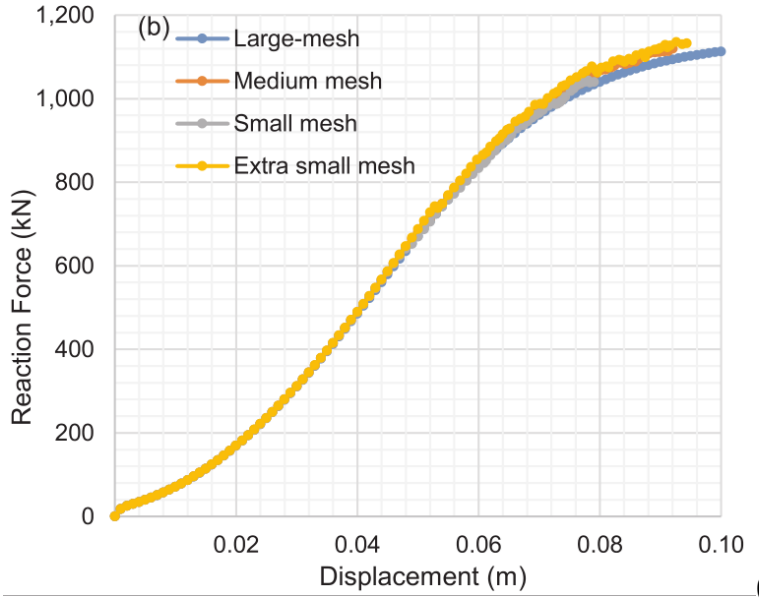

(b)

Figure 2.19 The force-displacement curves of undrained dense sand were predicted with (a) the Local NS model and (b) the Nonlocal NS model. (Mallikarachchi and Soga, 2020)

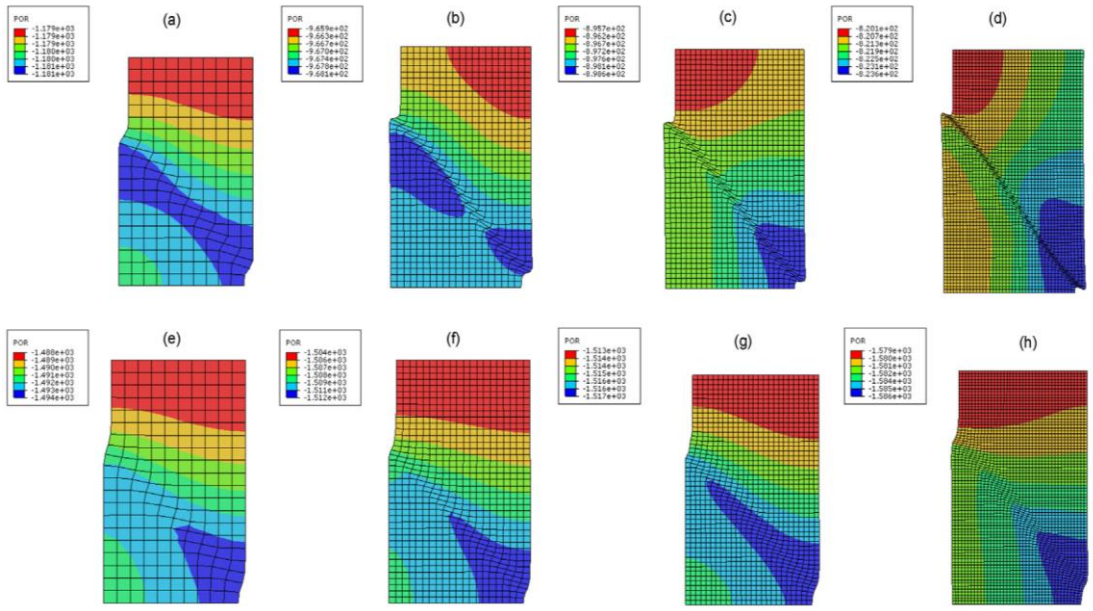

Figure 2.20 Contour plots of excess pore water pressure of undrained dense sand predicted by local NS model (upper) and nonlocal model (lower) for: (a)(d) large; (b)(e) medium; (c)(f) small; (g) extra-small meshes. (Mallikarachchi and Soga, 2020)

Jostad and Grimstad (2011) conducted a comparison between ON and G&S nonlocal methods under undrained direct, simple shear tests using the NGI-ADP Soft model. The NGI-ADP model is implemented into the in-house finite element code BIFURC, where the nonlocal strain increment (total strain increment) is calculated at the start of each iteration, and an implicit integration scheme is adopted to determine the local plastic strain. In this study, a one-dimensional shear column 100 mm high consisting of 50 horizontal layers of soft sensitive clay. The bottom of the column is fixed. The column is deformed by applying a horizontal shear stress at the top. Initially, the column is subjected to uniform deformation to produce a material shear stress - shear strain curve. To create a nonuniformity and initiate the formation of a shear band, the peak strength of the central layer is reduced by 0.1%.

Jostad and Grimstad (2011) emphasised that the thickness of the shear band will vary with the nonlocal methods. As shown in Figure 2.21, the ON method ($m = 1.58$) predicts wider shear band thickness than the G&S method when internal length ($l_c = 10\ mm$) is the same for both methods. Moreover, the ON method produced a very smooth strain distribution, whilst the G&S distribution produced a similar overall pattern with an irregular strain distribution (Jostad and Grimstad, 2011).

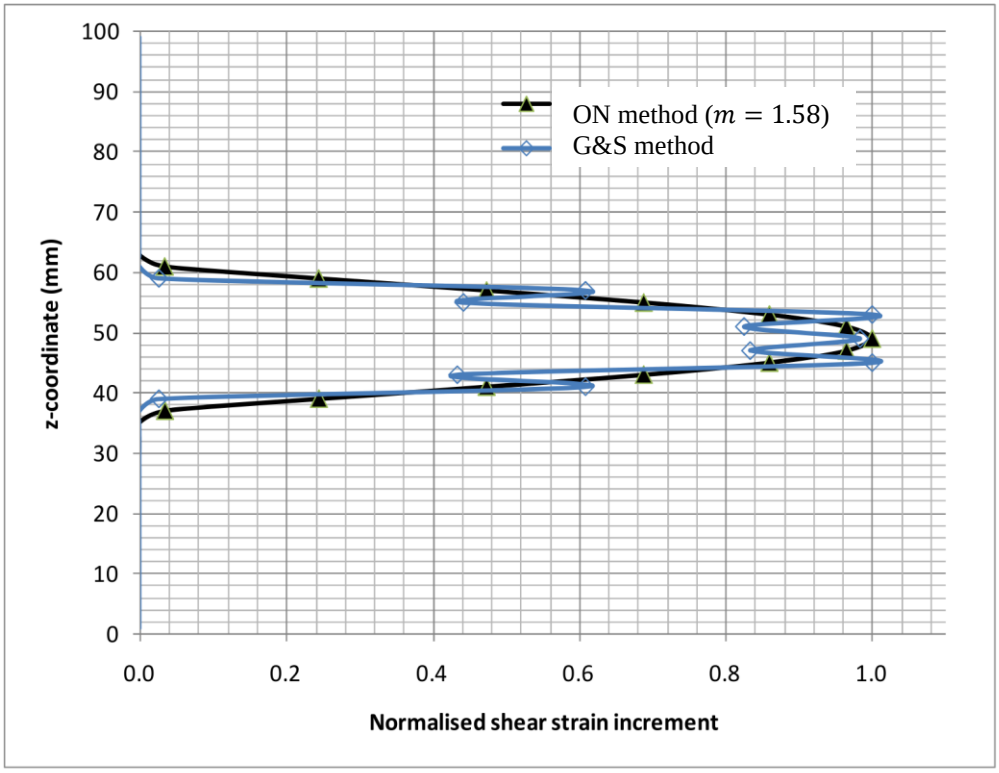

Figure 2.21 Distribution of the shear strain increment in the post-peak softening regime obtained with the ON method (black curve) and G&S method (blue curve) **(**Jostad and Grimstad, 2011)

The NGI-ADP Soft model and method are also implemented as a user-defined material model in the commercial finite element program PLAXIS (Jostad and Grimstad, 2011). This subroutine calculates the nonlocal strain from the plastic strain increment in the previous iteration. In this study, a plane strain compression test is considered. The top and bottom boundaries are assumed to be perfectly rough to trigger localisation without introducing an arbitrary perturbation. Moreover, three samples with 100 mm height and 50 mm width adopt triangular elements, and two of them are modelled by full biaxial compression named by medium and fine meshes, respectively. The bottom of the column is fully fixed, and a horizontal shear stress is applied at the top. The third model is one-quarter of the biaxial compression analysis using two lines of symmetry (SYM), which is used to study the effect of accounting for symmetry lines together with the nonlocal strain approach.

The load-displacement curves for three different nonlocal methods are shown in Figure 2.22. Various mesh sizes give almost the same results when considering the same method. The

post-peak softening rates are slightly different in the symmetric mesh. Both internal length and nonlocal method will affect the softening behaviour of the material. The suitable internal length will depend on the softening rate and the shear band thickness (Jostad and Grimstad, 2011). According to Figure 2.23, the difference in shear band thickness is obtained for different nonlocal methods. The thinnest shear band was produced by the GD method, the G&S method had thicker shear bands with the ON results producing the thickest band. Moreover, when the mesh size varies, the shear band thickness of the ON and G&S methods remains almost the same.

(a)

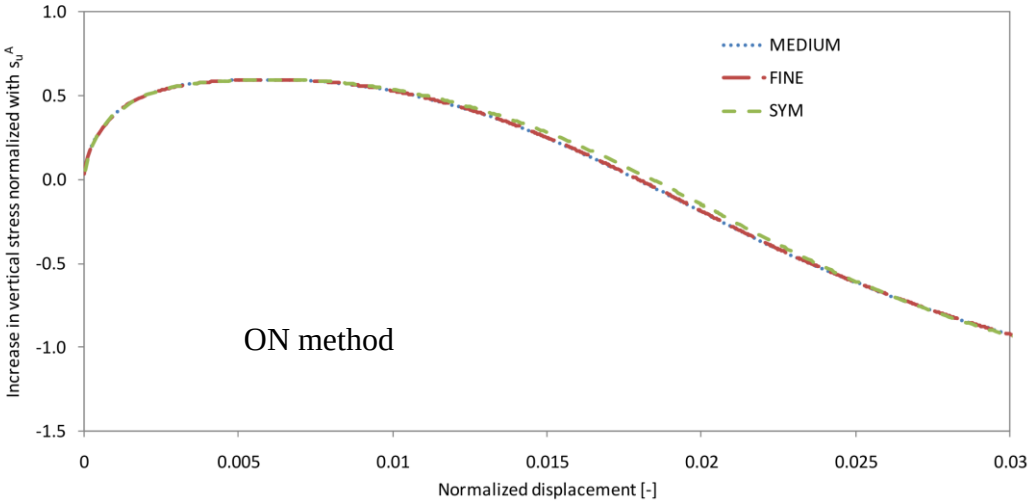

(b)

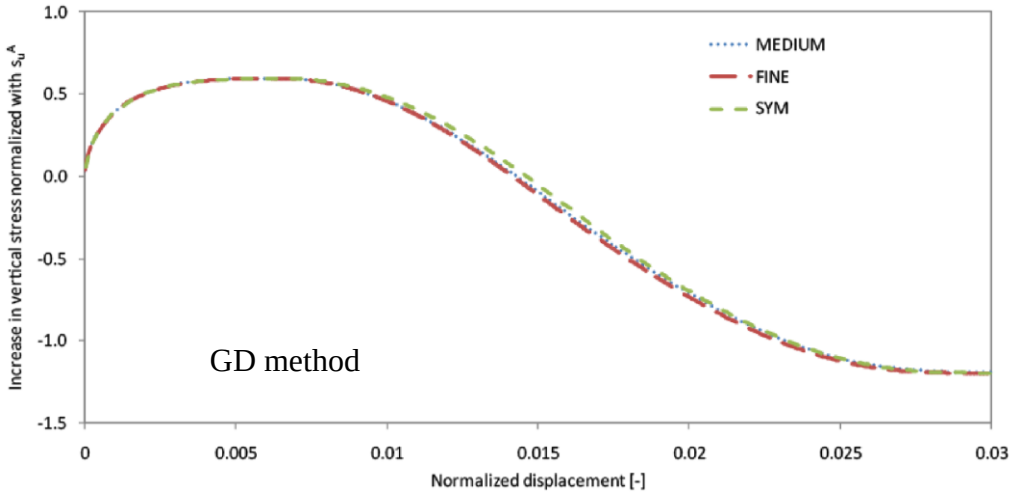

(c)

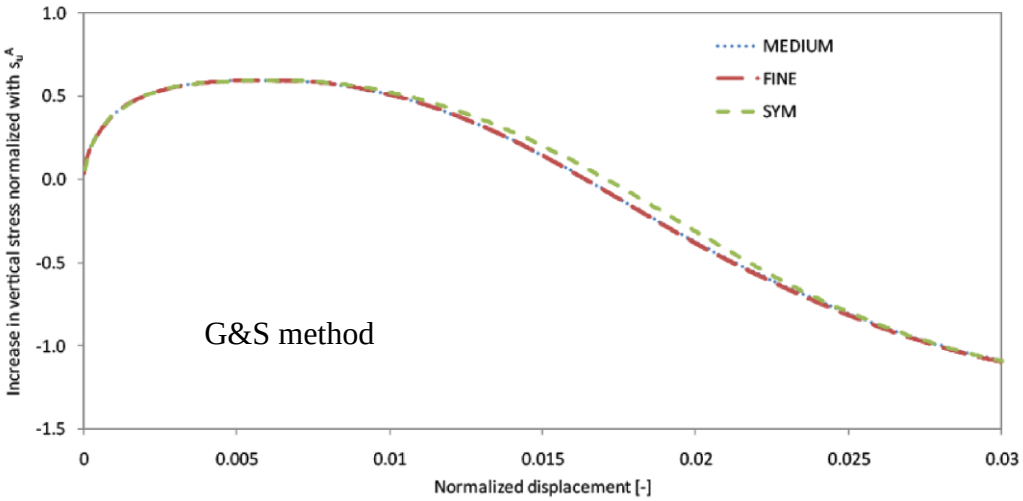

Figure 2.22 Comparison of biaxial compression results for three nonlocal strain softening methods and three meshes (Jostad & Grimstad, 2011).

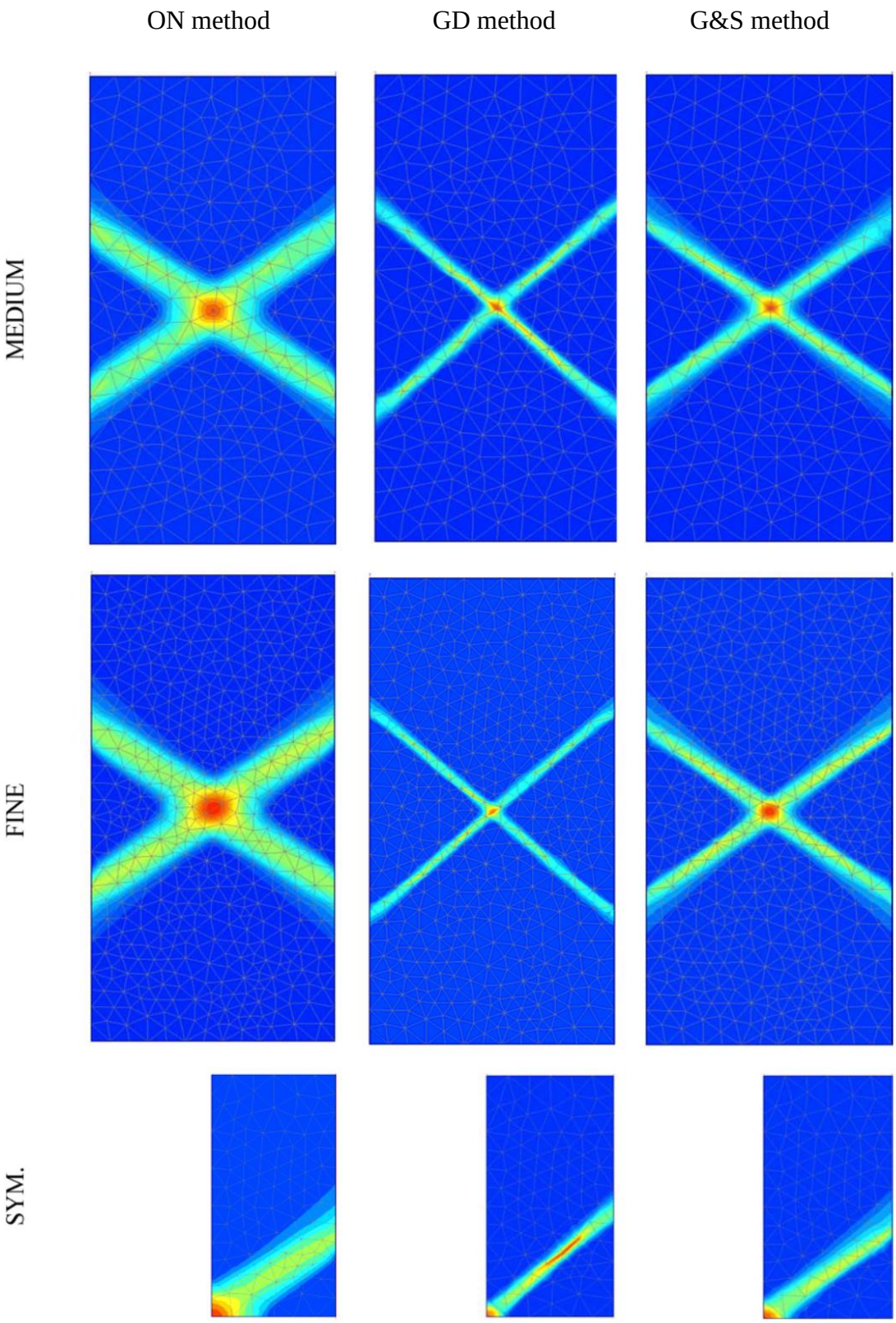

Figure 2.23 Contour plots of total shear strain for the nonlocal method

Summersgill et al. (2014) compared three nonlocal methods under undrained biaxial compression tests with the Tresca yield criterion on clay. Furthermore, the nonlocal softening variable in this study was chosen as plastic deviatoric strain. When the GD was incorporated, full objectivity of mesh intendancy could not be achieved. However, the ON and G&S methods demonstrated more efficient outcomes, as illustrated in Figure 2.24.

In the work conducted by Summersgill et al. (2017a), proposed in Figure 2.25, the simulation of biaxial compression on clay was extended using the Mohr-Coulomb yield surface under drained conditions. The nonlocal softening variable chosen for this analysis was the same as in Summersgill et al. (2014). Similar to the results shown in other papers, the nonlocal methods reduce mesh dependence in the analysis of drained biaxial compression tests, albeit not as satisfactorily as in the undrained condition (Figure 2.24). This was attributed to the formation of different patterns of slip surfaces. Summersgill et al. (2017a) concluded that the G&S method exhibits the least mesh dependence for drained and undrained simulations.

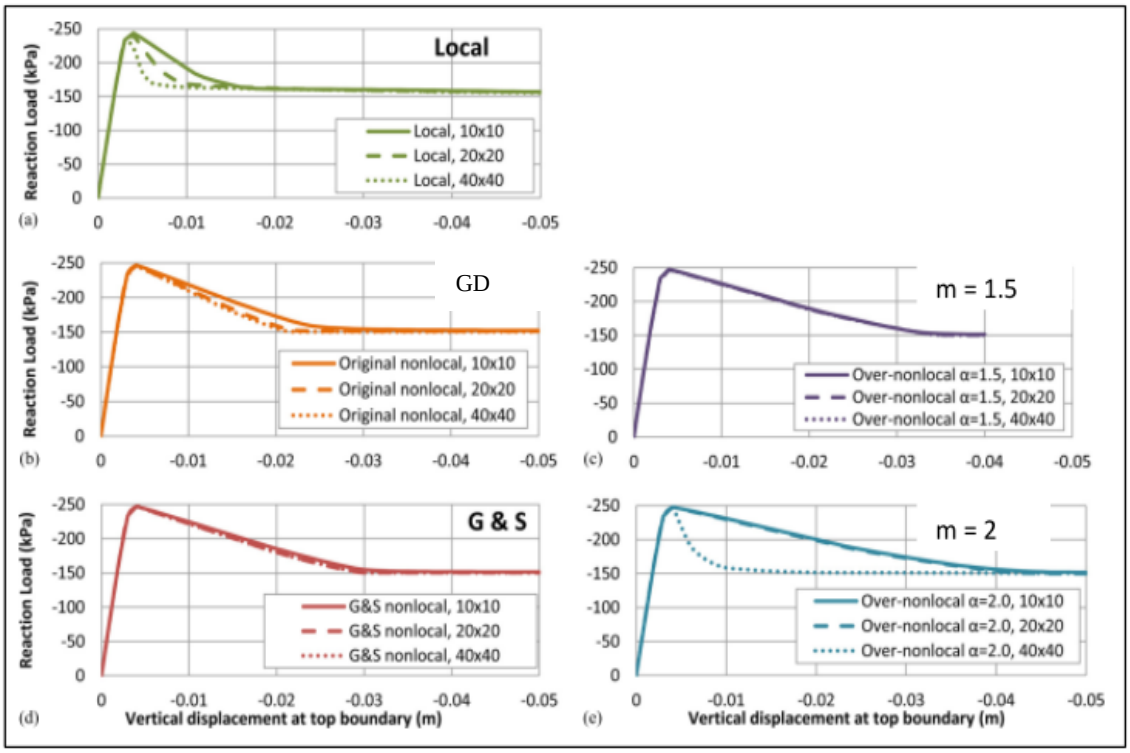

Figure 2.24 Local and nonlocal load-displacement curves for undrained analysis (Summersgill et al.,2014)

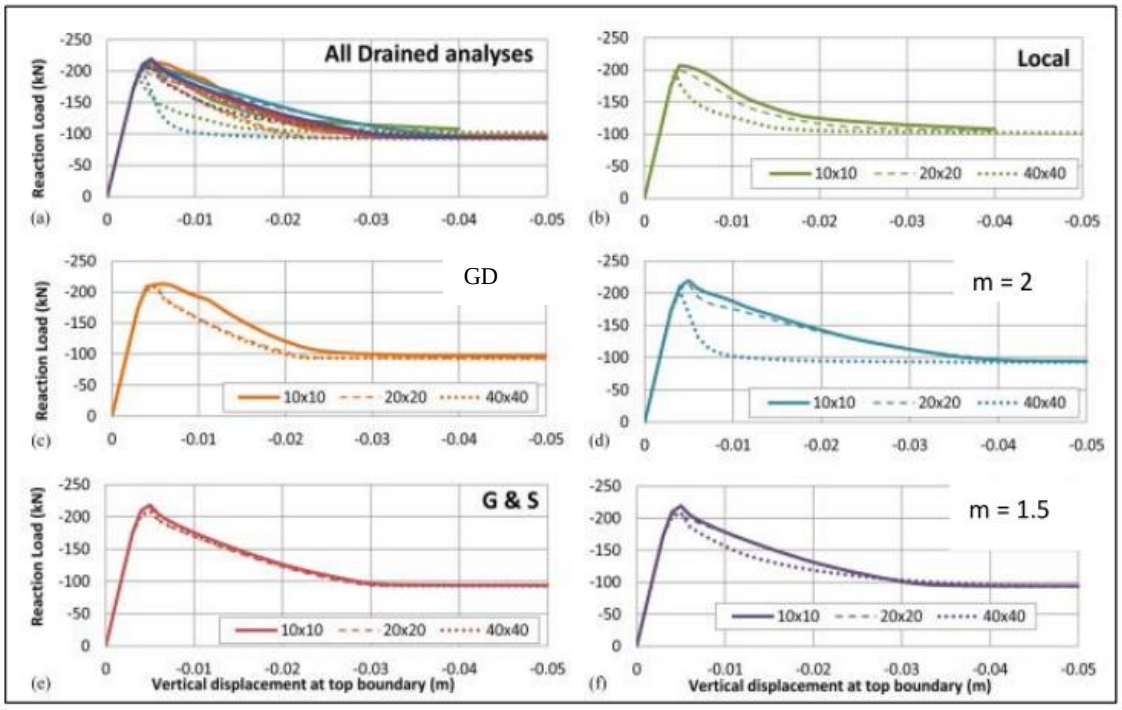

Figure 2.25 Local and nonlocal load-displacement curves for drained analysis (Summersgill et al., 2017a)

2.6 Summary

Four different regularisation methodologies were introduced and compared in this Chapter, including the viscosity regularisation method, the strain-gradient enhanced approach, the micro-polar continuum approach, and the nonlocal method. Ultimately, the decision was made to delve deeper into the nonlocal method for further investigation within this thesis, and the rest of the Chapter concluded by summarising the development and prior utilisation of the nonlocal method.

The strengths and weaknesses of each method were outlined, and the possibility of combining them was explored in the following.

(1) The primary advantage of viscosity regularisation is that it can be done at the local integration point without nonlocal averaging with neighbouring integration points. Implementation of this method is straightforward, and the computational efficiency is high. However, viscosity must be introduced to describe the material behaviour, even when the

material does not exhibit rate dependency. This limits its applicability to transient loading conditions. Furthermore, the regularising effect of viscosity regularisation diminishes rapidly for slow loading rates or when approaching the rate-independent limit.

(2) The explicit or implicit gradient-enhanced approaches avoid time-consuming calculations in nonlocal methods by introducing higher-order gradients of strain or other internal variables. However, the explicit gradient-enhanced softening formulation is considered local in a mathematical sense. This means that the nonlocal strain at a particular point depends solely on the local strain and its gradients at that same point. Therefore, the spatial interactions are limited to an infinitesimal neighbourhood around each point. Moreover, stronger continuity requirements were imposed on displacements by the explicit gradient-enhanced softening formulation. These stronger continuity requirements can pose challenges under some specific circumstances, for stance, singular deformation fields (wave propagation), or strongly localised (localisation at crack tips) (Peerlings et al., 2001). Meeting these requirements may be difficult, and it can significantly impact the predicted response of the material.

(3) From a physical standpoint, the micro-polar continuum approach aims to capture strain localisation accurately for modelling strain localisation in granular materials compared to the other methods. The micropolar approach considers the rotations of individual grains and the resulting couple stresses during shearing, even though these effects may remain negligible during homogeneous deformation. This consideration of grains' rotations and couple stresses align with the physical behaviour observed in experiments. Therefore, the micropolar approach is believed to provide a more appropriate representation of shear zones in granular materials. However, this method only becomes effective under shear loading conditions. Liu (2018) pointed out that the micro-polar is too weak to preserve the ellipticity of the boundary value problems. The rotational degrees of freedom are invalid, and the micro-curvatures and couple stresses remain zero when decohesion rather than frictional slip dominant failure mode.

(4) In the nonlocal method, long-range interactions are considered using weighted spatial averages of constitutive quantities. It is based on the use of nonlocal internal variables, which are obtained by spatially averaging local internal variables over a finite volume. However, even if the nonlocal theory is considered reliable among the various regularisation techniques, it is essential to note that the nonlocal method primarily applies to dilatant granular materials, as the inclusion of mesh-independent contributions is significant during

the strain softening phase. Additionally, the requirement of nonlocal integration in the nonlocal method can lead to computational inefficiency, posing challenges in terms of computational resources and time.

In summary, each regularisation method has its advantages and disadvantages. There is no one-size-fits-all regulation method that works perfectly in all scenarios. In cases where a single regularisation method may not be sufficient to deal with mesh-dependency issues, combining multiple regularisation approaches can be a viable solution. By combining the strengths of different methods, it is possible to achieve enhanced efficiency in dealing with the mesh-dependent issue during modelling. In general, the combination of viscosity with another regularisation technique has become a widely adopted approach to address the mesh-dependency issue. The combination of viscosity regularisation with the strain-gradient enhanced method was first proposed by Wang et al. (1997, 1998) and was effectively implemented for both quasi-static and dynamic problems. The work of de Borst and Pamin. (1996) presented a plastic constitutive model incorporating both rate and gradient dependence for analysing strain localisation. Building upon this, Oka et al. (2000, 2002) investigate strain localisation phenomena and deformation modes in clay by a gradient-dependent elastic-viscoplastic model. The interaction in controlling the thickness of shear bands has also been explored. Zhang et al. (2003, 2004) employed a one-dimensional example primarily from a mathematical perspective, examining the interactions between different length scale parameters in combination with viscosity and gradient plasticity models. Subsequently, a combination of viscosity regularisation with a micro-polar continuum approach was proposed by Tang and Li (2007). They introduced a coupled Biot-Cosserat model that combines Biot's theory of rate-dependency and the Cosserat continuum theory. The objective of this model was to simulate strain localisation phenomena resulting from strain softening in saturated porous media while demonstrating the developed model’s ability to maintain the well-posedness of boundary value problems.

Moreover, regardless of the regularisation method employed, it is generally necessary to incorporate at least one explicit or implicit internal length scale into the constitutive model. Researchers have hypothesised various relationships between characteristic internal length scales and microstructures, with random constants distribution, interactions or internal deformation. This suggests that a common understanding of the physical interpretations of the internal length scale has not yet been established. Therefore, further investigation into

the physical meanings of all internal length scales within each regularisation approach remains an important and urgent matter of significance.

Chapter 3：Constitutive model

3.1 Introduction

Anisotropy refers to the different mechanical properties of materials in different directions. From the micro perspective, the anisotropic characteristics are due to the preferred orientation of particles and void and/or crack (Oda et al., 1985; Duveau et al., 1998; Li and Dafalias, 2012; Gao et al., 2013). There has been extensive research on constitutive modelling of sand anisotropy. The anisotropic sand model used in this thesis is developed based on the anisotropic critical state theory (Li and Dafalias, 2012). The main feature of the anisotropic critical state theory is that sand fabric at the critical state has a unique magnitude and is codirectional with the loading direction. Several constitutive models have been developed within the framework of this theory (Li and Dafalias, 2015; Woo and Salgado, 2015; Zhao and Gao, 2016; Yang et al., 2018; Petalas et al., 2019; Papadimitriou et al., 2019). The model to be used here was proposed by Gao et al. (2020).

3.2 Constitutive model description

3.2.1 Yield function

The yield function of the model is expressed as:

$$f = \frac{R}{g(\theta)} - H = 0 \tag{3.1}$$

where $R = \sqrt{\frac{3}{2} r_{ij} r_{ij}}$, with $r_{ij} = (\sigma_{ij} - p\delta_{ij})/p)$ being the stress ratio tensor, σ_{ij} is the stress tensor, $p = \sigma_{ii}/3$ is the effective mean stress, δ_{ij} is the Kronecker delta ($= 1$ for $i = j$, and $= 0$ for $i \neq j$). Furthermore, H is the hardening parameter, and $g(\theta)$ is an interpolation function which describes the variation of critical state stress ratio with the Lode angle θ of r_{ij} as follows (Li and Dafalias, 2004).

$$g(\theta) = \frac{\sqrt{(1+c^2)^2 + 4c(1-c^2)\sin 3\theta} - (1+c^2)}{2(1-c)\sin 3\theta} \tag{3.2}$$

where $c = M_e/M_c$ is a material constant, with M_c and M_e being the critical state stress ratio in triaxial compression and extension, respectively.

The condition of consistency for the yield function can be expressed as:

$$df = \frac{\partial f}{\partial \sigma_{ij}} d\sigma_{ij} + \frac{\partial f}{\partial H} dH = 0 \tag{3.3}$$

The condition of consistency of the yield function (3.1) can also be rewritten as follows:

$$df = \frac{\partial f}{\partial \sigma_{ij}} d\sigma_{ij} - \langle L \rangle K_p = 0 \tag{3.4}$$

where L is the loading index; $\langle \rangle$ are the Macaulay brackets which make $\langle L \rangle = L$ for $L > 0$ and $\langle L \rangle = 0$ for $dL \leq 0$; The plastic modulus K_p is defined as below (Dafalias, 1986):

$$K_P = -\frac{\partial f}{\partial H} dH = r_H \tag{3.5}$$

3.2.2 Hardening law

The hardening law for the yield function (evolution of for H) determines how the size of yield surface evolves and is expressed as (Gao et al., 2020):

$$dH = \langle L \rangle r_H = \langle L \rangle \frac{G h_1 e^{h_2 A}}{(1+e)^2 \sqrt{p p_a R}} [M_c g(\theta) e^{-n\zeta} - R] \tag{3.6}$$

where h_1, h_2, and n are three model parameters; G is elastic shear modulus; A is an anisotropic variable; r_H is a function of the stress and internal variable H; ζ is the dilatancy state parameter and e is the void ratio; The term $e^{h_2 A}$ is introduced to give better prediction for the effect of anisotropy on the stress-strain relationship, making the plastic modulus smaller at smaller A (Li and Dafalias, 2012; Papadimitriou et al., 2019). This hardening law can capture the strain-softening response of dense sand.

The dilatancy state parameter ζ was proposed by Li (2002):

$$\zeta = \psi - e_A(A - 1) \tag{3.7}$$

e_A is a model parameter which describes the effect of fabric anisotropy and loading direction on dilatancy and plastic hardening of sand in shear. Moreover, $\psi = e - e_c$ is a state

parameter defined by Been and Jefferies (1985). It is a measure of the difference between the current void ratio e and the critical state void ratio e_c corresponding to the current mean effective stress p.

The location of the critical state line (CSL) in the $e-p$ space is given as below (Li and Wang, 1998):

$$e_c = e_\Gamma - \lambda_c \left(\frac{p}{p_a}\right)^{\xi_c} \tag{3.8}$$

where p_a is atmospheric pressure for normalisation (101 kPa); e_Γ (CSL location), λ_c (CSL slope), ξ_c(CSL shape) are three material constants.

The anisotropic state variable A is an index for the characterisation of the impact of fabric anisotropy on the stress-strain-strength response of sand (Li and Dafalias, 2002). The anisotropic variable A is defined as:

$$A = n_{ij} F_{ij} \tag{3.9}$$

where F_{ij} is the fabric tensor characterising the anisotropy of sand. The fabric tensor used here is a phenomenological term that is not directly related to the fabric or particle characteristics of sand, such as contact normal distribution, or particle orientation (Li and Dafalias, 2015). For convenience, F_{ij} is normalised such that in a critical state, F ($= \sqrt{F_{ij}F_{ij}}$) is unity. For an initially cross-anisotropic sand sample with the isotropic plane (deposition plane) being the x-y plane and deposition direction aligning with the z-axis, the initial F_{ij} can be expressed as:

$$F_{ij} = \begin{pmatrix} F_z & 0 & 0 \\ 0 & F_x & 0 \\ 0 & 0 & F_y \end{pmatrix} = \sqrt{\frac{2}{3}} \begin{pmatrix} F_0 & 0 & 0 \\ 0 & -F_0/2 & 0 \\ 0 & 0 & -F_0/2 \end{pmatrix} \tag{3.10}$$

where F_0 is the initial degree of anisotropy.

The loading direction tensor n_{ij} is expressed as follows:

$$n_{ij} = \frac{\frac{\partial f}{\partial r_{ij}} - \frac{1}{3}\left(\frac{\partial f}{\partial r_{mn}}\delta_{mn}\right)\delta_{ij}}{\left|\frac{\partial f}{\partial r_{ij}} - \frac{1}{3}\left(\frac{\partial f}{\partial r_{mn}}\delta_{mn}\right)\delta_{ij}\right|} \tag{3.11}$$

with,

$$\frac{\partial f}{\partial r_{ij}} = \underbrace{\frac{\partial f}{\partial R}\frac{\partial R}{\partial r_{ij}} + \underbrace{\frac{\partial f}{\partial g(\theta)} + \frac{\partial g(\theta)}{\partial \sin 3\theta} \times \left(\frac{\partial \sin 3\theta}{\partial J_{3D}}\frac{\partial J_{3D}}{\partial r_{ij}} + \frac{\partial \sin 3\theta}{\partial J_{2D}}\frac{\partial J_{2D}}{\partial r_{ij}}\right)}_{\frac{\partial f}{\partial \theta}\frac{\partial \theta}{\partial r_{ij}}}}_{N_{ij}} \tag{3.12}$$

3.2.3 Plastic potential function

The plastic potential function in the r_{ij} space is expressed as (Gao et al., 2020):

$$g = \frac{R}{g(\theta)} - H_g e^{-k_h(A-1)^2} = 0 \tag{3.13}$$

where k_h is a non-negative anisotropy constant. $H_g = \frac{R}{g(\theta)e^{-k_h(1-A)^2}}$ should be calculated based on the current stress state and A.

3.2.4 Flow rule and incremental of plastic relation

The plastic potential function in Equation (3.13) is used to obtain the direction of plastic deviatoric strain increment de_{ij}^p

$$de_{ij}^p = \langle L \rangle m_{ij} \tag{3.14}$$

where m_{ij} is a unit-norm deviatoric tensor containing only the information of the direction of de_{ij}^p and defined as below:

$$m_{ij} = \frac{\frac{\partial g}{\partial r_{ij}} - \frac{1}{3}\left(\frac{\partial g}{\partial r_{mn}}\delta_{mn}\right)\delta_{ij}}{\left|\frac{\partial g}{\partial r_{ij}} - \frac{1}{3}\left(\frac{\partial g}{\partial r_{mn}}\delta_{mn}\right)\delta_{ij}\right|} \tag{3.15}$$

with,

$$\frac{\partial g}{\partial r_{ij}} = \underbrace{\frac{\partial g}{\partial R}\frac{\partial R}{\partial r_{ij}} + \underbrace{\frac{\partial g}{\partial g(\theta)}\frac{\partial g(\theta)}{\partial \sin 3\theta} \times \left(\frac{\partial \sin 3\theta}{\partial J_{3D}}\frac{\partial J_{3D}}{\partial r_{ij}} + \frac{\partial \sin 3\theta}{\partial J_{2D}}\frac{\partial J_{2D}}{\partial r_{ij}}\right)}_{\frac{\partial g}{\partial g(\theta)}\frac{\partial g}{\partial \theta}\frac{\partial \theta}{\partial r_{ij}}}}_{\widetilde{N}_{ij}} + \frac{\partial g}{\partial A}\frac{\partial A}{\partial n_{ij}}\frac{\partial n_{ij}}{\partial r_{ij}} = \widetilde{N}_{ij} + \frac{\partial g}{\partial A}\frac{\partial A}{\partial n_{ij}}\frac{\partial n_{ij}}{\partial r_{ij}} \tag{3.16}$$

The total plastic strain increment $d\varepsilon_{ij}^p$ is expressed as (Zhao and Gao, 2016):

$$d\varepsilon_{ij}^{p} = de_{ij}^{p} + \frac{d\varepsilon_{v}^{p}\delta_{ij}}{3} = \langle L\rangle \underbrace{\left(m_{ij} + \sqrt{\frac{2}{27}}D\delta_{ij}\right)}_{x_{ij}} \tag{3.17}$$

in which the dilatancy relation can be expressed as:

$$D = \frac{d\varepsilon_{v}^{p}}{\left|d\varepsilon_{q}^{p}\right|} = \frac{d\varepsilon_{ii}^{p}}{\sqrt{2de_{ij}^{p}de_{ij}^{p}/3}} = \frac{d_1}{M_C g(\theta)}\left[M_C g(\theta)e^{m_1\zeta} - R\right] \tag{3.18}$$

where d_1 and m_1 are model parameters.

3.2.5 Fabric evolution

In this model, fabric evolution with plastic deformation is considered (Li and Li, 2009; Guo and Zhao, 2013; Zhao and Guo, 2013). It is assumed that F_{ij} becomes codirectional with the loading direction and reaches a magnitude of 1 at the critical state. Though fabric evolution is affected by both volumetric and shear strains, a simplified evolution law expressed in terms of the plastic shear strain is used.

$$dF_{ij} = \langle L\rangle k_f\left(n_{ij} - F_{ij}\right) \tag{3.19}$$

where, dF_{ij} is the increment of F_{ij}, k_f is a model parameter describing the rate of fabric evolution with plastic strain increment.

3.2.6 Elastic moduli and incremental of elastic relation

The following empirical pressure-sensitive elastic moduli (elastic shear modulus G and elastic bulk modulus K) are employed for this model (Li and Dafalias, 2004; Gao et al., 2014)

$$G = G_0\frac{(2.97-e)^2}{1+e}\sqrt{pp_a} \tag{3.20}$$

where G_0 is a material constant.

According to elasticity theory, the elastic bulk modulus K is related to G and Poisson's ratio ν which can be expressed as below：

$$K = G\frac{2(1+\nu)}{3(1-2\nu)} \tag{3.21}$$

Thus, the elastic deviatoric strain increment de_{ij}^{e} and elastic volumetric strain increment $d\varepsilon_{v}^{e}$ can be expressed as below:

$$de_{ij}^{e} = \frac{ds_{ij}}{2G} \text{ and } d\varepsilon_{v}^{e} = \frac{dp}{K} \tag{3.22}$$

and elastic stiffness tensor E_{ijkl} is defined based on elastic moduli.

$$E_{ijkl} = G\left(\delta_{ik}\delta_{jl} + \delta_{il}\delta_{jk}\right) + \left(K - \frac{2G}{3}\right)\delta_{ij}\delta_{kl} \tag{3.23}$$

The elastic stress-strain relationship for general stress condition is expressed as:

$$d\sigma_{ij} = E_{ijkl}d\varepsilon_{kl}^{e} \tag{3.24}$$

3.2.7 The elastoplastic stiffness tensor

Based on the additive decomposition of the total strain increment, one has:

$$d\varepsilon_{ij} = d\varepsilon_{ij}^{e} + d\varepsilon_{ij}^{p} \tag{3.25}$$

Substituting Equation (3.17) into (3.4), and combing with (3.24) and (3.25), then the condition of consistency of the yield function can now be written as:

$$df = \left(\frac{\partial f}{\partial \sigma_{ij}}\right)E_{ijkl}(d\varepsilon_{kl} - \langle L\rangle x_{kl}) - \langle L\rangle K_{p} = 0 \tag{3.26}$$

Thus, the loading index can also be expressed in terms of the total strain increment as:

$$L = \underbrace{\frac{\frac{\partial f}{\partial \sigma_{ij}}E_{ijkl}}{\frac{\partial f}{\partial \sigma_{ij}}x_{ab}E_{ijab} + K_{p}}}_{\Pi_{kl}} d\varepsilon_{kl} \tag{3.27}$$

Combining Equation (3.24), (3.25), and (3.27), the constitutive equation can be obtained as below:

$$d\sigma_{ij} = \Lambda_{ijkl}d\varepsilon_{kl} \tag{3.28}$$

with the elastoplastic stiffness tensor,

$$\Lambda_{ijkl} = E_{ijkl} - h(L)(E_{ijmn}x_{mn})\Pi_{kl} \tag{3.29}$$

where $h(L)$ is the Heaviside step function, with $h(L > 0) = 1$and $h(L \leq 0) = 0$.

3.2.8 Partial derivatives used in the constitutive relation

The $\frac{\partial f}{\partial r_{ij}}$ used in Equation (3.11) can be obtained according to the chain rule for partial derivatives based on Equation (3.1)

$$\frac{\partial f}{\partial r_{ij}} = \frac{\partial f}{\partial R}\frac{\partial R}{\partial r_{ij}} + \frac{\partial f}{\partial g(\theta)} + \frac{\partial g(\theta)}{\partial \sin 3\theta} \times \left(\frac{\partial \sin 3\theta}{\partial J_{3D}}\frac{\partial J_{3D}}{\partial r_{ij}} + \frac{\partial \sin 3\theta}{\partial J_{2D}}\frac{\partial J_{2D}}{\partial r_{ij}}\right)$$

$$= \frac{3r_{ij}}{2Rg(\theta)} - \frac{R}{g^2(\theta)}\frac{\partial g(\theta)}{\partial \sin 3\theta} \times \left(\frac{\partial \sin 3\theta}{\partial J_{3D}}\frac{\partial J_{3D}}{\partial r_{ij}} + \frac{\partial \sin 3\theta}{\partial J_{2D}}\frac{\partial J_{2D}}{\partial r_{ij}}\right)$$

$$= \frac{3r_{ij}Rg(\theta)}{2R^2g^2(\theta)} + \frac{9R\sin 3\theta r_{ij}\partial g(\theta)}{2R^2g^2(\theta)\partial \sin 3\theta} + \frac{27\partial g(\theta)r_{im}r_{jm}}{2R^2g^2(\theta)\partial \sin 3\theta} \tag{3.30}$$

$$N_{ij} = \frac{3}{2R^2g^2(\theta)}\left\{\left[Rg(\theta) + 3R\sin 3\theta\frac{\partial g(\theta)}{\partial \sin 3\theta}\right]r_{ij} + 9\frac{\partial g(\theta)}{\partial \sin 3\theta}r_{im}r_{jm}\right\} \tag{3.31}$$

where,

$$g(\theta) = \frac{\sqrt{(1+c^2)^2 + 4c(1-c^2)\sin 3\,\theta} - (1+c^2)}{2(1-c)\sin 3\,\theta} \tag{3.32}$$

$$\frac{\partial g(\theta)}{\partial \sin 3\theta} = \frac{c(1+c)}{\sin 3\theta\sqrt{(1+c^2)^2+4c(1-c^2)\sin 3\theta}} - \frac{g(\theta)}{\sin 3\theta} \tag{3.33}$$

The $\frac{\partial g}{\partial r_{ij}}$ used in Equation (3.15) can be expressed as:

$$\frac{\partial g}{\partial r_{ij}} = \underbrace{\frac{\partial g}{\partial R}\frac{\partial R}{\partial r_{ij}} + \underbrace{\frac{\partial g}{\partial g(\theta)}\frac{\partial g(\theta)}{\partial \sin 3\theta} \times \left(\frac{\partial \sin 3\theta}{\partial J_{3D}}\frac{\partial J_{3D}}{\partial r_{ij}} + \frac{\partial \sin 3\theta}{\partial J_{2D}}\frac{\partial J_{2D}}{\partial r_{ij}}\right)}_{\frac{\partial g}{\partial g(\theta)}\frac{\partial g}{\partial \theta}\frac{\partial \theta}{\partial r_{ij}}}}_{\widetilde{N}_{ij}} + \frac{\partial g}{\partial A}\frac{\partial A}{\partial n_{ij}}\frac{\partial n_{ij}}{\partial r_{ij}}$$

$$= \widetilde{N}_{ij} + \frac{\partial g}{\partial A}\frac{\partial A}{\partial n_{ij}}\frac{\partial n_{ij}}{\partial r_{ij}}$$

where,

$$\frac{\partial g}{\partial A} = 2k_h H_g (A-1) e^{-k_h (1-A)^2} \tag{3.34}$$

$$\frac{\partial A}{\partial n_{ij}} = F_{ij} \tag{3.35}$$

$$\begin{aligned}
\frac{\partial n_{ij}}{\partial r_{kl}} = {} & \frac{3\left(1 + \frac{3\sin 3\theta}{g(\theta)}\frac{\partial g(\theta)}{\partial \sin 3\theta}\right)}{4Rg(\theta)}\left(\delta_{ik}\delta_{jl} + \delta_{il}\delta_{jk}\right) + \frac{27\frac{\partial g(\theta)}{\partial \sin 3\theta}\left(r_{ik}\delta_{jl} + r_{il}\delta_{jk} + r_{lj}\delta_{ik} + r_{kj}\delta_{il}\right)}{4R^2 g^2(\theta)} \\
& + \frac{9\left(-1 + 9\frac{\sin 3\theta}{g(\theta)}\right)\left(\frac{2\sin 3\theta\left(\frac{\partial g(\theta)}{\partial \sin 3\theta}\right)^2}{g(\theta)} - \frac{\partial g(\theta)}{\partial \sin 3\theta} - \sin 3\theta\frac{\partial^2 g(\theta)}{\partial(\sin 3\theta)^2}\right)}{4R^3 g(\theta)} r_{ij} r_{kl} \\
& + \frac{81}{4R^4 g^2(\theta)}\left(\frac{6\sin 3\theta\left(\frac{\partial g(\theta)}{\partial \sin 3\theta}\right)^2}{g(\theta)} - 2\frac{\partial g(\theta)}{\partial \sin 3\theta} - 3\sin 3\theta\frac{\partial^2 g(\theta)}{\partial(\sin 3\theta)^2}\right)\left(r_{ij} r_{kP} r_{pl} + r_{ip} r_{pj} r_{kl}\right) \\
& + \frac{729}{4R^5 g^3(\theta)}\left(2\left(\frac{\partial g(\theta)}{\partial \sin 3\theta}\right)^2 - g(\theta)\frac{\partial^2 g(\theta)}{\partial(\sin 3\theta)^2}\right) r_{kp} r_{pl} r_{iq} r_{qj} \\
& - \frac{81}{2R^3 g^2(\theta)}\left(\frac{2\left(\frac{\partial g(\theta)}{\partial \sin 3\theta}\right)^2}{g(\theta)} - \frac{\partial^2 g(\theta)}{\partial(\sin 3\theta)^2}\right)\delta_{ij} r_{kp} r_{pl} \\
& - \frac{27\sin 3\theta}{2R^2 g^2(\theta)}\left(\frac{2\left(\frac{\partial g(\theta)}{\partial \sin 3\theta}\right)^2}{g(\theta)} - \frac{\partial^2 g(\theta)}{\partial(\sin 3\theta)^2}\right)\delta_{ij} r_{kl}
\end{aligned} \tag{3.36}$$

with,

$$\frac{\partial^2 g(\theta)}{\partial(\sin 3\theta)^2} = \frac{2}{(\sin 3\theta)^2}\left\{g(\theta) - \frac{c(1+c)[(1+c^2)^2 - 5c(1-c^2)(1-c^2)\sin 3\theta]}{\sqrt{[(1+c^2)^2 + 4c(1-c^2)\sin 3\theta]^3}}\right\} \tag{3.37}$$

The expression for $\frac{\partial f}{\partial \sigma_{ij}}$ used in Equation (3.3) expressed as below:

$$\frac{\partial f}{\partial \sigma_{ij}} = \frac{\partial f}{\partial r_{kl}} \frac{\partial r_{kl}}{\partial \sigma_{ij}} \tag{3.38}$$

where,

$$\frac{\partial r_{kl}}{\partial \sigma_{ij}} = \frac{\delta_{ki}\delta_{lj}}{p} - \frac{\sigma_{kl}}{3p^2}\delta_{ij} \tag{3.39}$$

The expression for $\frac{\partial f}{\partial H}$ in Equation (3.3) is:

$$\frac{\partial f}{\partial H} = -e^{-k_h(1-A)^2} \tag{3.40}$$

3.3 Model validation

The 17 material constants in Table 3.1 will be used in the proposed anisotropic sand model for Toyoura sand. The critical parameters M_c and c are determined based on the required state stress ratio in triaxial compression and extension. The parameter e_Γ (Location of CSL), λ_c (Slope of CSL) and ξ(Shape of CSL) can be directly calculated from critical state line in $e - p$ plane. The elasticity parameters G_0 and ν are determined using the stress-strain relationship at the very beginning of the triaxial tests. The remaining parameters are hardly obtained and can be determined by a trial-and-error approach to fit the different tests from the empirical range. The detailed model parameter determination can be found in previous studies (Zhao and Gao, 2016; Gao et al., 2020; Gao et al., 2021). The mean particle size for Toyoura sand is 0.2 mm. The minimum void ratio e_{min} and maximum void ratio e_{max} are determined to be $e_{min} = 0.6$ and $e_{max} = 0.98$ respectively.

Table 3.1 Summary of Anisotropic Model Parameters for Toyoura sand

Critical state	Elasticity	Dilatancy	Hardening	Fabric anisotropy
M_c=1.25 c=0.75 e_Γ=0.934 λ_c=0.019 ξ_c=0.7	G_0=125 $G_s = 2.97$ ν=0.1	d_1=0.5 m_1=3.5	h_1=0.45 h_2=0.5 n=2.0	e_A=0.075 k_f=0.5 F_0=0.4 $k_h = 0.03$

3.3.1 Results of anisotropic sand model

The test data of Toyoura sand reported in Oda et al. (1978) and Tatsuoka et al. (1986) are used to benchmark the anisotropic model simulation of drained plane strain compression test from different initial void ratios $e_0 = 0.66, 0.70, 0.80$ and confining pressures $\sigma_3 = 5, 50, 200, 400$ kPa, in which the orientation of the deposition plane 0 (horizontal) and 90 (vertical) are considered (Figures 3.1 and 3.2). Moreover, the test data of drained triaxial compression tests only with horizontal bedding obtained in Fukushima and Tatsuoka (1984) are compared with the prediction results of the anisotropic model under various loading conditions shown in Figure 3.3.

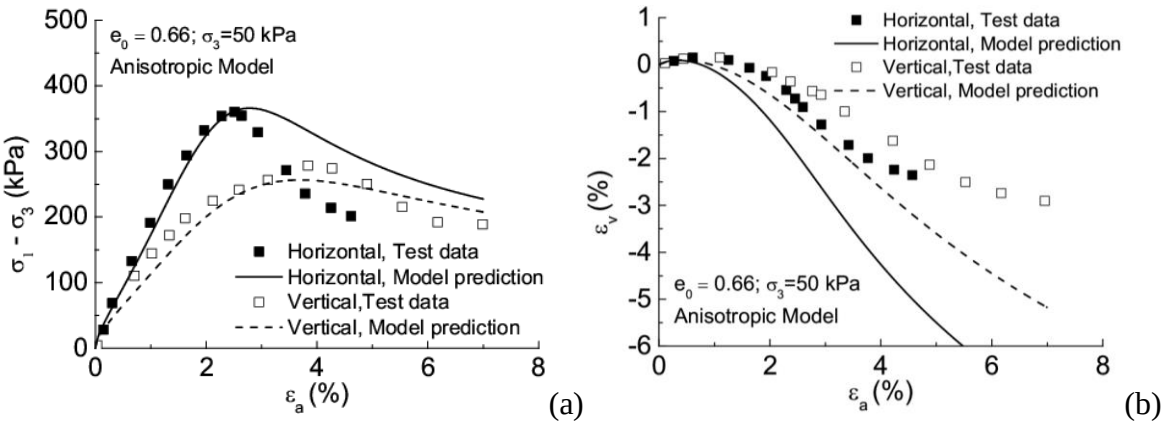

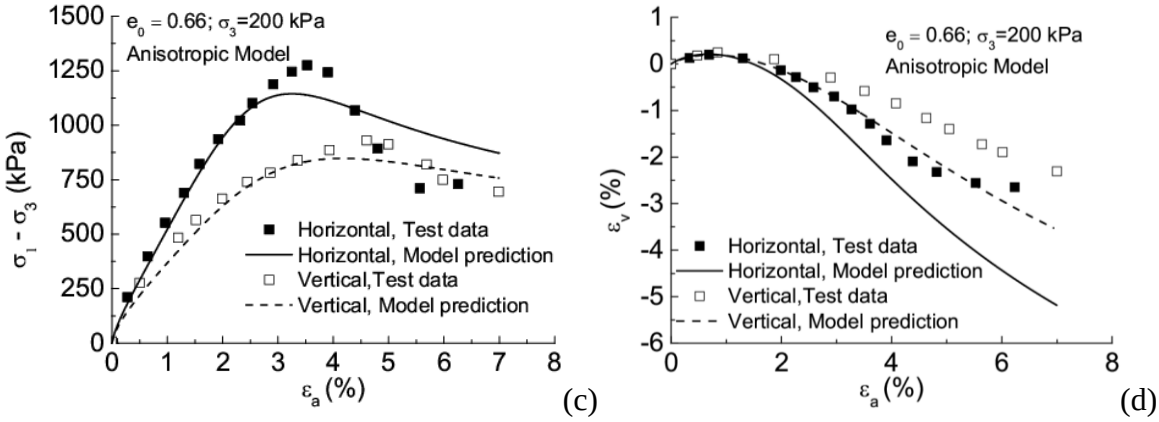

Figure 3.1 Comparison between the anisotropic model prediction and drained plane strain compression test data on Toyoura sand: (a)(b) $\sigma_3 = 50$ kPa; and (c)(d) $\sigma_3 = 200$ kPa (Oda et al., 1978)

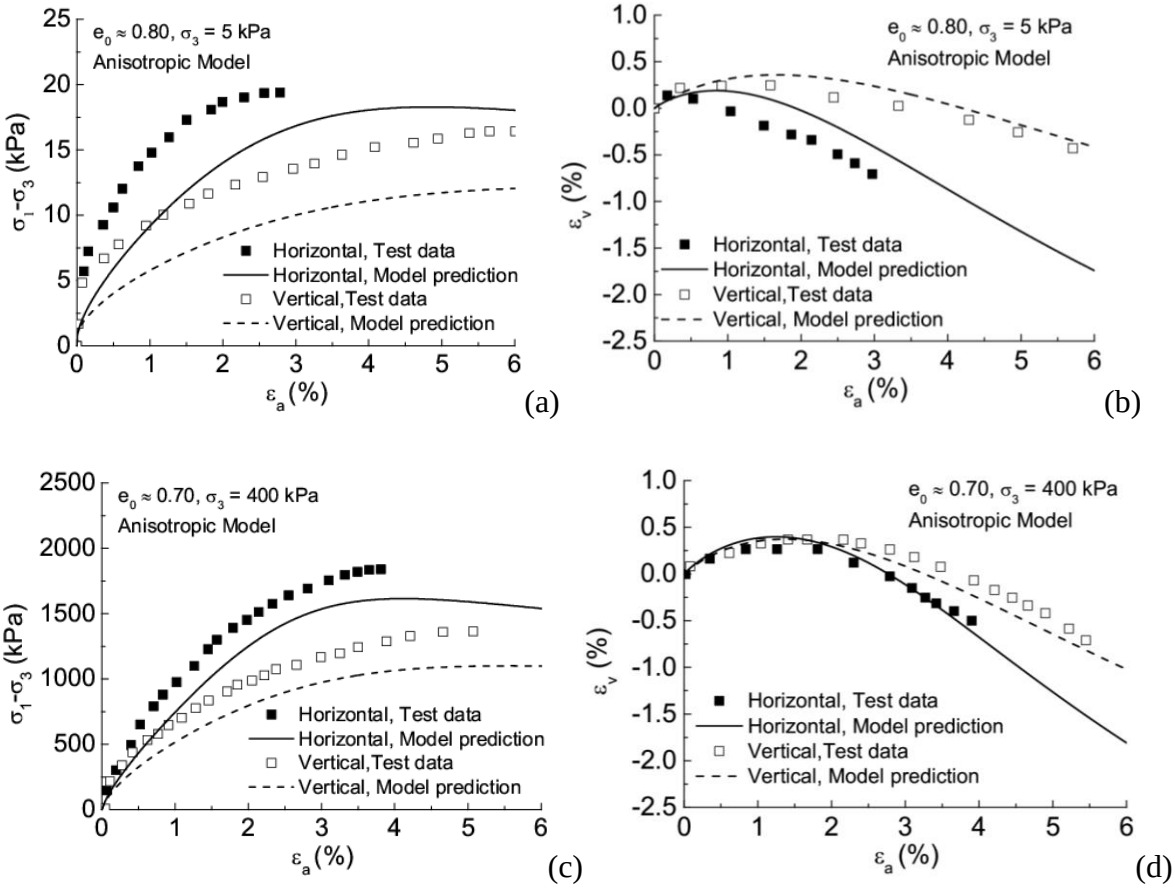

Figure 3.2 Comparison between the anisotropic model prediction and plane strain test data on Toyoura sand: (a)(b) $\sigma_3 = 5$ kPa; (c)(d) $\sigma_3 = 400$ kPa (Tatsuoka et al., 1986)

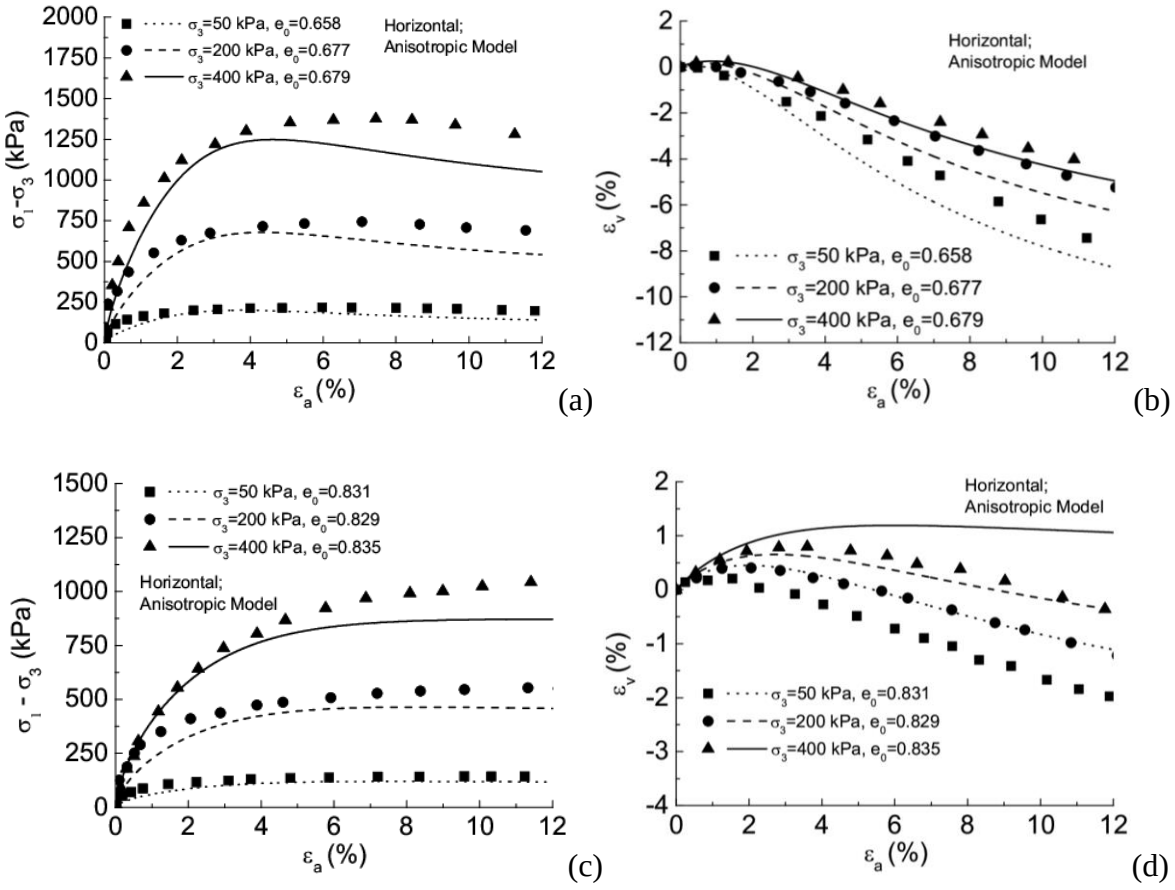

Figure 3.3 Comparison between the anisotropic model prediction and drained triaxial compression test data on Toyoura sand: (a)(b) dense sand; (c)(d) medium dense sand (Fukushima and Tatsuoka, 1984)

The dots and solid lines represent test data and the model simulations on Toyoura sand, respectively. According to the $q - \varepsilon_{\mathrm{a}}$ curves of both plane strain compression and triaxial compression test, the peak value of deviatoric stress q is increased with increasing confining pressure σ_3 and decreasing initial void ratio, and the model gives a better prediction of the peak deviator stress when the confining pressure is lower. From the $\varepsilon_v - \varepsilon_{\mathrm{a}}$ plots, the sand dilatancy is increased with decreasing initial void ratio and decreased with higher confining pressures. Moreover, the results showed that when the (normal to the) deposition plane and the major principal stress direction are aligned (e.g., vertical compression and horizontal deposition plane), the response becomes more dilative, thus increasing the strength of the sand. According to Figure 3.1(b), when ε_a is around 5%, the shear band maintains a constant volume at the critical state in tests, whereas in modelling, ε_v still decreases. It is assumed that uniform deformation and the critical state are reached at much larger strains. The model gives good predictions on the peak deviatoric stress and strain-hardening part but does not capture the strain-softening part well.

Chapter 4: Implementation of nonlocal regularisation method

4.1 Introduction

The weight function is the most important component of a nonlocal regularisation method. The Gaussian distribution (GD) function has been used in many early studies (Eringen, 1972; Bažant et al., 1984). The variable at the current stress point contributes most to the nonlocal one. Therefore, the nonlocal variable is concentrated at the local point and cannot spread to surrounding points. Galavi and Schweiger (2010) proposed a new weight function (G&S) in which the local variable does not affect the nonlocal one. Moreover, Vermeer and Brinkgreve (1994) have proposed the over-nonlocal method (ON), which uses a linear combination of the local and the nonlocal variables. A nonlocal parameter m was introduced to control the proportion of local and nonlocal variables in weight functions.

According to the physical consequences of the weighting functions, the weighting functions determine the extent and shape of the influence zone, introduce an internal characteristic length scale l_c, and affect smoothness (e.g., Gaussian function lead to smooth nonlocal fields, which help in avoiding numerical instabilities), continuity (discontinuous or sharply varying weighting functions can introduce artifacts or non-physical jumps in the solution), and anisotropy (in anisotropic materials or problems with directional features, the weighting function can be designed to reflect the directional dependency) of the problems. Applicable scenarios include strain localisation and fracture mechanics. In strain localisation appropriate weighting functions is used to prevent mesh dependency and to capture the physical width of localisation zones such as shear bands. In fracture mechanics weighting functions help in distributing the effects of damage or strain over a finite region, thus avoiding singularities and ensuring a more realistic representation of crack propagation (Bazant and Jirasek, 2002).To avoid unphysical results, the l_c should be calibrated based on physical considerations and experimental data, boundary effects should be smoothly handled, the symmetry and consistency of the weighting functions should be maintained, and the numerical implementation should accurately represent the weighting functions. This ensures that nonlocal regularisation produces physically consistent and realistic simulation results (Peerlings et al., 1996).

Some studies have compared three weighting functions in simple BVPs like plane strain compression. It is found that the G&S gives better regularisation results than the GD one (Galavi and Schweiger, 2010; Guo and Stolle, 2013; Summersgill et al., 2017; Mallikarachchi and Soga, 2020; Gao et al., 2022). However, the performance of these functions in real-world BVPs has not been evaluated.

This Chapter mainly focuses on nonlocal regularisation. Three different weight functions are introduced and compared first. Then, the nonlocal formulations used in the critical state model and the implementation in ABAQUS are presented. Finally, the determination of internal length is discussed.

4.2 Weight functions

There are three nonlocal methods designed to address mesh dependency. The weight function is typically represented by the Gaussian distribution function (GD) (Eringen, 1972; Bažant et al., 1984). However, Galavi and Schweiger (2010) introduced a modified weight function known as the G&S weight function, which offers several advantages over the Gaussian distribution function. Additionally, Vermeer and Brinkgreve (1994) proposed the over-nonlocal (ON) method, aiming to overcome the limitations of the Gaussian distribution. This method utilises a linear combination of local and nonlocal variables.

Moreover, it needs to be noticed that the selection of weight functions should obey the law that it will not alter a uniform field of strain. Thus, the area under the curve for the distribution function is equal to 1, as shown in Equation (4.1):

$$\int_{-\infty}^{+\infty} \omega(x,\xi) d\,\xi = 1 \tag{4.1}$$

where ω is the weight function; x is the global coordinate for the current integration point (IP); ξ is the local coordinate of all surrounding IPs.

4.4.1 Gaussian distribution (GD) function

The Gaussian weight function is expressed as:

$$\omega_i = \frac{1}{\sqrt{\pi} l_c} \exp\left(-\frac{r_i^2}{{l_c}^2}\right) \tag{4.2}$$

where ω_i represents the weight function of IP i, r_i is the distance between the current IP and the $i-$th IP used for calculating the averaged value. l_c is a nonlocal parameter termed internal length, which depends on the mean size of soil particles (Galavi and Schweiger, 2010). Figure 4.1 shows the physical significance of internal length l_c in a 2D problem. The integration point X^{IP} is coloured in red, and its neighbours are coloured in blue. To reduce the computational time, at the first step of the computation, each IP can be computed at the first step and store the coordinates of its neighbours within the effective influence area. Then, the weights for each neighbour and the sum of weights for each IP can be computed and stored.

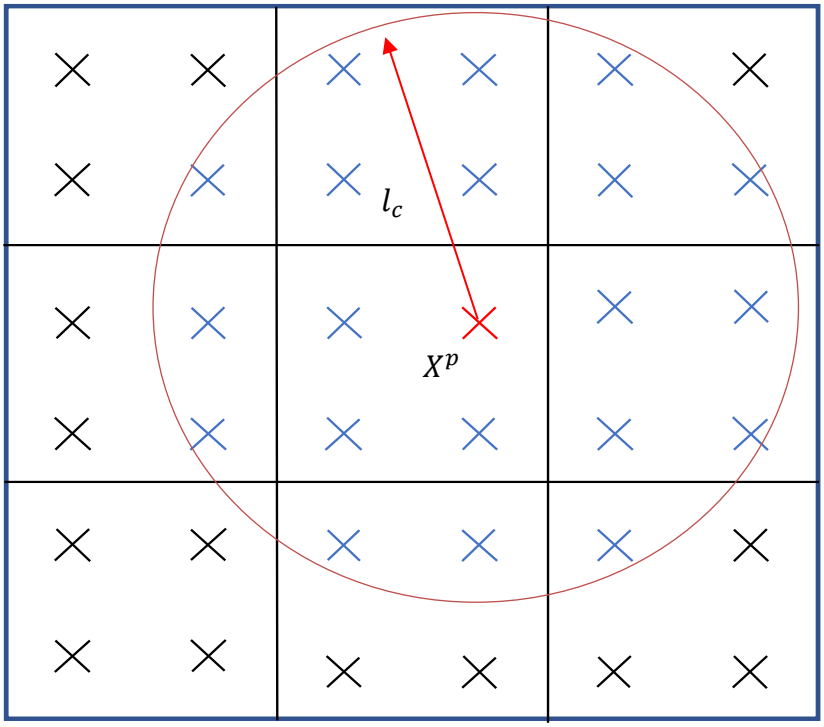

Figure 4.1. Schematic diagram showing the neighbouring integration point of X^{IP}

In two-dimensional cases of Gaussian distribution, the contribution of the weight function to the calculated nonlocal variable for different internal lengths l_c is shown in Figure 4.2. It is evident that the GD function shows the highest contribution to the calculated nonlocal variable at the centre and diminishes along the distance. As mentioned by Vermeer and Brinkgreve (1994), the nonlocal variable is concentrated at the local point. It cannot spread

to surrounding points, which has a negative effect on the nonlocal method. When $l_c < 1$, the contribution to the calculated nonlocal variable is nearly double to the case that $l_c \geq 1$. In addition, the GD method has an unbounded integration area, which means that the nonlocal interaction theoretically takes place at an arbitrary long distance (Jirásek and Rolshoven, 2003).

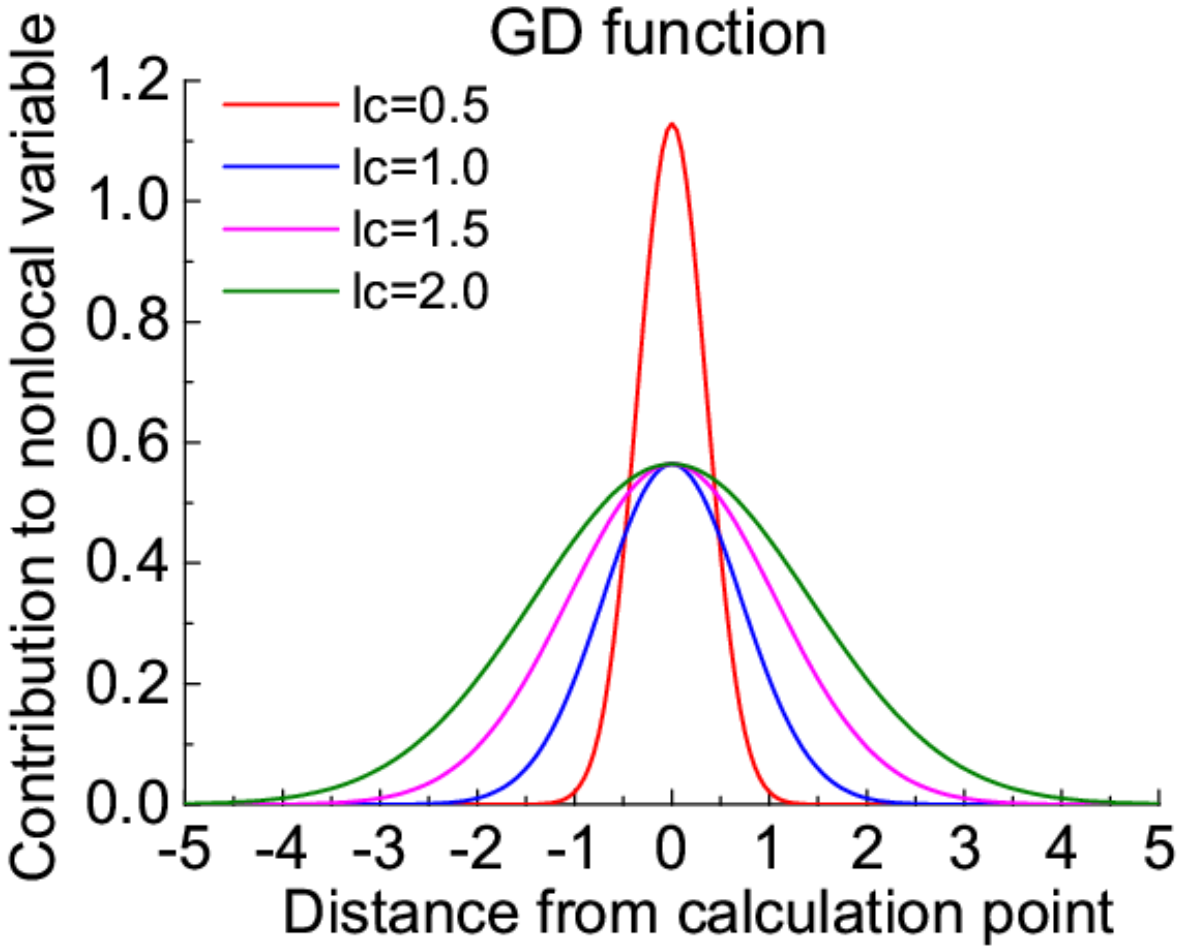

Figure 4.2 The Gaussian distribution function in 1D condition

If strain is chosen as the nonlocal variable for the GD method, then it coincides with the greatest contribution of strain to the nonlocal equation (Jostad and Grimstad, 2011). The increase in nonlocal strain can lead to a loss in material strength, which further increases the strain of the material. Thus, with the accumulation of calculation steps, a significant value for strain relative to the neighbouring points will have increased dominance for the nonlocal calculations at the centre point, causing the largest strain softening (Galavi and Schweiger, 2010). Therefore, the issue of mesh dependence in finite element analysis is not completely

solved (Brinkgreve, 1994; Galavi and Schweiger, 2010; Summersgill et al., 2017a, 2014, 2017b). Researchers have found that this issue could be tackled by changing the weight function (G&S weight function) or the averaging procedure itself.

4.4.2 G&S distribution (G&S) function

According to the hypothesis, the deformation at a point is more influenced by the response in the neighbourhood rather than the concentrated deformation at the point itself. Galavi and Schweiger (2010) have proposed the following weight function:

$$w_i = \frac{r_i}{l_c^2} \exp\left(-\frac{r_i^2}{l_c^2}\right) \tag{4.3}$$

As shown in Figure 4.3, the contribution of the G&S weight function to the calculated nonlocal variable is zero in the centre point and efficiently spreads from the concentrated local point to a more extensive zone. This is utterly different to the Gaussian weight function with the maximum value at the centre. In addition, the G&S weight function shows two same peaks with a distance of $0.707l_c$ from the centre (Galavi and Schweiger, 2010).

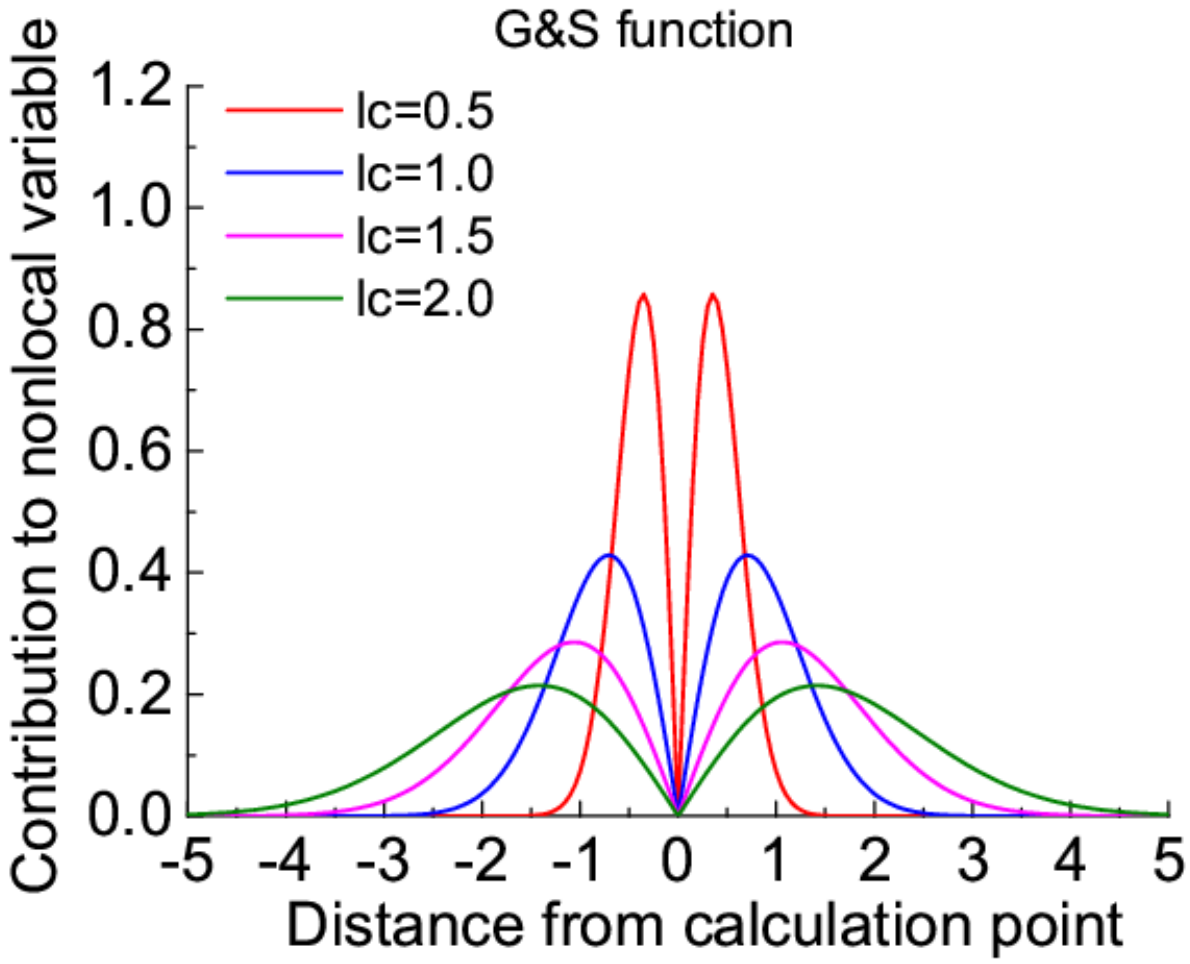

Figure 4.3 The Galavi and Schweiger (2010) distribution function in 1D condition

4.4.3 Over-nonlocal (ON) function

Moreover, another method to overcome the shortage of the GD method is proposed by Vermeer and Brinkgreve (1994), which is a linear combination of the local and the nonlocal variables. This method is different from the G&S weight function, which changes the averaging variable in the neighbourhood without changing the weight function. A nonlocal parameter m was applied to change the nonlocal averaging formulation. This method was called the over-nonlocal method. The ON formulation is expressed as below:

$$\bar{\varpi}(x) = (1-m)\varpi(x) + \frac{m}{V}\int_V \omega(x,\xi)\,\varpi(\xi)d\xi \tag{4.4}$$

where $\bar{\varpi}(x)$ is the nonlocal variable and $\varpi(x)$ is the local variable. The parameter m provides the relative contribution from local and nonlocal parts. When $m < 1$ in Equation

(4.4), the nonlocal variable produces less effect than the local one. On the contrary, the contribution of the local variable will be negative when $m > 1$. Existing research has shown that $m > 1$ should be used to achieve the best regularisation results (Vermeer and Brinkgreve, 1994; Lü et al., 2009; Xue et al., 2022). However, the exact value is dependent on the model and has to be determined via trial and error. The ON method ($m = 1.5$) distribution crosses the distance from the calculation point and is plotted in Figure 4.4.

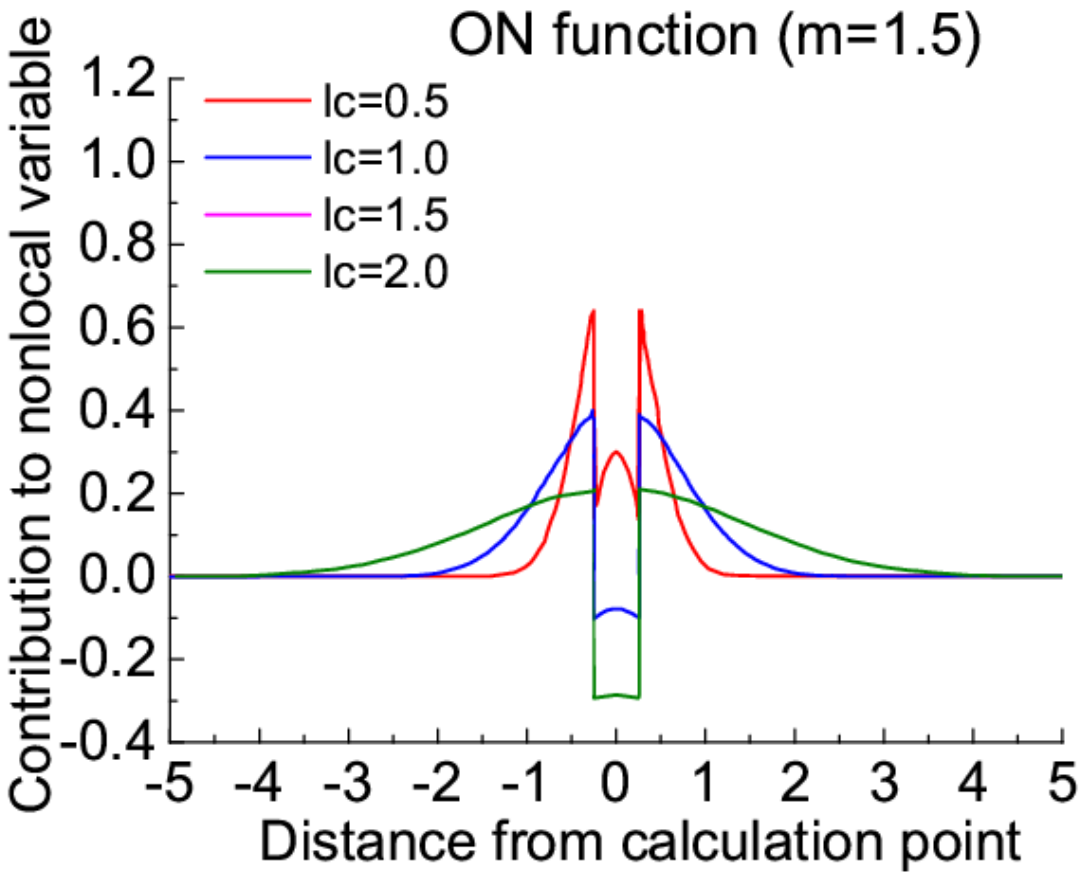

Figure 4.4 The Over-nonlocal method ($m = 1.5$) distribution function in 1D condition

The value of m plays an important role in the ON method and affects the thickness of the shear band (Brinkgreve, 1994). The influence of parameter m on shear band thickness is provided by Lü et al. (2009). The shear band thickness increases with the parameter, and the slope decreases. For example, in a one-dimensional problem, whether inside the bar or at the boundary, the distribution of the plastic strain (shear band thickness) increases with an increase in m. However, this result is only based on a simple problem. More complex

boundary value problems need to be considered. Moreover, the boundary conditions may have an impact on the outcome when the value of the parameter is low (Jostad and Grimstad, 2011).

The comparison of the Local model, GD method, G&S method, and ON method is plotted in Figure 4.5. The internal length is equal to one for all distributions.

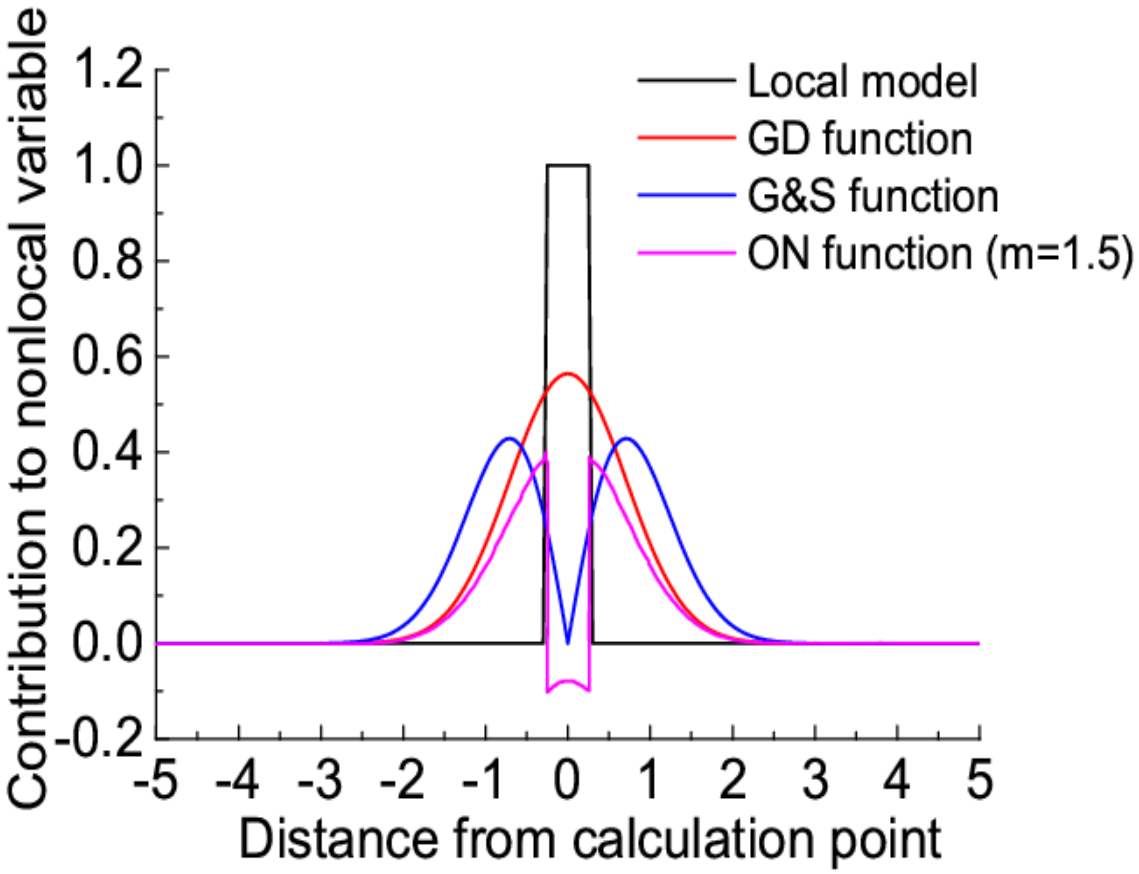

Figure 4.5 The comparison of three different functions with the same internal length

4.3 Nonlocal formulation of the constitutive model in this study

The strain-softening of the critical state model presented in the previous Chapter is mainly affected by e, F_{ij} and H. It is inconvenient to use nonlocal F_{ij} and H in the hardening law. There are several reasons for this. First, the evolution of F_{ij} and H is dependent on the plastic

shear strain increment, but their full form cannot be expressed explicitly in terms of the total plastic shear strain. It is therefore impossible to use the nonlocal plastic shear strain to get the nonlocal F_{ij} and H. Secondly, the plastic shear strain increment has to be calculated before the averaging calculation is carried out if the increment of F_{ij} and H is assumed nonlocal. Since the original model is complex, it has to be implemented using some advanced stress integration methods such as the explicit or implicit methods (Zhao et al., 2005; Gao and Zhao, 2013). In these stress integration methods, the plastic strain increment can only be obtained at the end of each step when the stress and state variables are already updated. This means that the nonlocal increment of F_{ij} and H has to be calculated at the end of each step. If the nonlocal increment of H is used without changing the previous stress integration (e.g., the stress increment), the condition of consistency for the yield function cannot always be satisfied. The evolution of F_{ij} is dependent on the loading direction n_{ij} which can change during the stress integration. It is thus inappropriate to simply take the average of dF_{ij} at the end of the step. However, the evolution of e is dependent on the total volumetric strain only, and therefore, it is convenient to make it nonlocal.

Following Mallikarachchi and Soga (2020), the increment of void ratio de is assumed to be nonlocal as below:

$$de = (1 + e)d\varepsilon_{vn} \tag{4.5}$$

where positive de is associated with volume contraction and $d\varepsilon_{vn}$ is the nonlocal volumetric strain increment.

$$d\varepsilon_{vn} = \frac{\sum_{k=1}^{N} w_i v_i d\varepsilon_{vi}}{\sum_{k=1}^{N} w_i v_i} \tag{4.6}$$

where N is the number of IPs within the averaging area, w_i , v_i and $d\varepsilon_{vi}$ represent the weight function, volume and local volumetric strain increment of integration point i. Note that Equations (4.5) and (4.6) can be used for the Gaussian and G&S functions. When the over-nonlocal method is used, the void ratio increment is expressed as:

$$de = (1 + e)\left[(1 - m)d\varepsilon_{vl} + \frac{m\sum_{k=1}^{N} w_i v_i d\varepsilon_{vi}}{\sum_{k=1}^{N} w_i v_i}\right] \tag{4.7}$$

where $d\varepsilon_{vl}$ is the total local volumetric strain increment for that step.

4.4 Implementation of the nonlocal method

The nonlocal methods can be directly applied in Abaqus by the user-defined material subroutine (UMAT) to analyse the strain localisation in soil. It is worth noting that nonlocal methods are implemented in finite element codes at the constitutive model level without changing equilibrium equations. The model has been implemented using the explicit stress integration method with automatic sub-stepping (Zhao et al., 2005; Gao and Zhao, 2013).

The increment of averaging nonlocal variable (void ratio) is calculated at each sub-increment for all the IPs since the total strain increment is divided into several calculation steps. However, this will raise the computational efficiency issue. Thus, a scaling variable r_v is applied in the nonlocal regularisation method, which is defined below:

$$r_v = \frac{d\varepsilon_{vn}}{d\varepsilon_{vl}} \tag{4.8}$$

where $d\varepsilon_{vn}$ is the nonlocal volumetric strain increment for each IP is calculated at the start of each increment. And $d\varepsilon_{vl}$ is the total local volumetric strain increment for each increment. At the end of each sub-increment, the void ratio is updated as below:

$$de^s = (1+e)d\varepsilon_{vl}^s r_v \tag{4.9}$$

where $d\varepsilon_{vl}^s$ is the local volumetric strain increment to obtain the nonlocal void ratio increment de^s for the sub-increment.

For Over-nonlocal method then can be expressed as:

$$de^s = (1+e)[(1-m)d\varepsilon_{vl}^s + md\varepsilon_{vl}^s r_v] \tag{4.10}$$

Moreover, two user subroutines, UMAT (user-defined materials) and USDFLD (user-defined field variables) are needed for implementing the nonlocal method in Abaqus.

The UMAT is called by the main finite element program at each IP, and it is only able to access information (stress, strain, state variables, etc) at the current IP (Mallikarachchi, 2019). However, in the nonlocal method, the information is accessed from IPs in the neighbourhood of the current IP. Thus, a common block array (ENCD) is provided to store information at each IPs and information is updated after each time step. A common block array is a three-dimensional array in which the first and second dimensions are element and IP identifiers, respectively. The third identifier can be chosen as IP coordinates and softening

parameters. Further, IP coordinates are used to calculate the relative distance to surrounding IPs (Mallikarachchi, 2019; Gao et al., 2021; Gao et al., 2022).

The nonlocal averaging is carried out at the beginning of each increment in the UMAT. First, the local volumetric strain increment $d\varepsilon_{vl}$ for each IP is calculated. The nonlocal strain increment $d\varepsilon_{vn}$ and scaling variable r_v are then computed using Equations (4.5) – (4.8). However, this process required lots of computing time. Thus, the IPs within the radius of four times the characteristic length are considered in the weight function to reduce the computational time because w_i becomes negligible when $r_i > 4l$. A common block array ENCD (NEL, NIP, 4) is used in UMAT to return the coordination [ENCD (NEL, NIP, 1–3)] and $d\varepsilon_{vl}$ [ENCD (NEL, NIP, 4)] of each IP (Mallikarachchi and Soga, 2020). The components of ENCD are obtained in the UMAT for each IP, which can then be used for the UMAT of the other IPs. The remaining part of the UMAT is the same as that for a local model, except that the void ratio is updated using Equations 4.9 and 4.10 at the end of each sub-increment.

The subroutine USDFLD is used to get the volume of each IP (IVOL) using the utility routine GETVRM. This variable IVOL is then returned as a common block array VOLINT (NEL, NIP, 1), where NEL is the total number of elements in a problem, and NIP is the number of IPs in each element. Specifically, the volume of each IP (NPT in Abaqus) of the associated element (NOEL in Abaqus) is obtained and then stored as a component VOLINT (NOEL, NPT, 1) in the USDFLD. The flowchart of implementation of the regularisation method in Abaqus is show in Figure 4.6.

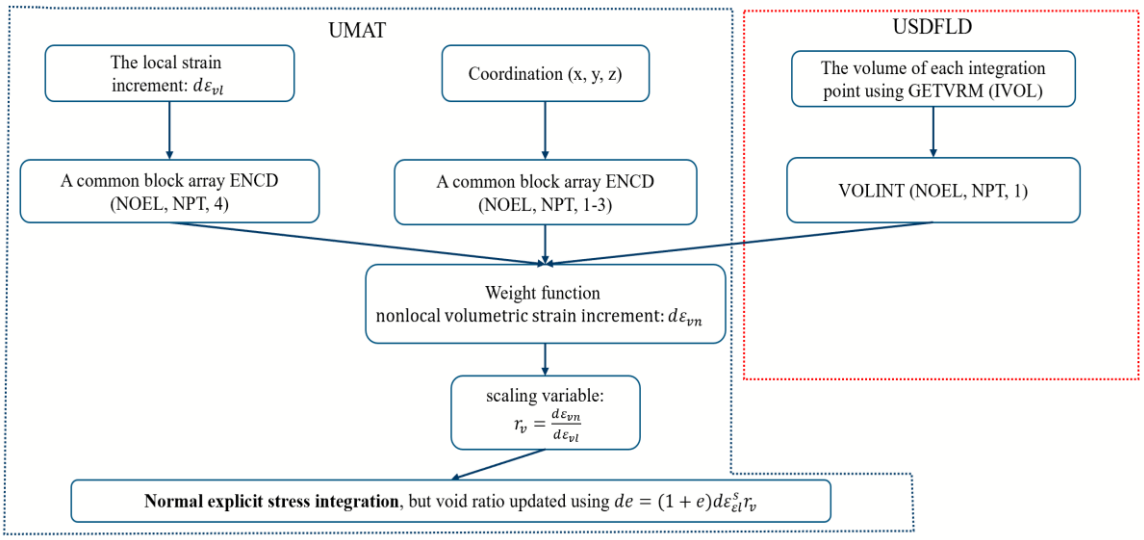

Figure 4.6 The flowchart of implementation of the regularisation method in Abaqus

4.5 The determination of internal length l_c in nonlocal method

l_c is an important parameter for nonlocal regularisation models, as it is used for the weight functions. The size of the internal length determines how many IPs can be involved in nonlocal regularising, averaging the local variables of the local integration point and neighbouring variables at the neighbouring IPs. As mentioned by Gao et al. (2021), l_c should be equal to or larger than the maximum mesh size to make sure that sufficient IPs are involved. Bigger l_c means that the stress–strain relationship of the current integration point is affected by that of IPs further away. In this way, the deformation region will remain above the resolution level of the material model. A wider shear band and a slower rate of strain-softening will be predicted as l_c increases. (Mallikarachchi, 2019)

Experimental evidence shows that the shear band thickness t_s is about 10 - 20$d_{50}$for most sand, where d_{50} is the mean particle size. For the Toyoura sand used here, $d_{50} \approx 0.2\,mm$ and $t_s \approx 2-4\,mm$. The predicted t_s is very close to l_c when the Galavi and Schweiger weight function is used, which will be shown in the subsequent sections. Therefore, $l_c \approx 2-4\,mm$ has to be used if realistic prediction of t_s is required.

But the maximum mesh size must always be smaller than l_c. While it is feasible to use very small l_c to simulate the response of small soil samples, it is impractical to use $l_c \approx 2-4\,mm$ in most real boundary value problems. There are two significant reasons. First, small mesh size causes numerical convenience issues for advanced soil models, which give a highly nonlinear stress-strain relationship. Secondly, the computational time will significantly increase when a small mesh size is used for a nonlocal model. Therefore, proper l_c is typically chosen based on the size of the solution domain, which can guarantee mesh-independent results but not realistic shear band thickness.

4.6 Summary

Three different nonlocal models were developed based on the weight functions, including GD, G&S and ON functions. Among them, the GD function shows the highest contribution to the calculated nonlocal variable at the centre. The leading nonlocal variable is concentrated at the local point and cannot spread to surrounding points, negatively affecting

the nonlocal method. Improvement was made by the G&S and ON functions. The nonlocal variable is no longer concentrated at the local point and is replaced with two same peaks near the local point. In addition, the ON function needs to find a proper nonlocal parameter, m which has a significant impact on this method.

In this thesis, the strain-softening of the critical state sand model is mainly affected by the void ratio. Therefore, the increment of the void ratio can be assumed to be a nonlocal variable. However, it only treats the void ratio as nonlocal, which makes it unable to eliminate the mesh dependency.

Chapter 5：Evaluation of three weight functions for nonlocal regularisation

5.1 Introduction

Some studies have been done on the comparison of three weight functions in simple BVPs like plane strain compression. It is found that the G&S function gives better regularisation results than the GD or the ON function (Galavi and Schweiger, 2010; Guo and Stolle, 2013; Summersgill et al., 2017; Mallikarachchi and Soga, 2020; Gao et al., 2022). However, the performance of these functions in real-world BVPs has not been evaluated. The main aim of this Chapter is to carry out a comprehensive comparison of these functions in various BVPs, including drained and undrained plane strain compression, the response of strip footings on level ground and near a slope and a retaining wall (passive and active conditions).

5.2. Plane strain compression tests

The samples used in this section are 60 mm wide and 120 mm high, as shown in Figure 5.1. The boundary condition is also shown in Figure 5.1. A confining pressure of $p_0 = 200$ kPa is applied on the two vertical sides. Vertical displacement is applied on the top side, with the horizontal displacement unconstrained. The bottom side is pinned at the left and free to move to the right. A square 'weak' area (12mm×12mm) with inclined bedding plane orientation ($\alpha = 45°$) is implemented, which is used to trigger a shear band in the plane strain compression test. For the remaining part of this specimen, the bedding plane orientation is horizontal and $\alpha = 0°$. The initial void ratio of the sample is $e_0 = 0.65$ (relative density $D_r = 85.6\%$), and the initial degree of anisotropy is $F_0 = 0.4$. All simulations in this study have used 8-noded plane strain quadratic elements with reduced integration (CPE8R). Note that all the simulations to be presented below use this element. The thickness of the soil is assumed to be 1m in processing the results.

Moreover, in undrained plane strain compression, the permeability of soil is set very small and water flow at all boundaries is closed. Transient consolidation analysis is selected for all simulations. The rest of the conditions are the same as the drained case.

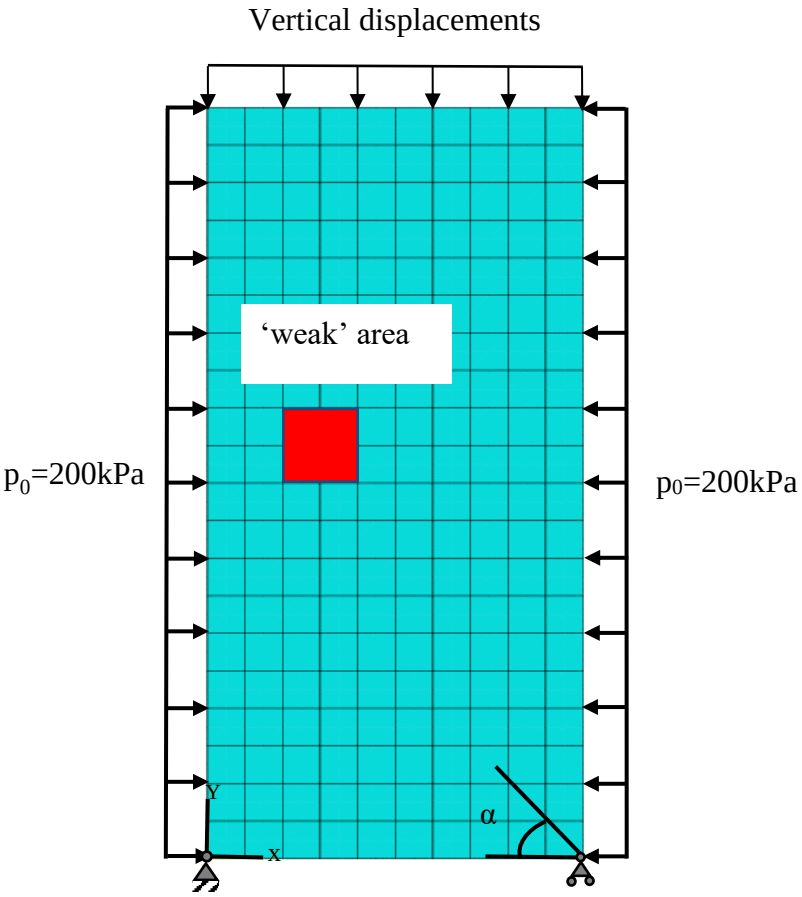

Figure 5.1 The boundary conditions and bedding plan orientation for the plane strain compression simulations

5.2.1 Selection of internal length for simulation

The internal length l_c is an important parameter for nonlocal regularisation models. The size of the internal length determines how many integration points can be involved in nonlocal regularisation. l_c should be equal to or larger than the maximum mesh size to make sure that sufficient integration points are involved. Bigger l_c means that the stress and strain relationship of the current integration point is affected by that of integration points further away. Figure 5.2 illustrates the effect of l_c on the vertical reaction force and displacement curves simulated by the different weight functions. In these models, the mesh size of 0.004 m was selected under drained conditions. The l_c does not affect the solutions before the peak reaction force. Higher peak vertical reaction force and a slower rate of strain-softening were obtained by increasing l_c during post-peak. Furthermore, the GD and ON functions predict a slower rate of the strain-softening curve than the GD function. The internal length

determines the range within which the integration points are considered in the nonlocal averaging. When it is bigger, more integration points are accounted for in the weight functions of each integration point. This means that the local load is artificially distributed to more neighbouring integration points, leading to a lower rate of strain softening. In the simulations for plane strain compression below, $l_c = 0.012\,m$ is used. It should be mentioned that l_c also has an influence on the shear band thickness, which will be shown in subsequent sections. The real shear band thickness of sand is about 10-20d_{50}, where d_{50} is the mean particle size (Galavi and Schweiger, 2010). If the real shear band thickness were to be matched in FE modelling, a very small mesh size has to be used because the shear band thickness is related to l_c. This would cause issues like excessive computation time and numerical divergence. Therefore, proper l_c is typically chosen based on the size of the solution domain, which can guarantee mesh-independent results but not realistic shear band thickness.

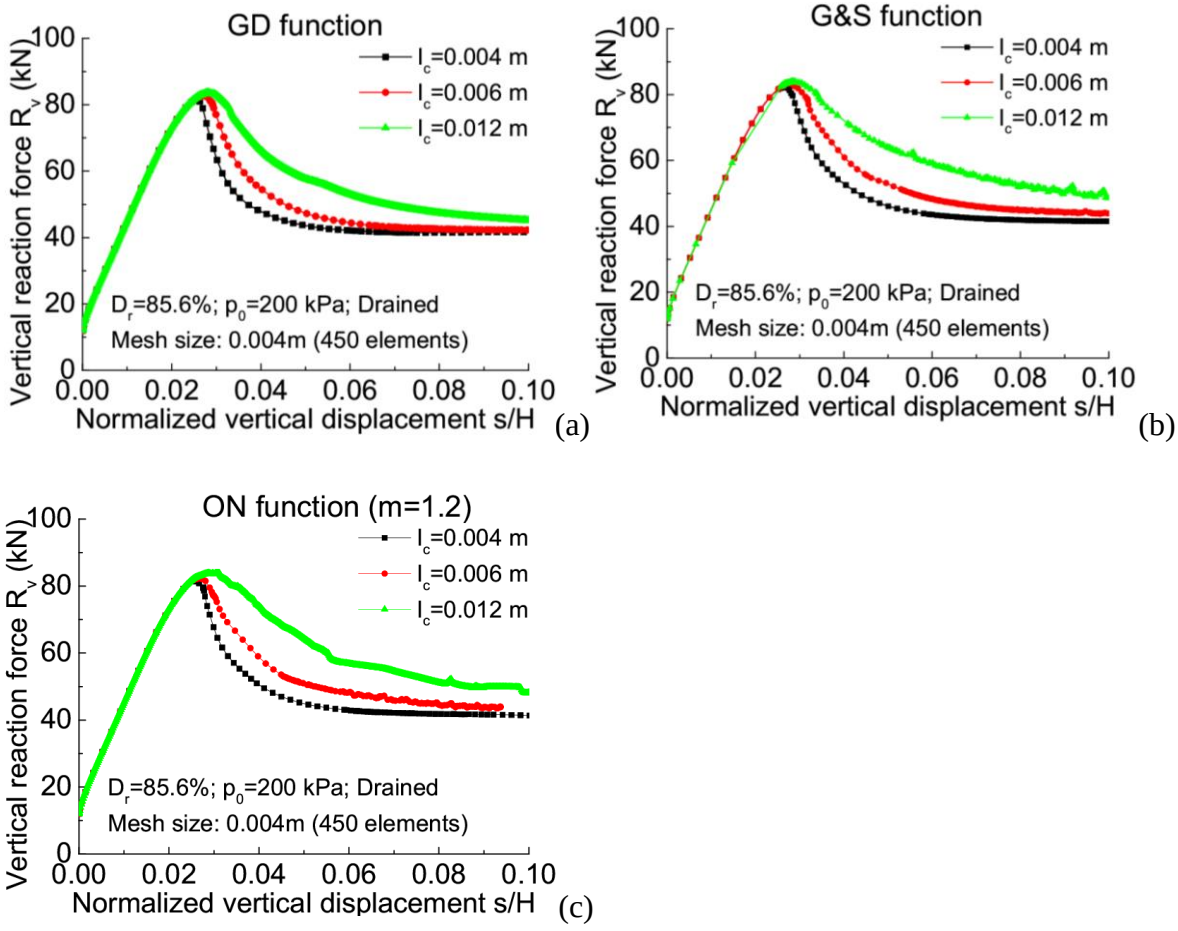

Figure 5.2 The effect of internal length on the force-displacement relationship in drained plane strain compression test: (a) GD function; (b) G&S function; (c) ON function

5.2.2 Investigation of parameter m for the Over-nonlocal Method

The over-nonlocal parameter m provides the relative contribution from local and nonlocal parts. According to the previous Chapter, the parameter m affects the contribution of the nonlocal variable along the calculation point and the thickness of the shear band (Brinkgreve, 1994; Lü et al., 2009; Summersgill et al., 2017). Thus, the selection of the value of m plays an important role in the ON method. In this section, biaxial compression tests for brained and undrained conditions were set to evaluate the influence of parameter m on force-displacement response and strain distribution over the cross-section.

The load-displacement responses for m =1.0, 1.2, 1.5 and 2.0 are shown in Figures 5.3 and 5.4 under drained and undrained conditions, respectively. The results show that m =1.5 and 2.0 is unstable, but the response for $m = 1.0$ and 1.2 is stable. Under the drained condition, when $m = 1.5$, the degree of softening decreases as the mesh size decreases. This phenomenon becomes more pronounced when $m = 2.0$. Under the undrained condition, as m increases, the force-displacement curve becomes increasingly unstable. In fact, when $m = 1.0$, which is equivalent to the Gaussian distribution function. Compared to when $m =$ 1.0, the use of the over-nonlocal method shows more effective alleviation of mesh dependency when $m = 1.2$.

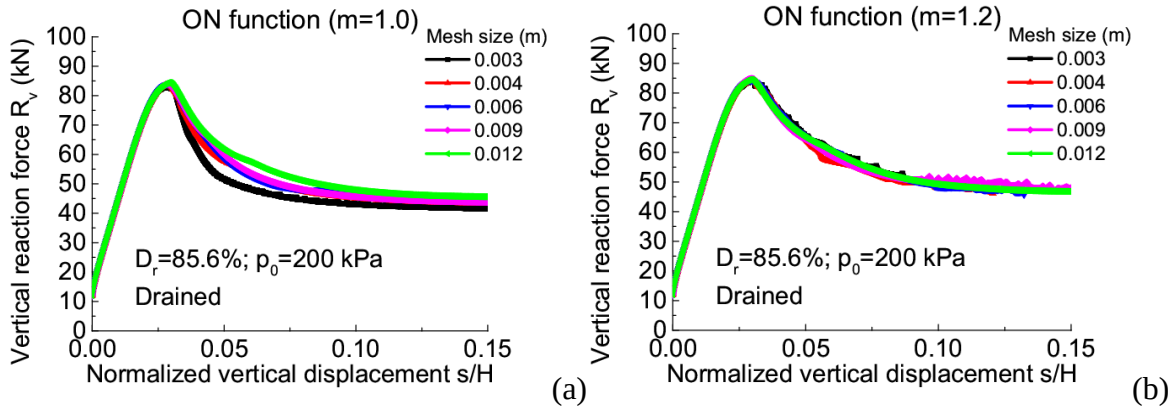

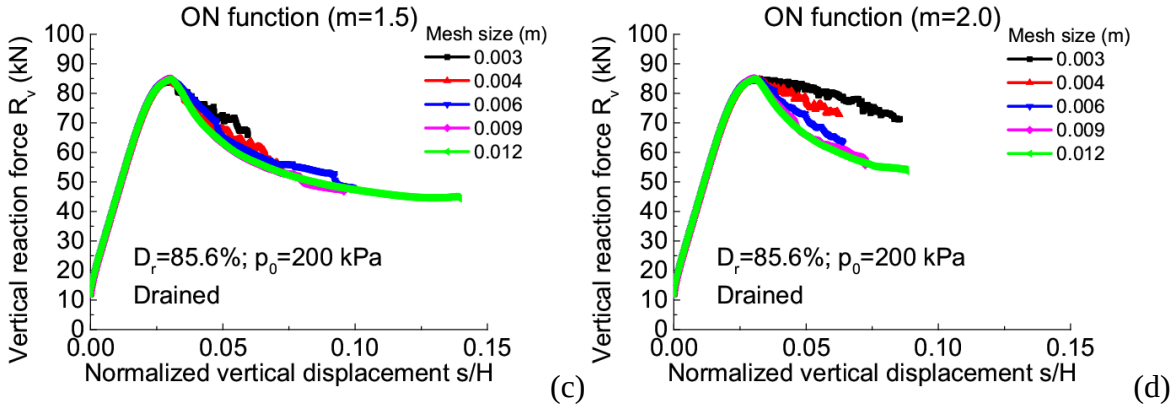

Figure 5.3 The influence of parameter m of ON function on the force-displacement relationship for drained plane strain compression: (a) $m = 1.0$; (b) $m = 1.2$; (c) $m = 1.5$; (d) $m = 2.0$

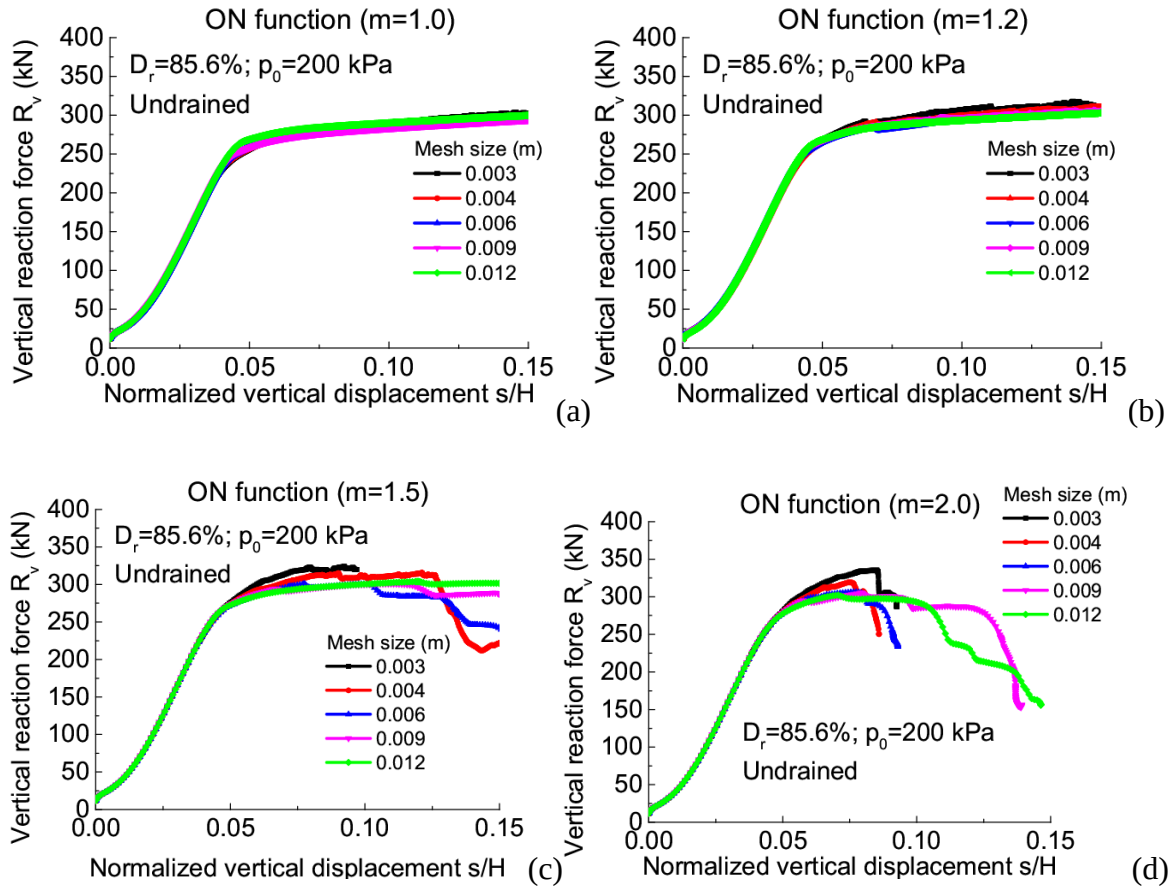

Figure 5.4 The influence of parameter m of ON function on force-displacement relationship for undrained plane strain compression: (a) $m = 1.0$; (b) $m = 1.2$; (c) $m = 1.5$; (d) $m = 2.0$

The strain distribution over cross sections at displacement 7% are plotted in Figure 5.5 and Figure 5.6 for drained and undrained conditions, respectively. Regardless of the drained or undrained condition, the shear band thickness increases with an increase in parameter m, while the maximum strain within the shear band decreases. The parameter m controls the distribution of nonlocal strain and influences its magnitude. The summary of the influence of the parameter m on the shear band for a fine mesh size (0.004 m) is depicted in Table 5.1.

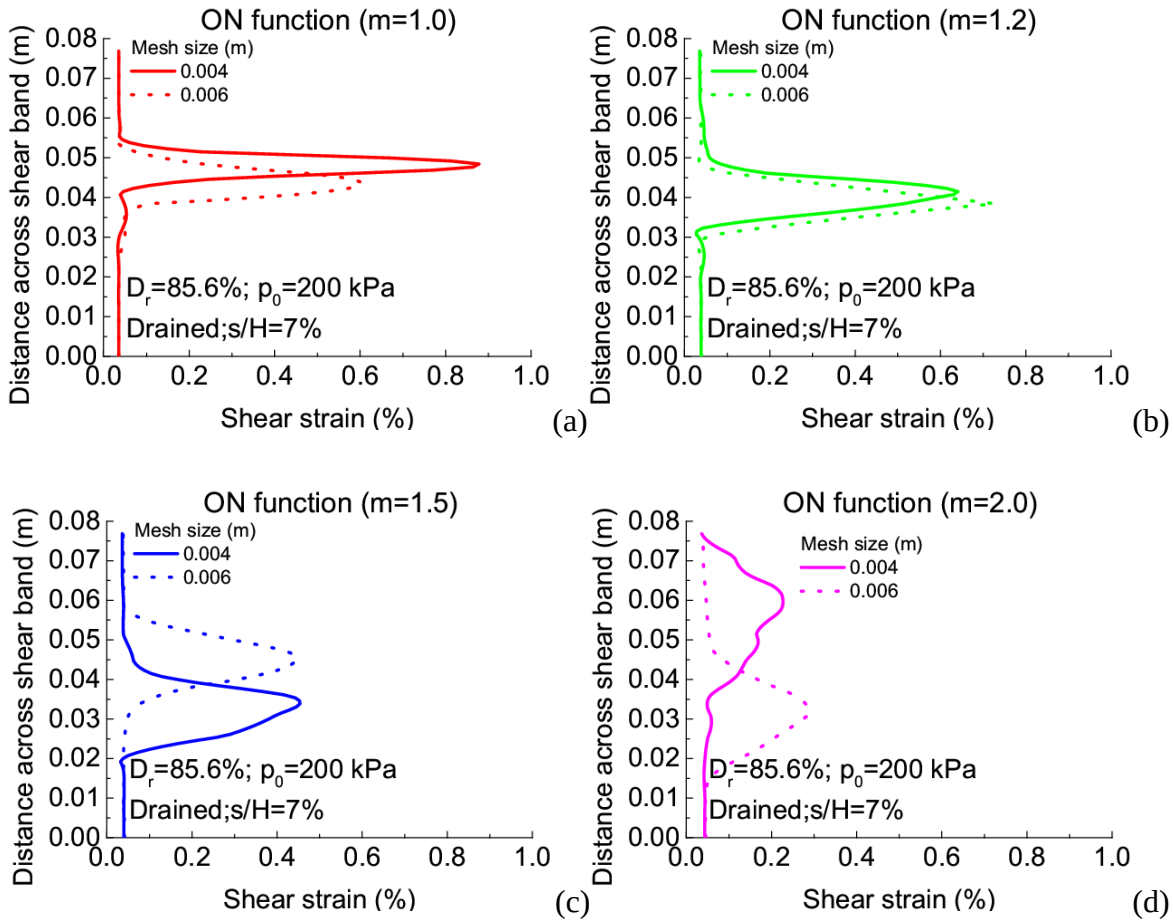

Figure 5.5 The influence of parameter m of ON function on the cross-section profiles based on the shear strain under the drained condition: (a) $m = 1.0$; (b) $m = 1.2$; (c) $m = 1.5$; (d) $m = 2.0$

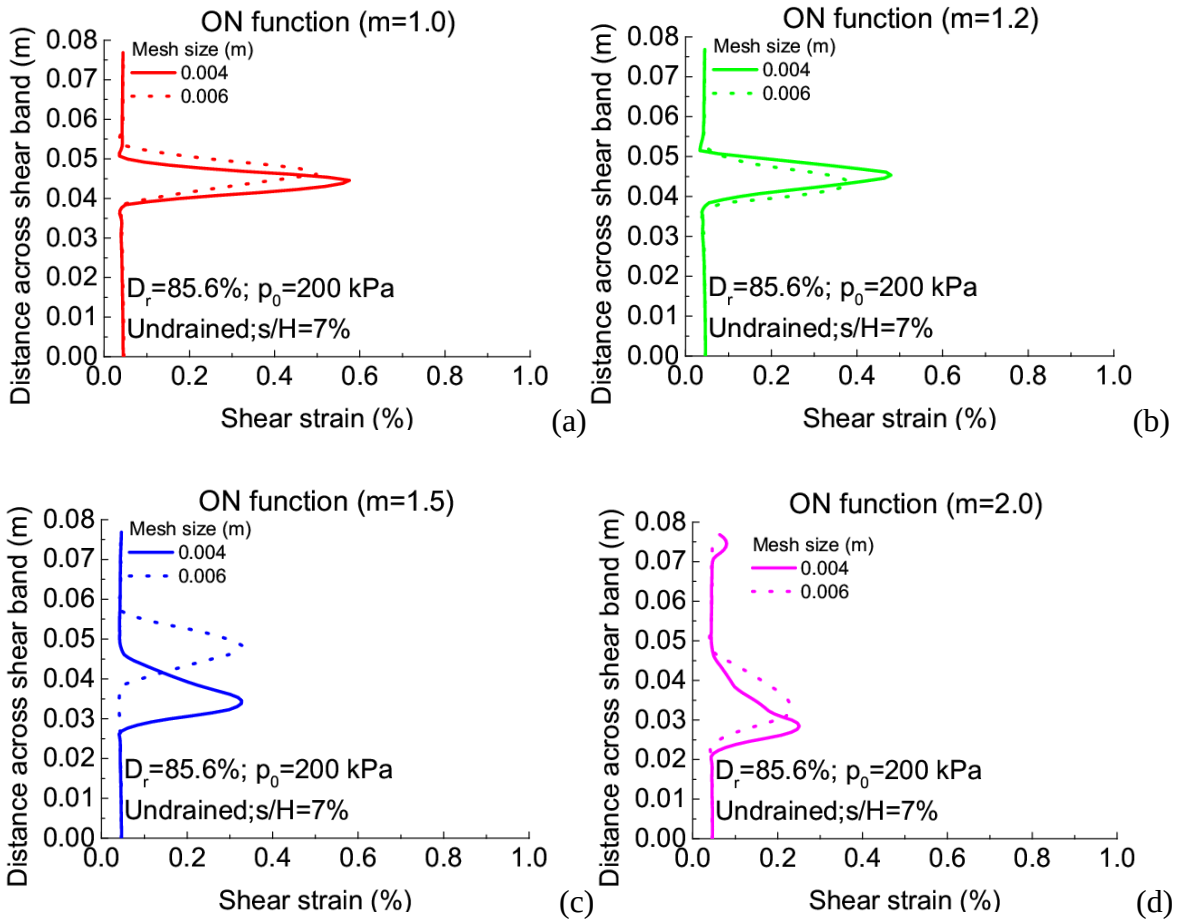

Figure 5.6 The influence of parameter m of ON function on cross-section profiles based on the shear strain under the undrained condition: (a) $m = 1.0$; (b) $m = 1.2$; (c) $m = 1.5$; (d) $m = 2.0$

Table 5.1 The summary of the influence of parameter m on the shear band

	Value of parameter m	Shear band thicknesses (m)	Maximum strain within the shear band
Drained condition	1.0	0.015	0.9%
	1.2	0.02	0.6%
	1.5	0.025	0.45%
	2.0	0.045	0.2%
Undrained condition	1.0	0.012	0.55%
	1.2	0.015	0.5%
	1.5	0.019	0.3%
	2.0	0.025	0.25%

In summary, a premature softening and wider shear band thickness was previously observed in both drained and undrained conditions when m increased. A higher m indicates that the ON method could produce erroneous results under some conditions. Contrary to the results of Summersgill et al. (2017), the sudden decrease in reaction load appears when the parameter m increases is not caused by excessive local strain, but rather wider shear band thickness. Moreover, to utilise the ON method effectively, it is essential to closely monitor the results for any signs of sudden excessive softening. This requirement for careful monitoring reduces the advantages of using the ON method compared to other nonlocal methods (GD and G&S methods. It should be mentioned that $m = 1.2$ is chosen for the ON method through trial and error. Smaller m gives mesh-dependent solutions, but higher m causes numerical divergence in the simulations. In the strip footing problem to be discussed in the subsequent Chapter, higher m is found to give a steep reduction of reaction force acting on the footing after peak, which is not consistent with the experimental observations in centrifuge tests.

5.2.3 Drained plane strain compression tests

Figure 5.7 shows the force-displacement curves predicted by the local and three nonlocal models. Compared with local and nonlocal models, the strain hardening part is insensitive to the mesh size until the peak and becomes mesh-dependent in the strain softening part. In the local model, a finer mesh size results in earlier and faster softening, consistent with previous findings (Conte et al., 2010; Schädlich, 2012). Moreover, similar to Mohr-Coulomb (MC) models, forces at the critical state exhibit mesh dependence issues. When a larger mesh is employed, the critical state strength increases. In nonlocal models, the study examines the effectiveness of three nonlocal methods in regularising the post-localisation response of the model using a l_c of 0.012 m, as depicted in Figures 5.7(b)-(d). Figure 5.7(b) shows that the GD method does not fully eliminate mesh dependency for the given characteristic length. In contrast, both GS and ON methods adequately produce force-displacement responses independent of the mesh, as demonstrated in Figures 5.7(c)-(d). The main reason is that the local variable significantly influences the results when the GD function is used. Moreover, the critical state strengths obtained are nearly unaffected by changes in the mesh size. Across all nonlocal methods, the softening rate is reduced, leading to a delay in reaching the critical state.

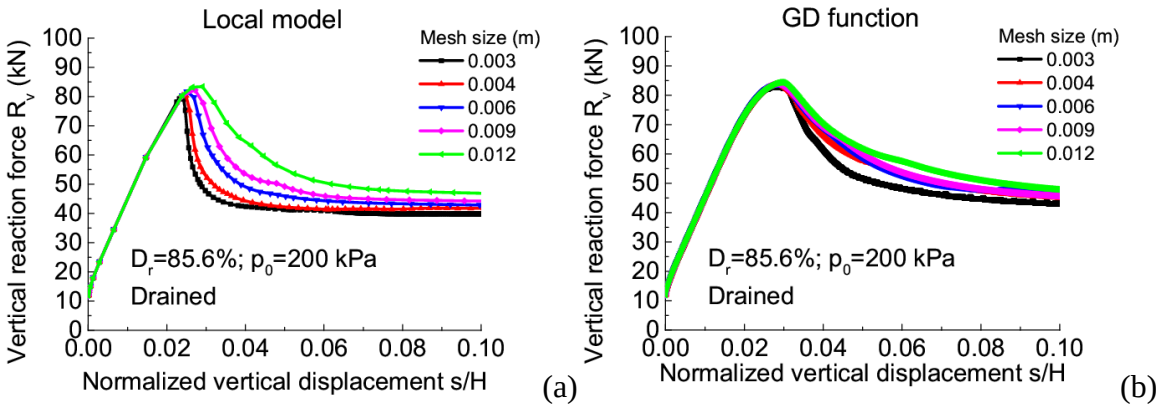

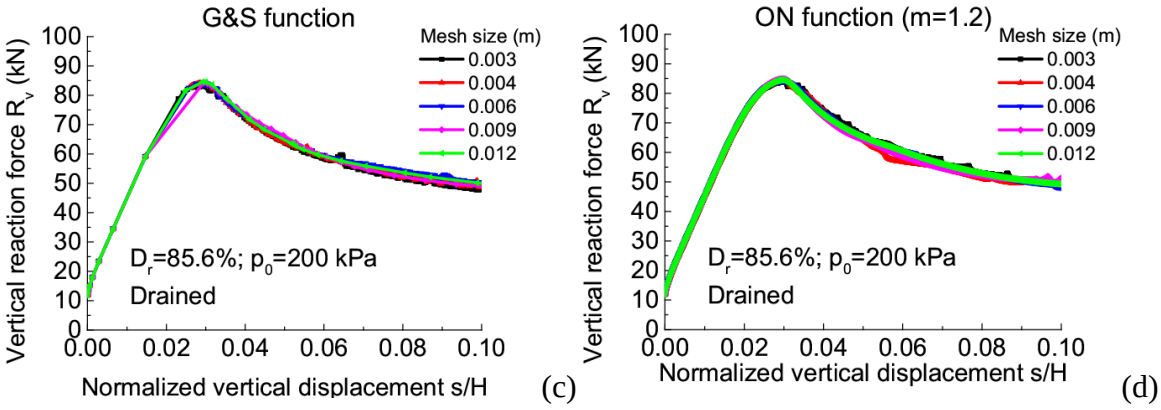

Figure 5.7 Comparison of the local and nonlocal models on the force-displacement relationship for drained plane strain compression: (a) Local model; (b) GD function; (c) G&S function; (d) ON function

Shear strain contours at the strain softening for the local and three different nonlocal models at displacement $s/H = 9\%$ are shown in Figures 5.8-5.11, where SDV11 represents the total shear strain. Figure 5.8 exhibits that the thickness of the shear strain zone predicted by the local model is sensitive to the mesh size. On the contrary, contour plots of total shear strain from GS and ON nonlocal methods in Figure 5.10 and Figure 5.11 provide almost similar shear strain zone irrespective of the mesh size during the strain softening period.

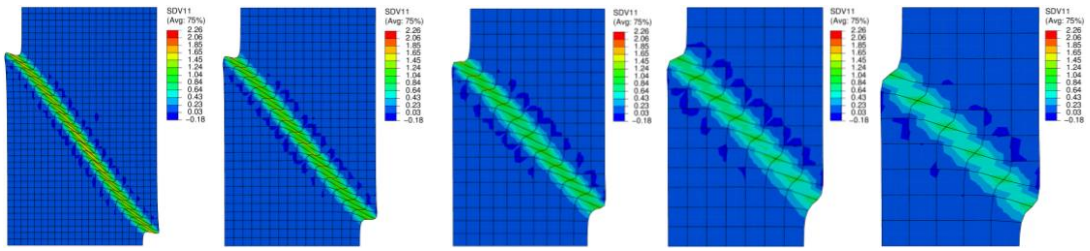

Figure 5.8 Shear strain contour for the Local model at $s/H = 9\%$ for different mesh sizes: (a) 0.003 m; (b) 0.004 m; (c) 0.006 m; (d) 0.009 m; (e) 0.012 m

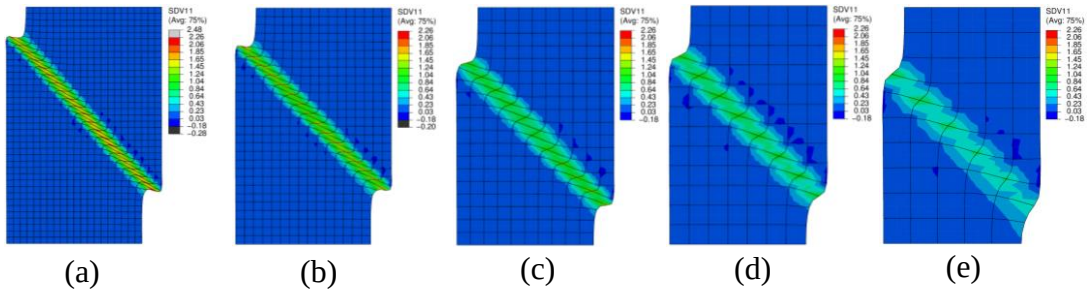

(a) (b) (c) (d) (e)

Figure 5.9 Shear strain contour for the GD function in plane strain compression at $s/H = 9\%$ for different mesh sizes: (a) 0.003 m; (b) 0.004 m; (c) 0.006 m; (d) 0.009 m; (e) 0.012 m

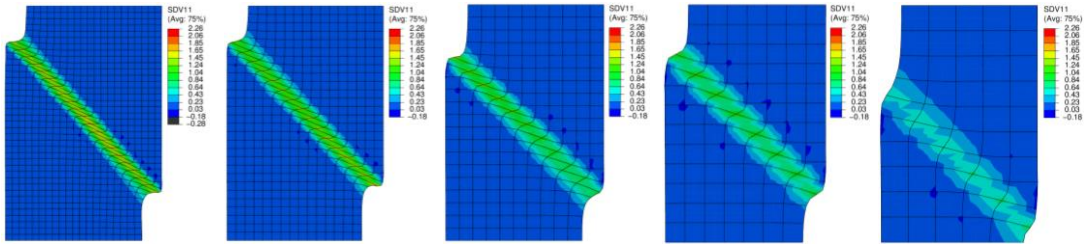

(a) (b) (c) (d) (e)

Figure 5.10 Shear strain contour for the G&S function in plane strain compression at $s/H = 9\%$ for different mesh sizes: (a) 0.003 m; (b) 0.004 m; (c) 0.006 m; (d) 0.009 m; (e) 0.012 m

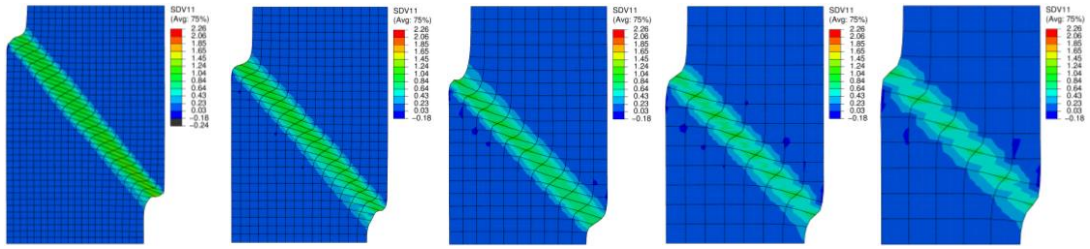

(a) (b) (c) (d) (e)

Figure 5.11 Shear strain contour for the ON function in plane strain compression at $s/H = 9\%$ for different mesh sizes: (a) 0.003 m; (b) 0.004 m; (c) 0.006 m; (d) 0.009 m; (e) 0.012 m

The orientation of the shear band in plane strain is sensitive to the boundary condition and the size of material particles. In FE simulation, the angle of the shear band is determined by factors such as mesh alignment, shape, the type of element used, and the number of nodes. The positions of nodes directly influence both the thickness and the orientation in which the shear band develops. The orientation of the shear band (β) is directly measured from shear strain contours, as shown in Figure 5.12.

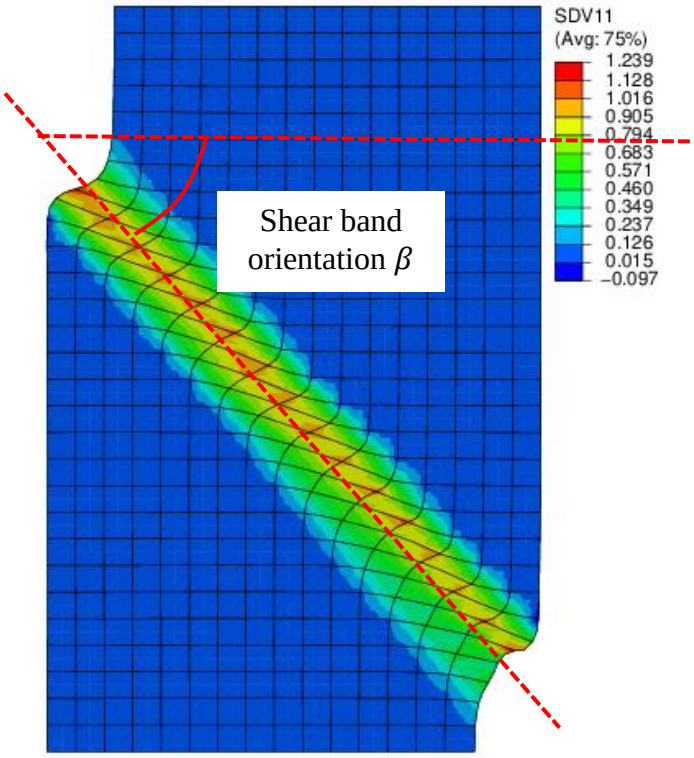

Figure 5.12 Shear strain contour for measuring the shear band orientation

According to Figure 5.13, the predicted angle of the shear band decreases as the mesh size increases. The orientations of shear bands from the local model are mesh-dependent. The difference in angle between the finest mesh and the coarsest mesh is 16.98%. All the nonlocal functions reduce but cannot eliminate the mesh dependency of shear band orientation. This could be partly nonlocal because only one variable (void ratio) is regularised within the constitutive level that affects the strain softening, which is assumed nonlocal. In this circumstance, the direction of nodal degrees of freedom is hardly affected. (Mallikarachchi, 2019). The differences between the various nonlocal methods are minor. For finer mesh, the ON method displays a higher shear band orientation compared to other

nonlocal models. For example, when the mesh size is 3mm, the angle for the ON method is 50° and 49° for GD and GS. On the contrary, three nonlocal models have the same angle at coarse mesh (12mm). The mesh dependency could be further reduced if more state variables in the hardening law are assumed nonlocal. However, this would significantly reduce the computation efficiency.

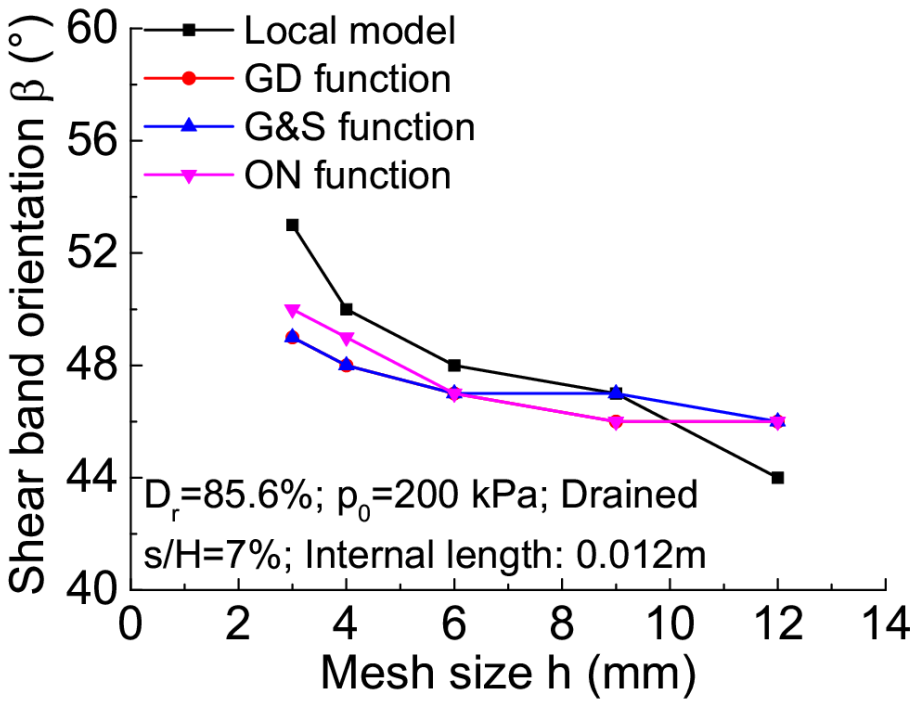

Figure 5.13 Comparison of shear band orientation for drained plane strain compression test

Moreover, the determination of shear band orientation is also affected by the type and size of weak elements used to trigger strain localisation. While the same element type is applied to all mesh sizes, the finer meshes exhibit more flexibility during the strain softening than the larger meshes. As a result, they display greater inclination angles due to mobilised dilation. In contrast, with coarser meshes, the shear band angle is primarily determined by square weak elements (Mallikarachchi, 2019).

The measurement of shear band thickness primarily involves two methods. In Method A, the shear band is directly measured by a cross-section in the shear strain contour plot, this cross-section is perpendicular to the shear band. This method is simple and convenient, but because the endpoints of the cross-section are taken at the nodes of the elements, achieving

a cross-section that is completely perpendicular to the shear band in simulation results can be challenging, leading to slight errors. On the other hand, in Method B, a path is selected in the shear strain plot that traverses the entire soil specimen horizontally. The length where this path coincides with the shear band is denoted as normalised shear band thickness (l). The thickness of the shear band is then calculated by the shear band orientation. Although this method is more complicated, it provides accurate results. It is important to note that calculating the shear band thickness using Method B requires prior computation of the shear band orientation. For the method A, the thickness of the shear band is directly measured based on the shear strain distribution from a cross-section at $s/H = 7\%$ is shown in Figure 5.14.

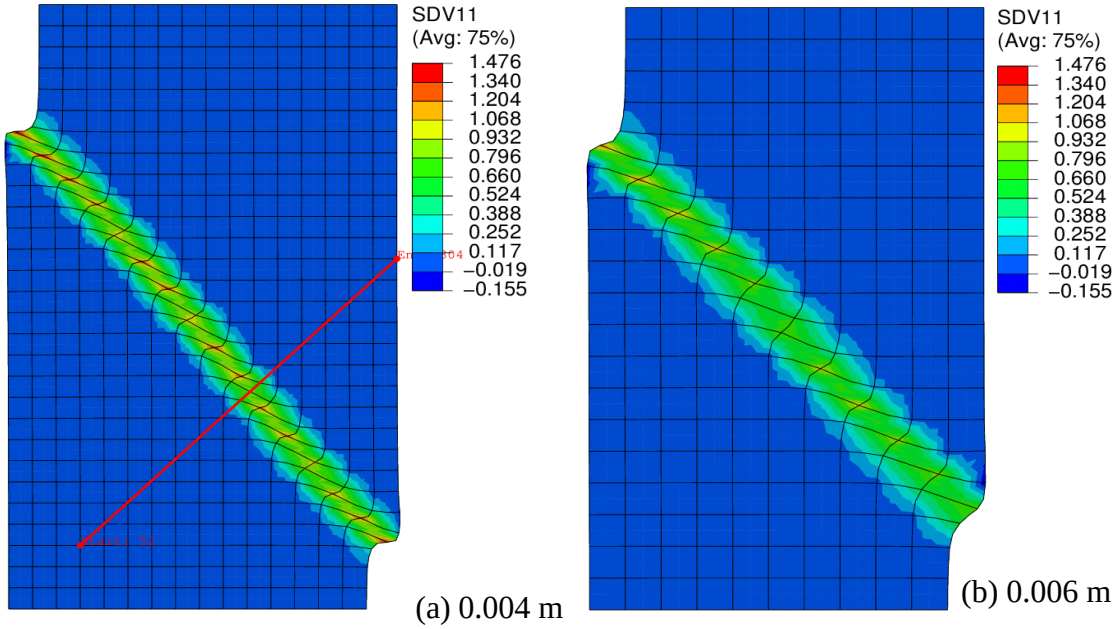

(a) 0.004 m (b) 0.006 m

Figure 5.14 Cross-section contour based on the shear strain under the drained condition with a mesh size of (a) 0.004 m and (b) 0.006 m for the local model

Figure 5.15 shows the determination of shear band thickness for different models. In Figure 5.15(a) t_{s1} and t_{s2} represents shear band thickness for mesh size of 0.004 m and 0.006 m, respectively. The thickness measured from the coarse mesh is wider than the fine mesh. The difference in thickness between different mesh sizes is reduced after nonlocal regularisation but cannot be eliminated because only one state variable (void ratio) is treated in this model

and is known as partial nonlocal. Moreover, the ON model exhibits smaller shear strain in the shear band for fine mesh size than other models. As described in Figure 5.15(d), the shear strain for coarse mesh (0.006 m) is greater than fine mesh (0.004 m) for the over-nonlocal model, which is significantly different from the other models.

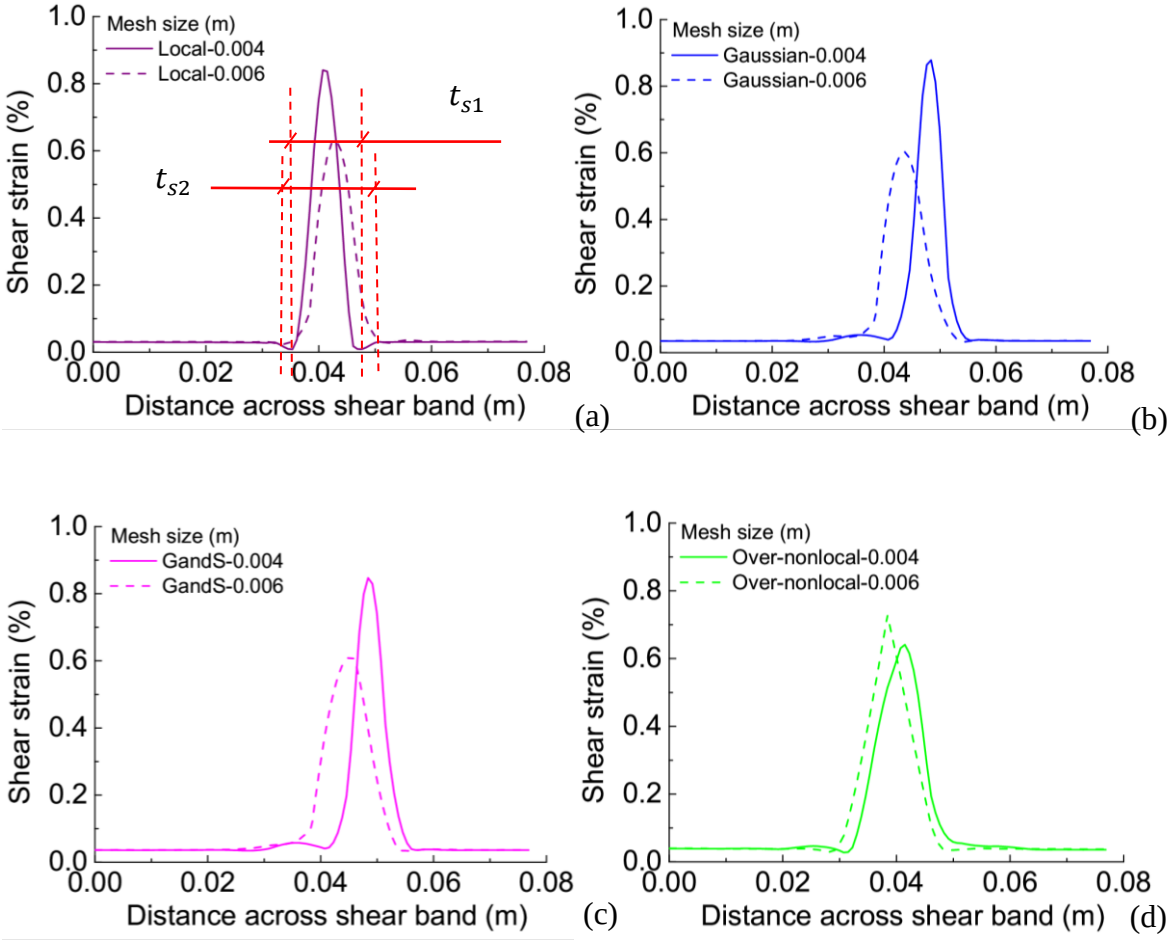

Figure 5.15 Comparison of cross-section profiles based on the shear strain: (a) Local model; (b) GD function; (c) GS function; (d) ON function

According to the previous discussion, the thickness of the shear band is determined by shear strain cross-section profiles. However, other state variables, such as void ratio, anisotropy variable A, and degree of anisotropy F, can also be extracted and recorded to represent the shear band. A path crossing through the centre of soil samples (Method B) is selected to further analyse the influence of local and nonlocal models on the shear band thickness shown in Figure 5.16. The shear band thickness based on various state variables can be calculated by the shear band orientation β a normalised shear band thickness l ($t_s = l \cdot sin\,\beta$).

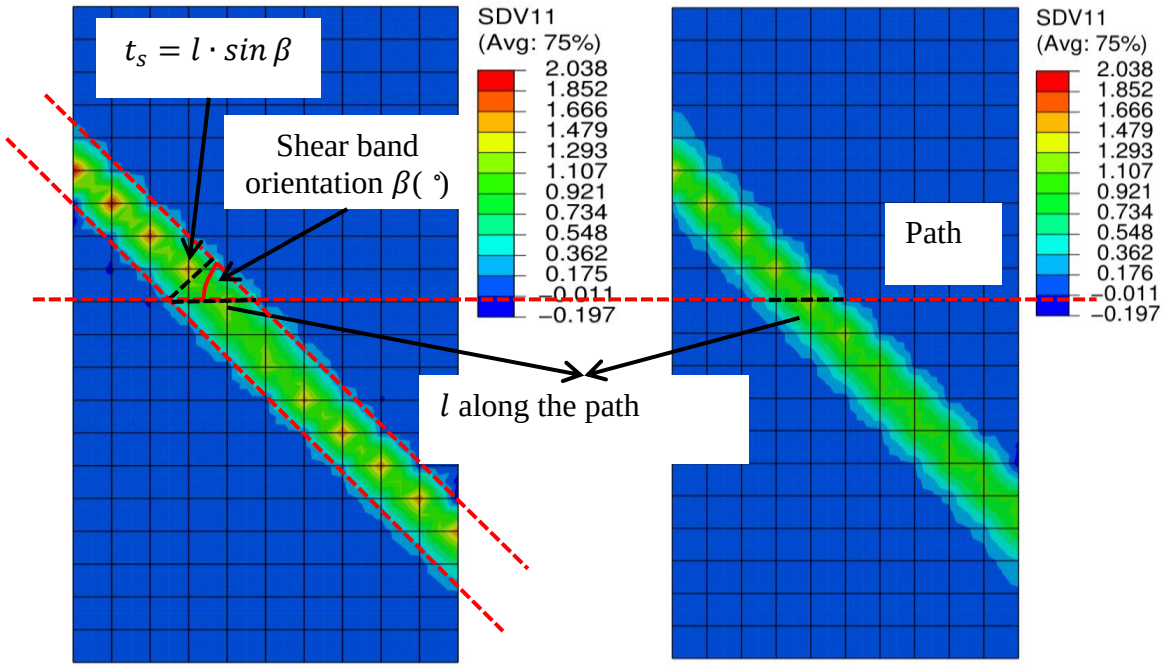

(a) Local model (b) G&S function

Figure 5.16 The selection of path of shear band thickness by total shear strain

As illustrated in Figure 5.17, the mesh size ($h = 0.006\ m$) and vertical displacement ($s/H = 7\%$) are the same for different state variables, ensuring a proper comparison of the impact of related state variables on the shear band between local and nonlocal models. In all simulations, variables reach their peak values at the centre of the normalised shear band l, with shear strain showing the most noticeable variation because of the largest deformation gradients. In addition, excessive strain localisation is primarily caused by significant rearrangements and rotations of particles, resulting in dilation inside the shear band. Furthermore, in all simulation results, the normalised shear band thickness l (t_s) in the nonlocal model is greater than that in the local model. Additionally, between these two models, the void ratio exhibits the maximum difference, while the difference in shear strain is minimal. Among different state variables, the gradient and the change of shear strain are the most noticeable in the shear band. Therefore, when determining the shear band thickness, similar to the Method A, the shear strain contour plot should serve as the benchmark.

A comparison between Method A and Method B is presented in Table 5.2, revealing no significant difference between these two methods.

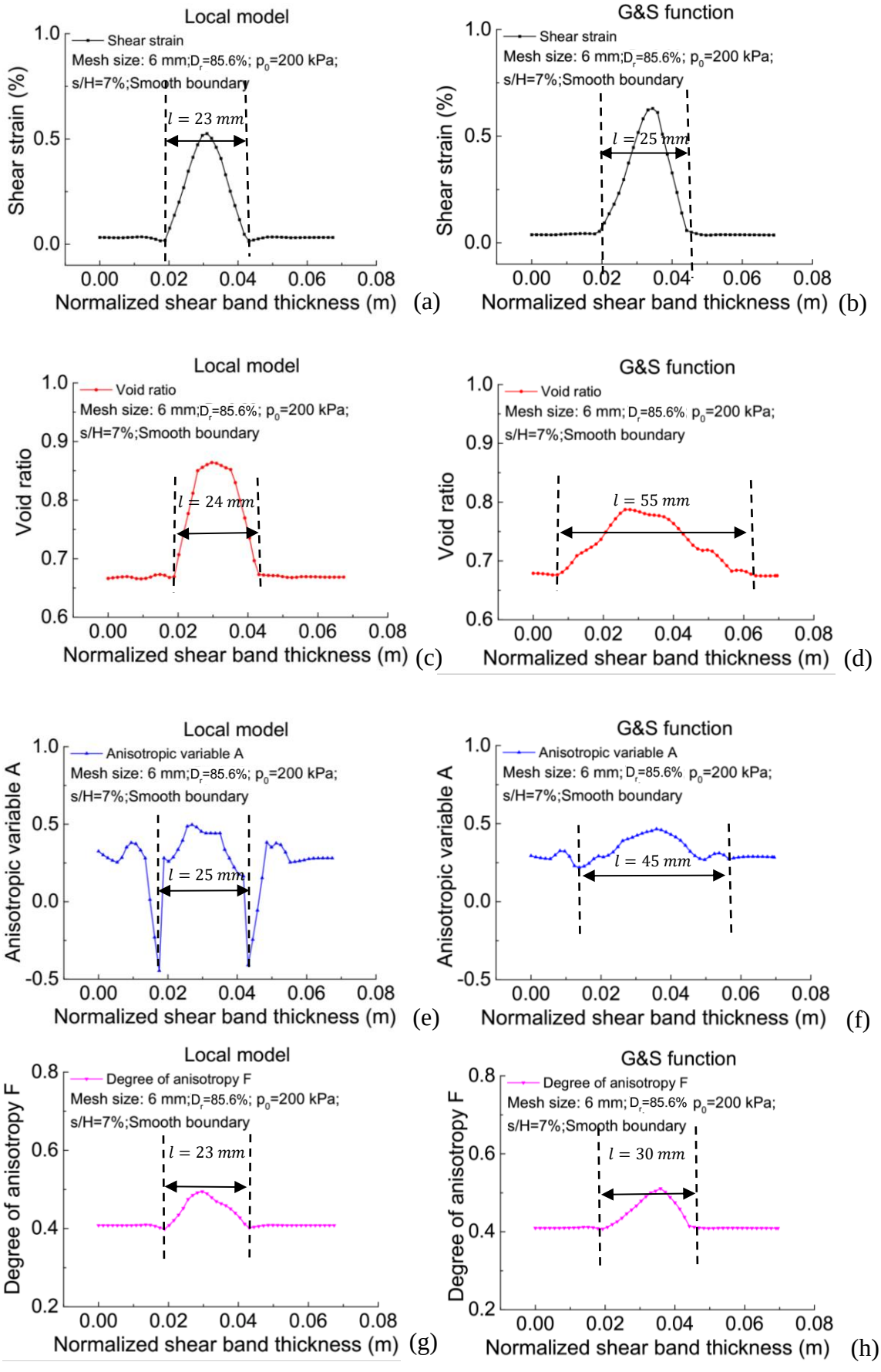

Figure 5.17 Calculation of Shear band thickness by different variables under smooth boundary

Table 5.2 Comparison of t_s from two different methods

	Method A (Cross-section)	Method B (Path)
Local model	$t_s = 17\ mm$	$t_s = l \cdot sin\,\beta$ $= 23 \times sin\,48$ $= 17.08\ mm$
G&S method	$t_s = 17$ mm	$t_s = l \cdot sin\,\beta$ $= 25 \times sin\,47$ $= 18.28\ mm$

The effect of mesh size on shear band thickness is shown in Figure 5.18(a). The shear band thickness simulated by the local model increases significantly with the mesh size. The nonlocal models give a slight variation of shear band thickness when the mesh size $h < l_c$. All nonlocal models provide the same shear band thickness as that of the local model when size $h = l_c$. The shear band thickness predicted by the nonlocal models increases with l_c (Figure 5.18b), and the ON model predicts wider shear bands.

It should be noted that in Figure 5.18(a), even after nonlocal regularisation, the thickness of the large mesh is significantly higher. Ortiz et al. (1987) emphasised that iso-parametric elements have inherent limitations in representing strain localisation. When using iso-parametric interpolation, elements attempt to adjust to the deformation field by averaging deformations on both sides of the discontinuity, as depicted in Figure 5.19. As a result, true discontinuous interfaces are spread across several elements, causing the minimum shear band thickness to exceed the width of a single element. Finer meshes enable element boundaries to follow shear band directions, which larger iso-parametric elements cannot accurately resolve. Triangular elements, on the other hand, are found to be more effective in representing these localisations. The shear band boundaries are hard to model by continuum methods, making particle methods more suitable for capturing this transition.

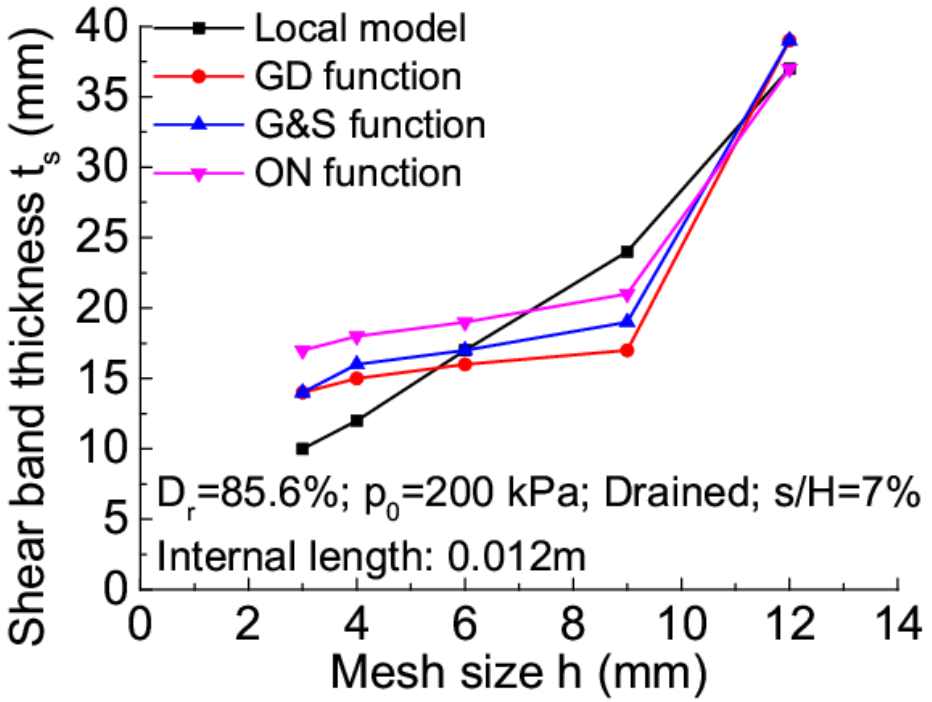

(a)

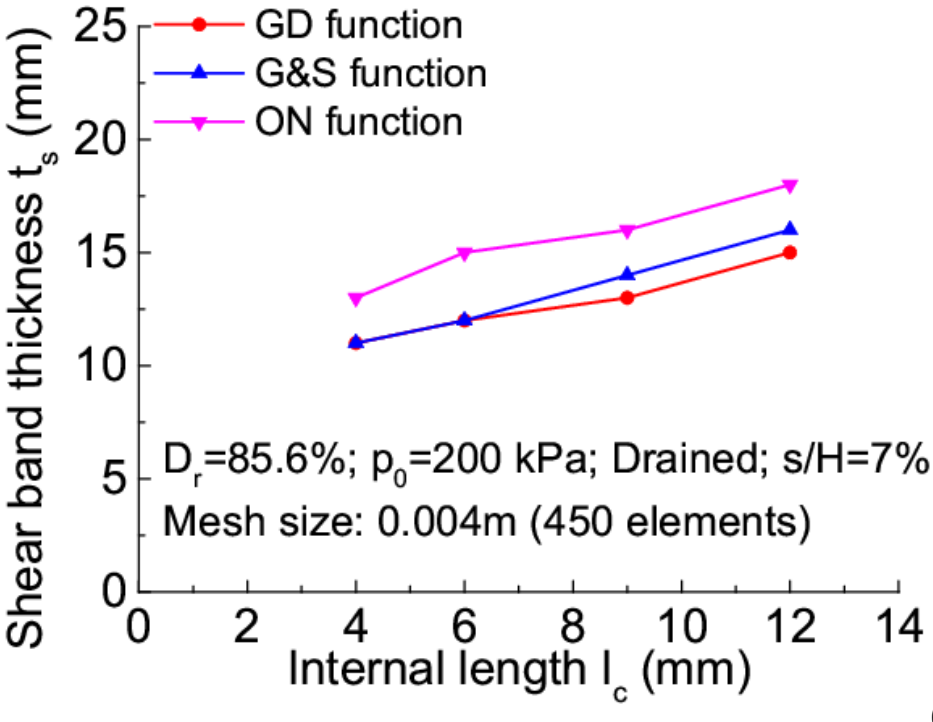

(b)

Figure 5.18 Comparison of the effect of (a) Mesh size and (b) Internal length on the shear band thickness in plane strain compression

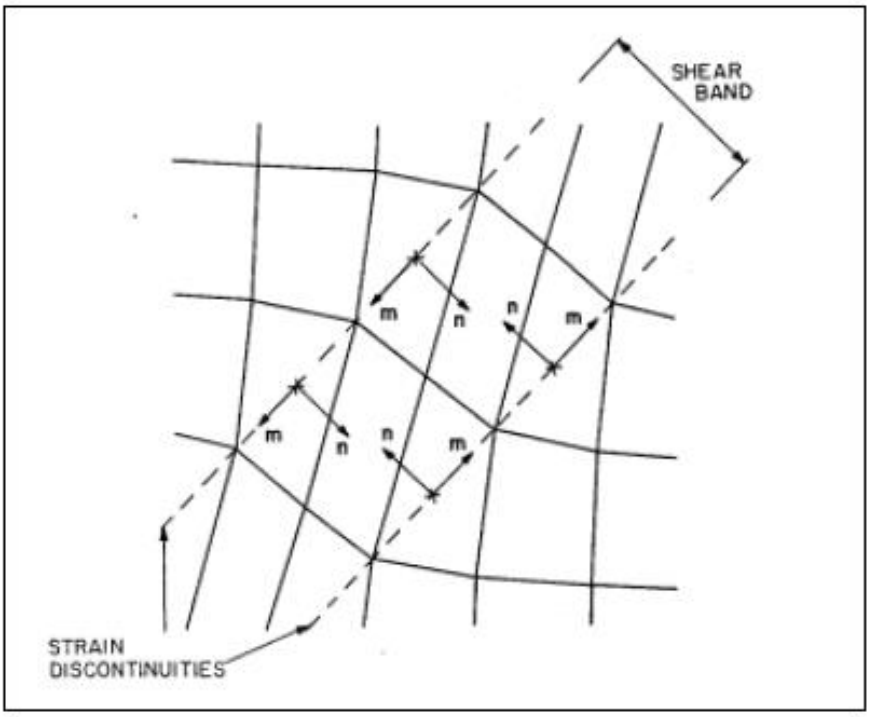

Figure 5.19 Iso-parametric elements in a strain discontinuity (Ortiz et al., 1987)

Furthermore, both Marcher (2003) and Galavi & Schweigher (2010) have argued that using a large value for l_c leads to a much larger and unrealistic shear band thickness, even when an appropriate mesh size is chosen. This discrepancy arises because the selected l_c does not match the physical length of the sand being studied. To effectively apply the nonlocal method, the mesh size would need to be smaller, which is practically challenging to achieve to match the actual shear band thickness. Therefore, it becomes necessary to scale the load-displacement response to align with real soil behaviour. A method of softening scaling is implemented to obtain a realistic shear band thickness in addressing this issue (Which will discuss in The Chapter 6).

5.2.4 Undrained plane strain compression tests

Figure 5.20 shows the relationship between vertical displacement and reaction force for different models. In the local model, vertical reaction force increases with mesh size and is sensitive to the mesh size, and it is evident that the nonlocal models give mesh-independent results.

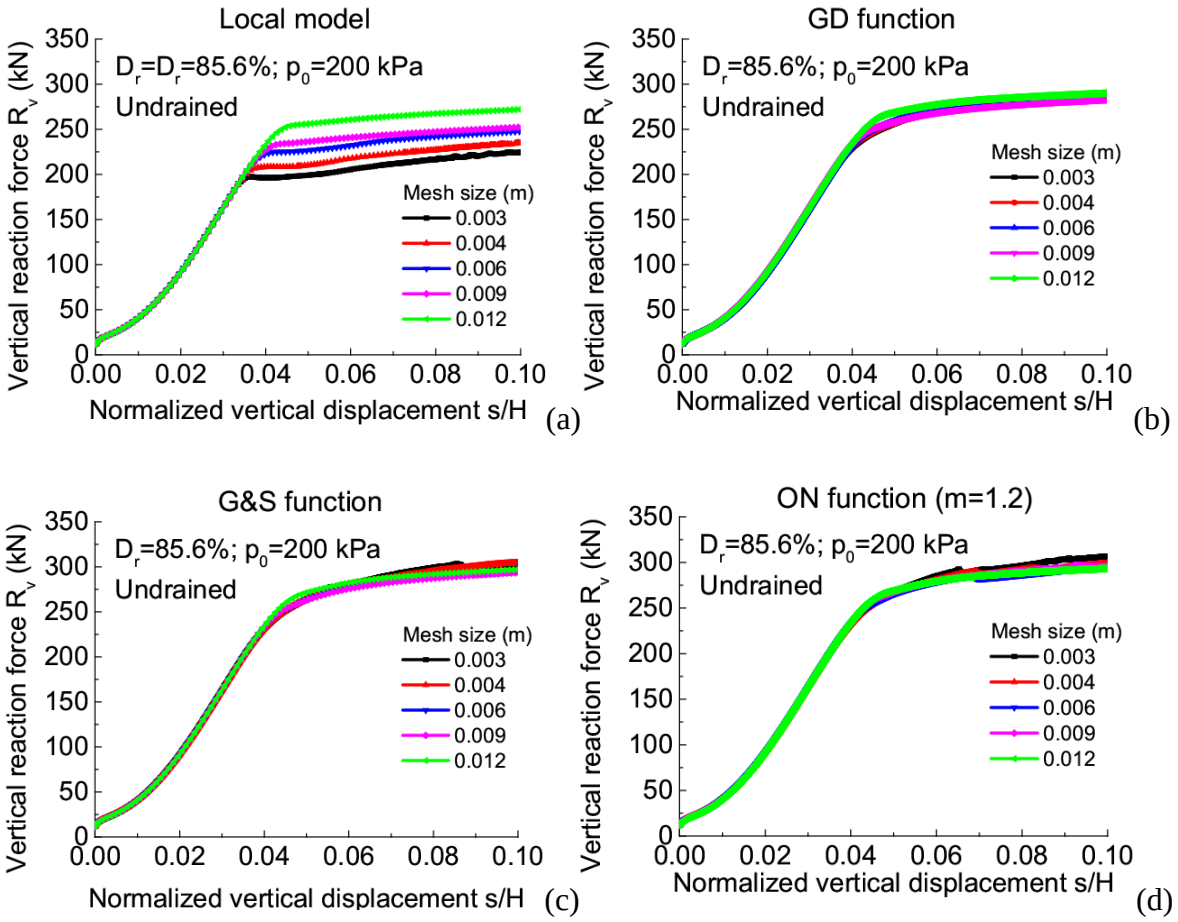

Figure 5.20 Comparison of the force-displacement relationship for undrained plane strain compression test: (a) Local model; (b) GD function; (c) G&S function; (d) ON function

The shear band orientation in undrained plane strain compression increases when the mesh is refined for all models. The mesh dependency can be reduced but not eliminated by the nonlocal treatment (Figure 5.21). It is worth noting that the nonlocal models give the same shear band orientation as the local model when the mesh size is more significant than 0.009 m. The nonlocal models also provide a more significant variation of shear band orientation in undrained tests than in drained ones. The main reason is that there is a smaller change in the void ratio in an undrained test, which makes the nonlocal regularisation using the void ratio less effective.

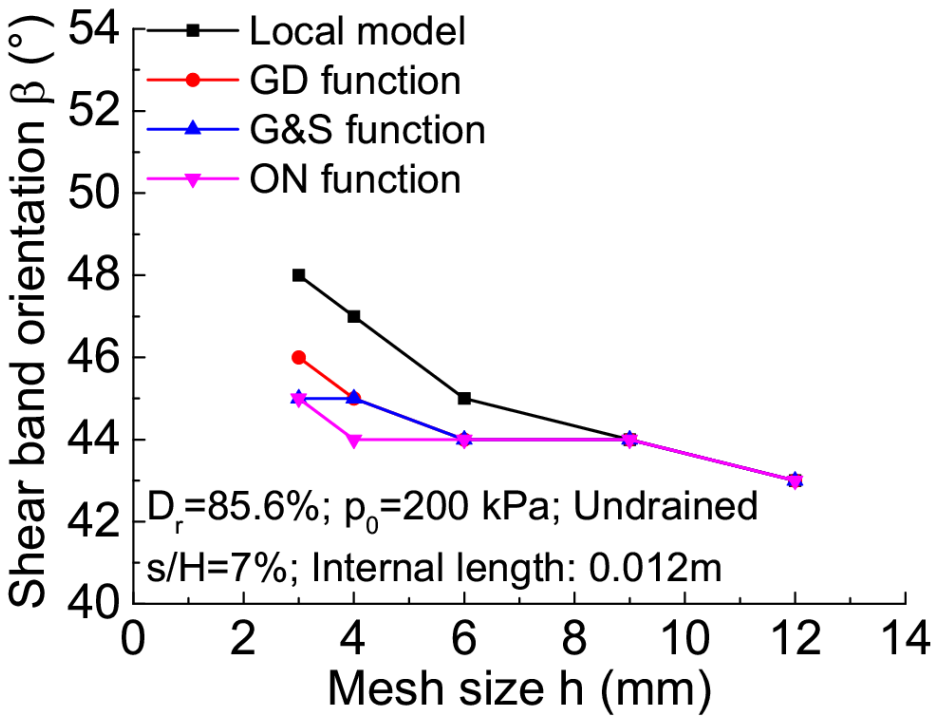

Figure 5.21 Shear band orientation predicted by different models in undrained plane strain compression tests

According to Figure 5.22, the value of the shear strain in the shear band under the undrained case is smaller than in the drained case. For example, under drained condition, when the mesh size is 0.004 m, the maximum value of the shear strain in the shear band for the ON model is around 0.65 and 0.85 for other models. In contrast, under undrained condition, the shear strain is 0.6 for other models and 0.5 for the ON model.

The shear band thickness predicted by the models is shown in Figure 5.23. Similar to the drained case, the nonlocal models give a slight variation of shear band thickness when the mesh size is smaller than the internal length. But the shear band thickness predicted by the nonlocal models at $h = l_c$ is more significant than that of the local model. Moreover, it is found that the drainage condition has little influence on the shear band thickness at different internal lengths (Figure 5.23b).

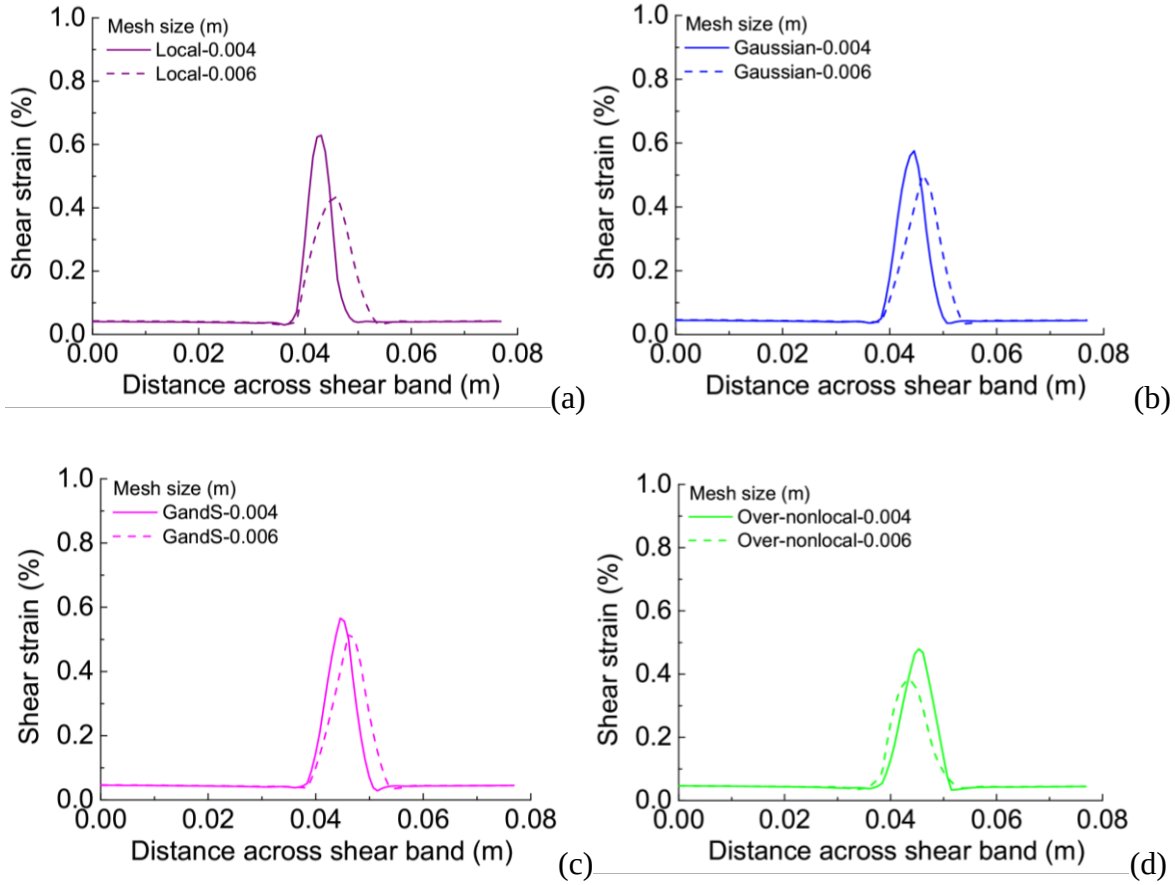

Figure 5.22 Cross-section profiles based on the shear strain after peak state: (a) Local model; (b) Gaussian distribution model; (c) G&S distribution model; (d) Over-nonlocal model

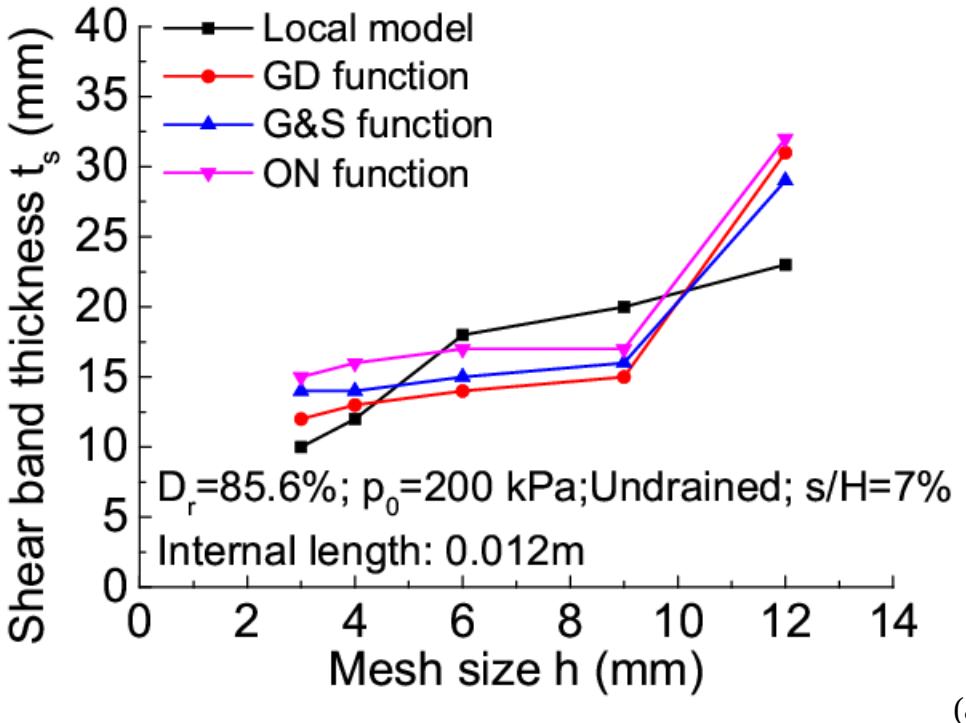

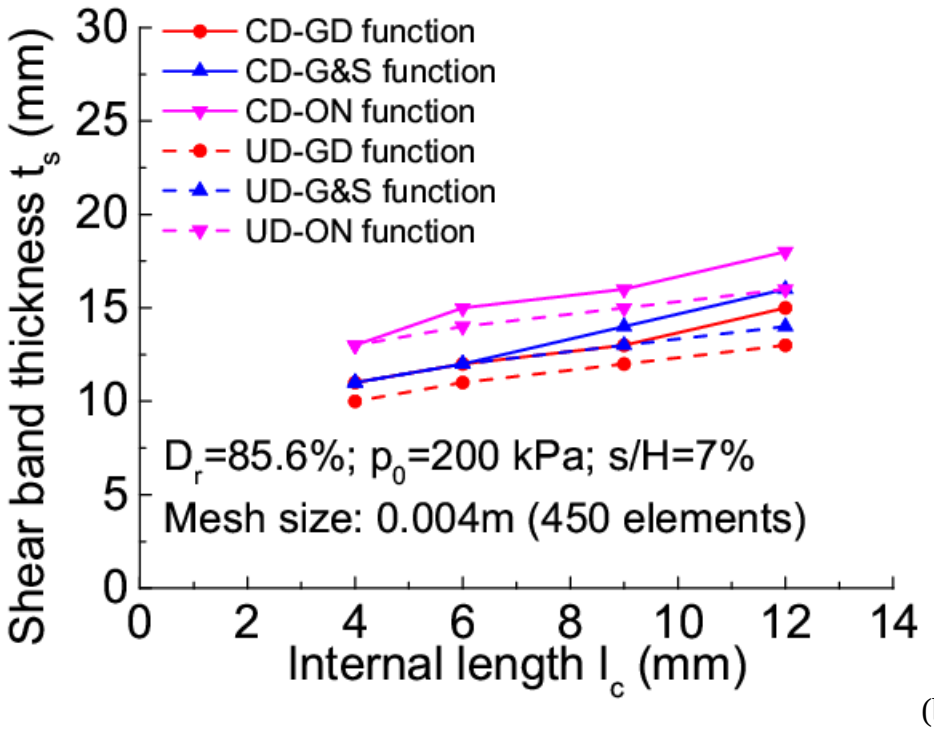

(b)

Figure 5.23 Comparison of the effect of (a) Mesh size and (b) Internal length on the shear band thickness under undrained condition

5.2.5 Comparison of three weight functions in dynamic liquefaction

Liquefaction is a phenomenon involving a significant reduction in effective stress caused by excess pore water pressures. The sudden and significant loss of shear strength is accompanied by excessive plastic strains (Yamamuro and Lade, 1997). The criteria for liquefaction failure can be divided into two main groups depending on the type of loading: static liquefaction and cyclic mobility (Kramer, 1996; NRC, 1985).

It is also meaningful to testify the validation of nonlocal regularisation during static liquefaction. During static liquefaction, rapid monotonic shearing generates significant excess pore water pressures in a nearly or fully saturated soil due to the contractive tendency and undrained softening behaviour (Yamamuro and Lade, 1997; Chu et al., 2003; Take and Beddoe, 2014; Gens, 2019). Based on the response of sand with different densities under monotonic undrained loading, static liquefaction can be classified into three types: static liquefaction, limited liquefaction, and non-flow behaviour. The behaviour of static

liquefaction and limited liquefaction under static loading indicates a strain-softening type of undrained response (Vaid and Sivathayalan, 2000).

According to past studies, the very loose sand was liquefied under low confining pressures of 100 kPa or less, which refers to 'complete static liquefaction' (Ishihara, 1993; Riemer et al., 1990; Yamamuro and Lade, 1997). However, when the initial confining pressure increased after 100 Kpa, the specimens exhibited stable behaviour with less liquefaction susceptibility, which became 'Limited liquefaction' (Sabbar et al., 2017). Thus, the simulation of loose sand ($D_r = 34.2\%$) with two different initial confining pressure ($p_0 = 200, 50\ kPa$) is considered.

As illustrated in Figures 5.24 and 5.25, mesh sensitivity issues still exist, and the random distribution of mesh size was obtained, which usually occurs at the post-bifurcation point when failure modes transfer into a localised mode (Wan et al., 2012). Figure 5.24 shows the force and displacement relationship for loose sand in undrained plane strain compression. Though the vertical reaction force decreases after the peak, the mesh size has little influence on the results when the original model is used (Figure 5.24a). The nonlocal models give similar results (Figure 5.24c and d). The reason is that the stress ratio of soil elements keeps increasing, though the deviator stress decreases. This is a strain-hardening response based on the model, as increasing stress ratio means increasing hardening parameter H. In coupled dynamic loading (e.g., earthquake), the soil response will be a combination of that in Figure 5.20 and Figure 5.24, wherein the nonlocal regularisation method is found to work. Therefore, it is expected that the nonlocal regularisation technique also works for coupled analysis in earthquakes.

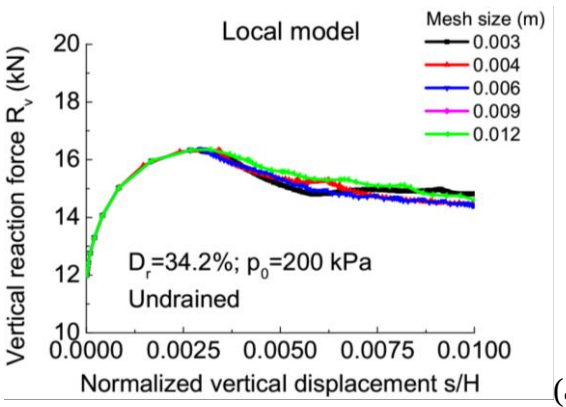

(a)

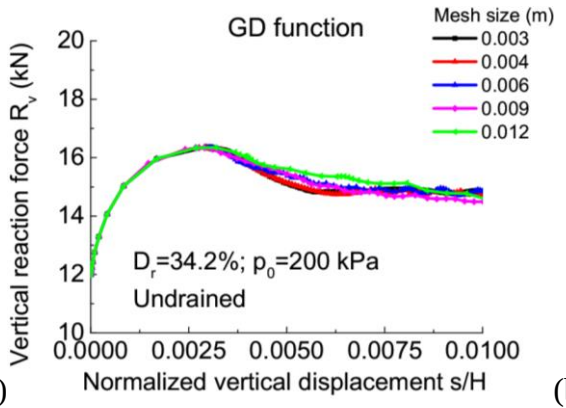

(b)

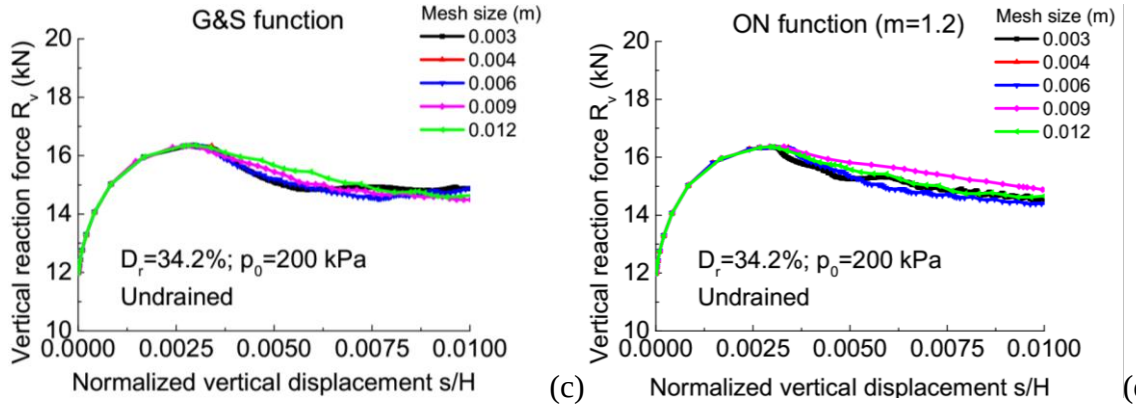

Figure 5.24 Comparison of the local and nonlocal models on the force-displacement relationship for limited liquefaction with high confining pressure: (a) Local model; (b) GD function; (c) G&S function; (d) ON function

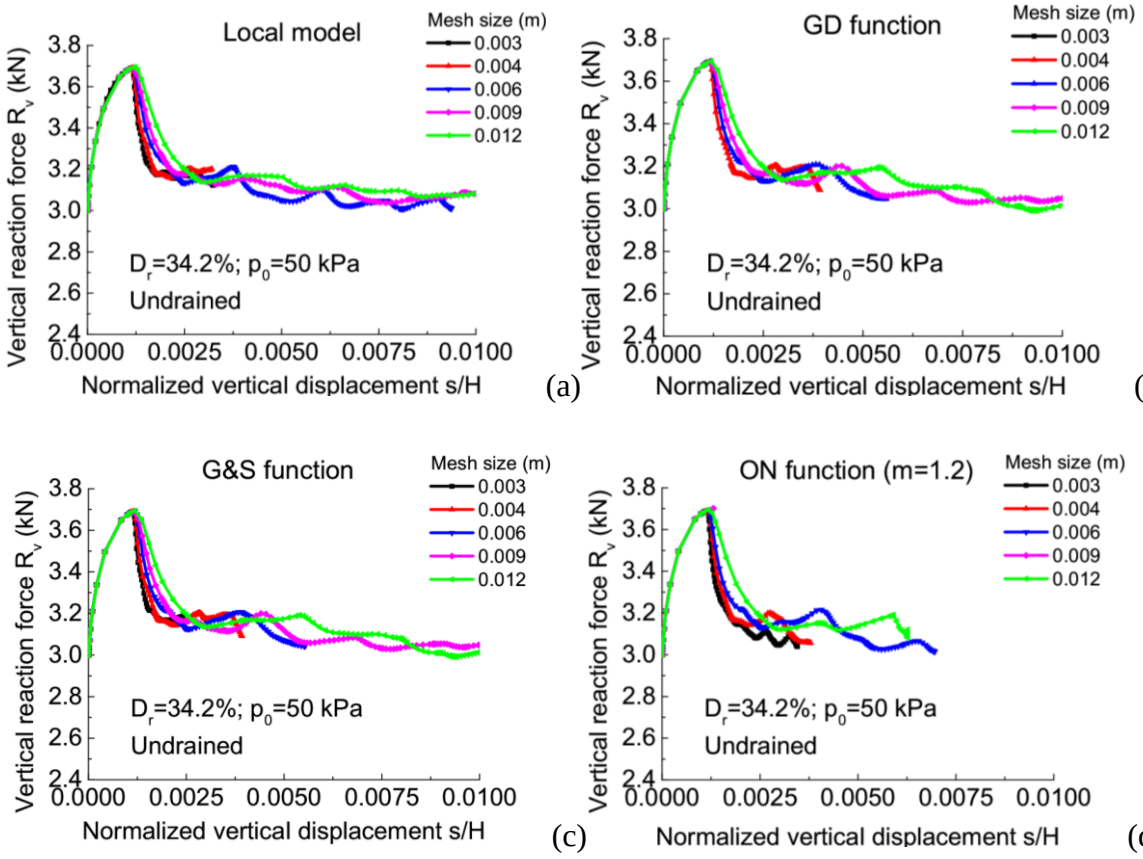

Figure 5.25 Comparison of the local and nonlocal models on the force-displacement relationship for limited liquefaction with low confining pressure: (a) Local model; (b) GD function; (c) G&S function; (d) ON function

5.3 Strip footing problem

5.3.1 Strip footing on level sand ground

The dimension of the strip footing problem is shown in Figure 5.26. The footing with B =0.9m is deformed by applying a uniform vertical deformation. The horizontal displacement is fixed to simulate rough footings. Constant vertical pressure (1 kPa) is applied on the top surface to avoid soil collapse with zero mean effective stress. The initial lateral earth pressure coefficient $K_0 = 0.4$ (Okochi and Tatsuoka 1984), and the effective weight of Toyoura sand is $\gamma' = 16\text{kN/m}^3$ as there is no water in the sand. Two sides of the sample are horizontally fixed, while both horizontal and vertical movement is restricted for the bottom boundary. Details can be found in Gao *et al.* (2020). Since the vertical load and vertical settlement relationship is mainly affected by the rectangle area beneath the footing, hence, the mesh size far away from the footing is setting a fixed value (0.6m) for all models. The bedding plane orientation is horizontal and $\alpha = 0^\circ$. The relative density $D_r = 85.6\%$, and the initial degree of anisotropy is $F_0 = 0.4$.

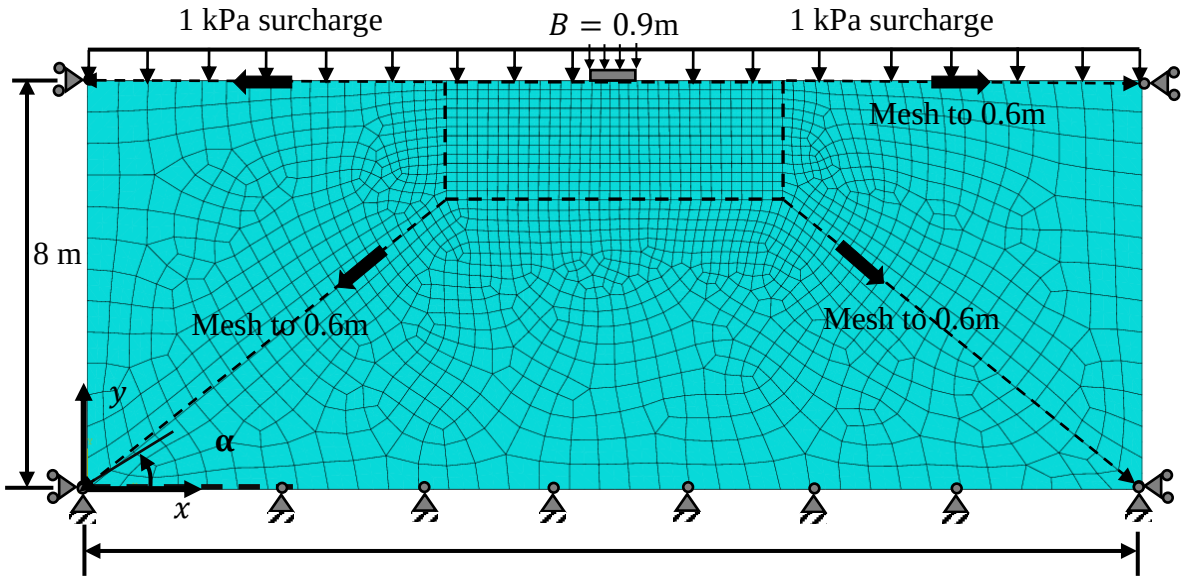

Figure 5.26 The boundary conditions of the strip footing problem

Figure 5.27 shows the prediction of local and nonlocal models with $l_c = 0.8\,m$. It is evident that the local model prediction is highly mesh-dependent. The G&S function gives the least mesh-dependent results. The strain softening predicted by the GD and G&S functions is in good agreement with the centrifuge test data (Kimura et al., 1985). However, the ON model gives a steep reduction of Q after the peak, which does not match the experimental observations. There are two reasons for this. First, this method gives excessive volume expansion of sand under the strip footing (Figure 5.28). The location of the elements in Figure 5.28 is shown in Figure 5.29. The GD and GS models give similar predictions of void ratio evolution, while the void ratio increase predicted by the ON model is about 90% higher. A higher void ratio causes lower strength and failure of some elements, which leads to a fast reduction of Q. Secondly, the ON method assumes that the local variable makes a negative contribution to the local one, which may not be realistic. In these cases, such an assumption causes failure or lower shear strength of more sand elements. Moreover, it is found that a bigger m value gives an even steeper strain softening curve for the ON function. Therefore, the ON function should not be used for this problem.

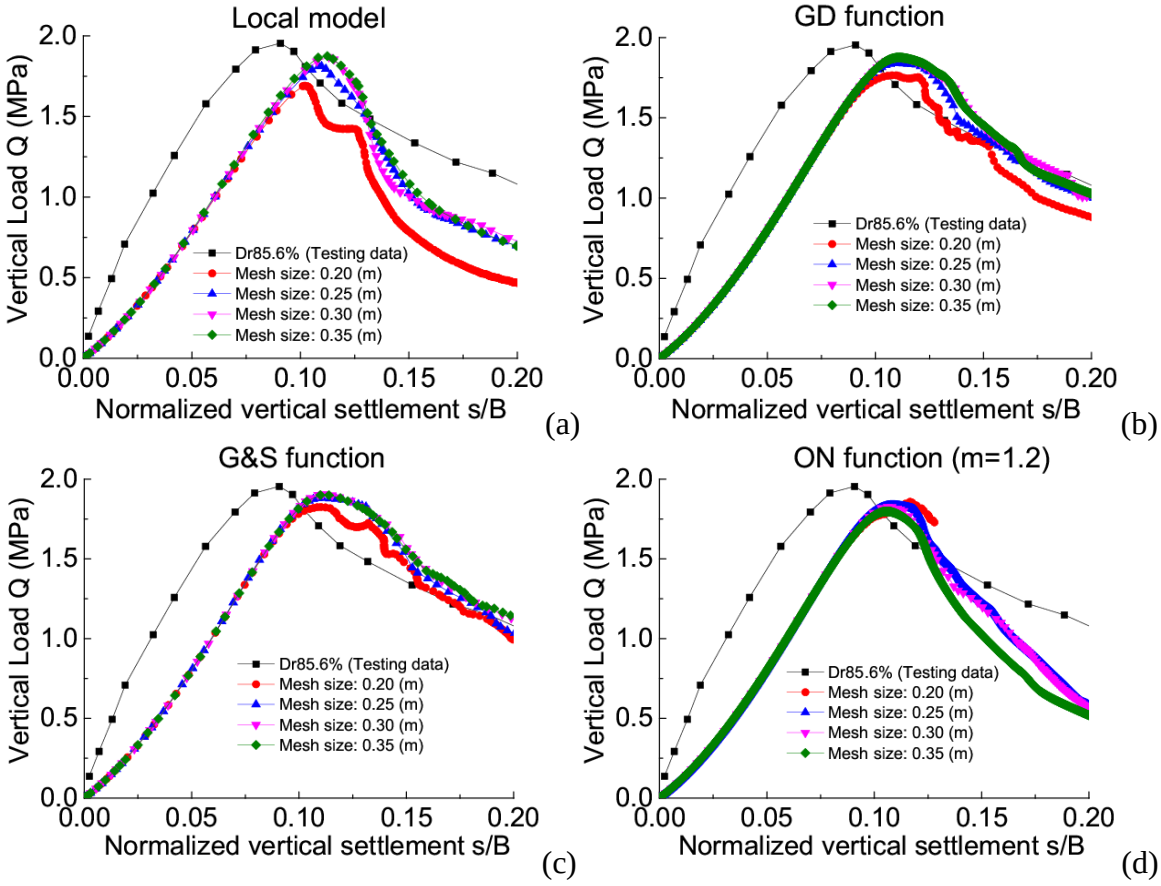

Figure 5.27 The comparison of the strip footing response on the sand with horizontal bedding plane: (a) Local model; (b) GD function; (c) G&S function; and (d) ON function

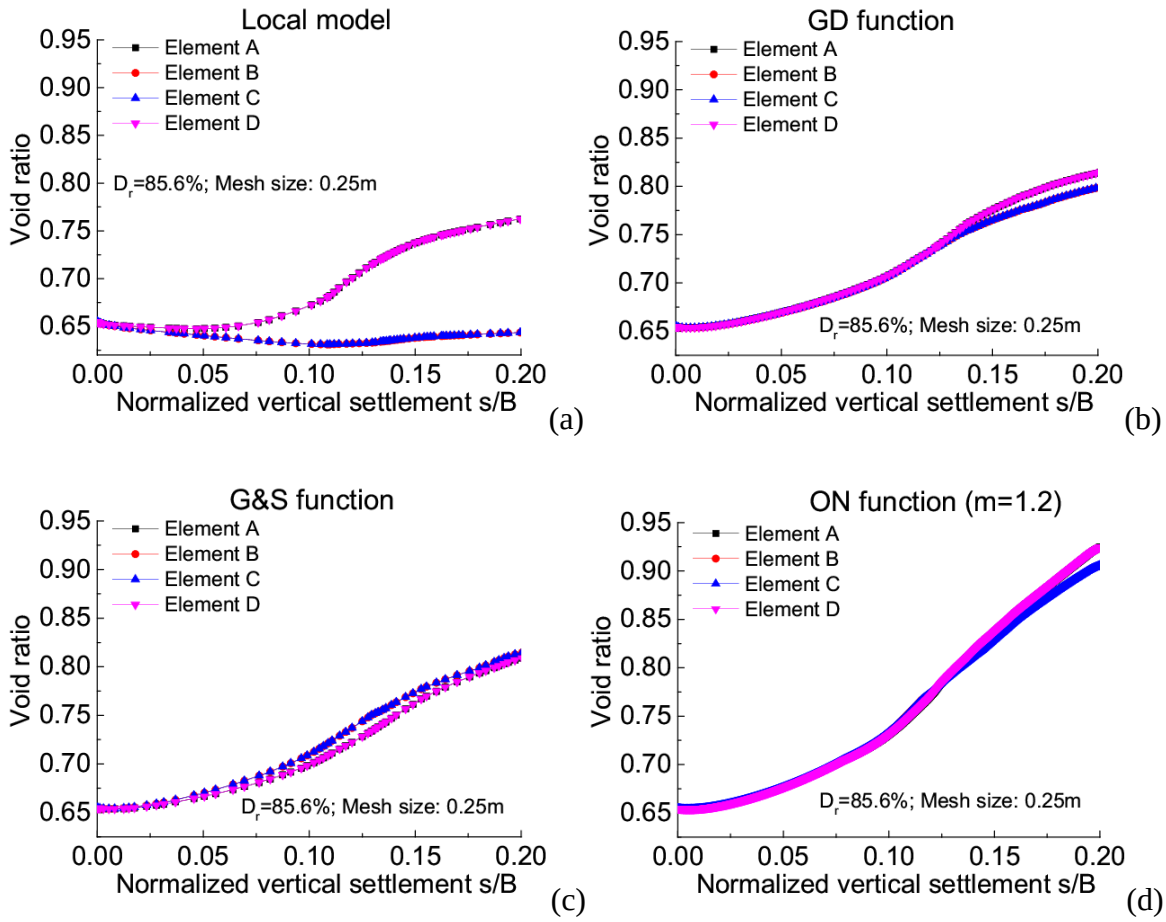

Figure 5.28 Comparison of void ratio evolution for elements under the strip footing: (a) Local model; (b) GD function; (c) G&S function; (d) ON function

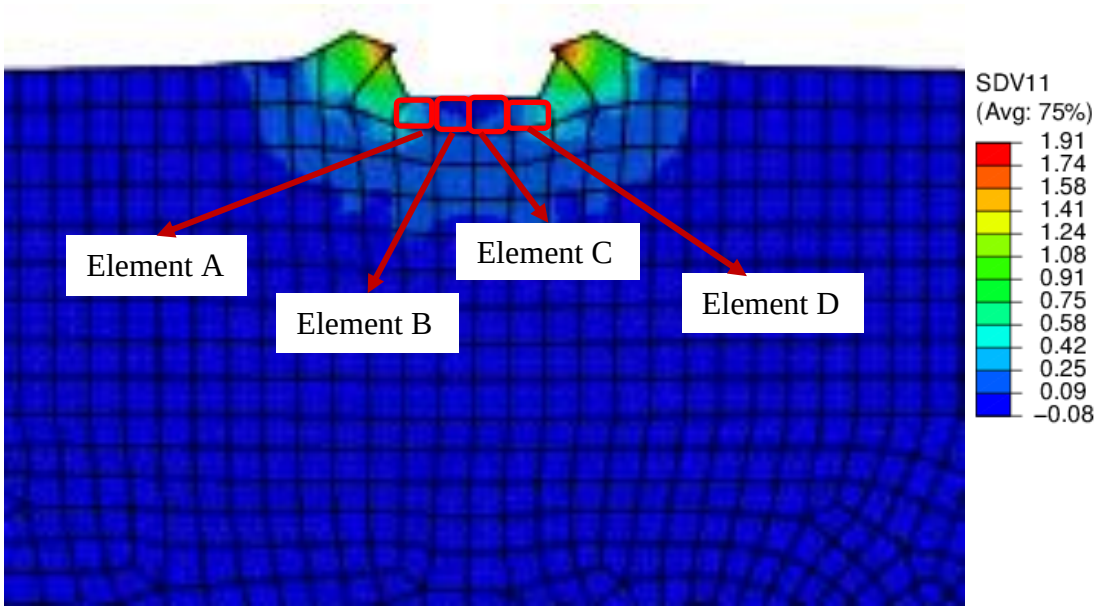

Figure 5.29 Location of elements under the strip footing

5.3.2 Strip footing near a sand slope

This problem is based on the simulations in Gao et al. (2021). The strip footing ($B = 1.2m$) and the slope angle β varies between 25° and 30° to explore its influence on nonlocal methods. The distance between the footing and slope crest is λB, with λ varying between 0.5 and 1.5. The confining pressure is 5 kPa to ensure the simulations can continue after reaching the bearing capacity. Since the ground surface is not level, a constant K_0 cannot be applied. Therefore, the gravity loading method is used to generate the initial stress state (Gao et al., 2021). First, gravity is applied on the same soil body by assuming that the soil is elastic with a Poisson's ratio of $\nu = 0.286$, making $K_0 = 0.4$ for a flat ground surface (Gao et al., 2021). After that, the stress state is extracted and imported into the model as the initial stress, which is used for the subsequent modelling. The slope dimension and boundary conditions are shown in Figure 5.30

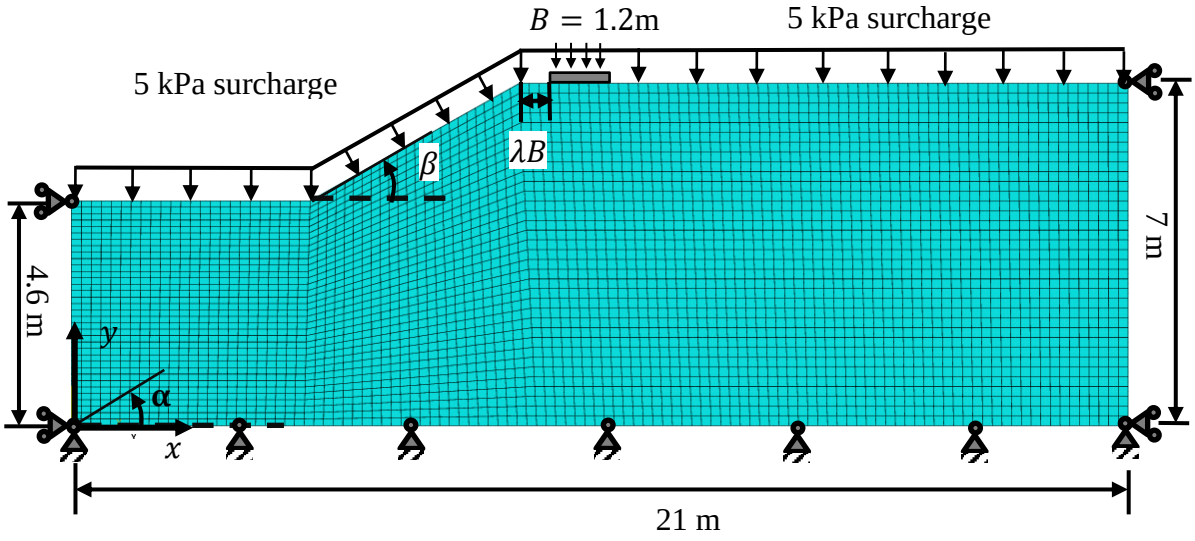

Figure 5.30 The boundary conditions of the strip footing near a slope

Figure 5.31 shows the prediction of local and nonlocal models with $l_c = 0.4\,m$. In these simulations, the slope angle is 30° and $\lambda = 0.5$. The local model gives different peak bearing capacities and $s - Q$ curves after the peak as the mesh size changes (Figure 5.31a). Nonlocal regularisation reduces the mesh-dependent of $s - Q$ curves (Figure 5.31c and d). The rate of strain softening is also reduced due to the nonlocal averaging of void ratio

increment. To further reduce the mesh sensitivity, more nonlocal variables could be used, but this may increase the complexity of the model formulations and its implementation. Figure 5.32 shows the contour of shear strain distribution in the soil after the state for the G&S function. A clear slip surface can be seen, which is independent of the mesh size.

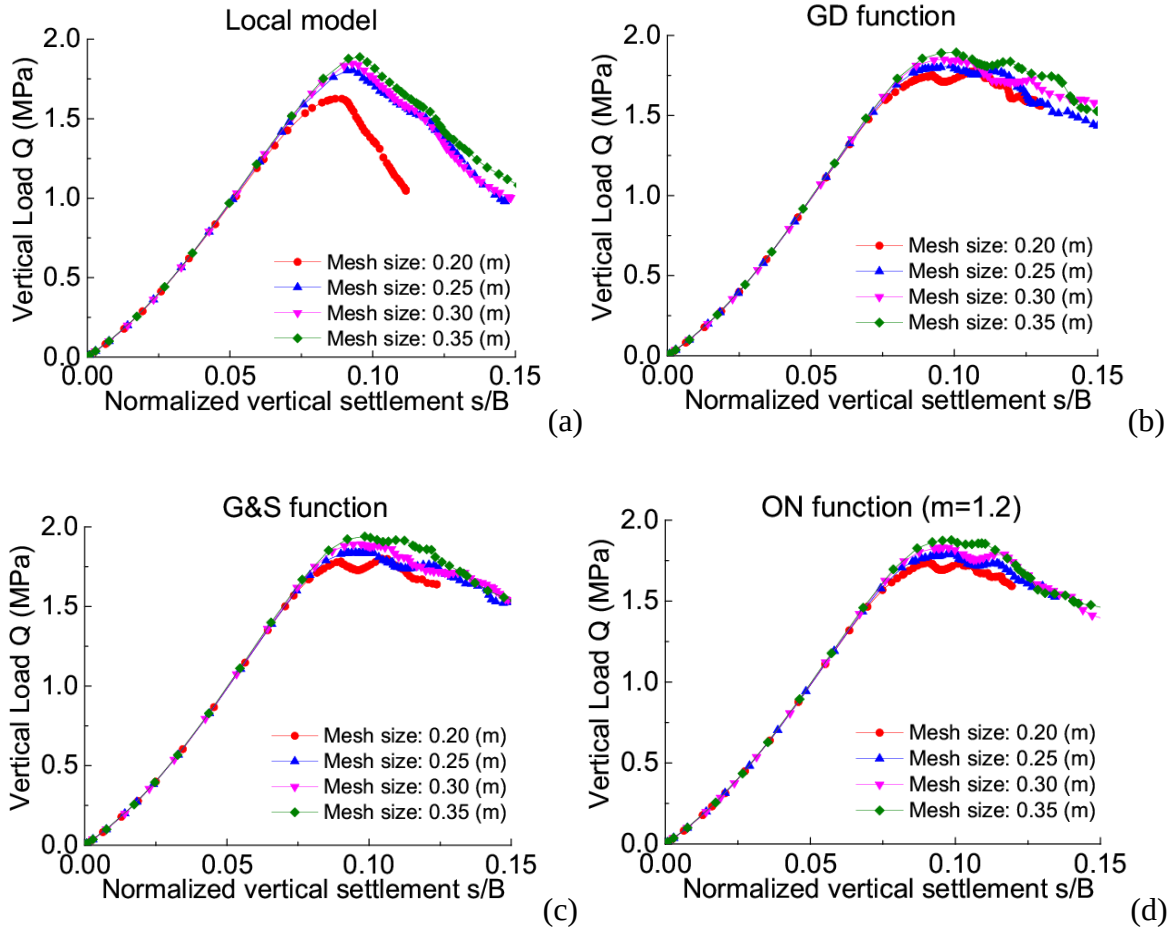

Figure 5.31 The comparison of the strip footing response near a slope with a horizontal bedding plane: (a) Local model; (b) GD function; (c) G&S function; (d) ON function

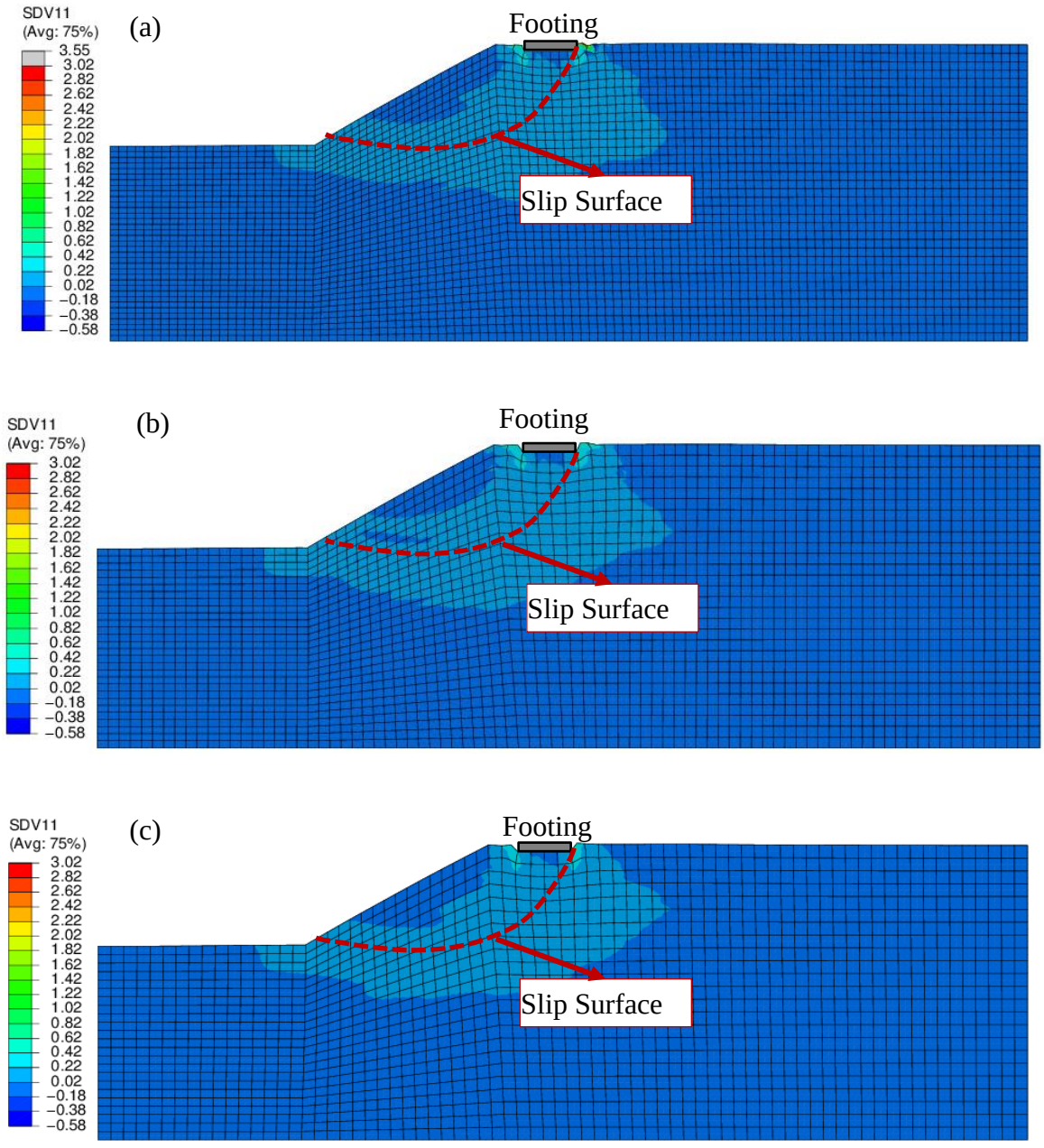

Figure 5.32 Shear strain distribution in the soil predicted by the G&S model at $s/B = 0.12$ with different mesh sizes: (a) 0.20 m; (b) 0.25 m; (c) 0.30 m

The effect of slope angle β and crest distance λ on nonlocal three weight functions is shown in Figure 5.33 and Figure 5.34. Figure 5.33 displays the predictions of the $s - Q$ relationship for local and nonlocal models with different slope angle β. When the distance (λ) between the slope crest and footing is same, the vertical load Q increases with a decreased slope angle. Thus, the bearing capacity can be improved by reducing the slope angle, and the mesh-sensitive issue cannot be affected by β. However, in nonlocal models, the model with a

higher slope angle predicts more consistent results for different mesh sizes than the lower slope angle model.

As portrayed in Figure 5.34, in the local model, when the slope angle β is kept unchanged, the higher vertical load Q is predicted by the smaller λ model. Thus, it is expected that the overprediction is caused when the footing is closer to the edge of the slope crest, where soil may be more easily mobilised due to less lateral support. Moreover, in nonlocal models, the slope model with $\lambda = 1.0B$ reduces more difference in peak vertical load between different mesh sizes than the case that $\lambda = 0.5B$. It should be noted that when the mesh size is very small, the simulations were stopped. Although fine mesh elements can improve the accuracy of the solution, they also lead to numerical instability during the solving process which called numerical divergence.

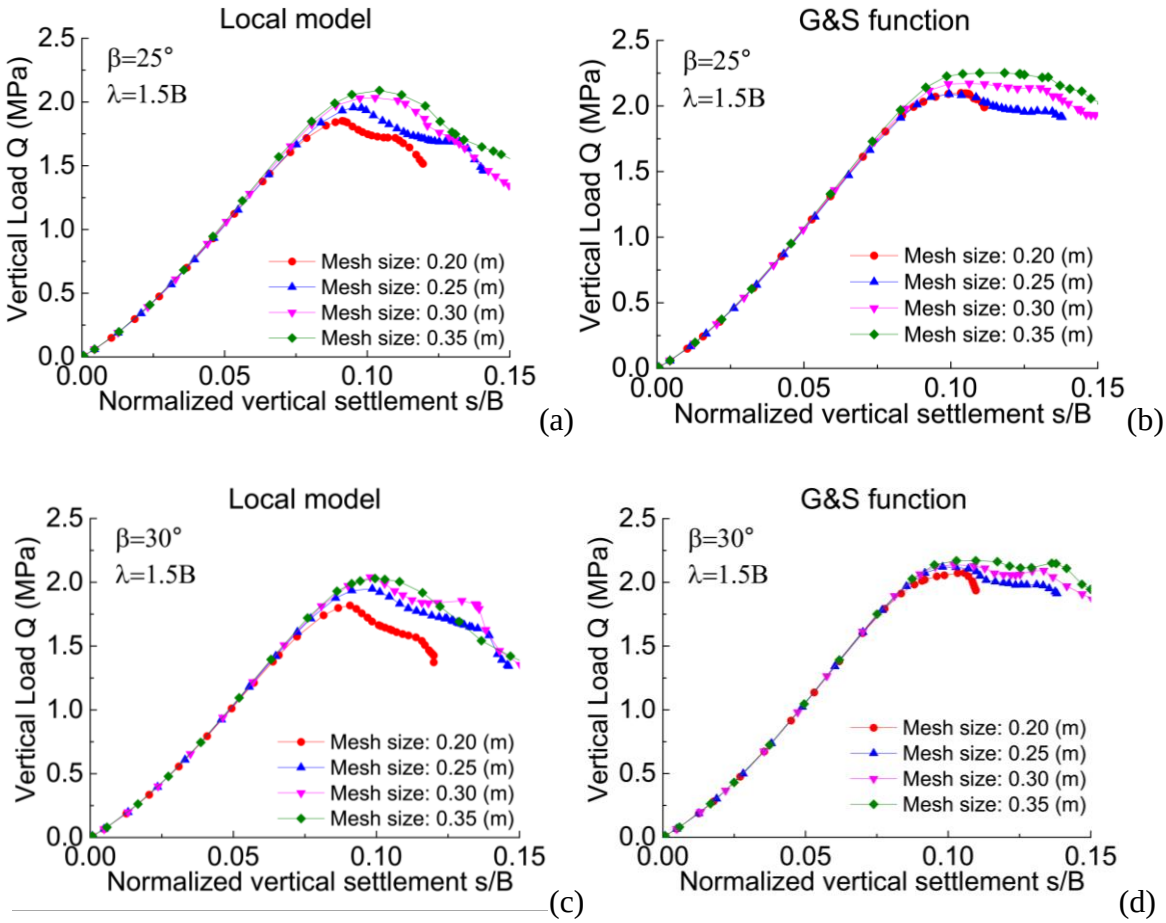

Figure 5.33 The effect of β on local and nonlocal model for strip footings near a sand slope

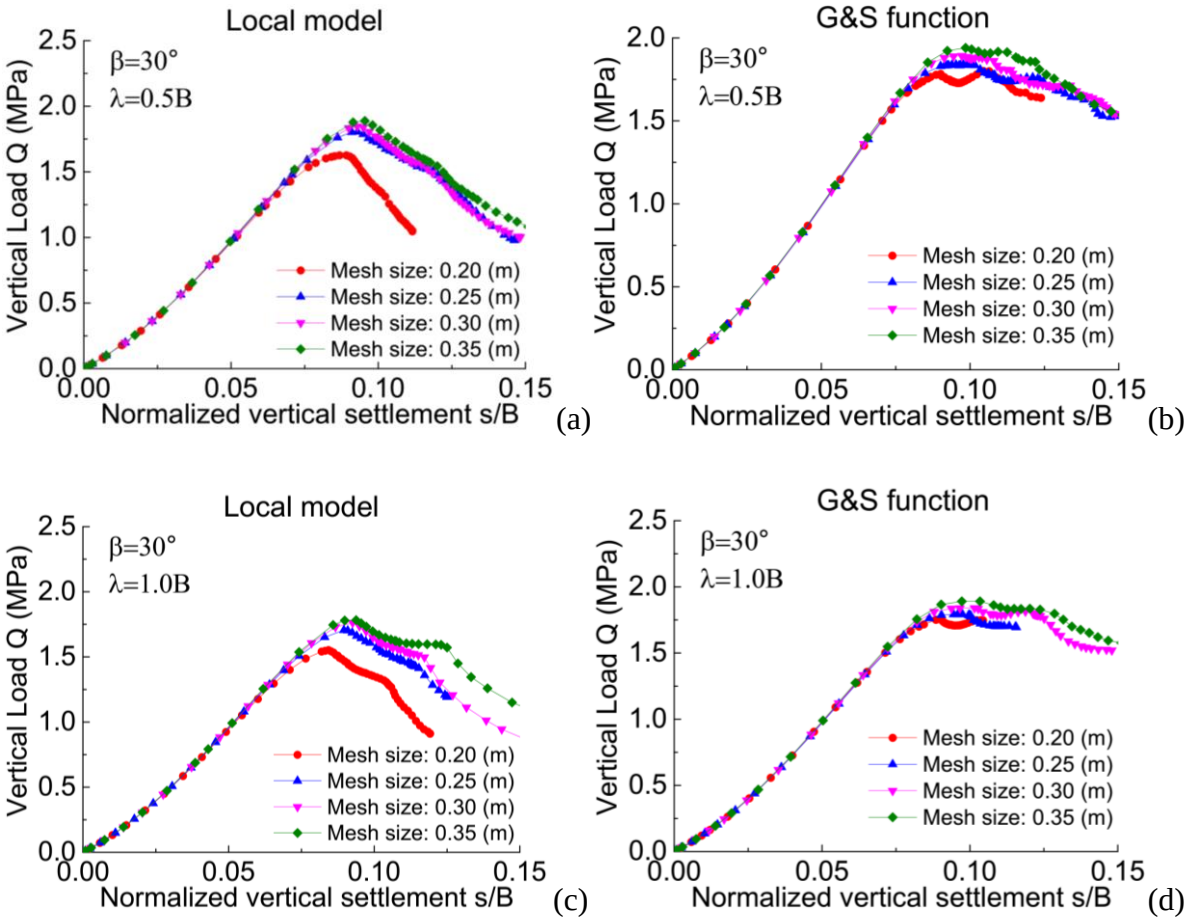

Figure 5.34 The effect of local and nonlocal models for strip footings near a sand slope

Regardless of whether a local or nonlocal model is employed, using excessively small mesh sizes beneath the footing is inadvisable. Extremely small mesh sizes tend to result in numerical divergence issues. As demonstrated in Figure 5.35, when a mesh size of 0.1m is applied to the strip footing on a slope problem ($\beta = 30^\circ$, $\lambda = 1.0B$), the simulation cannot completely converge, even during strain hardening. However, the result obtained from the nonlocal model is smoother compared to the local model due to the averaging effect of the nonlocal method. As the mesh is refined, the vertical settlement of the nonlocal method converges to a more stable value. Thus, the nonlocal theory without strain-softening can achieve and improve the convergence.

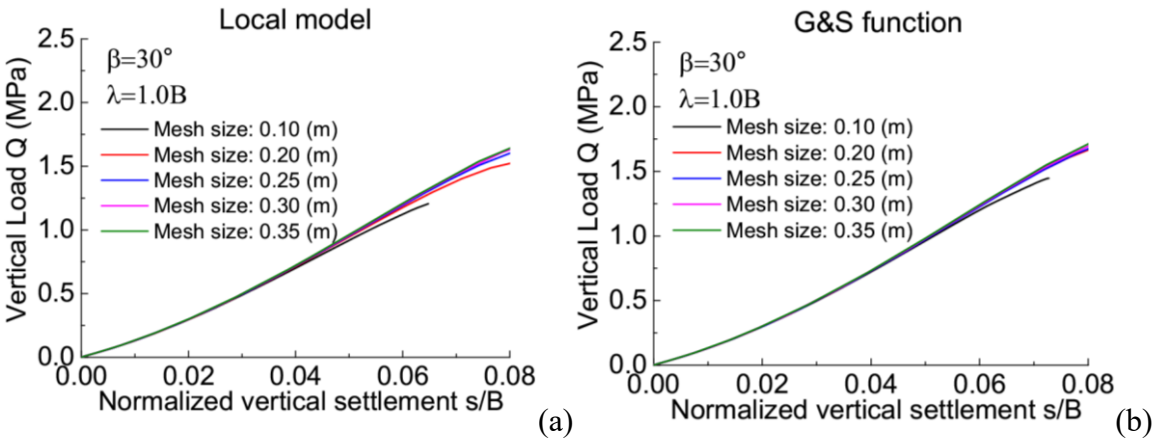

Figure 5.35 Convergence achieved using nonlocal theory without strain-softening

5.4 Response of retaining wall for level sand ground

Figure 5.36 shows a soil domain measuring 10 m in length and 4.5 m in depth, with a rigid retaining wall positioned on the right side of the backfill soil. The wall has a height of $h_w = 4\ m$ and is assumed to have an ideally smooth surface that prevents the transmission of shear stresses at the interface with the soil. The retaining wall can undergo passive and active horizontal translation, with passive movement towards the backfill and active movement away from it. The bottom, left-side, and right-side boundaries are fully fixed. In all simulations, the bedding plane orientation is horizontal ($\alpha = 0^{\circ}$), and the gravity is applied to the backfill soil while the top surface of the backfill soil is subjected to a uniformly distributed surcharge of 1 kPa. The same soil conditions as in Figure 5.26 are used. $l_c = 0.8\ m$ is applied for all simulations. The lateral earth pressure is expressed as σ_h and the wall displacement u is normalised by the height of the wall h_w.

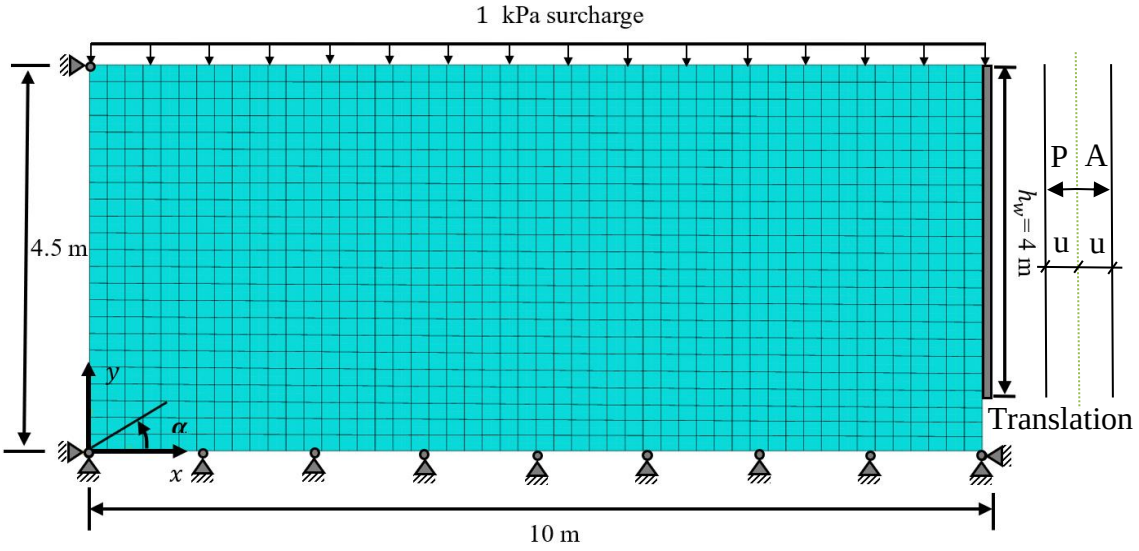

Figure 5.36 The boundary conditions of the retaining wall problem

Figure 5.37 shows the evolution of σ_h for the active condition. The local model gives mesh-dependent $\sigma_h - u/h_w$ curves. The G&S and ON functions are more efficient in reducing the mesh-dependency than the GD function σ_h reaches the smallest value at $u/h_w \approx 0.015$ and then increases with u/h_w. This is caused by the strain-softening of sand. Similar results have been proposed by Nübel and Huang (2004), Widulinski et al. (2011) and Guo and Zhao (2015). For the passive condition, the nonlocal models give similar results (Figure 5.38).

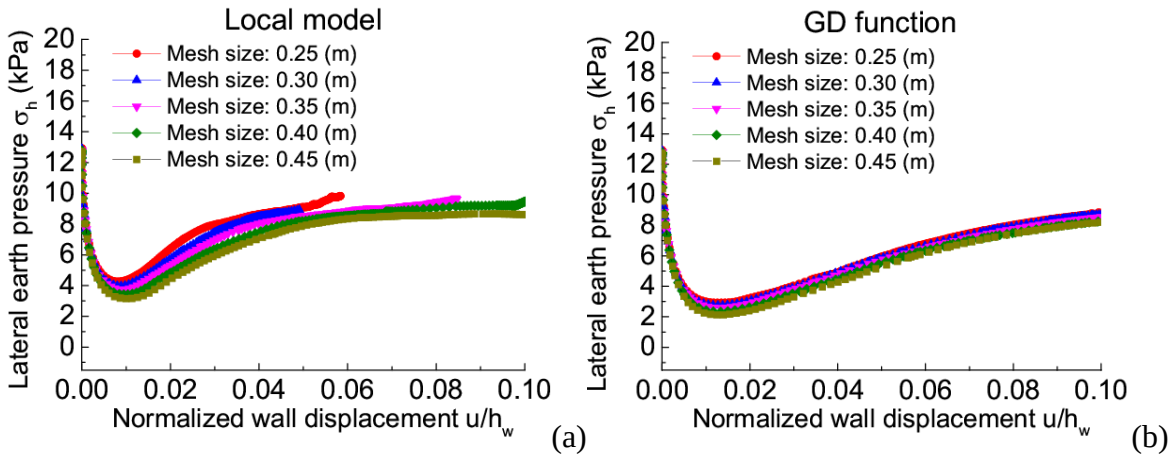

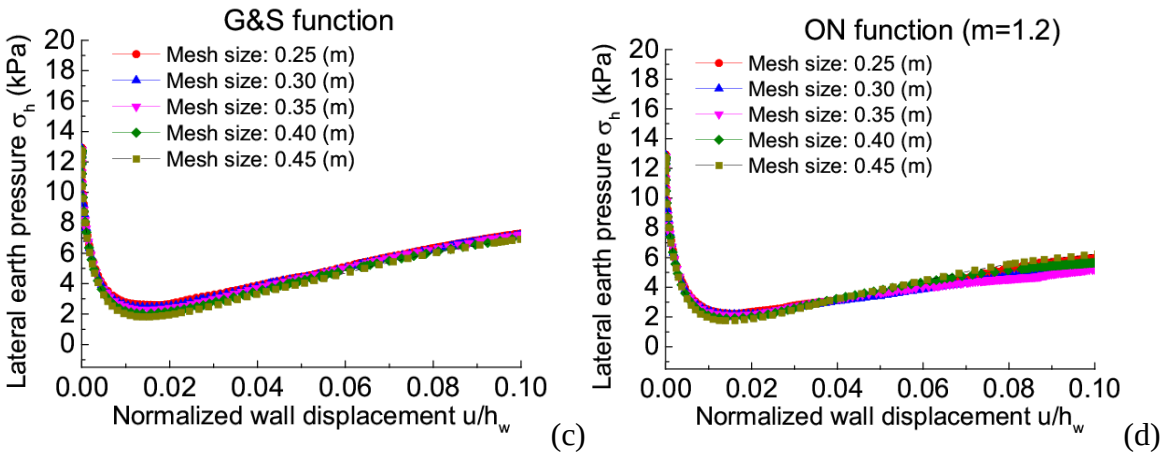

Figure 5.37 The comparison of the retaining wall response on the sand under active failure condition: (a) Local model; (b) GD function; (c) G&S function; (d) ON function

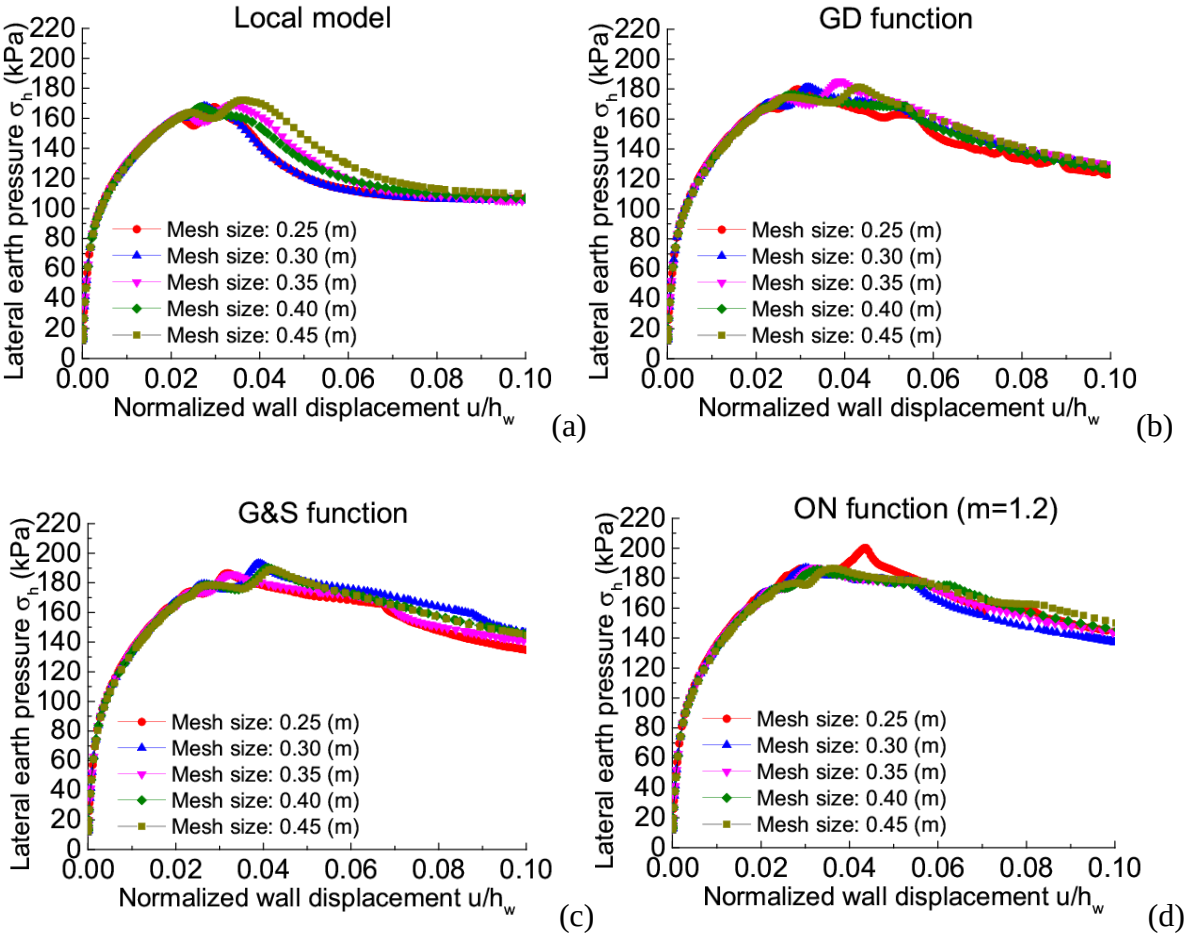

Figure 5.38 Comparison of the retaining wall response on the sand under passive failure condition: (a) Local model; (b) GD function; (c) G&S function; (d) ON function

Figure 5.39 shows the strain localisation pattern predicted by the local model. The shear band orientation in the backfill is directly measured from shear strain contours at $u/h_w = 5\%$ (Figure 5.40). The angle of the shear band under active earth condition is more significant than that under passive one. The angle of the shear band under active earth pressure decreases with increasing mesh size, while that under passive earth pressure increases. For both cases, the angle range of the local model ($62^\circ - 66^\circ$) is larger than that of the nonlocal models ($31^\circ - 36^\circ$). The nonlocal functions reduce the range of measured angle, which means they reduce mesh dependency, especially for the G&S function, which is almost constant under active earth pressure. Moreover, under passive earth pressure, the angle measured from the G&S function is slightly larger than that of the GD and ON functions.

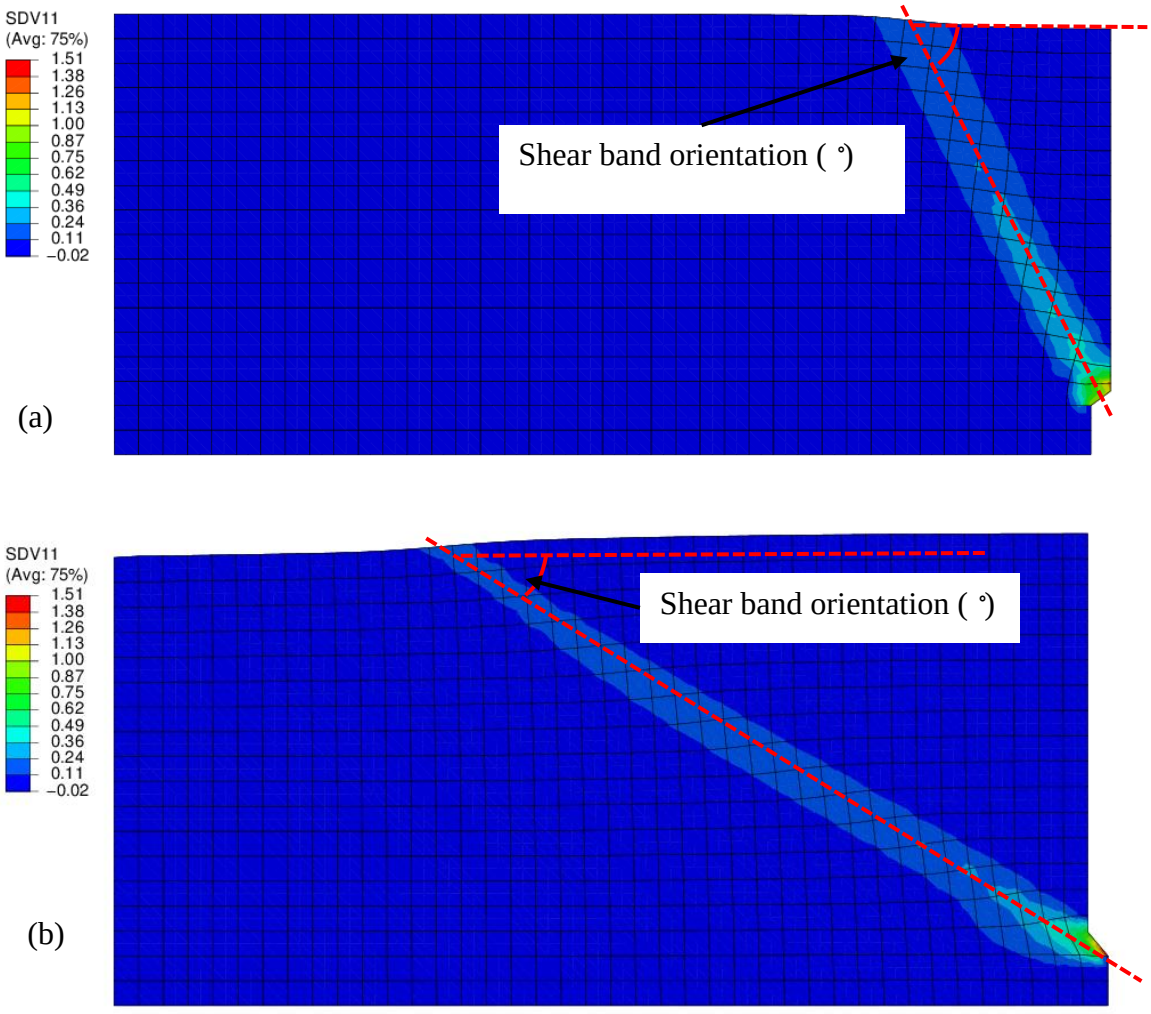

Figure 5.39 Shear band predicted by the G&S model after the retaining wall at $u/h_w = 0.05$: (a) active condition and (b) passive condition

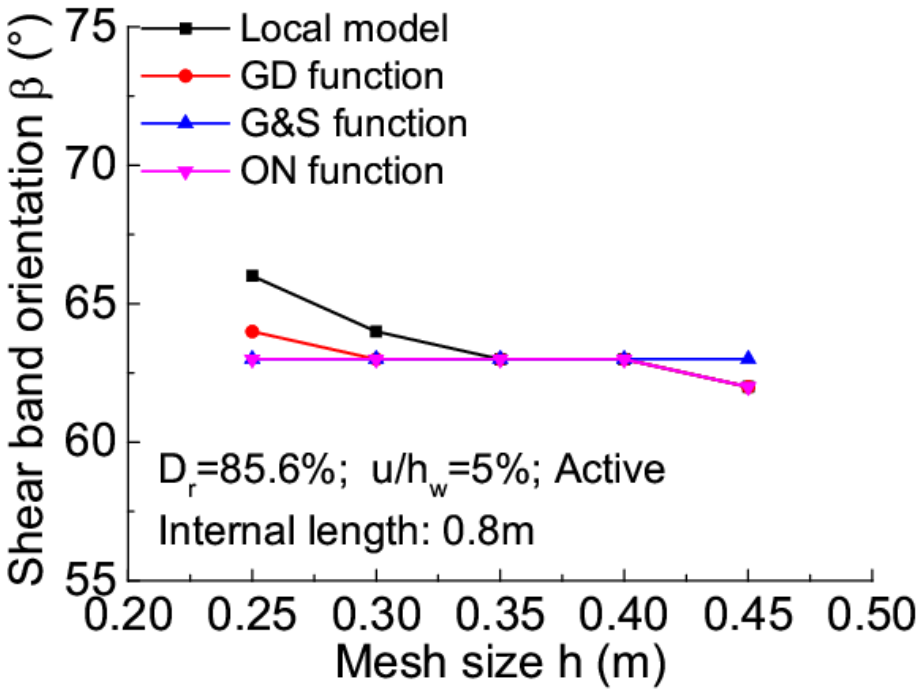

(a)

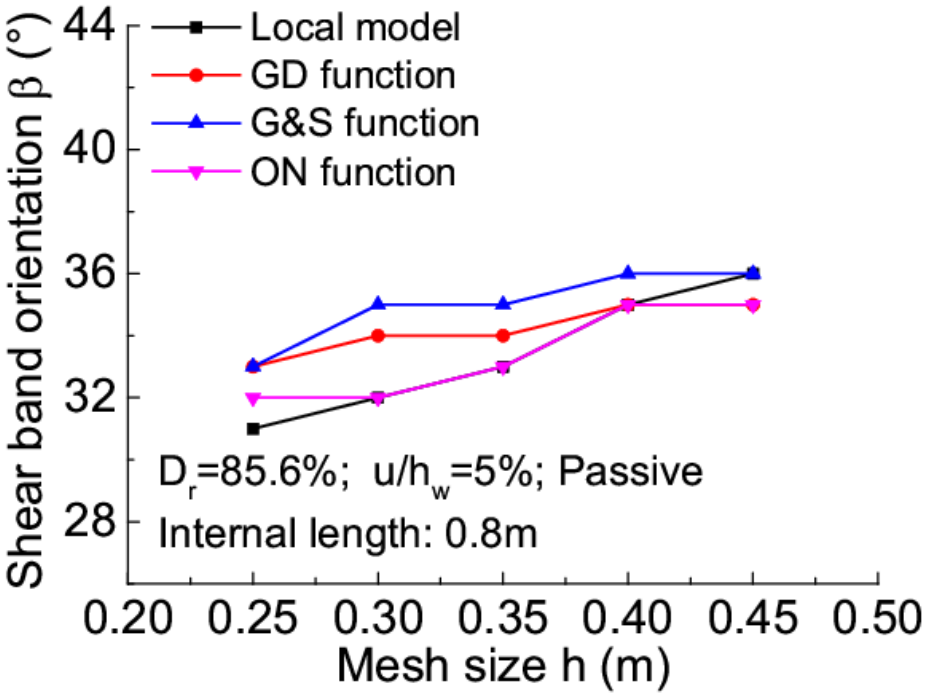

(b)

Figure 5.40 Comparison of shear band orientation for retaining wall: (a) Active failure condition (b) Passive failure condition

Figure 5.41 shows the $\sigma_h - u/h_w$ curves for the retaining wall under rough boundary conditions. In both local and nonlocal models, the rough boundary conditions applied to the retaining wall imposes more constraints than in the smooth boundary conditions, leading to the prediction of lower σ_h under active and higher σ_h under passive failure condition. The rough boundary conditions allow no relative movement between the wall and the sand immediately, causing overprediction of the bearing capacity of the retaining wall. Moreover, the nonlocal predicts lower σ_h in active failure mode and higher σ_h in passive failure mode than the local model, while the nonlocal can reduce the mesh dependency issue in post-peak but is unable to reduce the difference in peak value.

The shear zone pattern for a nonlocal model under rough boundary conditions is demonstrated in Figure 5.42. The retaining wall under rough boundary produces more slip lines than in smooth boundary conditions, and the apparent post-peak drop of lateral pressure in each case is accompanied with the occurrence of a well-developed shear band in the backfill soil. Guo and Zhao (2016) proposed that the shear band angle of the smooth wall case results in a very close value to the theoretical angle, whereas the rough wall case yields a significantly higher inclination angle for the slip line. This difference in behaviour may be attributed to the boundary condition and the limited domain width.

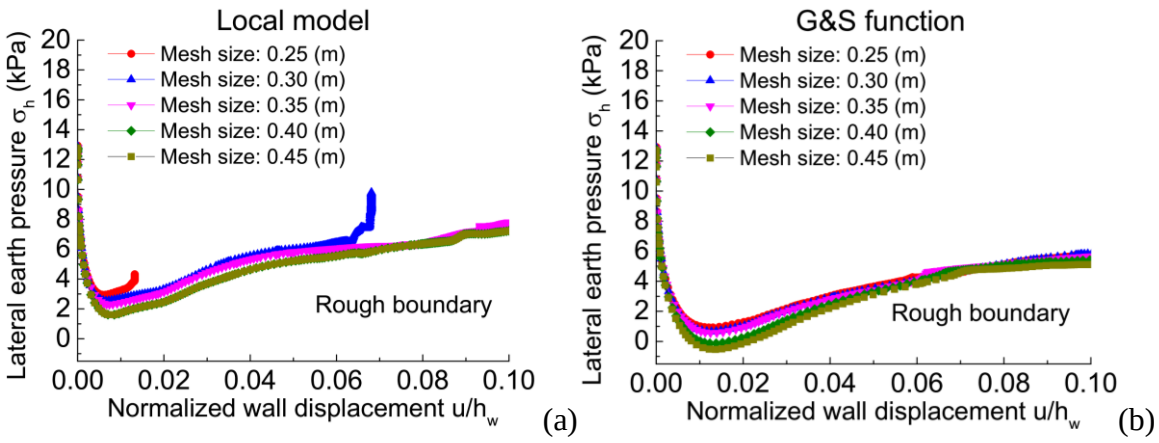

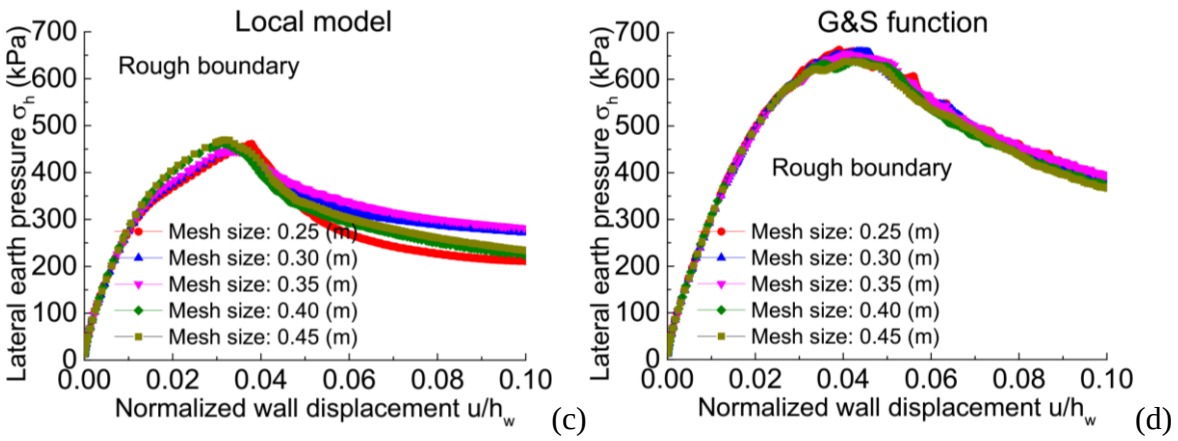

Figure 5.41 The effect of rough boundary on local and nonlocal models for retaining wall response under active and passive failure conditions

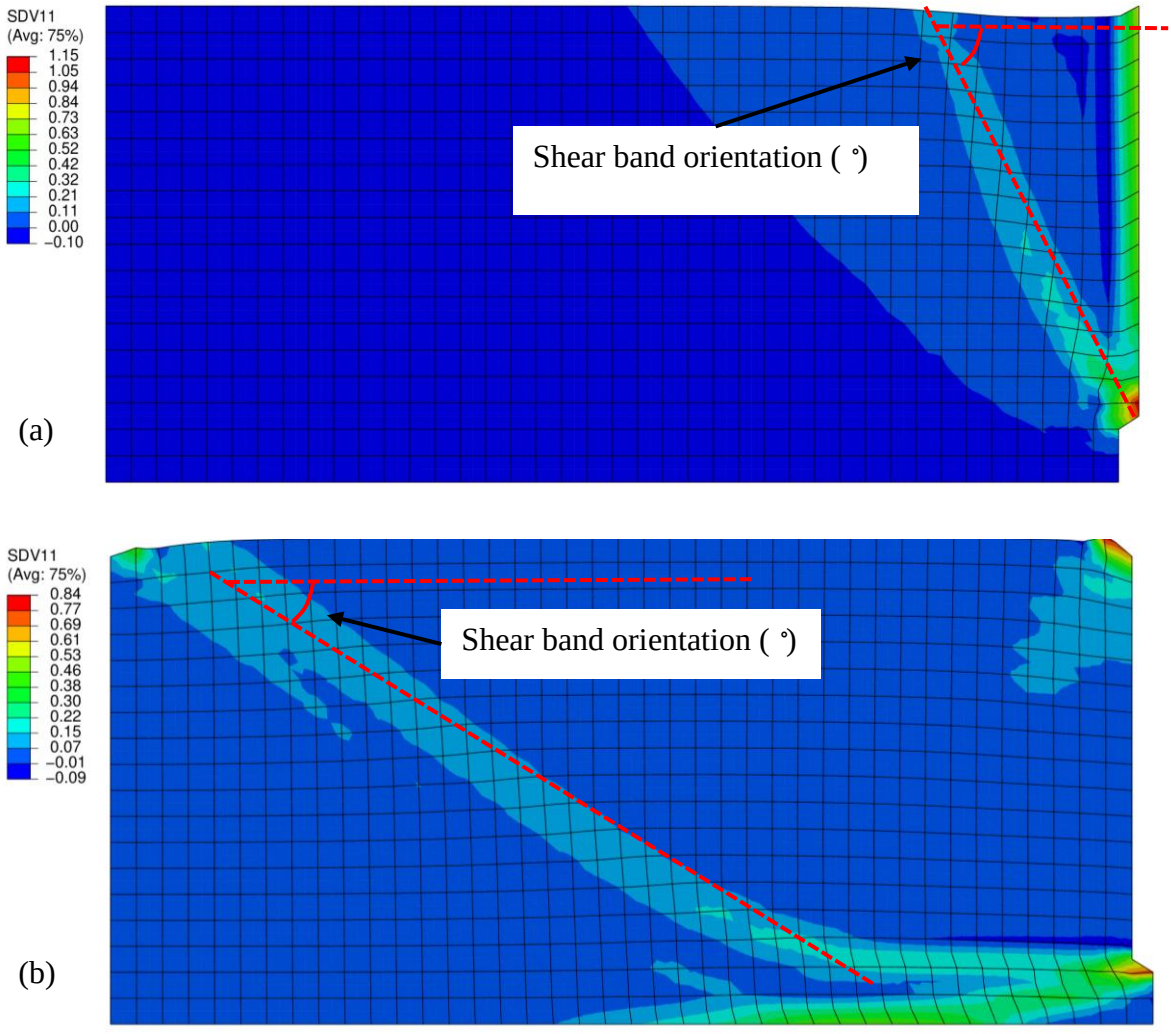

Figure 5.42 Shear band predicted by the G&S model after the retaining wall at $u/h_w = 0.05$ under rough boundary conditions: (a) active condition and (b) passive condition

5.5 Summary

The performance of three different weight functions for nonlocal regularisation, including the GD, G&S, and ON functions, has been evaluated. An anisotropic sand model accounting for the evolution of anisotropy is used. The increment of void ratio is assumed nonlocal, which significantly influences strain softening. Different BVPs have been simulated, including drained and undrained plane strain compression, the response of strip footings (level ground and slope) and a retaining wall (passive and active conditions). The main conclusions are:

(a) All the nonlocal methods are effective in reducing the mesh dependency of the force-displacement relationship in plane strain compression. The GD method gives less satisfactory results because the local value contributes most to the nonlocal variable. The nonlocal regularisation can reduce the mesh dependency of shear band thickness when the mesh size is smaller than the internal length. It is challenging to get mesh-independent shear band orientation in either drained or undrained condition. This could be due to the fact that only the void ratio increment is assumed nonlocal. More mesh-independent results could be obtained if more state variables that affect strain softening are assumed to be nonlocal.

(b) Nonlocal regularisation can effectively reduce the mesh dependency of the force-displacement curves for strip footings. The ON method gives excessive overprediction of volume expansion for soil elements around the footings on level ground, leading to an unrealistically steep reduction of the reaction force after the peak.

(c) All three nonlocal functions give mesh-independent results for the active and passive earth pressures on the retaining wall. The shear band orientation predicted by the three functions shows a slight variation in the mesh size.

The G&S method is thus a better option for nonlocal regularisation of sand models. It does not require extra parameters and assumes that the local variable does not contribute to the nonlocal one. The GD function gives more mesh-dependent results than the G&S function. The additional parameter m for the ON method can be determined using plane strain compression and used for the other BVPs. However, the assumption that the local variable can make a negative contribution to the nonlocal one may not be realistic. For instance, this

assumption can cause a steep reduction of the reaction force on a strip footing on level sand ground.

Chapter 6：Strain localisation in plane strain compression

6.1 Introduction

In the previous Chapter, a comparison of three different nonlocal methods demonstrated that the G&S method is the most effective in mitigating mesh dependency issues. Therefore, in Chapter 6, there will be a more in-depth discussion and analysis of the G&S method.

In this Chapter, plane strain compression tests with rough boundary under both drained and undrained conditions are simulated. The efficiency of the G&S method is justified through force-displacement relationship curves and shear strain contours. The effect of initial density and confining pressure on the nonlocal regularisation method is discussed. The evolution of state variables within the shear band under smooth boundary conditions is examined by cross-sections and selected elements inside and outside the shear band. These state variables include void ratio e, anisotropic variable A, degree of anisotropy F and shear strain. The effect of anisotropy on strain localisation is investigated using soil samples with various bedding plane orientations (α=15°, α=30°, and α=45°). Finally, the performance of the nonlocal method under 3D loading conditions is presented.

6.2 Drained plane strain compression with rough boundary

6.2.1 Boundary condition

In the simulation of the plane strain compression test, five mesh sizes were chosen, as shown in Figure 6.1, to test the impact of the nonlocal method on mesh dependency. Detailed information, such as mesh size, total elements, total nodes, and degrees of freedom, can be found in Table 6.1.

In this Chapter, both smooth and rough boundary conditions are considered. The smooth boundary conditions is detailed in Section 5.2. For the rough boundary conditions, both the horizontal and vertical displacements are fixed at the bottom end, and the top end does not

deform in the horizontal direction (Figure 6.2). In the simulations for plane strain compression with both smooth and rough boundary conditions in this chapter, $l_c = 0.012\ m$ is used for all simulations.

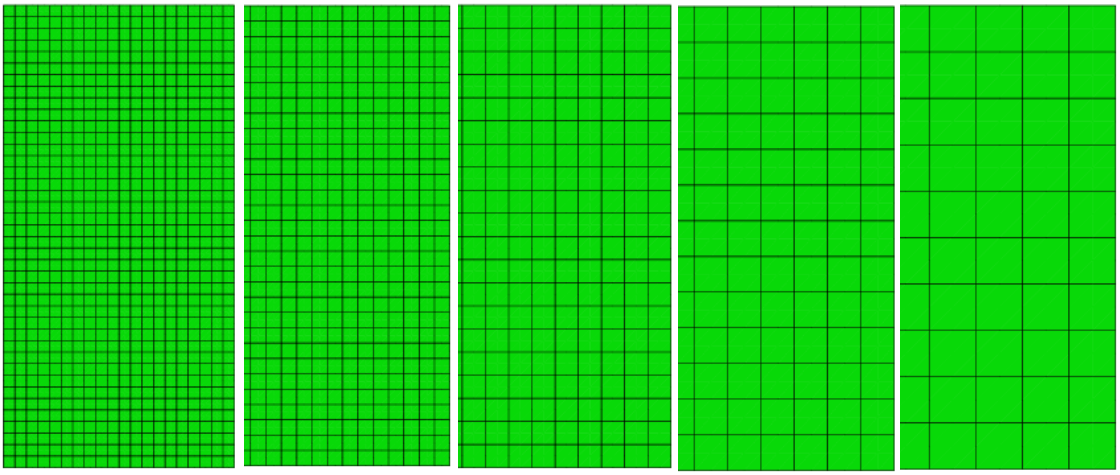

(a) (b) (c) (d) (e)

Figure 6.1 The mesh size used in plane strain compression modelling: (a) 0.003 m; (b) 0.004 m; (c) 0.006 m; (d) 0.009 m; (e) 0.012 m

Table 6.1 Mesh size information for plane strain compression modelling

Mesh Size (m)	Total Elements	Total Nodes	Degrees of Freedom
0.003	800	2521	7563
0.004	450	1441	4323
0.006	200	661	1983
0.009	91	314	942
0.012	50	181	543

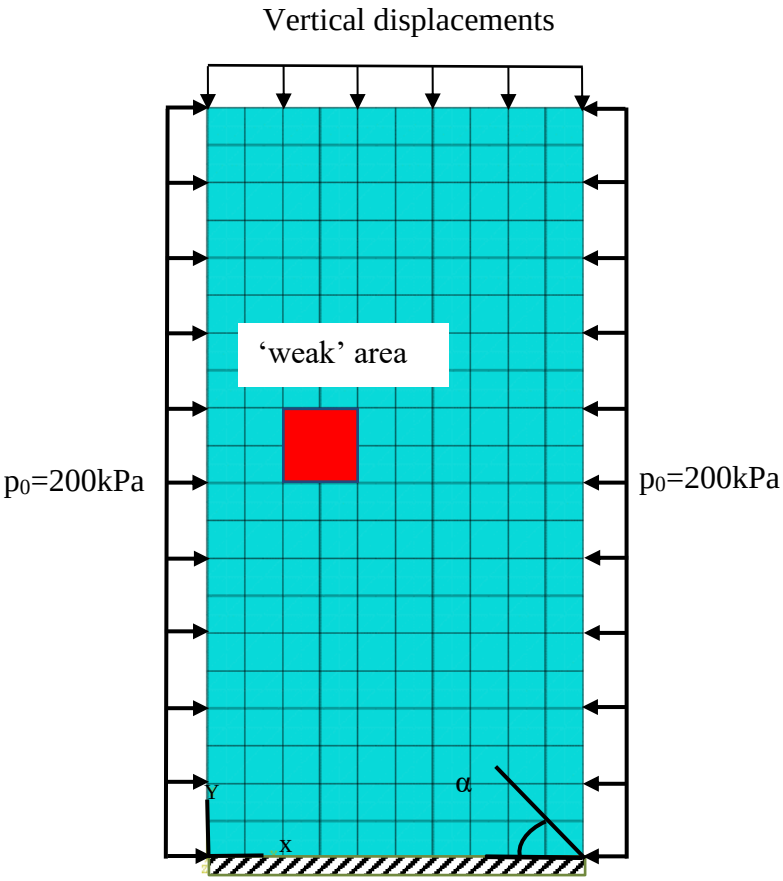

Figure 6.2 The boundary condition and bedding plan orientation for the plane strain compression simulations with rough boundary

6.2.2 Force-displacement relationship

Figure 6.3 shows that the nonlocal method can reduce the mesh dependency under rough boundary conditions. In the local model, the peak value of the reaction force of the coarse mesh is higher and delayed than the other fine mesh models. This conclusion agrees with findings from other studies (Summersgill, 2017; Liu, 2018; Mallikarachchi, 2019). However, Liu (2018) demonstrated that the specimen exhibits stiffer behaviour in the softening regime of a coarse mesh, which is in contrast to the results presented here. When comparing the rough boundary conditions to the smooth boundary condition (in Figure 5.7), it is observed that the peak value is reached earlier under the rough boundary conditions. For instance, for the models with the same mesh size of 0.003 m, under the smooth boundary condition, the peak occurs at $s/H = 2.5\%$, whereas under the rough boundary conditions, the peak occurs

at $s/H = 2.0\%$. As for nonlocal models, it is consistently observed that the peak value under rough boundary conditions is slightly higher than that under smooth boundary conditions.

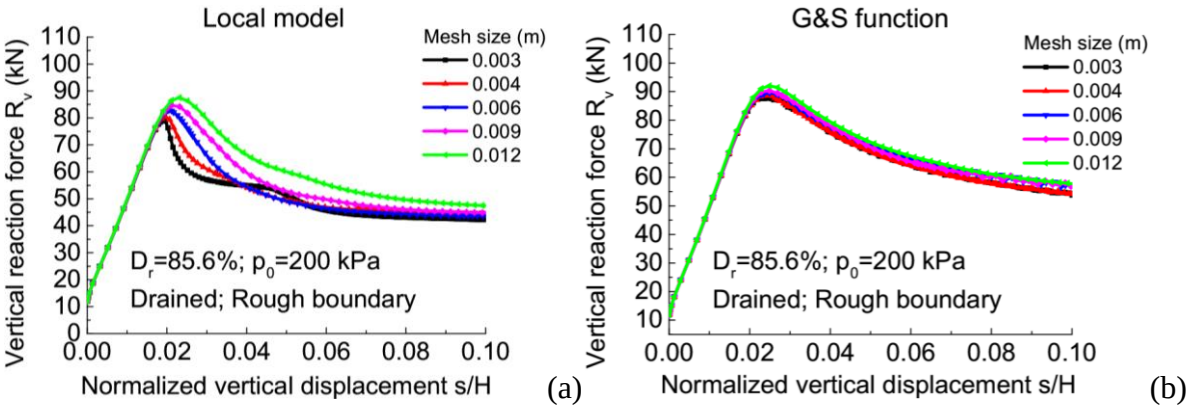

Figure 6.3 Comparison of the local and nonlocal models on the force-displacement relationship for drained plane strain compression: (a) Local model, (b) G&S function

6.2.3 Shear strain contours

Shear strain contours at the strain softening phase for the local and the nonlocal model at displacement $s/H = 9\%$ is shown in Figures 6.4-6.5, where SDV11 represents the total shear strain. As illustrated in Figures 6.4-6.5, under rough boundary conditions, the shear band transitions from a single shear band observed under smooth boundary conditions to a cross shear band. In the local model, the thickness of the shear bands significantly enlarged with increasing mesh size. Conversely, after nonlocal regularisation, the issue of mesh dependency is improved. This improvement is consistent with the results observed under smooth boundary conditions.

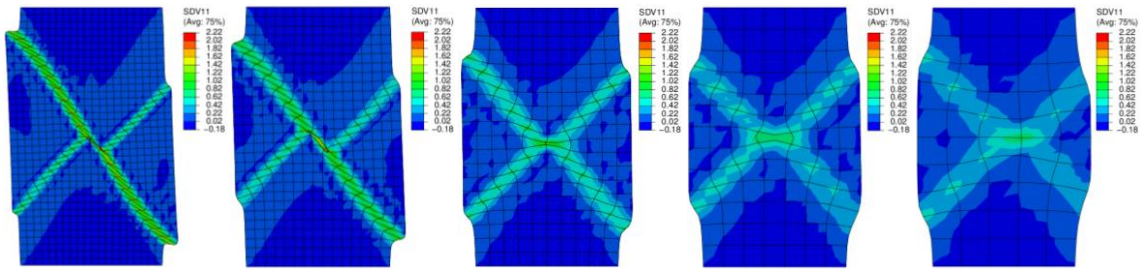

(a) (b) (c) (d) (e)

Figure 6.4 Shear strain contour for the Local model at $s/H = 9\%$ for different mesh sizes: (a) 0.003 m; (b) 0.004 m; (c) 0.006 m; (d) 0.009 m;(e) 0.012 m

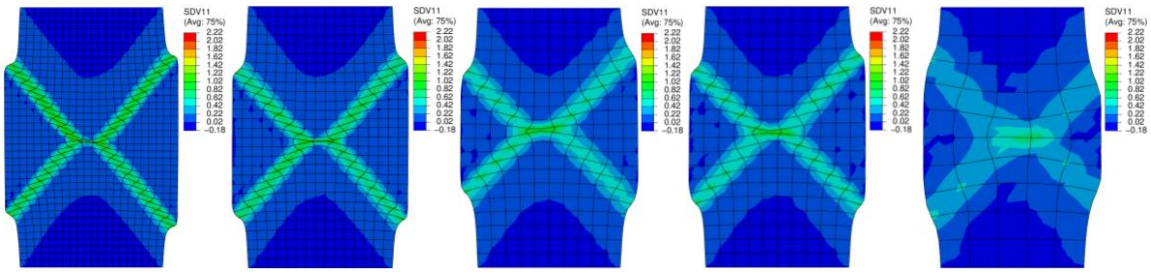

(a) (b) (c) (d) (e)

Figure 6.5 Shear strain contour for the G&S function at $s/H = 9\%$ for different mesh sizes: (a) 0.003 m; (b) 0.004 m; (c) 0.006 m; (d) 0.009 m;(e) 0.012 m

6.2.4 Evolution of shear band

The evolution of the shear band for the Local model and the G&S function at different s/H values (1%, 3%, 5%, and 9%) is shown in Figures 6.6-6.7. At the start of loading, there's not much difference between the Local model and the G&S function; both trigger strain localisation through a weak area of the same position and size. However, as the shear band evolves, the Local model first produces one shear band, followed by another. In contrast, the G&S function produces two shear bands simultaneously.

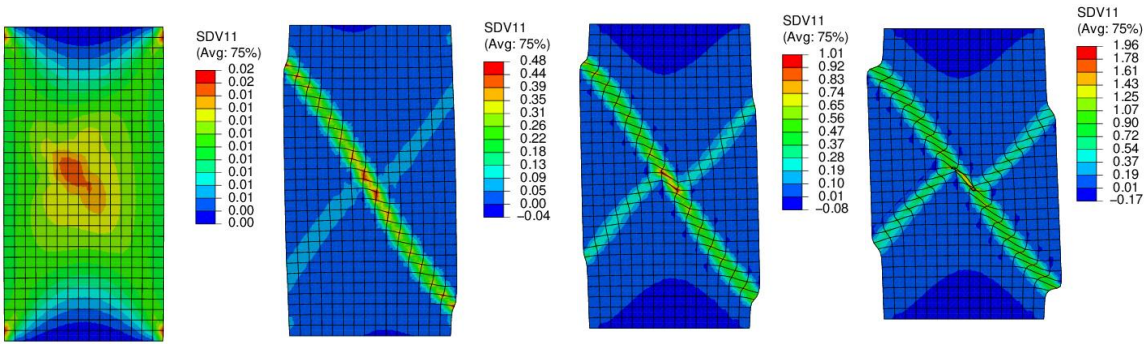

(a) (b) (c) (d)

Figure 6.6 Evolution of the shear band for the Local model at different s/H: (a) 1%; (b) 3%; (c) 5%; (d) 9%

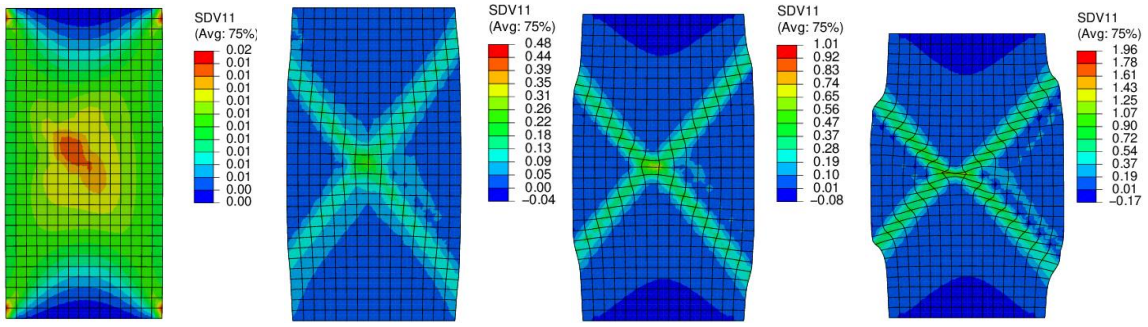

(a) (b) (c) (d)

Figure 6.7 Evolution of the shear band for the G&S function at different s/H: (a) 1%; (b) 3%; (c) 5%; (d) 9%

6.2.5 Orientation of shear band

For simplification, a horizontal path through the specimen centre was chosen as the reference direction for all simulations, and the orientation of the cross-shear band (β) is directly measured from shear strain contours, as shown in Figure 6.8.

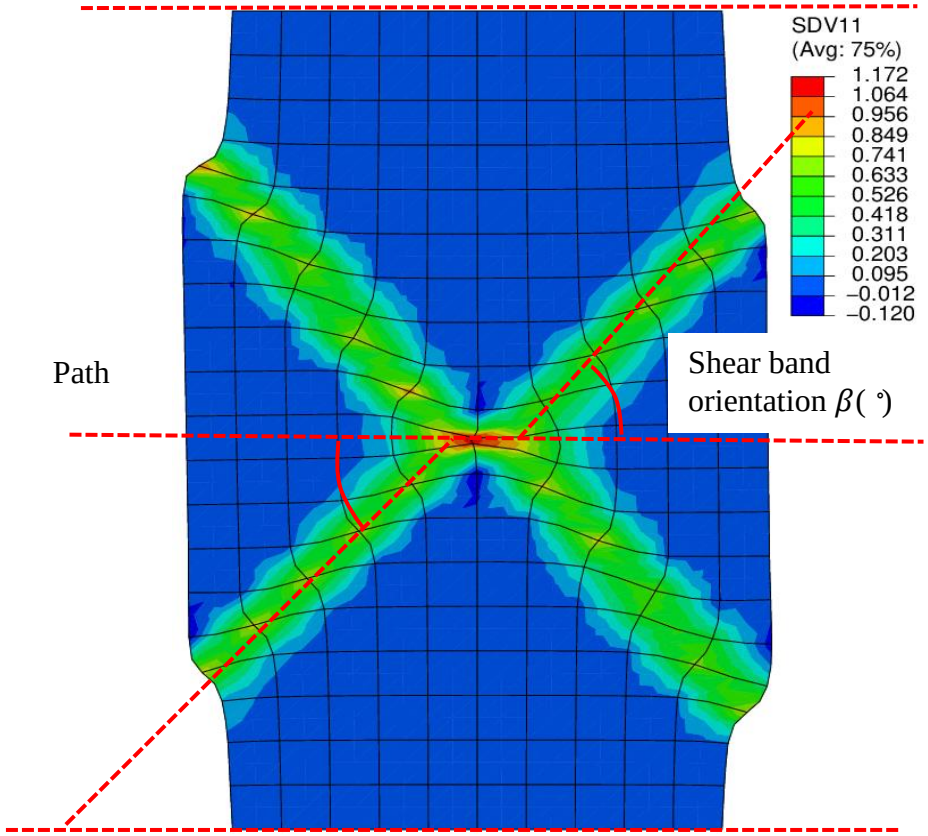

Figure 6.8 Shear strain contour for measuring the shear band orientation under rough boundary

As shown in Figure 6.9, the shear band orientation decreases with increasing mesh size, with the results being more pronounced in the local model than in the nonlocal models. This suggests that nonlocal regularisation can effectively reduce the dependency of shear band orientation on mesh size. The mesh dependency issue in the nonlocal model is not entirely resolved.

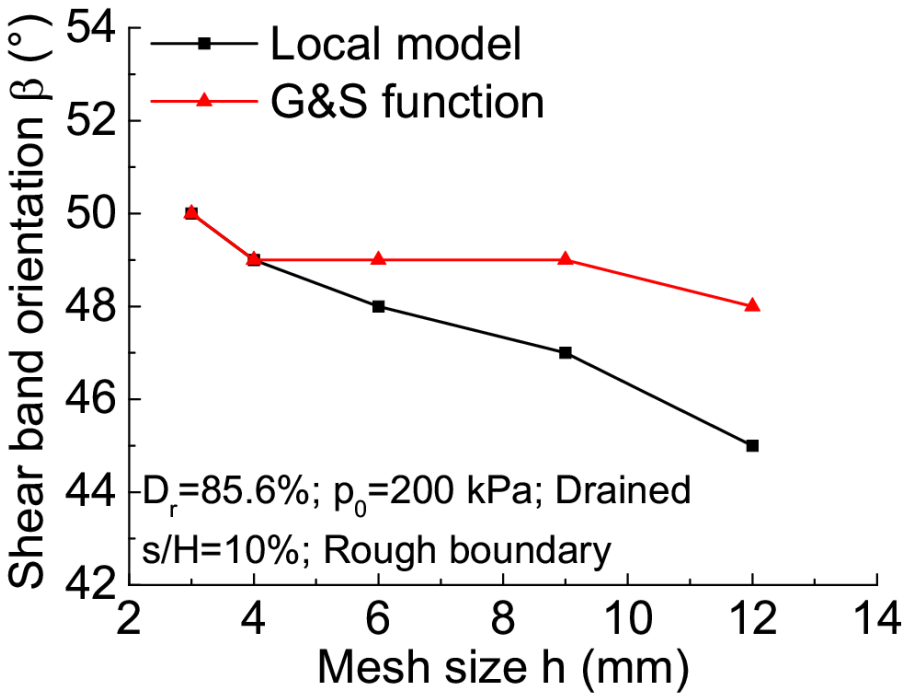

Figure 6.9 Comparison of shear band orientation for drained plane strain compression test under rough boundary

6.2.6 Thickness of shear band

The shear band thickness can be calculated from the shear band orientation: $t_s = \frac{1}{2} l \cdot \sin\beta$. In this way, the shear band thickness of different simulations can easily be compared.

Table 6.2 and Figure 6.10 show that the t_s increases with mesh size under the rough boundary conditions. The differences between the maximum and minimum shear band thickness for the Local model and G&S function are 7.72 mm and 4.57 mm, respectively. From this, it can be concluded that a nonlocal model can mitigate the issue of mesh dependency. The nonlocal model predicts a thicker shear band compared to the local model.

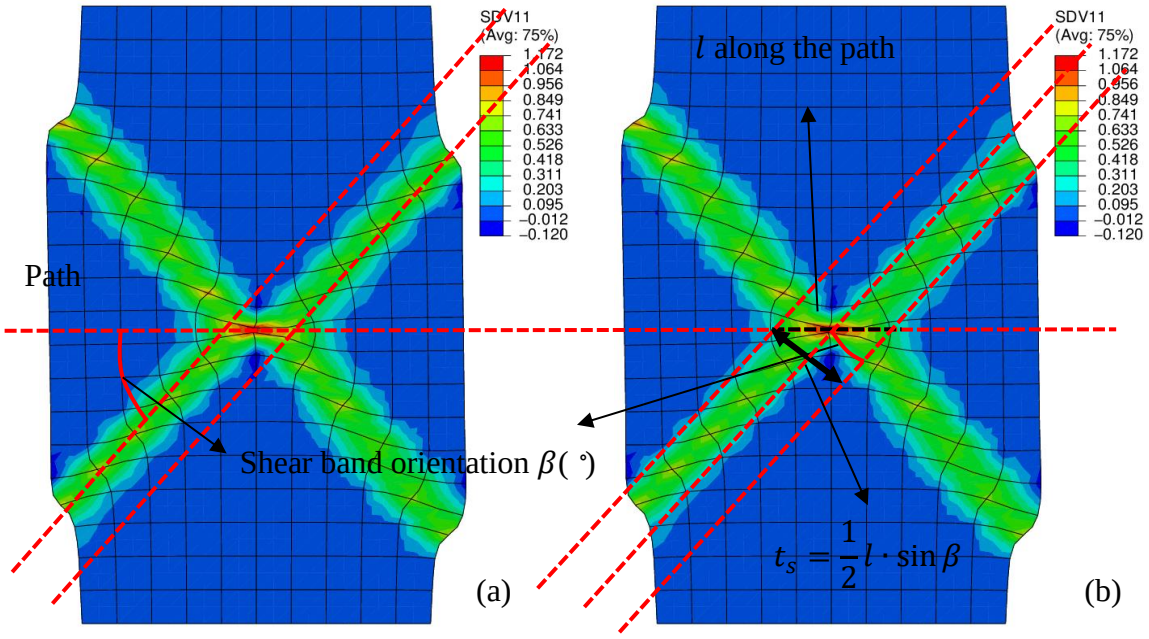

Figure 6.10 Calculation of shear band thickness by total shear strain under rough boundary

Table 6.2 Calculation of shear band thickness under the rough boundary conditions

Model	Mesh size (mm)	Shear band orientation β(°)	l (mm)	$t_s = \frac{1}{2} l \cdot \sin\beta$(mm)
Local model	0.003	50	26	9.96
	0.004	49	34.5	13.02
	0.006	48	36	13.38
	0.009	47	38.5	14.08
	0.012	45	50	17.68
GS model	0.003	50	38.5	14.75
	0.004	49	40.5	15.28
	0.006	49	45	16.98
	0.009	49	50.5	19.06
	0.012	48	52	19.32

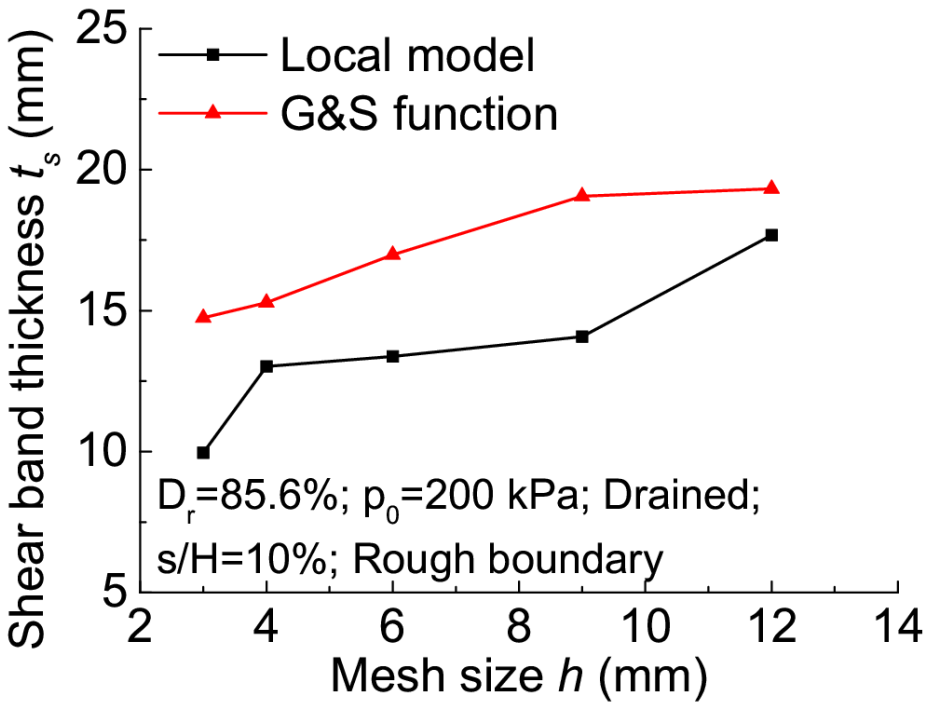

Figure 6.11 Comparison of the effect of mesh size on the shear band thickness under rough boundary

According to Figure 6.12, under rough boundary conditions, the shear band thickness (t_s) for the nonlocal method is more significant than the local model. This is consistent with the results under smooth boundary conditions. However, when the mesh size ($h = 0.006\,m$) and vertical displacement ($s/H = 10\%$) are the same, the t_s for all models are greater than those under smooth boundary conditions.

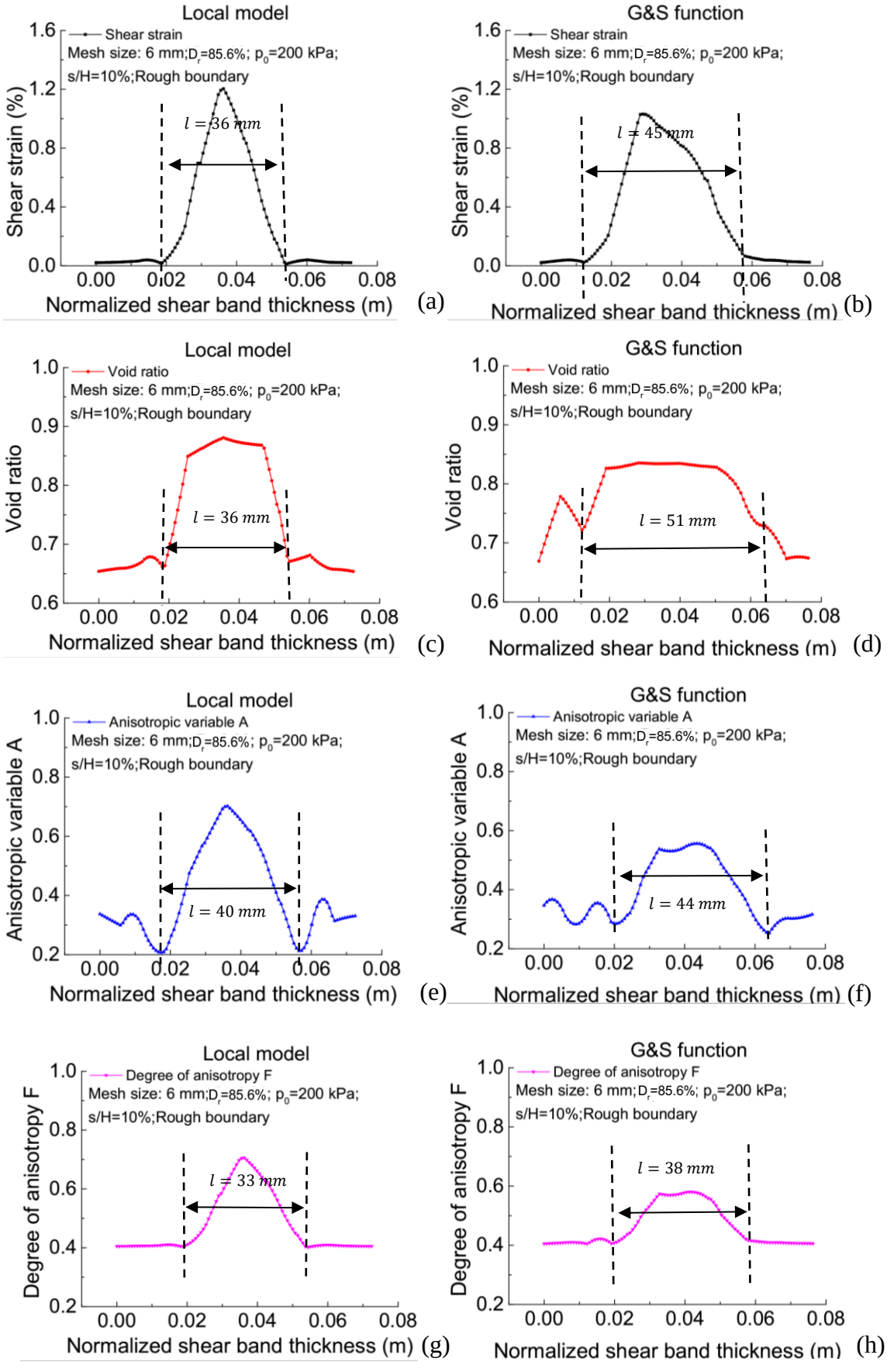

Figure 6.12 Calculation of Shear band thickness by different variables under rough boundary conditions at $s/H = 10\%$

6.2.7 Undrained plane strain compression with rough boundary

In undrained plane strain compression, the permeability of soil is set very small and water flow at all boundaries is closed. Transient consolidation analysis is selected for all simulations. The rest of the conditions are the same as the drained case. As shown in Figure 6.13, the nonlocal method is also applicable in undrained plane strain compression under rough boundary conditions.

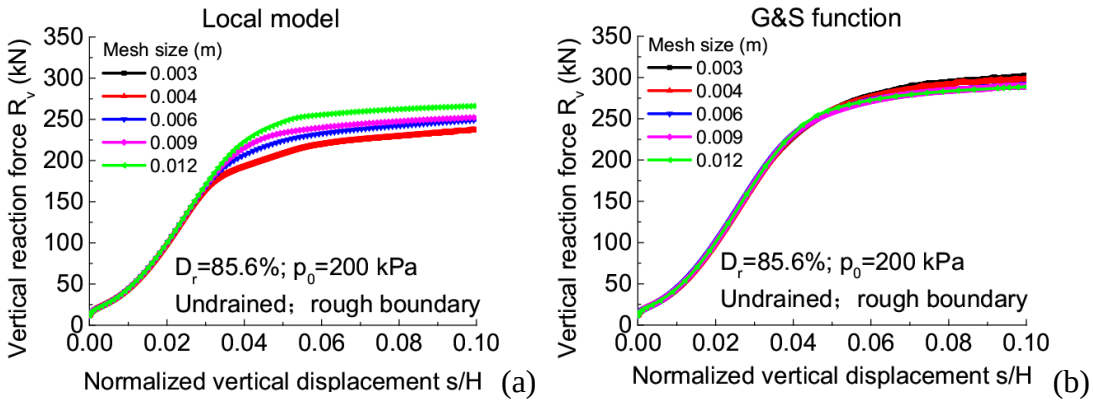

Figure 6.13 Comparison of the local and nonlocal models on the force-displacement relationship for undrained plane strain compression: (a) Local model; (b) G&S function

6.3 Evolution of the shear band

6.3.1 Evolution of state variables along the cross-section

The variation of state variables across the shear band can be analysed by examining cross-sectional profiles. These cross-sections are perpendicular to the shear band and are chosen for both fine mesh ($h = 0.004\ m$) and coarse mesh ($h = 0.006\ m$). In Figures 6.14-6.21, the variation of void ratio e, anisotropic variable A, degree of anisotropy F and shear strain along the cross-section is discussed. Profiles from both local and G&S methods are presented. Four stages of deformation (vertical displacement at $s/H = 2.5\%, 4\%, 7\%$ and 10%) are depicted to provide insight into the growth of the shear band. A noticeable difference is observed between the pre-peak homogeneous deformation ($s/H = 2.5\%$) and the post-

localised deformation ($s/H = 10\%$). This section only discusses the smooth boundary. Details regarding rough boundary conditions can be found in Appendix A.

(1) Void ratio e

As demonstrated in Figure 6.14, the width of the concentration of e for the local model is smaller than the nonlocal model. In the local model, the width of the concentration of e increases with mesh size, and the mesh dependency issue disappears after nonlocal regularisation.

The cross-sectional profiles shown in Figure 6.15, the width of the concentration and the peak value of e at $s/H = 2.5\%$ are smaller than others. The width becomes constant when $s/H > 2.5\%$. When the shear band reaches a particular stage, the width no longer changes, but the peak value of e continues to increase. This observation of the evolution of the shear band for different mesh sizes is consistent with the results from micro-polar models (Bardet and Proubet, 1992) and gradient flow theories (Han and Drescher, 1993).

Under rough boundary conditions (see Appendix A), the results from the G&S function indicate a significantly larger width of concentrated volumetric expansion compared to the local model, approximately 2.0 times larger (Figure A-2). However, under the same mesh size for smooth boundary conditions, the width of e concentration predicted by the nonlocal model is only about 1.25 times that of the local model.

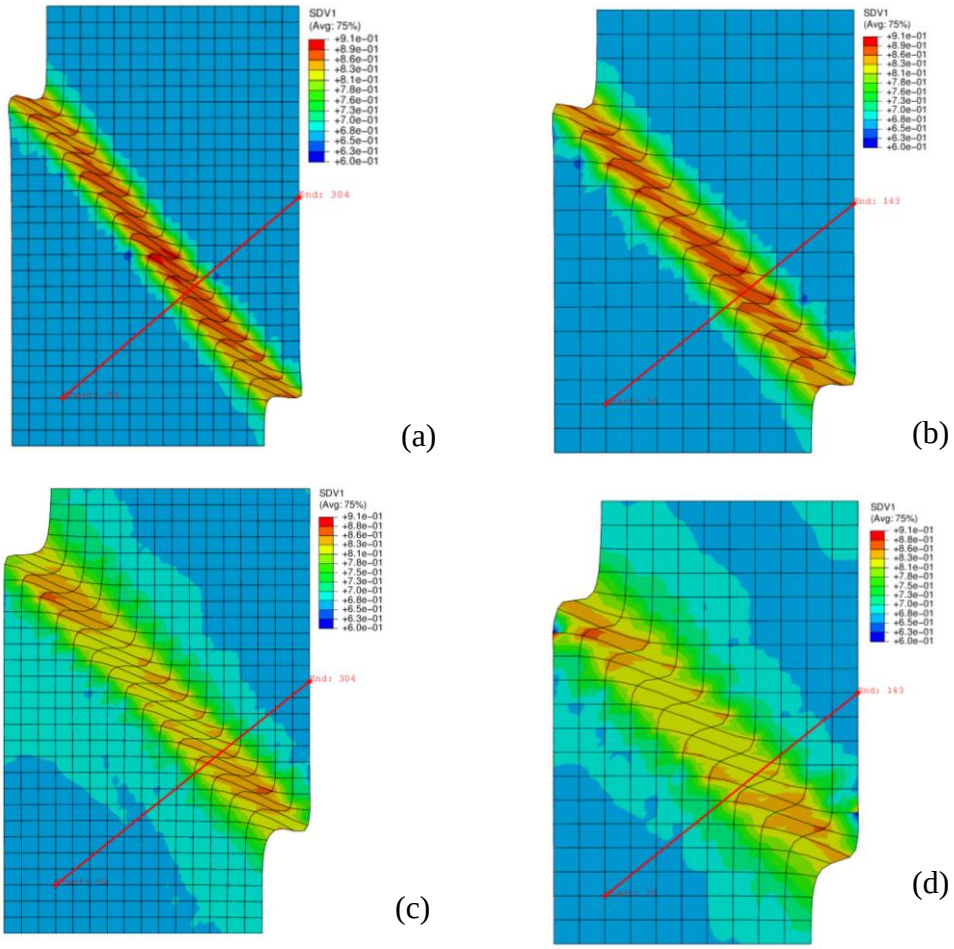

Figure 6.14 Contours of the void ratio e from local and nonlocal models: (a) Local (0.004 m); (b) Local (0.006 m); (c) G&S function (0.004 m); (d) G&S function (0.006 m)

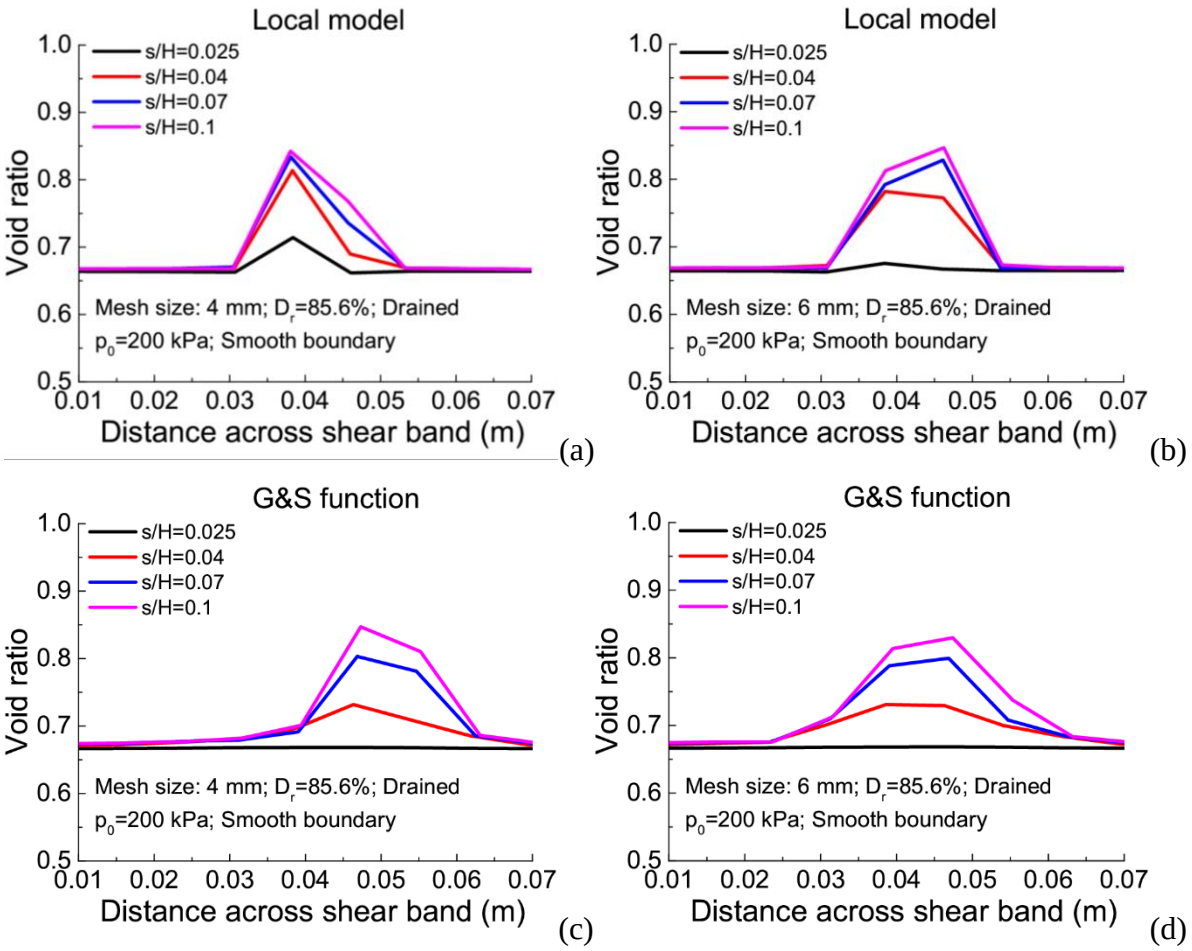

Figure 6.15 Cross-sectional profiles of the void ratio e from local and nonlocal models: (a) Local (0.004 m); (b) Local (0.006 m); (c) G&S function (0.004 m); (d) G&S function (0.006 m)

(2) Anisotropic variable A

Figures 6.16 and 6.17 show the evolution of the anisotropic variable A. The anisotropy variable A inside the shear band increases as the shear band develops, whereas it decreases at the shear band boundary with the progression of the shear band. After nonlocal regularisation, not only does the fluctuation in the change of A decrease, but the mesh dependency issue observed in the width of concentration of A is also addressed.

In the local model, similar to the smooth boundary condition, the value of A is negative at the shear band boundary under rough boundary conditions (Figure A-4a). When the mesh size $h = 0.006\ m$, the minimum value is -0.75 for rough boundary conditions, significantly smaller than the -0.1 observed under smooth boundary conditions. This is mainly due to the

overlapping influence of multiple surrounding cross-shear bands. Under rough boundary conditions, the maximum A (0.55) is noticeably smaller than that under smooth boundary conditions (0.7).

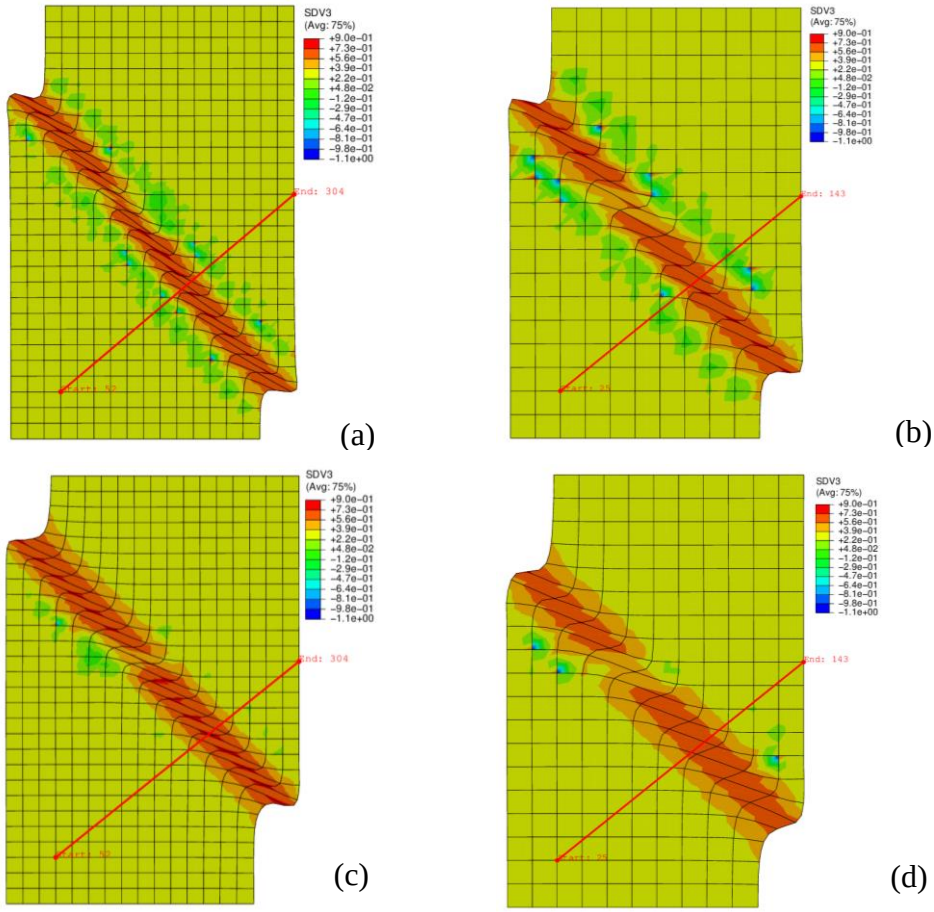

Figure 6.16 Contours of the anisotropy variable A from local and nonlocal models: (a) Local (0.004 m); (b) Local (0.006 m); (c) G&S function (0.004 m); (d) G&S function (0.006 m)

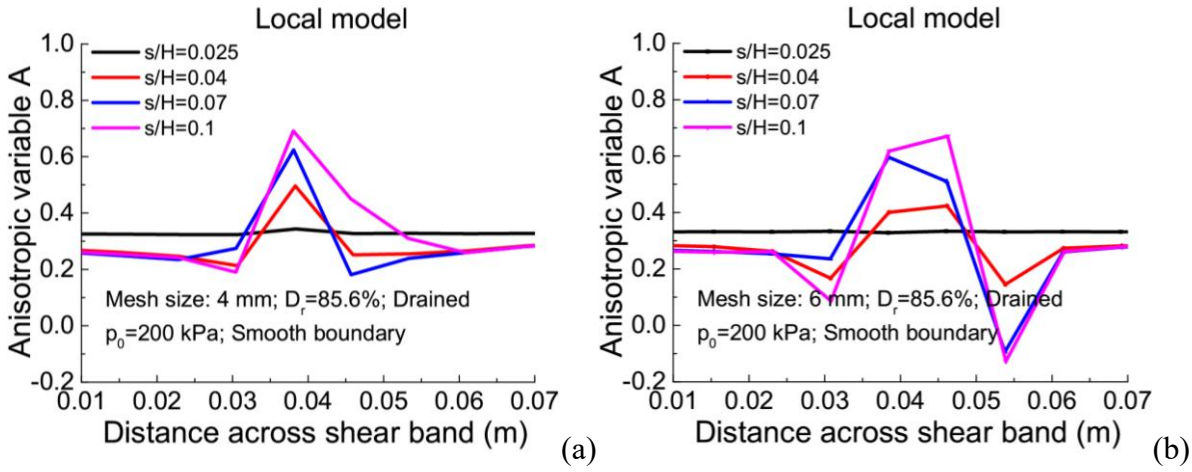

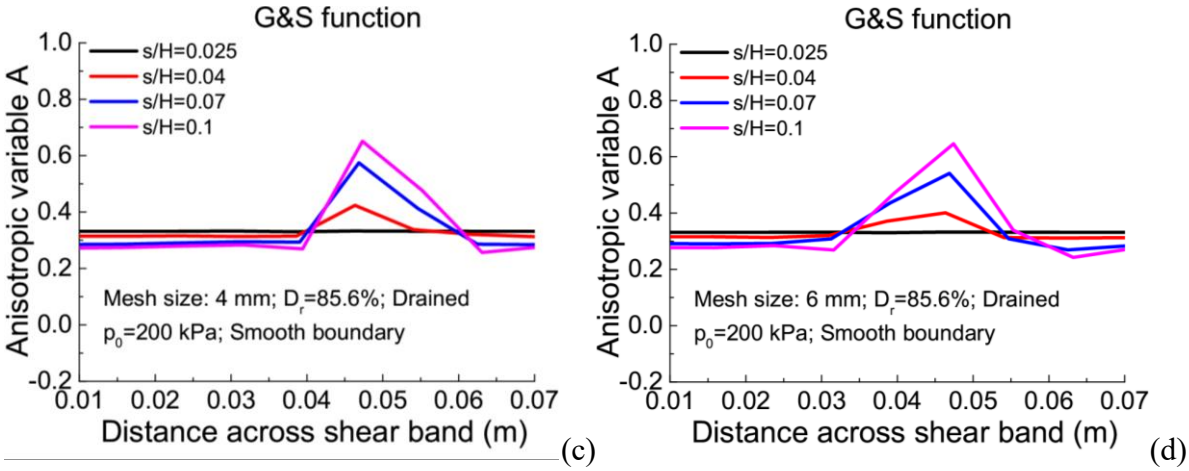

Figure 6.17 Cross-sectional profiles of the anisotropy variable A from local and nonlocal models: (a) Local (0.004 m); (b) Local (0.006 m); (c) G&S function (0.004 m); (d) G&S function (0.006 m)

(3) Degree of anisotropy F

In the local model (Figure 6.19a and b), the maximum F inside the shear band of fine mesh is larger than that in the coarse mesh at vertical displacements $s/H = 4\%$ and 7%. Conversely, when $s/H = 10\%$, the peak value of F in the coarse mesh is larger than that in the fine mesh. However, the F at $s/H = 10\%$ for coarse mesh size is smaller than that for fine mesh size in rough boundary (Appendix A). This is opposite to the observations made in the smooth boundary condition. Moreover, in the local model, the width of concentration of F for coarse mesh size is more significant than that for fine mesh size. In contrast, in the nonlocal model, the width tends to be consistent across different mesh sizes.

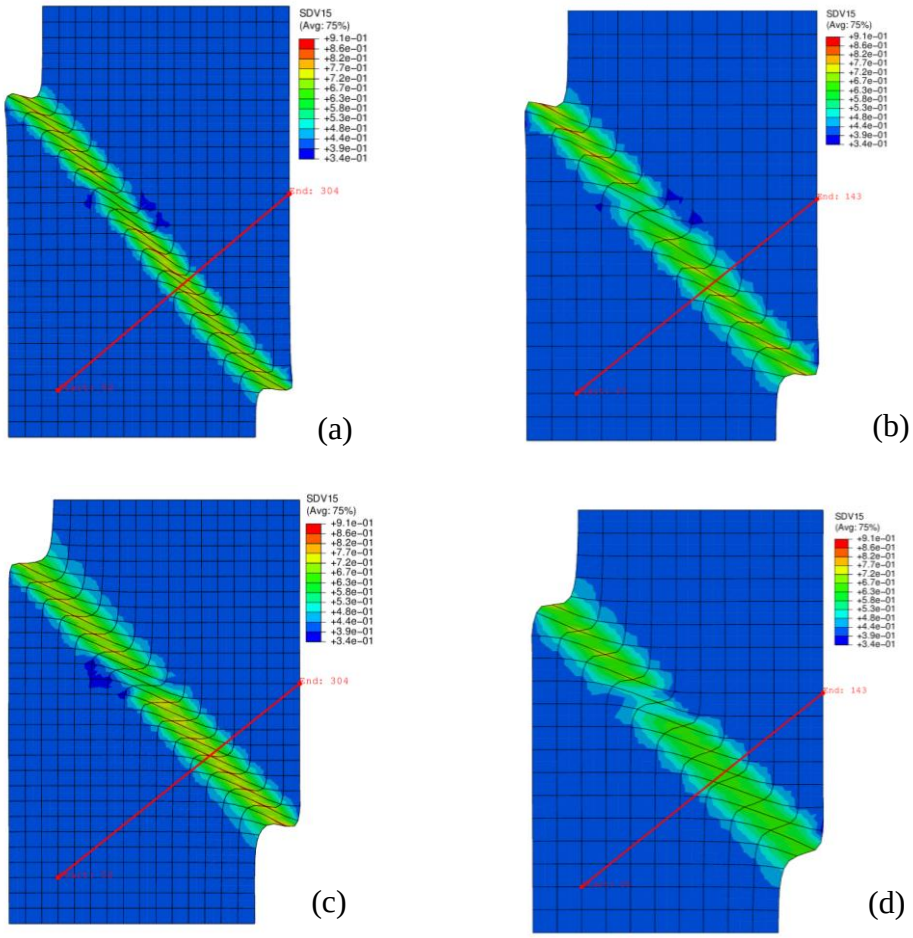

Figure 6.18 Contours of the degree of anisotropy F from local and nonlocal models: (a) Local (0.004 m); (b) Local (0.006 m); (c) G&S function (0.004 m); (d) G&S function (0.006 m)

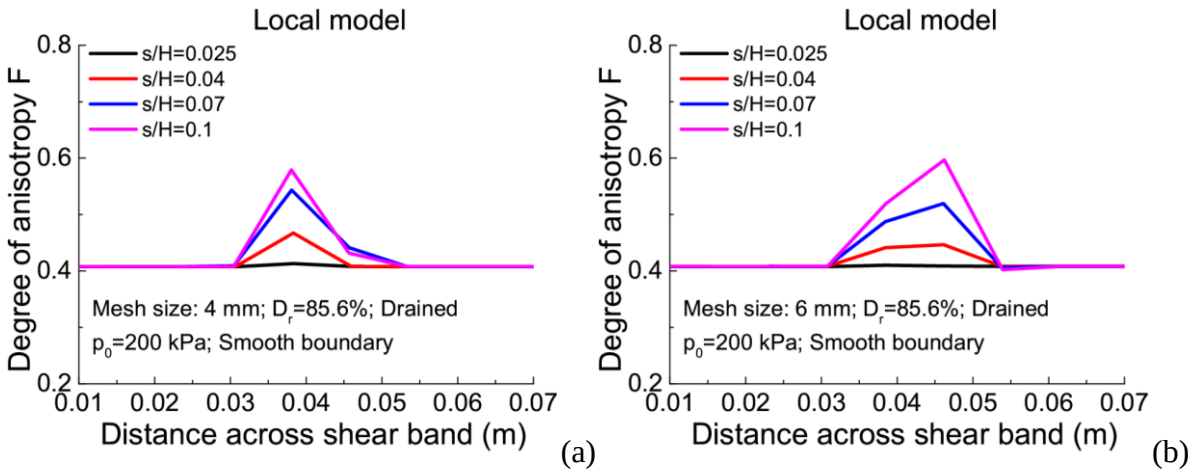

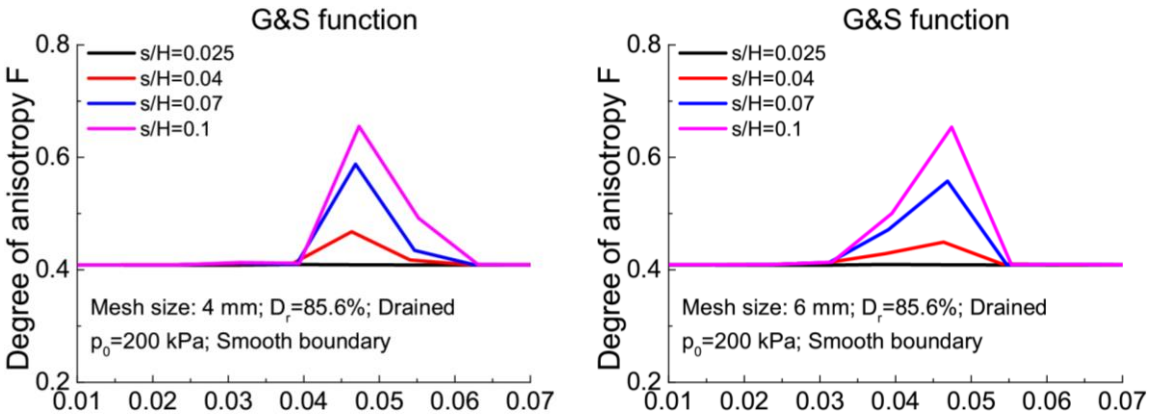

(c) (d)

Figure 6.19 Cross-sectional profiles of the degree of anisotropy F from local and nonlocal models: (a) local (0.004 m), (b) local (0.006 m), (c) G&S function (0.004 m), (d) G&S function (0.006 m)

(4) Shear strain

The cross-section contours of shear strain for local and nonlocal models are compared in Figure 6.20. The local model exhibits that t_s predicted by the local model is sensitive to the mesh size. On the contrary, contours of shear strain from the nonlocal model portray almost similar shear band thickness. Four vertical displacements for each mesh are portrayed to get an insight into the growth of the band in Figure 6.21. The cross-section profiles illustrate that the shear strain increased when the shear band developed. The maximum shear strain obtained by the nonlocal model is greater than that of the local model.

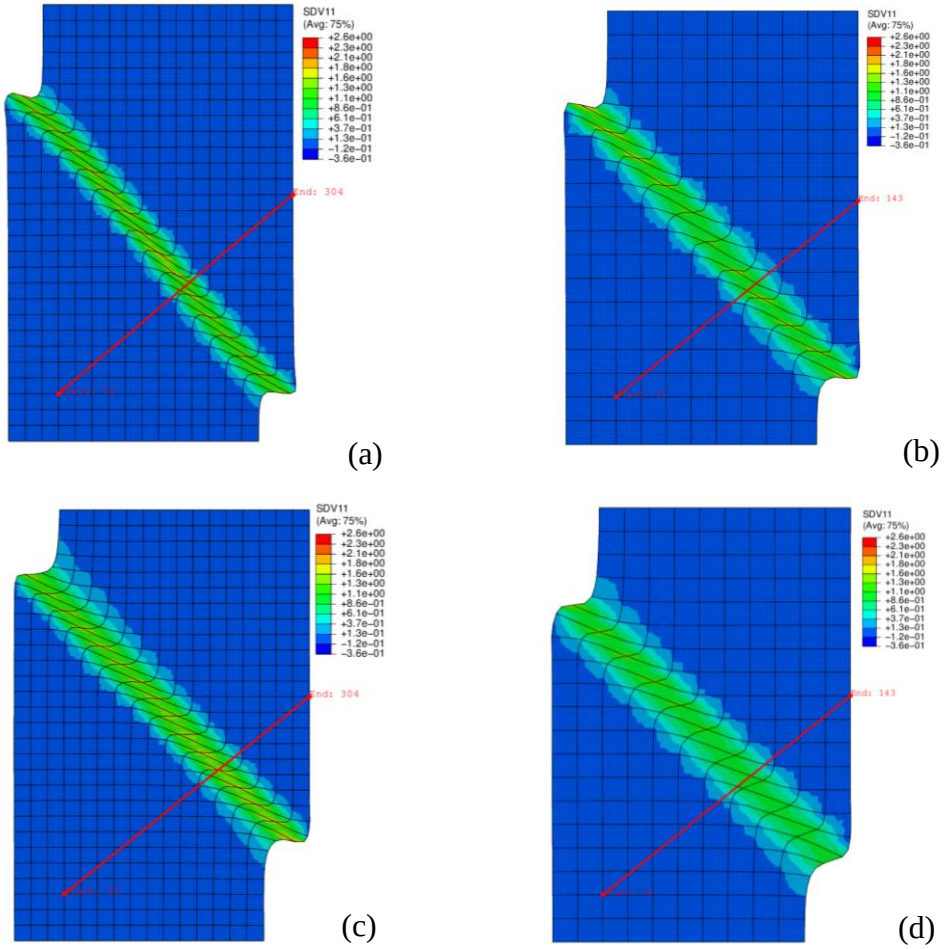

Figure 6.20 Contours of the shear strain from local and nonlocal models: (a) Local (0.004 m); (b) Local (0.006 m); (c) G&S function (0.004 m); (d) G&S function (0.006 m)

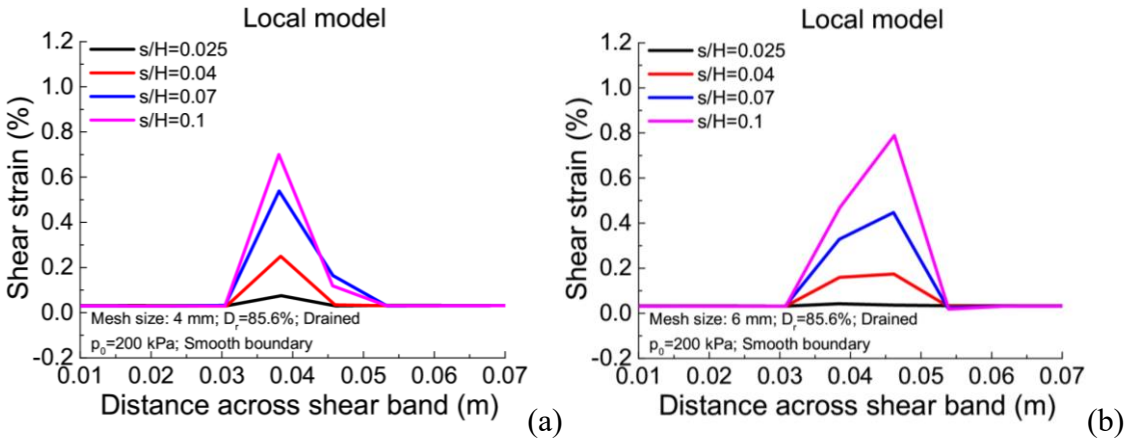

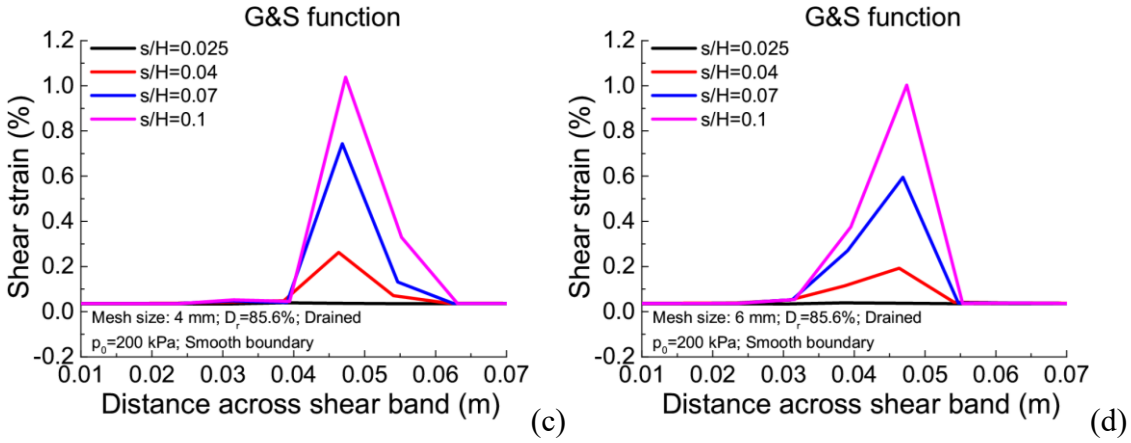

Figure 6.21 Cross-sectional profiles of the shear strain from local and nonlocal models: (a) local (0.004 m), (b) local (0.006 m), (c) G&S function (0.004 m), (d) G&S function (0.006 m)

6.3.2 Evolution of state variables in elements inside and outside the shear bands

To better compare the effect of local and nonlocal models on the development of the shear band, the evolution of the state variables inside and outside the shear band is presented in this section.

Results for simulations with different mesh sizes are presented (Figure 6.22). The mesh size of the first simulation is 0.004 m (with element A inside the shear band and element B outside), while the mesh size of the second simulation is 0.006 m (with element C inside the shear band and element D outside).

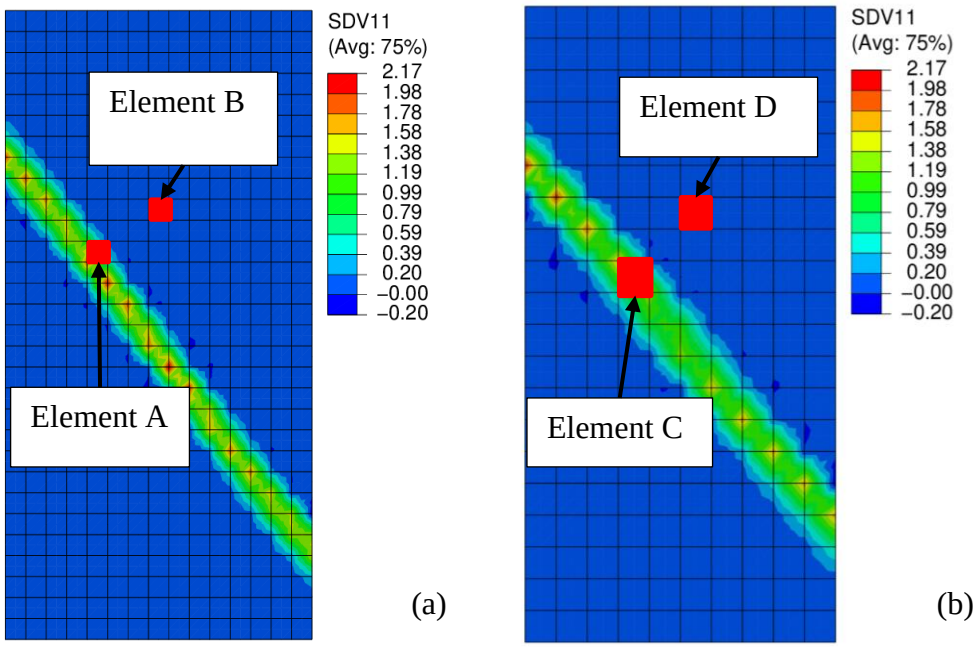

Figure 6.22 Location of the selected elements for the single shear band: (a) Fine mesh, (b) Coarse mesh

(1) Evolution of void ratio *e*

Within the shear band, the volume expansion gradually increases with loading. When the element is outside the shear band, the *e* remains constant after reaching its peak. Thus, the maximum *e* within the shear band is significantly greater than those outside (Figure 6.23). Indeed, existing research has shown that there is much smaller plastic deformation and less volume expansion outside the shear band (Gao and Zhao, 2013; Mallikarachchi and Soga, 2020). Moreover, when elements are inside the shear band, the local model with a fine mesh exhibits a significant gradient and higher *e* than coarse mesh. In contrast, the *e* of the fine mesh is smaller than that of the coarse mesh when the elements are outside the shear band. However, under rough boundary conditions (Appendix B), the *e* for fine mesh size is larger than that in coarse mesh both inside and outside the shear band.

Both the local and nonlocal models predict volume expansion in dense soil. Since the evolution of *e* is assumed to depend on the volumetric strain increment of local and neighbouring integration points in the nonlocal model, the increase in *e* in the nonlocal model becomes smaller than that predicted by the local model inside the shear band. The

local model predictions exhibit mesh-dependent issues, and the difference between two different meshes is reduced by the nonlocal model (Figure 6.23b and d).

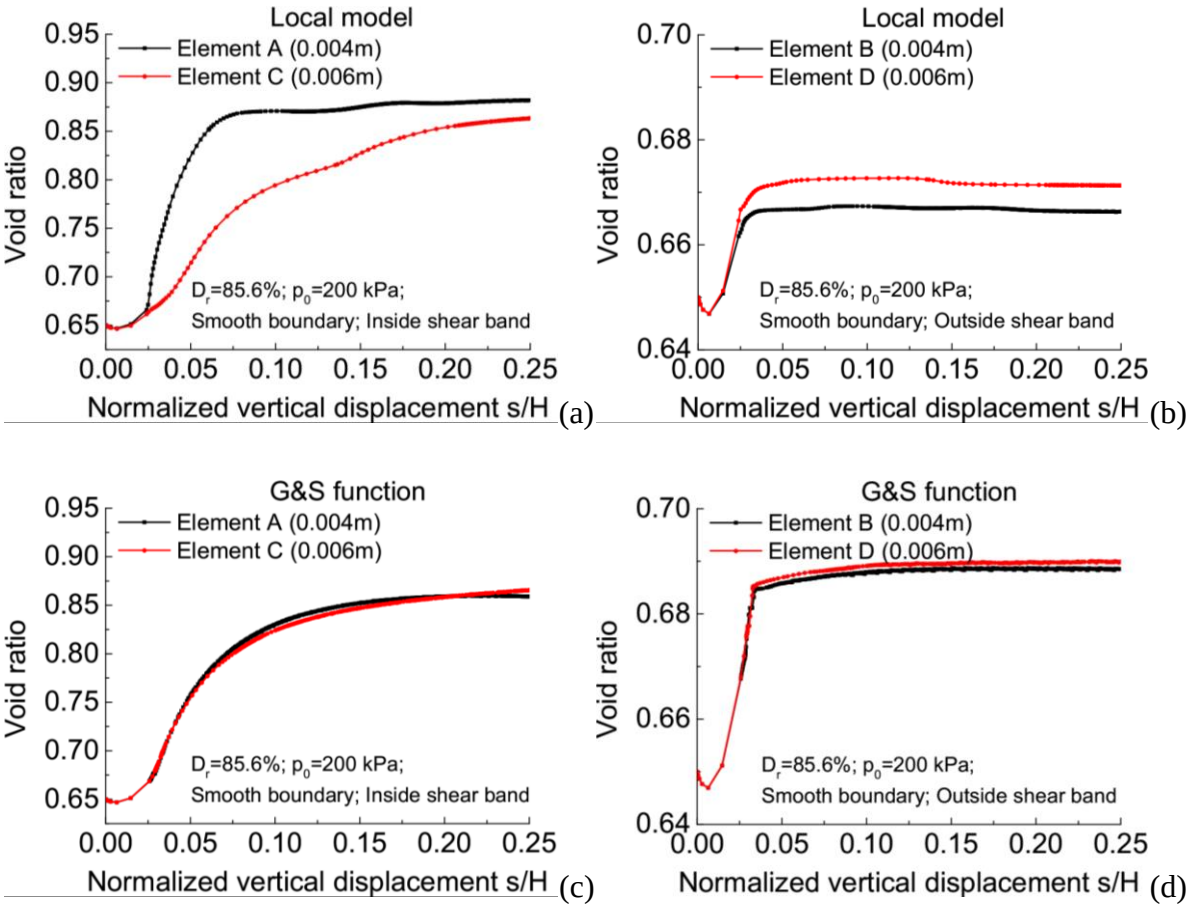

Figure 6.23 The local evolution of the void ratio *e* for the elements inside and outside the shear band under smooth boundary condition

(2) Local fabric evolution

As depicted in Figure 6.24, both inside and outside the shear band, the local models show a larger difference between different mesh sizes than nonlocal models. However, it can be inferred that even though nonlocal treatment alleviates the mesh size dependency issue of the evolution F outside the shear band (Figure 6.24d), the mesh dependency inside the shear band by the nonlocal method remains unresolved.

The degree of anisotropy F inside the shear band is more significant than that outside the shear band. This is because shear strain concentration is higher within the shear band, and

more significant fabric evolution is induced by plastic shear strain. Additionally, when the elements are outside the shear band (Figures 6.24c and d), the degree of anisotropy F for the nonlocal model is greater than that for the local model.

Moreover, there is a decrease after the initial values, followed by an increase. The initial decrease during the loading stage occurs because the initial fabric and the loading direction are non-coaxial, and the fabric needs to rotate towards the loading direction with plastic shear strain (Gao et al., 2013). However, there is no decrease observed within the shear band for the nonlocal models with both fine and coarse mesh sizes under smooth boundary conditions, which is significantly different from the behaviour under rough boundary conditions where a drop occurs in both mesh sizes (Appendix B).

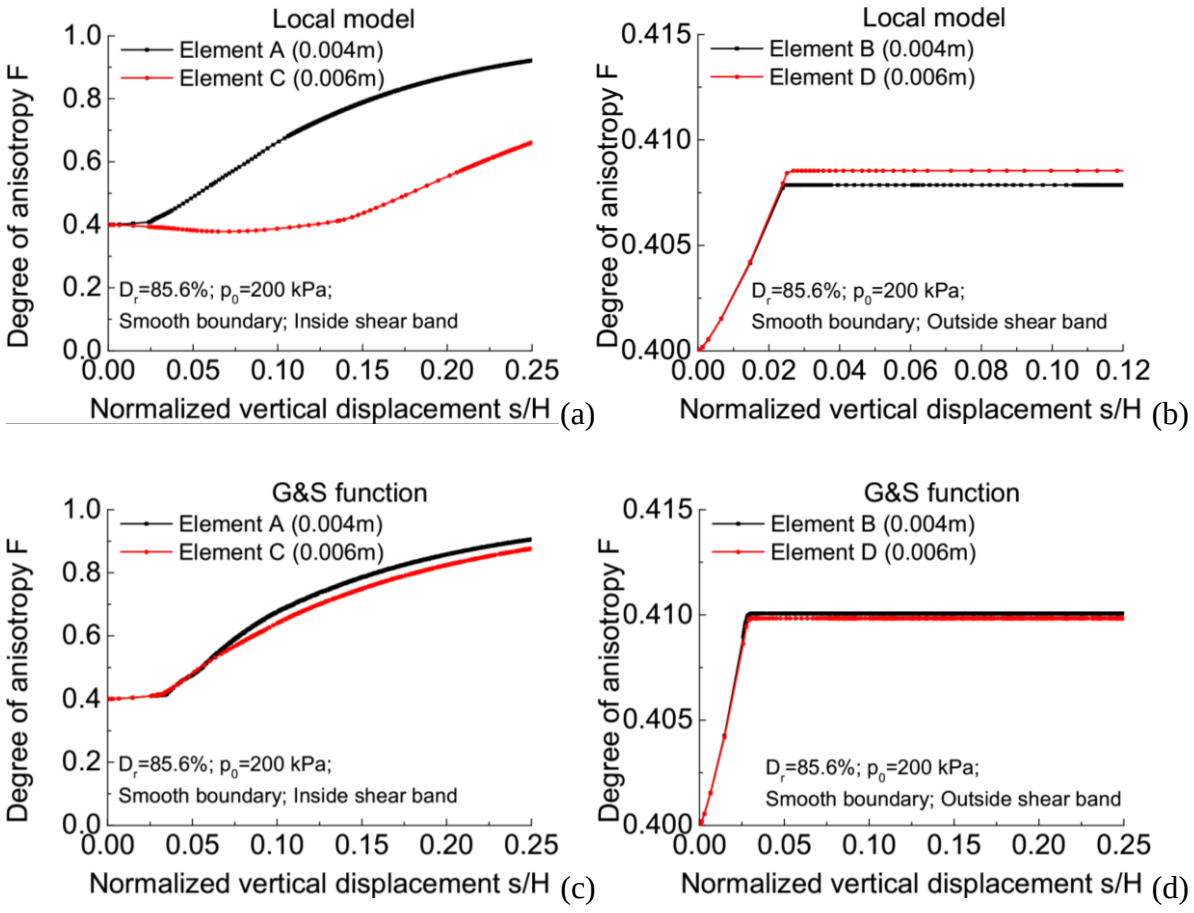

Figure 6.24 The local evolution of the fabric for the elements inside and outside the shear band under smooth boundary condition

(3) Local evolution of A

At the initial state, the evolution of the anisotropic variable A inside the shear band decreases slowly compared to outside the shear band. As the shear band develops, the anisotropic variable A inside the shear band gradually increases, whereas the value outside the shear band decreases. Whether it is increasing or decreasing, the gradient of the anisotropic variable A of the local model is greater than that of the nonlocal model, and it tends to be stable at the critical state outside the shear band.

Moreover, in the local model, the anisotropic variable A has different initial values for models with various mesh sizes inside the shear band (Figure 6.25a). The initial value for the fine mesh size is greater than that for the coarse mesh size. In contrast, in the nonlocal model, the initial values for models with different mesh sizes are all set to 0.1. Both the local and nonlocal models gradually decrease during the initial stages and reach their lowest points at around $s/H = 2\%$, and then followed by a gradual increase.

The evolution processes of different mesh sizes for the local model are distinct. This variation occurs due to the effect of evolution on plastic hardening and plastic shear strain increments. However, the differences between different mesh sizes essentially disappear after nonlocal regularisation.

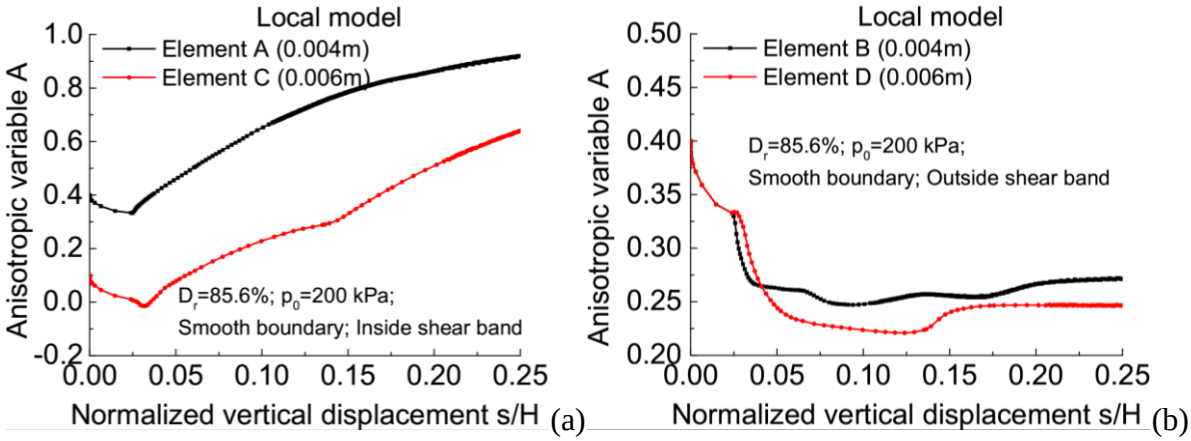

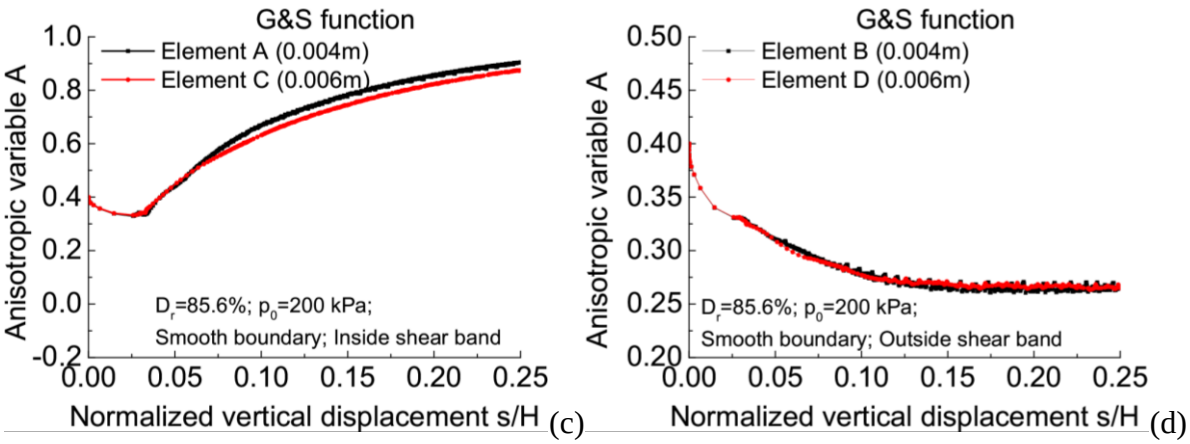

Figure 6.25 The local evolution of the anisotropic variable A for the elements inside and outside the shear band under smooth boundary condition

6.3.3 Evolution of state variables along the cross-section under undrained condition

(1) Magnitude of displacement

The evolution of displacement gradients within the shear band is shown in Figure 6.24. During the loading process, there is sliding along the shear band above the shear band until no significant change in static displacement occurs. Vermeer and Marcher (2000) and Galavi and Schweiger (2010) also used velocity and displacement profiles to estimate the shear zone.

Regarding contours and cross-sectional profiles (Figure 6.27), the magnitude of displacement within the shear band increases with the development of the shear band. However, for different mesh sizes, the peak value of the magnitude of displacement does not vary significantly. In the local model, the width of displacement gradient for fine mesh size (Figure 6.27a) is significantly smaller than that for coarse mesh size (Figure 6.27b) and the results in the nonlocal model (Figure 6.27c and d). The displacement gradients in Figures 6.27 (c) and (d) are flatter than their local counterparts in Figures 6.27 (a) and (b). Nonlocal regularisation reduces the difference in width of displacement gradient and maximum displacement between large and small mesh sizes.

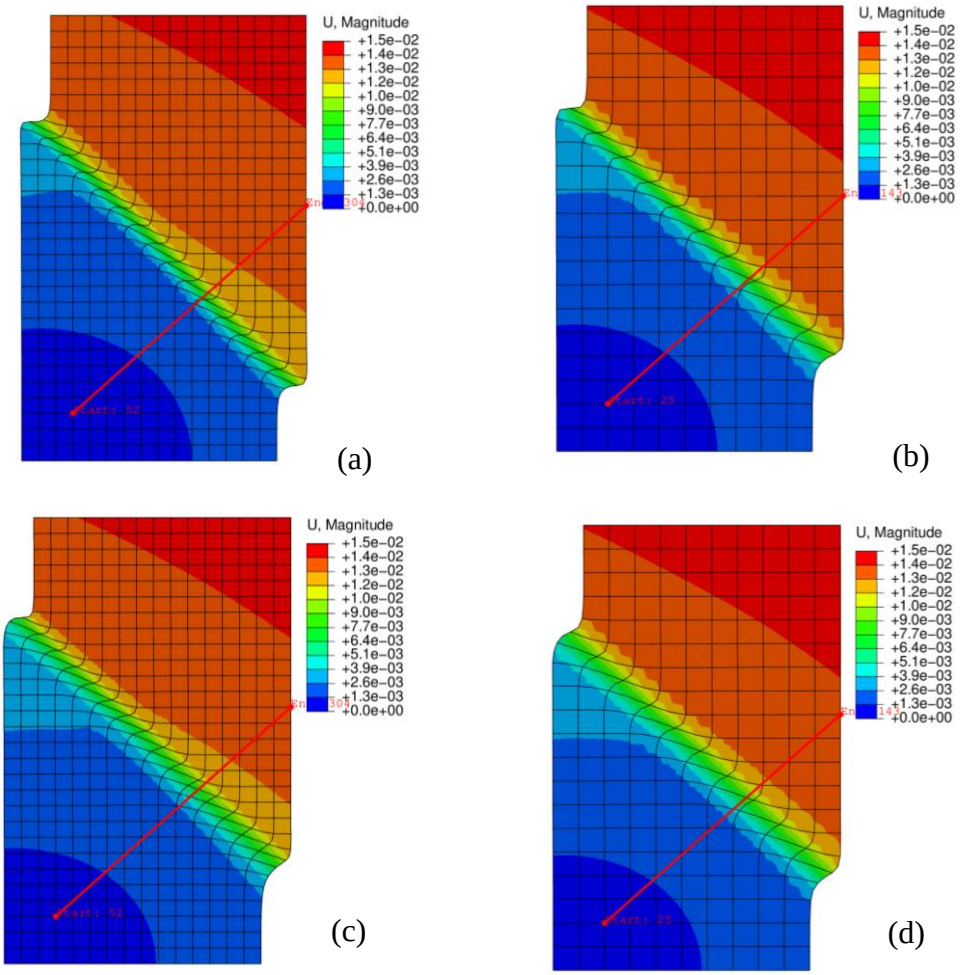

Figure 6.26 Contours of the magnitude of the displacement from local and nonlocal models: (a) Local (0.004 m); (b) Local (0.006 m); (c) G&S function (0.004 m); (d) G&S function (0.006 m)

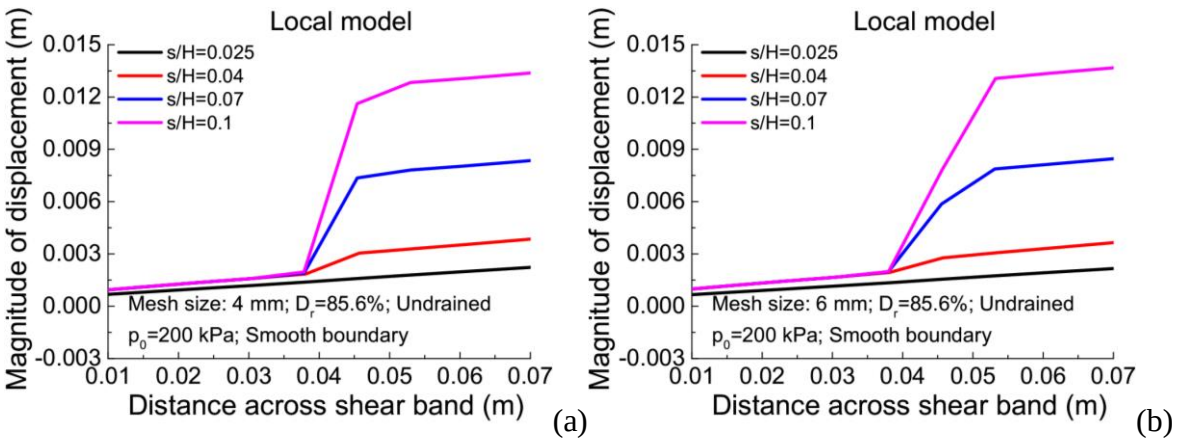

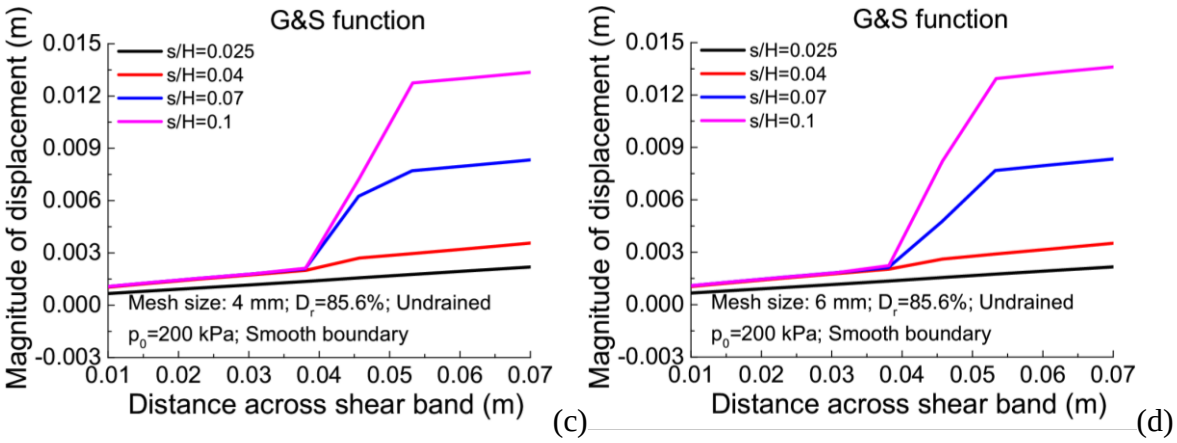

Figure 6.27 Cross-sectional profiles of the magnitude of the displacement from local and nonlocal models: (a) Local (0.004 m); (b) Local (0.006 m); (c) G&S function (0.004 m); (d) G&S function (0.006 m)

(2) Void ratio e

Figure 6.28 compares the cross-sectional contours of the e for the local and nonlocal models under undrained conditions. The local model shows that the width of e concentration predicted by the local model is sensitive to the mesh size. Conversely, the contours of the e from the nonlocal model depict almost similar widths. The maximum void ratio under the undrained condition is smaller than the drained condition (Figure 6.29). For example, when the mesh size ($h = 0.004\ m$) and vertical displacement ($s/H = 7\%$) are the same, the peak value of the e under drained conditions is around 0.85, whereas under undrained conditions, the e noticeably decreases, with a peak value of 0.71. The primary reason for this is the direct influence of pore water pressure, which hinders the development of the shear band. Furthermore, the concentration of volumetric expansion inside the shear band under rough boundary conditions is larger than that under smooth boundary conditions in the local model. Interestingly, this result is reversed in the nonlocal model.

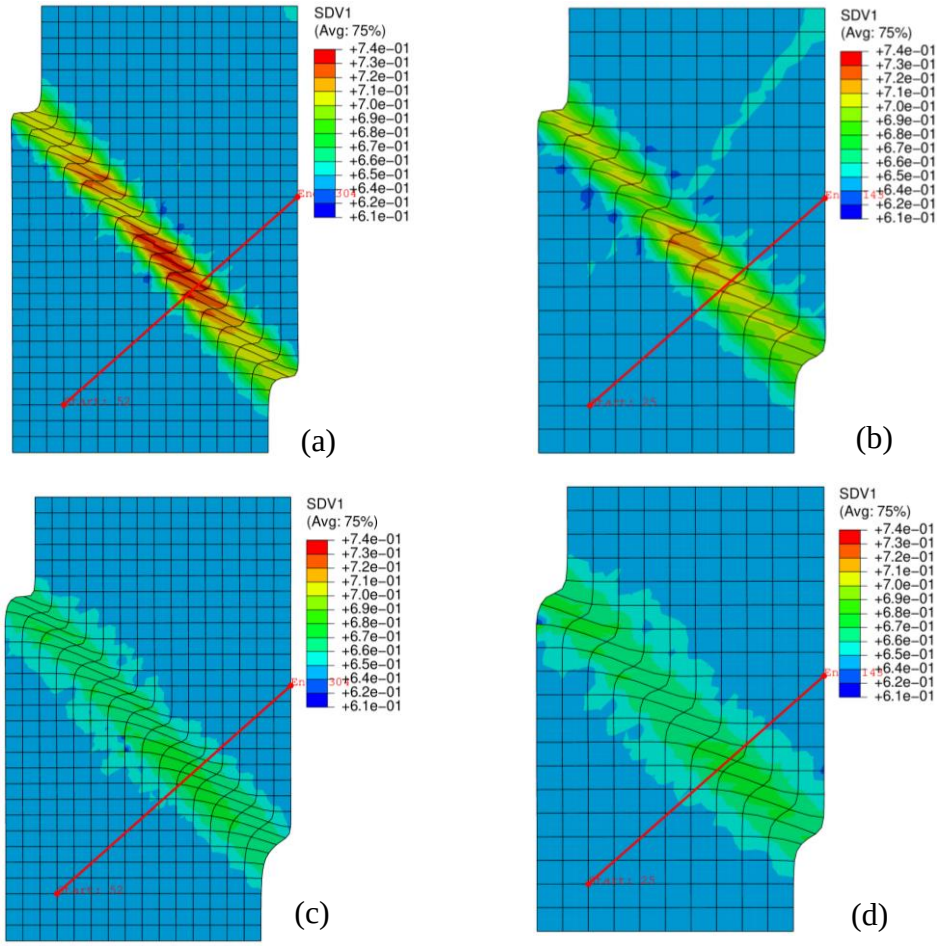

Figure 6.28 Contours of the void ratio e from local and nonlocal models: (a) Local (0.004 m); (b) Local (0.006 m); (c) G&S function (0.004 m); (d) G&S function (0.006 m)

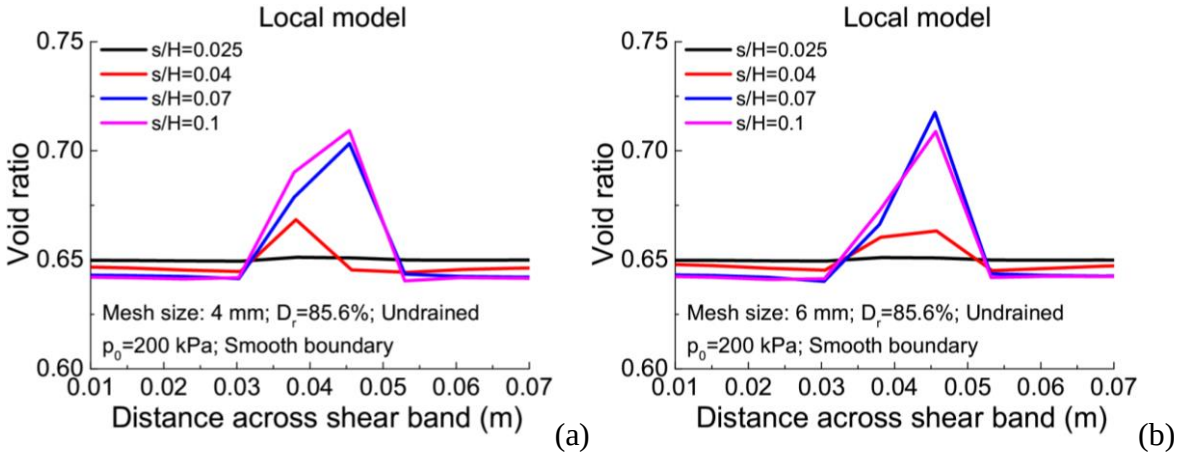

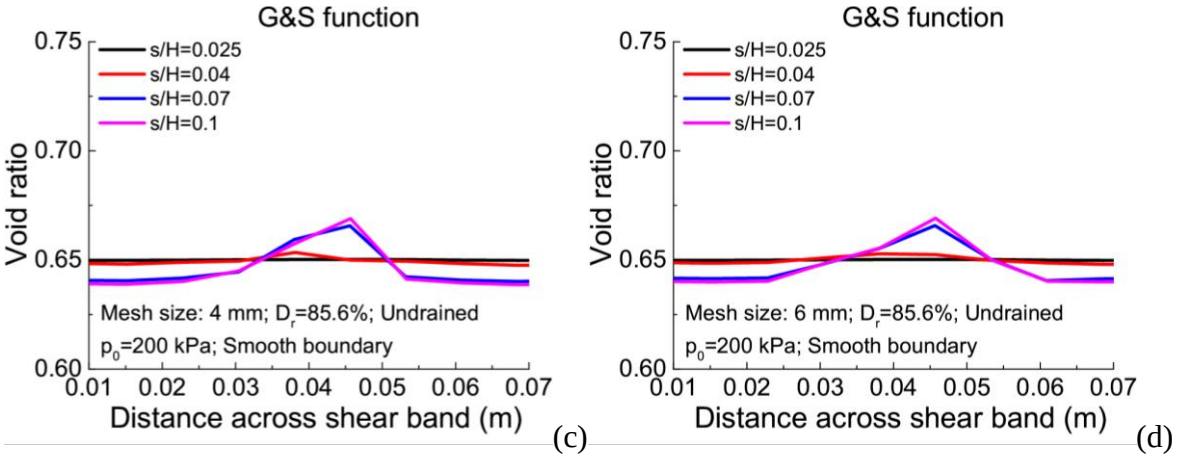

Figure 6.29 Cross-sectional profiles of void ratio e from local and nonlocal models: (a) Local (0.004 m); (b) Local (0.006 m); (c) G&S function (0.004 m); (d) G&S function (0.006 m)

6.4 Effect of Initial Density and Confining Pressure

6.4.1 Effect of Initial Density D_r

The initial density has a significant impact on strain localisation (Gao and Zhao, 2013; Liu, 2018; Mallikarachchi, 2019; Li and Gao, 2024). The influence of initial density on the nonlocal method under both smooth and rough boundary conditions is shown in Figure 6.28. Three different void ratios $e = 0.65$ ($D_r = 85.6\%$), $e = 0.70$ ($D_r = 73.6\%$) and $e = 0.75$ ($D_r = 60.5\%$) for Toyoura sand under different mesh sizes are considered.

Figure 6.30 illustrates that the peak value of the R_v decreases as the e becomes higher for both local and nonlocal methods. In contrast, the stiffness of sand increases for a lower e and finer mesh size.

In the local model, the mesh-dependency issue is obvious during the strain softening. Conversely, in the nonlocal model, there is a noticeable improvement in the mesh-dependency issue. However, the nonlocal method cannot eliminate the mesh-dependency issue completely. In nonlocal predictions, the difference between fine and coarse mesh sizes under rough boundary conditions is larger than the result under smooth boundary conditions. Meanwhile, the ability of the nonlocal method to reduce the mesh-dependency issue is influenced by the initial density. As shown in Figure 6.30 (b) and (d), when $e = 0.75$, the

consistency among models with different mesh sizes is notably better than in models with other two initial densities. The effectiveness of the nonlocal method becomes more pronounced with a higher e.

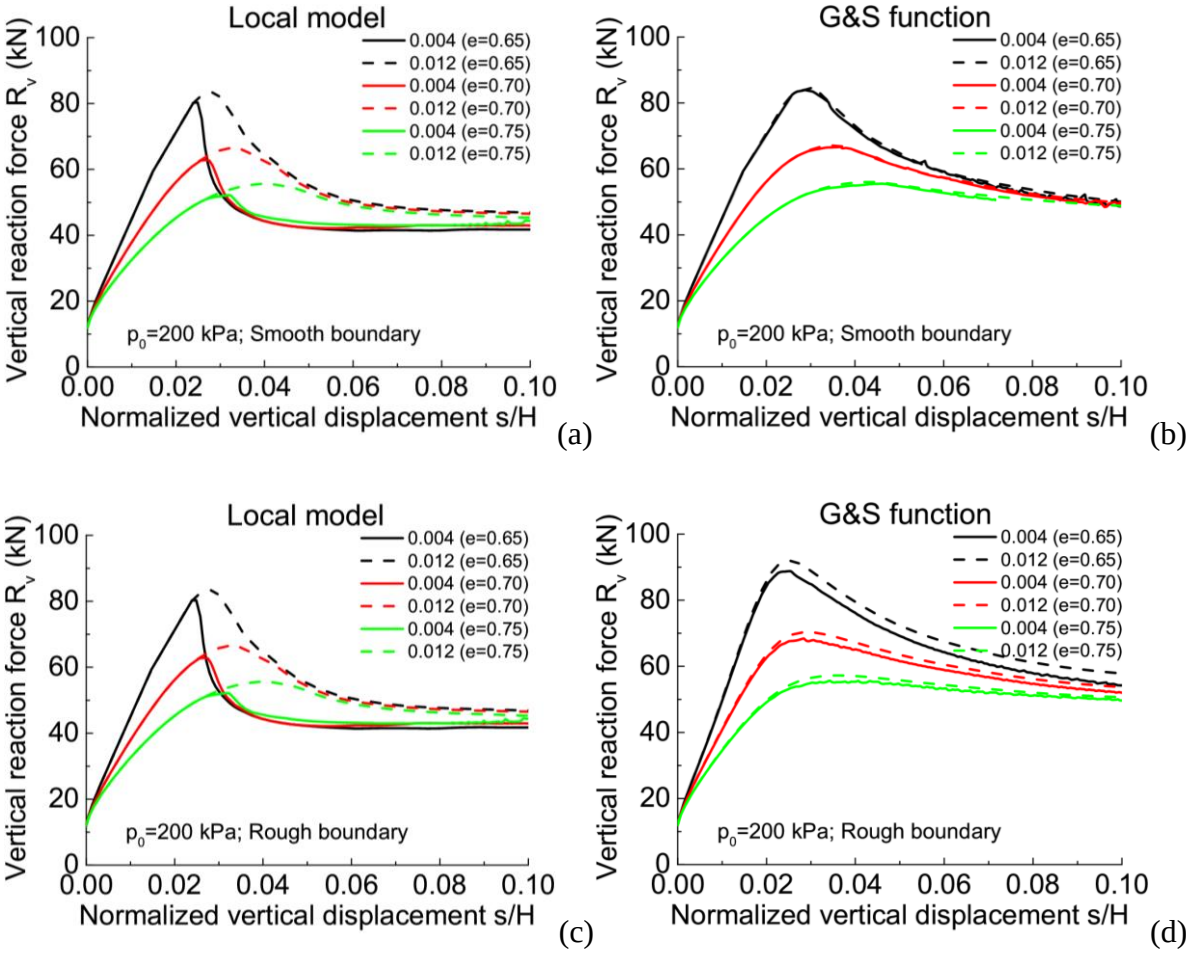

Figure 6.30 The influence of initial density on the nonlocal methods based on the load-displacement curve

According to the local model (Figure 6.31a and c), when $e = 0.65$, the shear band thickness of the coarse mesh is nearly double that of the fine mesh, and t_s increases with the e (Figure 6.33). The difference in shear band thickness between the coarse and fine mesh sizes decreases as the e becomes higher. In contrast, the shea band orientation β decreases with e.When $e = 0.65$ and $h = 0.004\ m$ (Figure 6.31a), the shear strain inside the shear band is significantly greater than the shear strain in other predictions, and the differences between coarse and fine mesh sizes decrease as the e increases. For instance, under rough boundary

conditions (Figure 6.31c), the peak shear strain in the fine mesh size is more than three times that in the coarse mesh size when $e = 0.65$. When $e = 0.7$, the peak shear strain in the fine mesh size is approximately twice that in the coarse mesh size. At $e = 0.75$, the peak shear strain in the fine mesh size is almost equivalent to that in the coarse mesh size.

As for the nonlocal model (Figure 6.31b and d), the difference in t_s for different void ratios is smaller than in the local model. Meanwhile, the t_s of the nonlocal model is wider than that of the local model. In addition, the differences in shear strain within the shear band between the different mesh sizes are smaller than those in the local model, and these differences increase as the e becomes lower. Thus, the e has a significant impact on the nonlocal method.

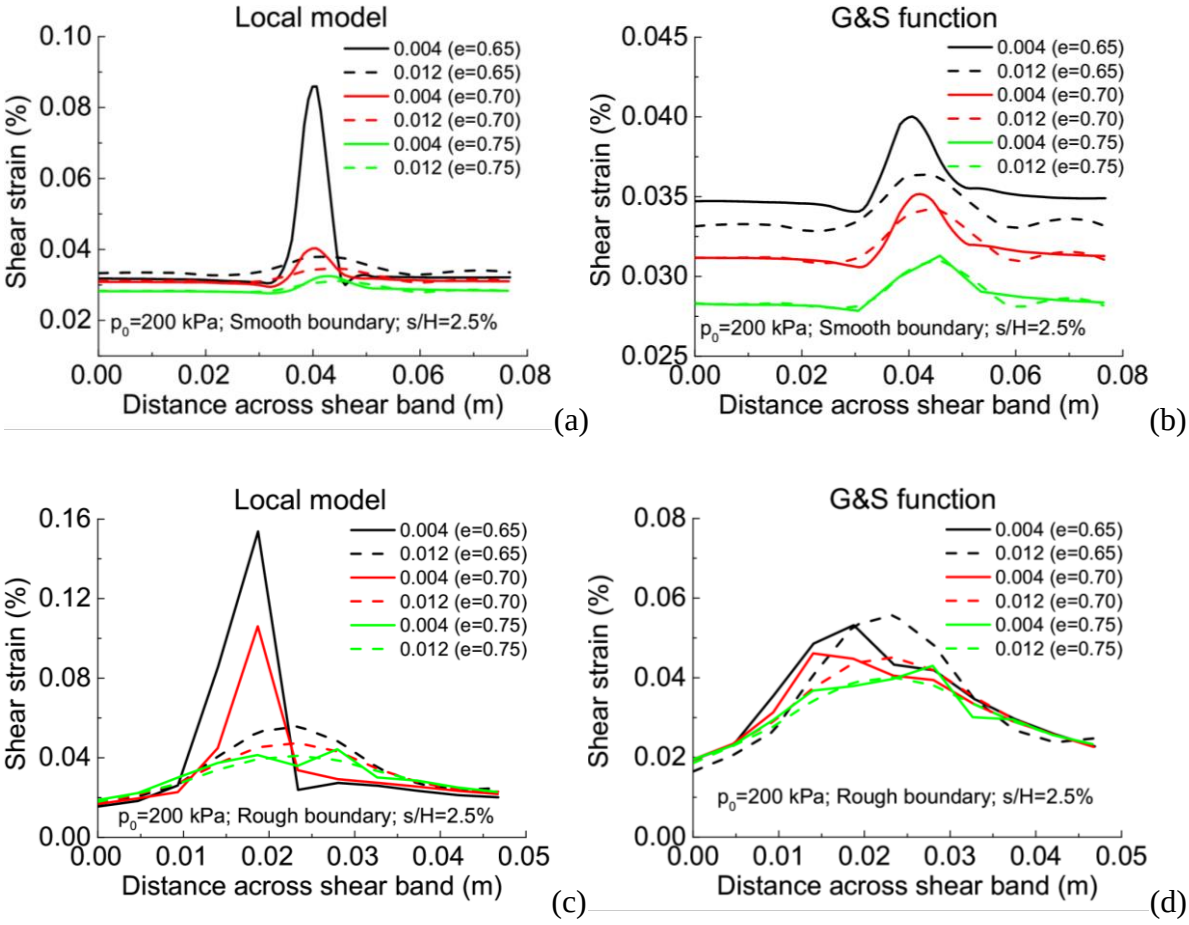

Figure 6.31 The influence of initial density on the nonlocal method based on the cross-section

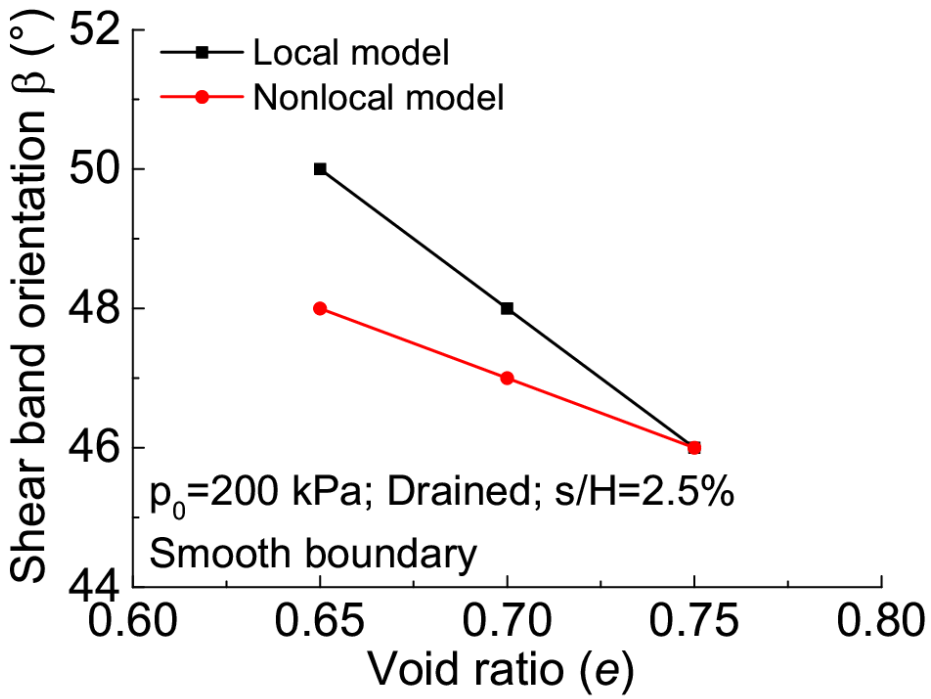

Figure 6.32 The relationship between void ratio (e) and shear band orientation β

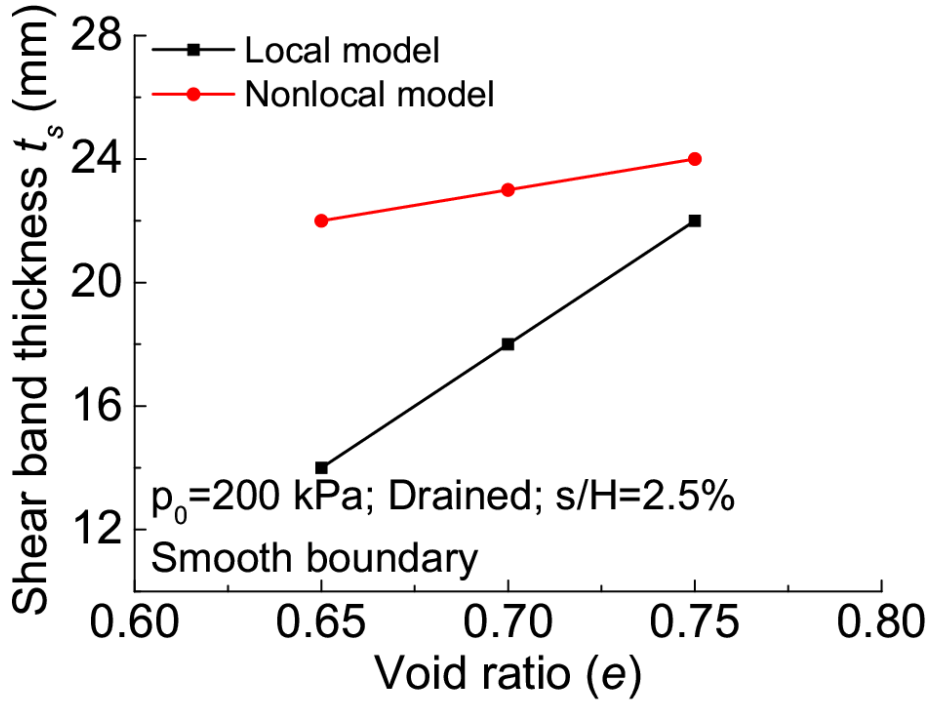

Figure 6.33 The relationship between void ratio (e) and shear band thickness t_s

6.4.2 Effect of Confining Pressure p_0

The influence of confining pressure on the load-displacement curve of the nonlocal model is shown in Figure 6.34. The different confining pressures ($p_0 = 100$ kPa, $p_0 = 150$ kPa and $p_0 = 200$ kPa) under both smooth and rough boundary conditions were considered.

Figure 6.34 shows that the confining pressure significantly affects the load-displacement curves. The vertical reaction force R_v and stiffness increases with confining pressure. This is similar to the findings of Han and Drescher (1993), Alshibli and Sture (2000), and Desrues and Viggiani (2004). A more mesh-independent result of the nonlocal method can be attained when the confining pressure becomes lower.

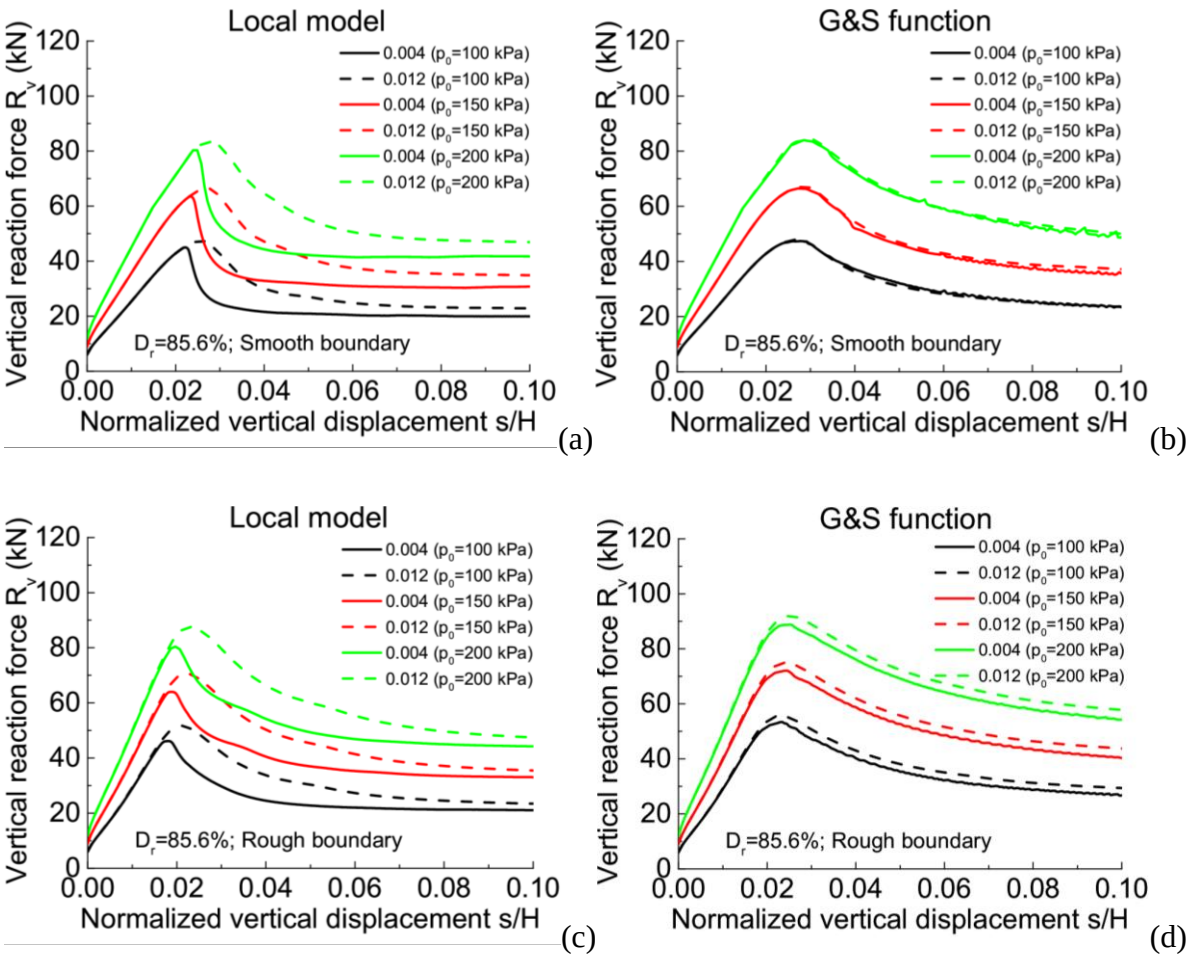

Figure 6.34 The influence of confining pressure on the nonlocal methods based on the load-displacement curve

Figure 6.35 shows that the confining pressure p_0 significantly affects the shear strain inside the shear band. The shear strain decreases with an increase in p_0. However, the reduction in shear strain for fine mesh size under smooth boundary conditions (Figure 6.35a) is more obvious than in rough boundary conditions (Figure 6.35c). Moreover, the shear strain inside the shear band varies significantly between different mesh sizes, especially in the local model. The shear strain for small mesh sizes is much greater than that for corresponding large mesh sizes under the same p_0. The differences between different mesh sizes are noticeably improved after being processed by the nonlocal method but do not eliminate them.

In addition, both β and t_s are decreased with p_0 (Figures 6.36 and 6.37). The difference in t_s between the local and nonlocal models is also shown in Figure 6.35. The t_s significantly differs from fine and coarse mesh for the local model. When the p_0 is constant, the t_s of models with small mesh sizes is smaller than that of models with large mesh sizes. Similar to the influence of initial density, the mesh-dependency issues of β and t_s in the nonlocal method, obtained from cross-sections, are significantly improved.

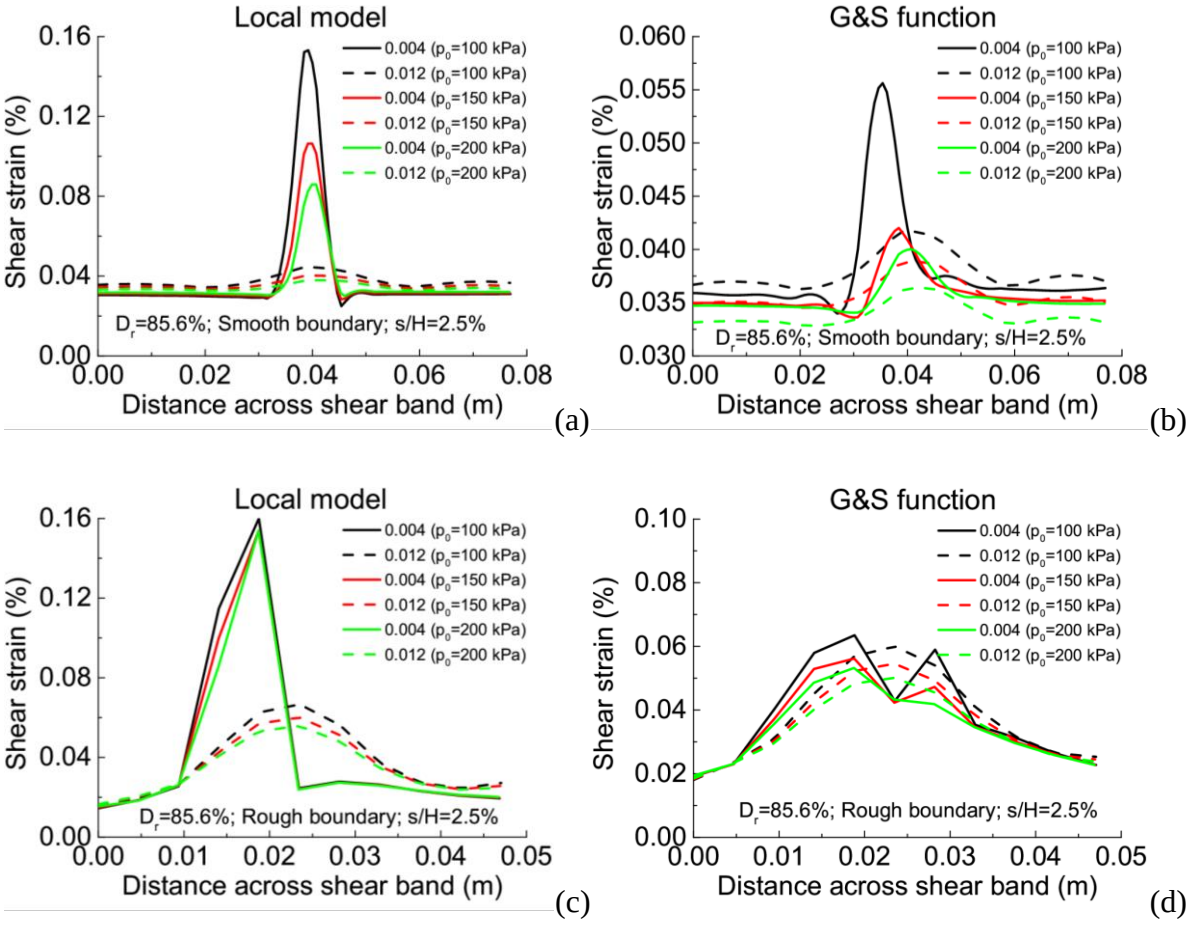

Figure 6.35 The influence of initial density on the nonlocal method based on the cross-section

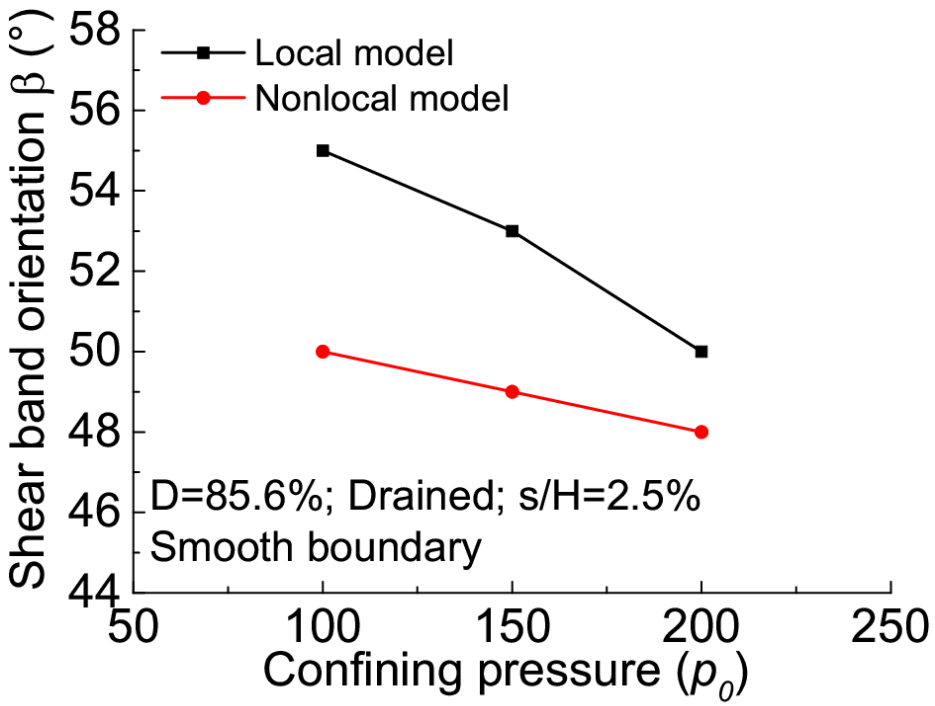

Figure 6.36 The relationship between confining pressure p_0 and shear band orientation β

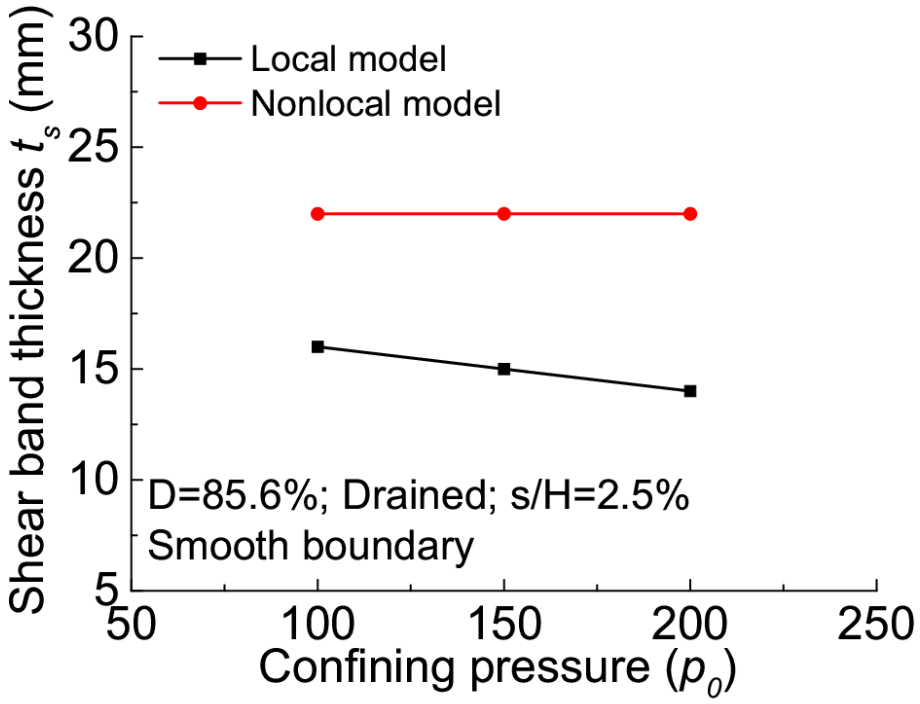

Figure 6.37 The relationship between confining pressure p_0 and shear band thickness t_s

6.5 Scaling of nonlocal method

The above biaxial compression results illustrate the validity of the nonlocal method as a regularisation technique. However, for geotechnical engineering applications, the shear band thickness is minimal compared to the dimension of geometry. The practical mesh size utilised in simulations is several orders of magnitude larger than the physical shear band thickness.

The physical shear band thickness of sand (t_s^{sand}) is found to be $10{-}20d_{50}$ (Muhlhaus and Vardoulakis, 1987). For Toyoura sand used in this thesis, $d_{50} \approx 0.0002\,m$ and $t_s^{sand} \approx 0.002 - 0.004\,m$. The numerical shear band thickness is determined by mesh properties such as size, shape, number of nodes and the internal length scale l_c (and over-nonlocal parameter m) used in nonlocal methods. Empirical correlations between numerical band thickness and the internal length scale l_c are found in some research (Brinkgreve, 1994; Galavi and Schweiger, 2010; Vermeer and Marcher, 2000; Mallikarachchi and Soga, 2020). Galavi and Schweiger (2010) reported that the numerical shear band thickness is the same as l_c. Mallikarachchi and Soga (2020) suggested that the numerical shear band thickness during softening can be approximately correlated as twice the l_c, whereas it is 2.2 times at the critical state. In this thesis, the numerical shear band thickness (t_s^{num}) is approximated as $2l_c = 0.024\,m$.

However, using the physical shear band thickness of sand in the FEM simulations can be a challenge. It is practically impossible to refine the mesh to comply with the real shear band thickness. First, small mesh size causes numerical convenience issues for advanced soil models which give a highly nonlinear stress–strain relationship. Secondly, the computational time will be significantly increased when a small mesh size is used for a nonlocal model (Gao et al., 2020).

Therefore, it is necessary to obtain a physically realistic force-displacement response by scaling the nonlocal method in some cases. Some studies have combined nonlocal regularisation with softening scaling to obtain physically realistic force-displacement curves (Brinkgreve, 1994; Vermeer and Marcher, 2000; Galavi and Schweiger, 2010; Mallikarachchi and Soga, 2020). Initially, Brinkgreve (1994) proposed to employ the softening scaling along with the nonlocal regularisation by Equation 6.1.

$$h^{num} = h^{sand} \frac{t_s^{num}}{t_s^{sand}} \tag{6.1}$$

where, h^{num} is the numerical softening stiffness; h^{sand} is the physical softening stiffness, t_s^{sand} is the physical shear band thickness of sand and t_s^{num} is the numerical shear band thickness. The scaling factor is defined as the ratio between the numerical shear band thickness t_s^{num} to physical band thickness t_s^{sand}. The rate of softening is dependent on the softening modulus and shear band thickness. The physical softening stiffness h^{sand} multiplied by this scaling factor bestows a realistic post-peak softening in the load-displacement response.

However, Mallikarachchi and Soga (2020) indicated that the application of Equation 6.1 is not suitable for the Nor-sand model since the softening modulus is not constant. The softening stiffness in the Nor-sand model is governed by the state parameter and, hence, the volumetric strain. Therefore, they used Equation 6.2 to scale the softening rate. Similarly, in this thesis, Equation 6.2 is also applicable. The scaling factor of softening stiffness is calculated to be $\frac{t^{sb,num}}{t^{sb,sand}} = 8$ when $l_c = 0.012$ m.

$$e = e - (1 + e) d\varepsilon_{vn} \frac{t_s^{num}}{t_s^{sand}} \tag{6.2}$$

According to Figure 6.38, in the anisotropic fabric model used in this thesis, the scaling reduces the R_{pv} in the load-displacement curve. It is opposite to the results predicted by the nonlocal NS model (Mallikarachchi and Soga, 2020) and the nonlocal HS model (Vermeer and Marcher, 2000). Moreover, as illustrated in Figure 6.38 (b), the difference becomes larger at the residual stage. This is because the volumetric regularisation is ineffective at the critical state. Additionally, the gradient of strain-softening for scaling result is larger than the simulation without scaling.

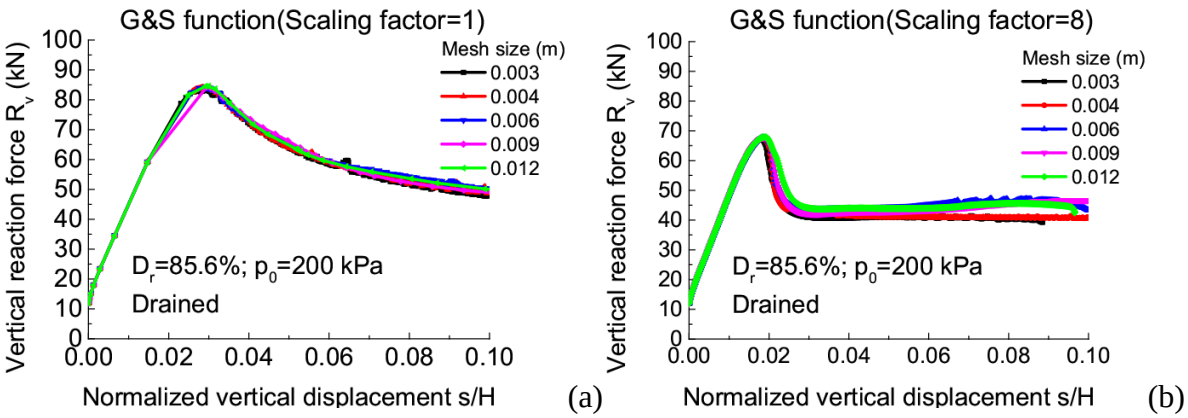

Figure 6.38 Load-displacement curve of G&S weight function (a) Without scaling (b) Scaling by 8

It is important to note that scaling is a mathematical artefact and not an inherent characteristic of the nonlocal method. It can be employed with other regularisation techniques or even without regularisation. For example, Pietruszczak and Mroz (1981) first used this simple strategy to produce reasonably objective load–displacement curves without any regularisation. It should be acknowledged that the nonlocal averaging and scaling do not create a realistic shear band thickness or its direction (Mallikarachchi, 2019).

6.6 Effect of anisotropy on strain localisation

The impact of anisotropy on strain localisation is being studied through a plane strain compression test conducted under drained conditions with smooth boundaries. Three different bedding plane orientations ($\alpha = 15^\circ$; $\alpha = 30^\circ$; $\alpha = 45^\circ$) are being considered and compared within both local and nonlocal models. Additionally, the influence of negative bedding plane orientations is also examined.

6.6.1 Force-displacement relationship

Figure 6.39 depicts the force-displacement relationship of the local model with various bedding plane orientations. The mesh dependency issue of the local model is not affected by the bedding plane orientation. However, the peak vertical reaction force decreases as the

bedding plane orientation increases. Conversely, the vertical displacement corresponding to the peak value increases with the increase in bedding plane orientation. Furthermore, when the bedding plane orientations are significant ($\alpha = 45^\circ$), models with small mesh sizes struggle to converge.

For the nonlocal model (Figure 6.40), only the peak vertical reaction force decreases as the bedding plane orientation increases. Simultaneously, for models with different bedding plane orientations, the vertical displacement corresponding to the peak value remains constant at $s/H = 2.8\%$.

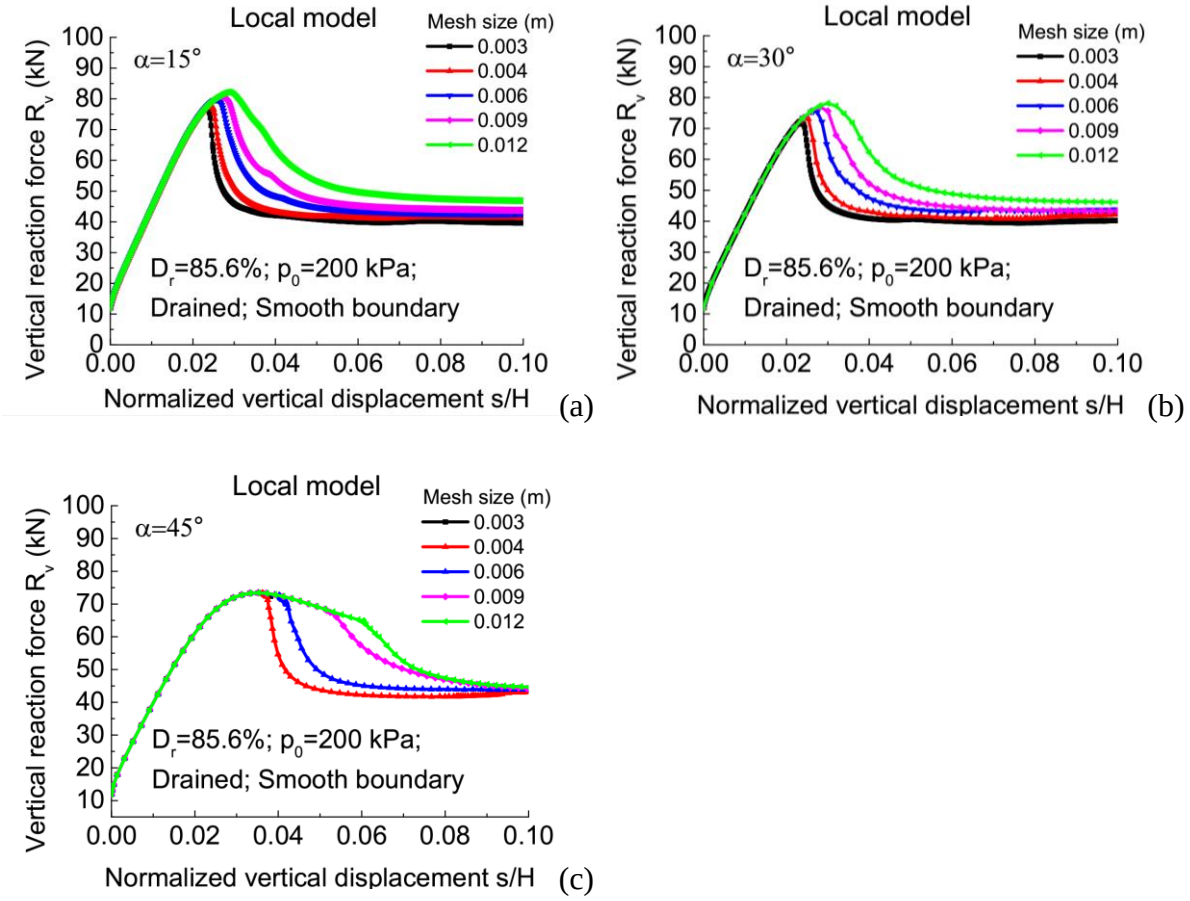

Figure 6.39 Force-displacement relationship of the local model with various bedding plane orientations: (a) $\alpha = 15^\circ$; (b) $\alpha = 30^\circ$; (c) $\alpha = 45^\circ$

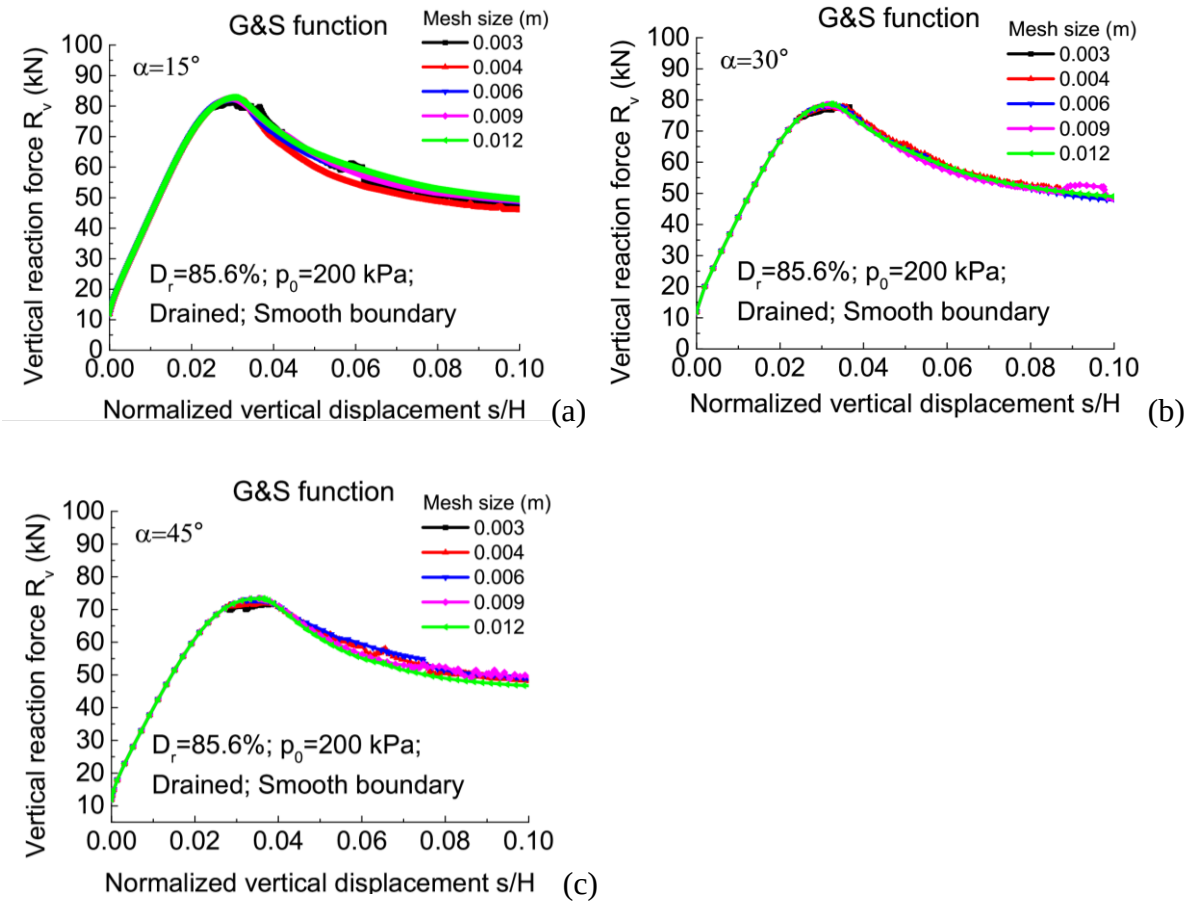

Figure 6.40 Force-displacement relationship of the nonlocal model with various bedding plane orientations: (a) $\alpha = 15^\circ$; (b) $\alpha = 30^\circ$; (c) $\alpha = 45^\circ$

6.6.2 Evolution of the shear band from selected elements

According to Figure 6.41, two elements have been chosen to explore the influence of different bedding plane orientations on the development of the anisotropic variable A and the degree of anisotropy F. Both elements are situated within the shear band, where Element A represents the fine mesh (0.004 m) and Element C represents the coarse mesh (0.006 m).

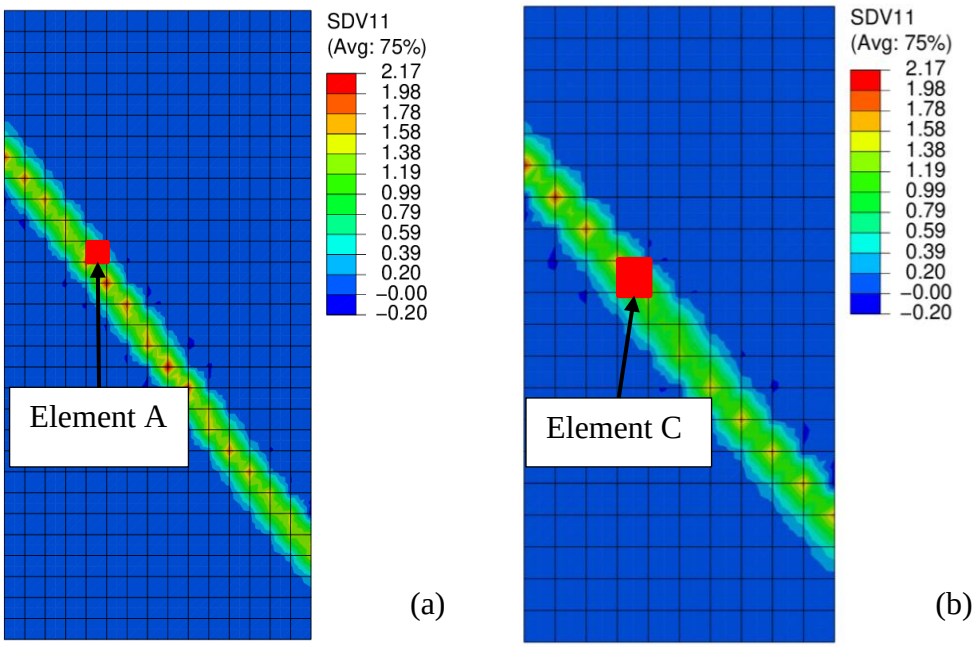

Figure 6.41 Location of the selected elements for the single shear band: (a) Fine mesh, (b) Coarse mesh

(1) Anisotropic variable A

The initial value of the Anisotropic variable A decreases with an increase in bedding plane orientation (Figure 6.42), aligning with the findings of Gao et al. (2021). However, in the local model with a mesh size of 0.006 m (Figure 6.42c), models with different bedding plane orientations exhibit the same initial value of A. This indicates a pronounced mesh dependency in the local model, where simulation outcomes become more reliable as the mesh size decreases. In contrast, the nonlocal model mitigates the mesh dependency issue and provides more reliable results, particularly with larger mesh sizes. Moreover, in the local model, when $\alpha = 45°$, the value of A gradually surpasses that of other models as the loading progresses, which contradicts the observed facts.

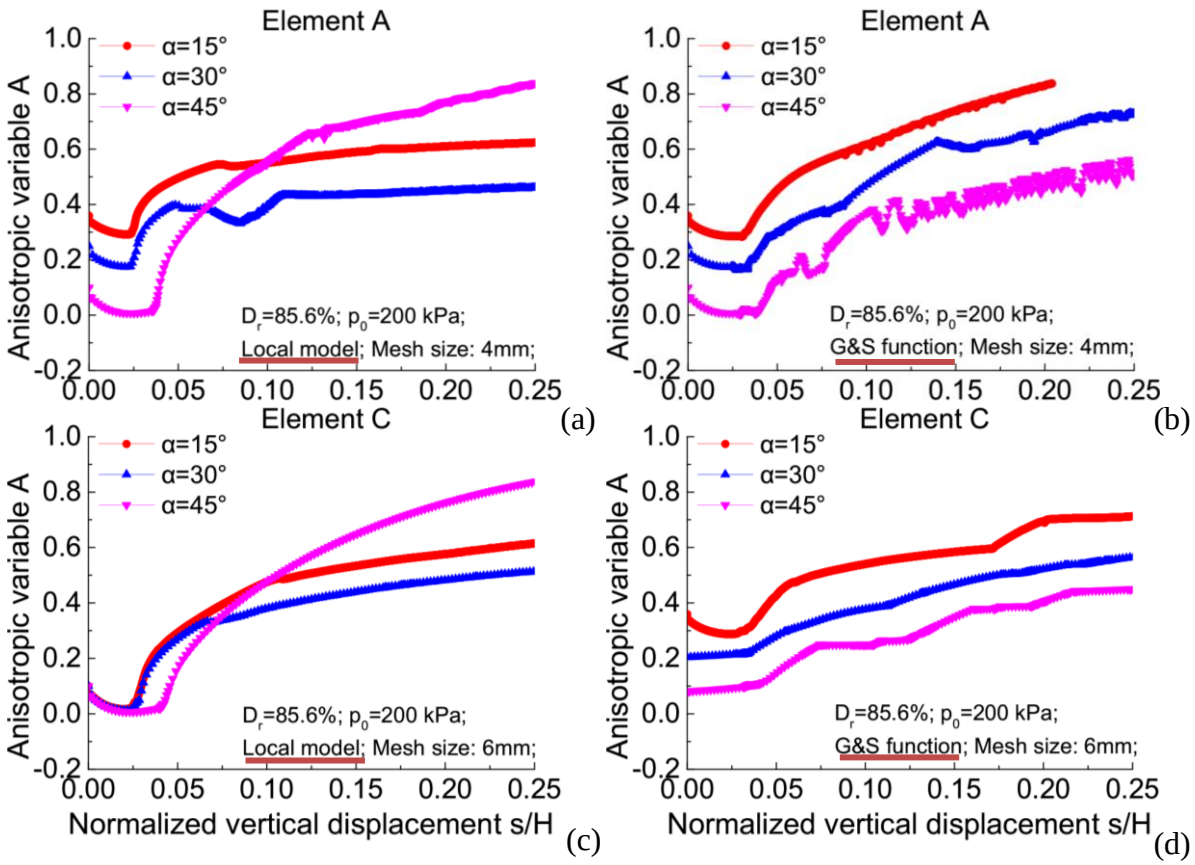

Figure 6.42 The local evolution of Anisotropic variable A for the elements inside the shear band with various bedding plane orientations

(2) Local fabric evolution F

In the local model (Figures 6.43a and c), when the bedding plane orientation is set to 45 degrees, the slope of F is greater than in models with other bedding plane orientations. Conversely, in the nonlocal model (Figures 6.43b and d), the F increases as α decreases, akin to the findings in Gao et al. (2021).

Moreover, the local model demonstrates a mesh dependency issue. In the local model with fine mesh size (Figure 6.43a), when $\alpha = 45°$, the F decreases first and then increases. However, when $\alpha = 15°$ and 30°, the F first increases slowly, and then the gradient of the increase becomes larger. In the local model with coarse mesh size (Figure 6.43c), the F for three different bedding plane orientations all gradually decreases first and then increases. On the contrary, after nonlocal regularisation, whether it is the result of a fine mesh size (Figure 6.43b) or a coarse mesh size (Figure 6.43d), when $\alpha = 45°$, the F first decreases slowly and

then increases. When $\alpha = 15°$ and 30°, in both cases, there is a slow increase followed by a rapid increase in the F.

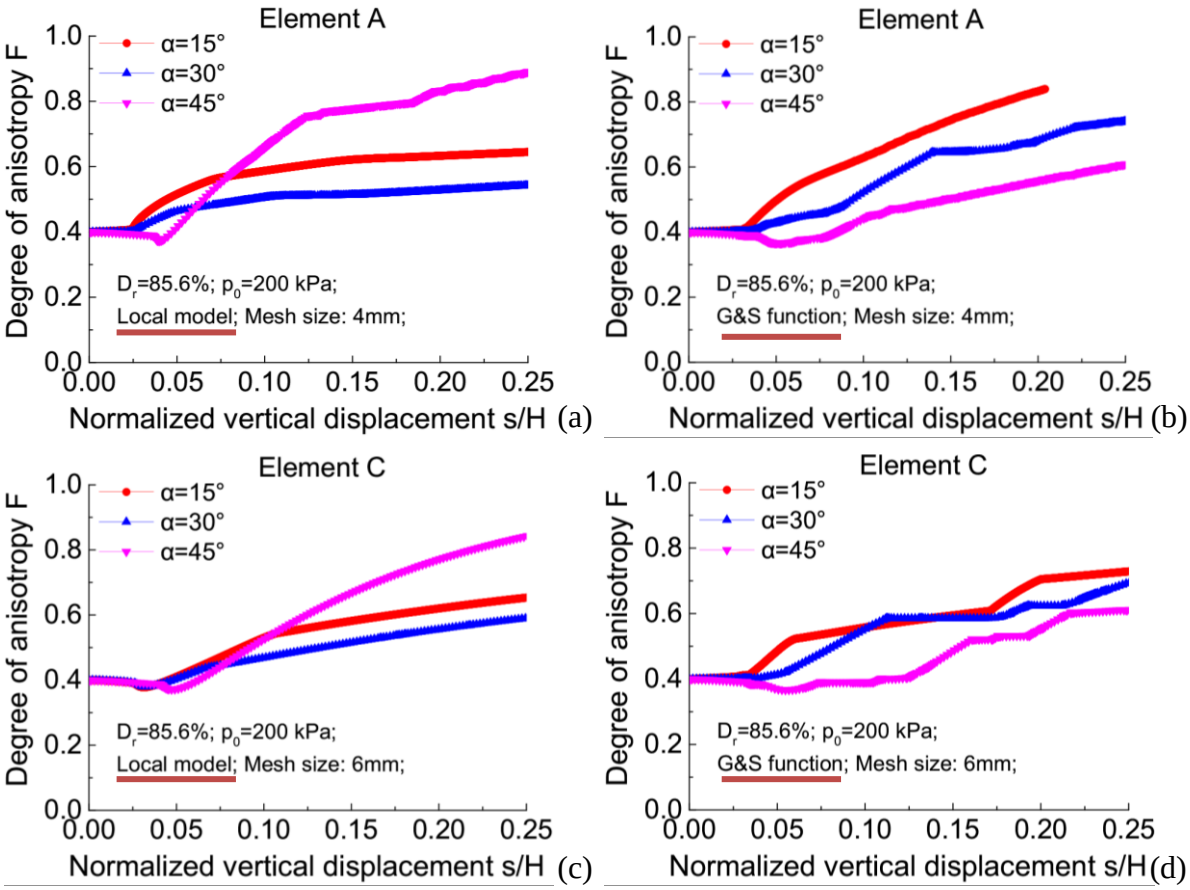

Figure 6.43 The local evolution of fabric for the elements inside the shear band with various bedding plane orientations

6.6.3 Effect of negative bedding plane orientation

The simulations conducted previously utilised positive α (major principal stress direction tilting right to the vertical). However, real bedding plane orientations can also be negative α. The outcomes with negative α may be different when the bedding plane is not vertical. To illustrate this, Figure 6.44 presents further simulations depicting the force-displacement relationship of both local and nonlocal models with a negative bedding plane orientation of $\alpha = -30°$. The initial slope of the force-displacement curve remains similar for both positive and negative α cases. However, there's a slower decrease of R_v with s/H after reaching the peak R_v in the case of negative α (as observed in Figure 6.39c and Figure 6.44a).

Figure 6.45 illustrates that the value of the peak reaction force R_{pv} increases with the mesh size. In the local model, the R_{pv} for negative bedding plane orientation is greater than the R_{pv} for positive bedding plane orientation. Conversely, in the nonlocal model, the situation is reversed. Moreover, when the mesh size remains constant, the disparity between the R_{pv} for positive and negative bedding plane orientations in the nonlocal model is significantly smaller than in the local model. Furthermore, these differences gradually diminish with an increase in mesh size.

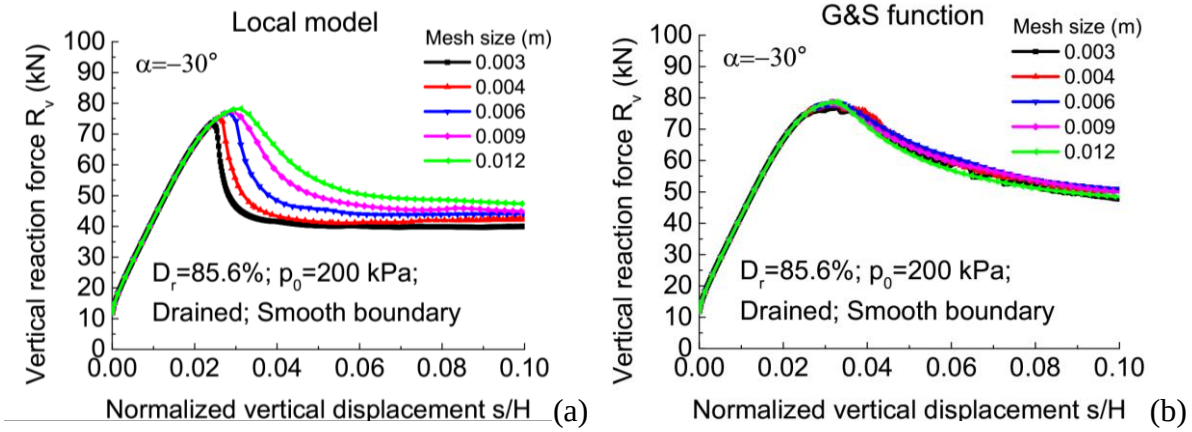

Figure 6.44 Comparison of the local and nonlocal models on the force-displacement relationship with negative bedding plane orientation: (a) Local model; (b) G&S function

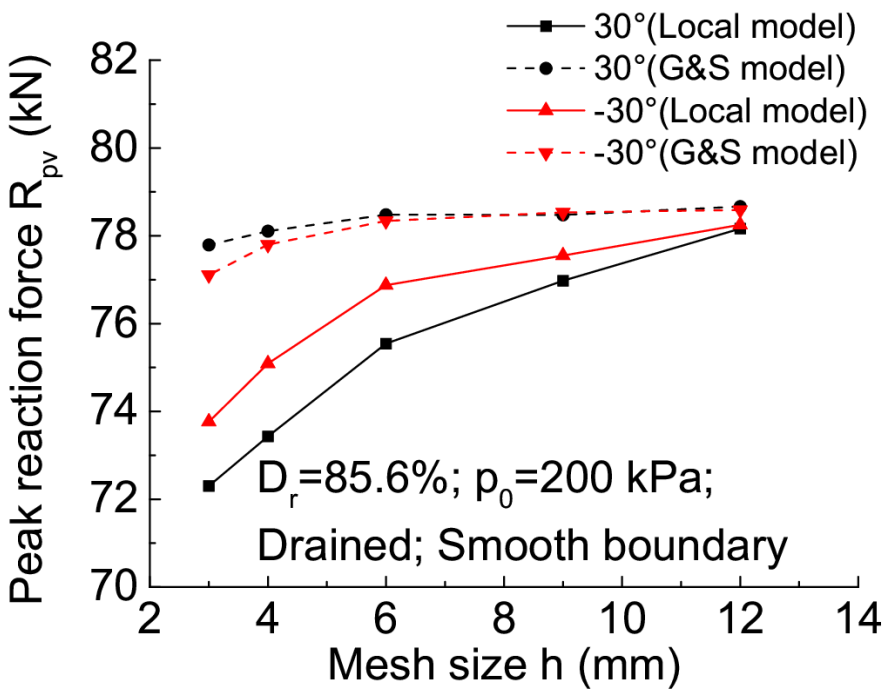

Figure 6.45 Comparison of the local and nonlocal models on the peak reaction force R_{pv} with positive and negative bedding plane orientations

6.7 Extension of the nonlocal model from 2D to 3D

The aforementioned research based on the nonlocal method focuses chiefly on two-dimensional problems. However, most actual engineering structures belong to the three-dimensional domain. Extension of the current two-dimensional nonlocal model to make it three-dimensional is needed. An advanced constitutive model for sand with the notion of a critical state has never been generalised from 2D to 3D by the nonlocal method. To validate the correctness of the 3D nonlocal method, a series of test simulations, including biaxial drained and undrained tests for dense sand, are considered.

6.7.1 Nonlocal regulisation of 3D biaxial drained test

The dimension of the sample used in the 3D study is the same as the 2D plane strain problem, which is 60 mm wide and 120 mm high with a thickness of 0.01 m. The rough boundary conditions is only considered in the study because, under smooth boundary conditions, the

shear bands are less likely to form, making it challenging to justify the improvement of the nonlocal method in addressing mesh dependency issues related to shear band thickness. The bottom side is constrained in X, Y, and Z directions, and the other sides are only fixed in the Z direction. A confining pressure of $p_0 = 200$kPa is applied on the two vertical sides, and the vertical displacement is applied on the top side. Furthermore, the bedding plane orientation is horizontal and $\alpha = 0°$. The initial void ratio of the sample is $e_0 = 0.65$ (relative density $D_r = 85.6\%$), and the initial degree of anisotropy is $F_0 = 0.4$. All simulations in this study have used 8-noded plane strain liner elements with 8 integration points (C3D8).

The shear strain contours at the strain softening for the local and nonlocal model (G&S distribution weight function) at displacement $s/H = 9\%$ were shown in Figures 6.46-6.47, where SDV11 represents the total shear strain. The shear band can be distinguished by the concentrated plastic deformation. Figure 6.46 shows that the width of the shear strain zone predicted by the local model is sensitive to the mesh size. On the contrary, contour plots of total shear strain from G&S nonlocal methods in Figure 6.47 portray almost similar shear strain zones irrespective of the mesh size during the strain softening period.

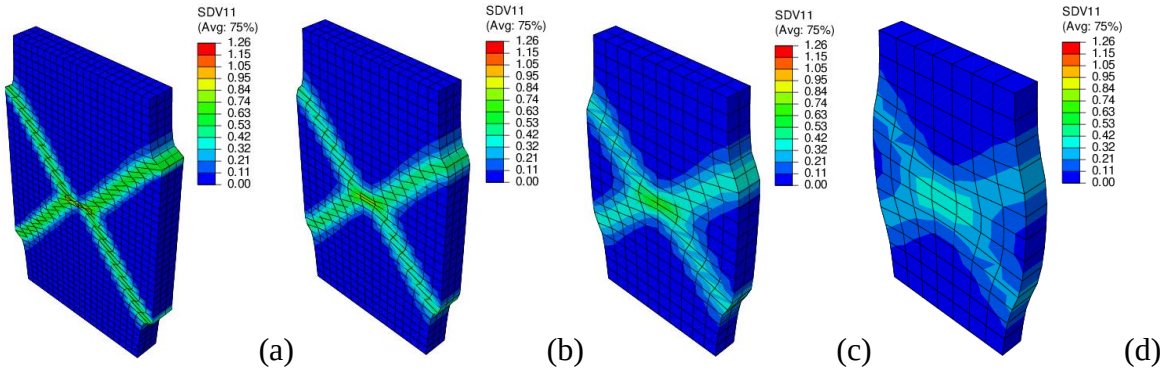

Figure 6.46 Shear strain contour for the local model under drained condition at $s/H = 9\%$ for different mesh size: (a) 0.003 m; (b) 0.004 m; (c) 0.006 m; (d) 0.009 m

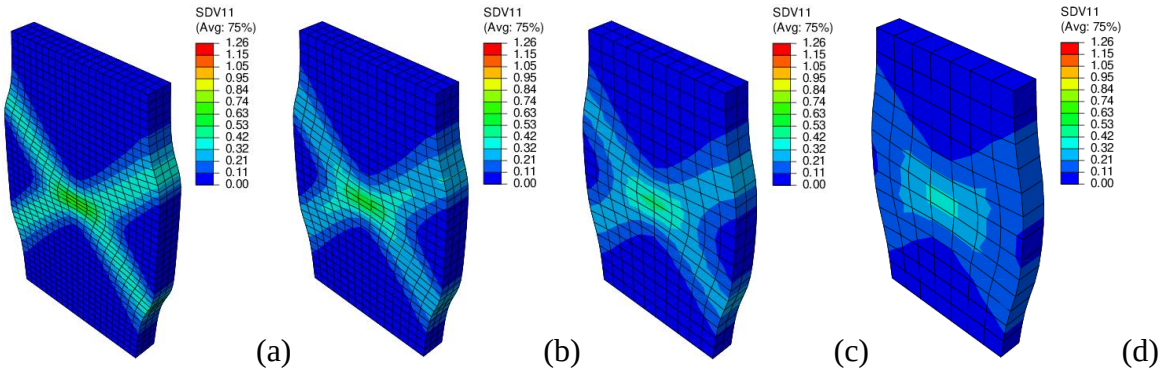

Figure 6.47 Shear strain contour for the nonlocal model under drained condition at $s/H = 9\%$ for different mesh size: (a) 0.003 m; (b) 0.004 m; (c) 0.006 m; (d) 0.009 m

Figure 6.48 shows the force-displacement curves predicted by the local model and nonlocal model for drained dense sand with different mesh sizes. The strain-hardening part of the global force–displacement relationships for both local and nonlocal models is insensitive to the mesh size until the peak and becomes mesh-dependent in the strain-softening part. In the local model, a finer mesh size results in earlier and faster softening, which has the same results in 2D. On the contrary, the nonlocal method adequately produces force-displacement responses that are independent of the mesh, reducing the softening rate and difference in peak vertical reaction force. It facilitates the convergence of extra-small mesh by providing a positive-definite global stiffness matrix.

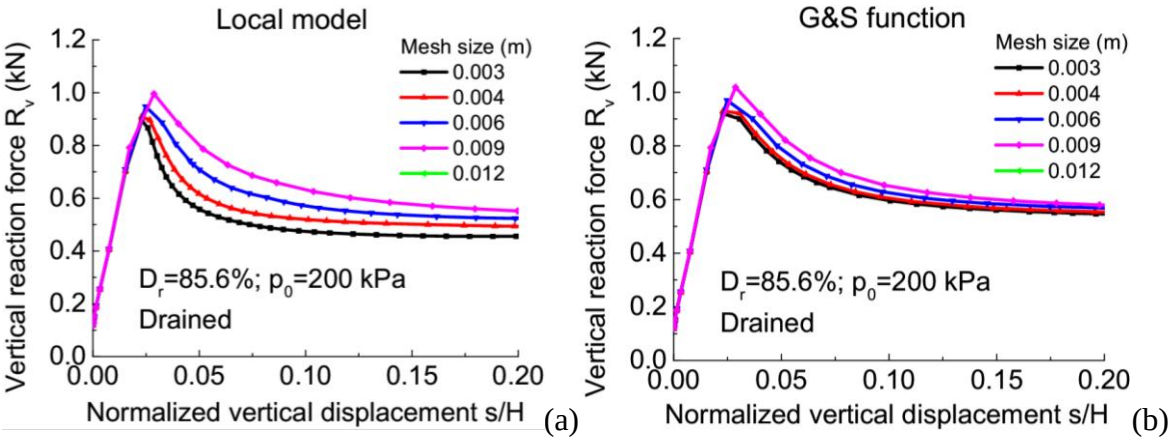

Figure 6.48 Comparison of the local and nonlocal models on the force-displacement relationship for 3D drained biaxial compression test under drained condition

Numerous experimental evidence indicates that when a shear band occurs, significant volumetric expansion will concentrate inside the shear band while the volumetric change is generally very small outside (see, e.g., Oda et al., 1982; Desrues et al., 1996). According to Figures 6.49 and 6.50, the nonlocal model predicts a wider shear band than the local model and the mesh dependency of shear band thickness is reduced by nonlocal regularisation. Moreover, since the evolution of e is assumed to depend on the volumetric strain increment of local and neighbouring integration points in the nonlocal model, the e inside the shear band is smaller than that predicted by the local model.

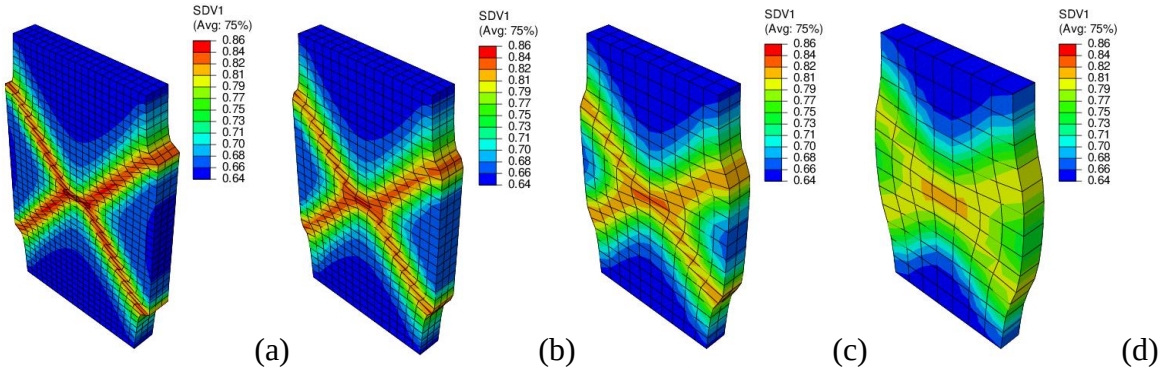

Figure 6.49 Void ratio e contour for the local model under drained condition at $s/H = 9\%$ for different mesh size: (a) 0.003 m; (b) 0.004 m; (c) 0.006 m; (d) 0.009 m

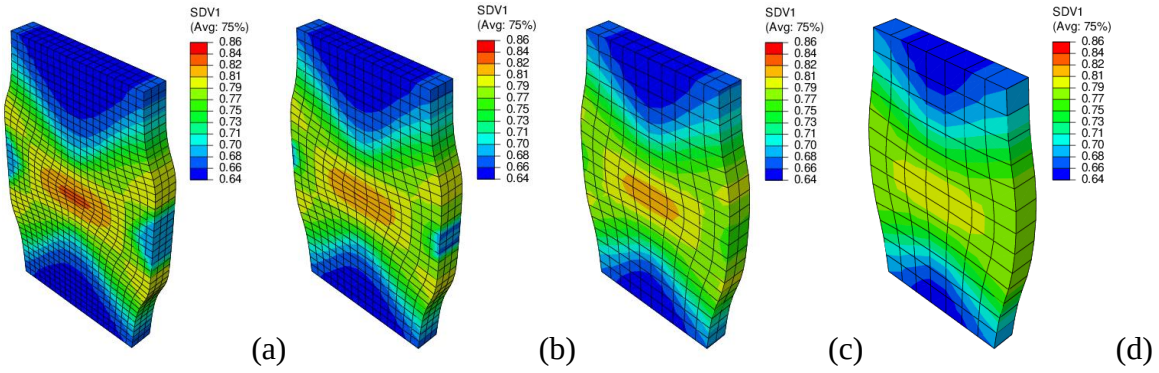

Figure 6.50 Void ratio e contour for the nonlocal model under drained condition at $s/H = 9\%$ for different mesh size: (a) 0.003 m; (b) 0.004 m; (c) 0.006 m; (d) 0.009 m

6.7.2 Nonlocal regularisation of 3D biaxial undrained test

In the 3D biaxial undrained test, the permeability of soil is set very small and water flow at all boundaries is closed. Transient consolidation analysis is selected for all simulations. The rest of the conditions are the same as the drained case.

The smaller shear band thickness observed under undrained conditions compared to the drained conditions is primarily attributed to the pore water pressure inhibiting the development of the shear band. Additionally, the shear strain within the shear band is also smaller under undrained conditions compared to the shear strain under drained conditions.

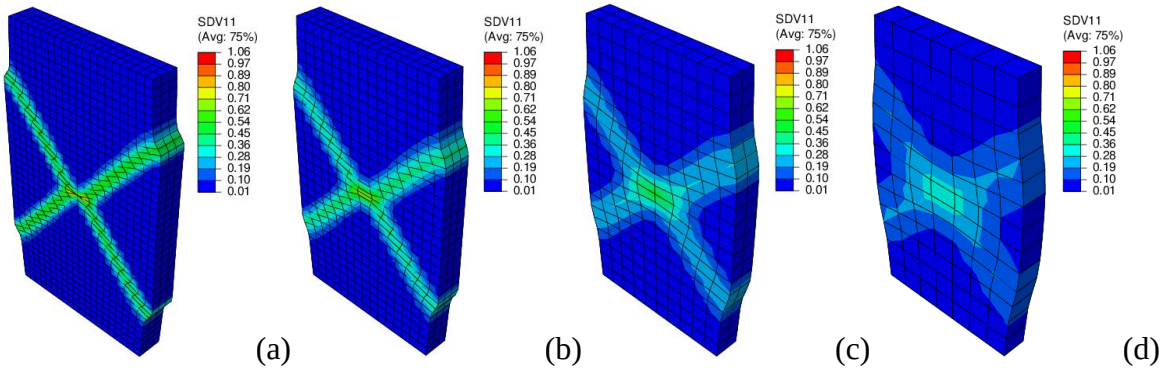

Figure 6.51 Shear strain contour for the local model under undrained condition at $s/H = 9\%$ for different mesh size: (a) 0.003 m; (b) 0.004 m; (c) 0.006 m; (d) 0.009 m;(e) 0.012 m

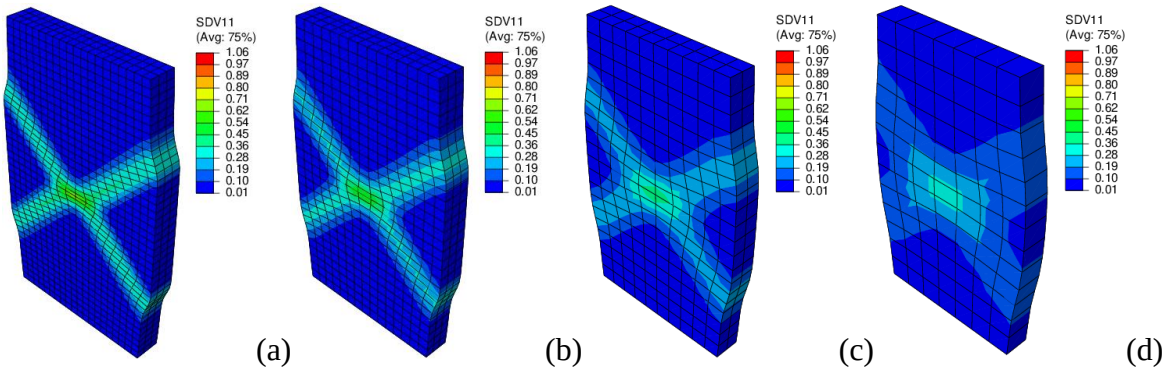

Figure 6.52 Shear strain contour for the nonlocal model under undrained condition at $s/H = 9\%$ for different mesh size: (a) 0.003 m; (b) 0.004 m; (c) 0.006 m; (d) 0.009 m

Figure 6.53 illustrates the correlation between vertical displacement and reaction force for various models under undrained conditions. In the strain-hardening region, there is no issue of mesh dependency. However, during the strain-softening region, the mesh sensitivity of force–displacement curves disappear after the nonlocal regularisation is applied.

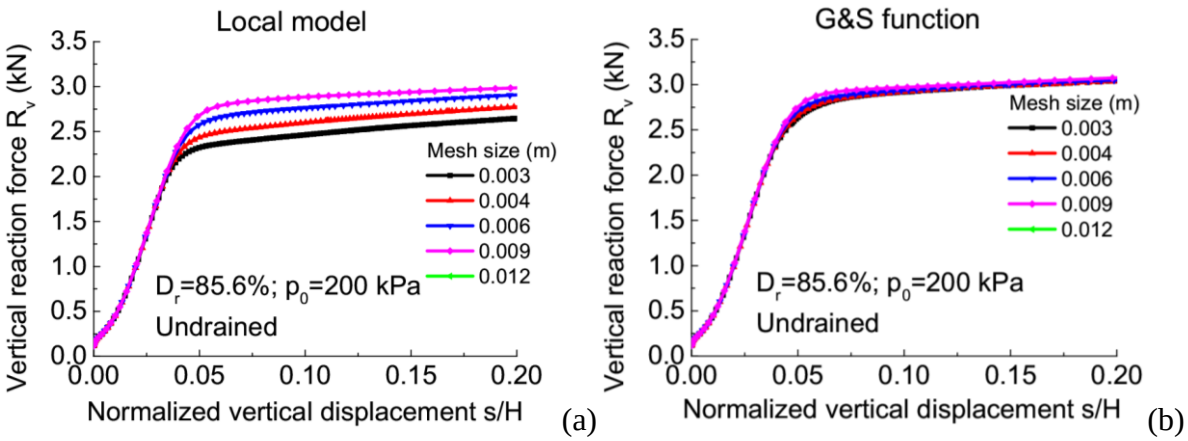

Figure 6.53 Comparison of the local and nonlocal models on the force-displacement relationship for 3D undrained biaxial compression test under undrained condition

In Figure 6.542 and Figure 6.55, the *e* contours for the local and nonlocal models are compared. The results from the local model indicate that the predicted shear band thickness is sensitive to the mesh size. In contrast, the *e* contours from the nonlocal model display nearly consistent shear band thickness, and the shear band is wider compared to the shear band in the local model. Furthermore, the *e* within the shear band under undrained analysis is lower than the *e* under drained analysis.

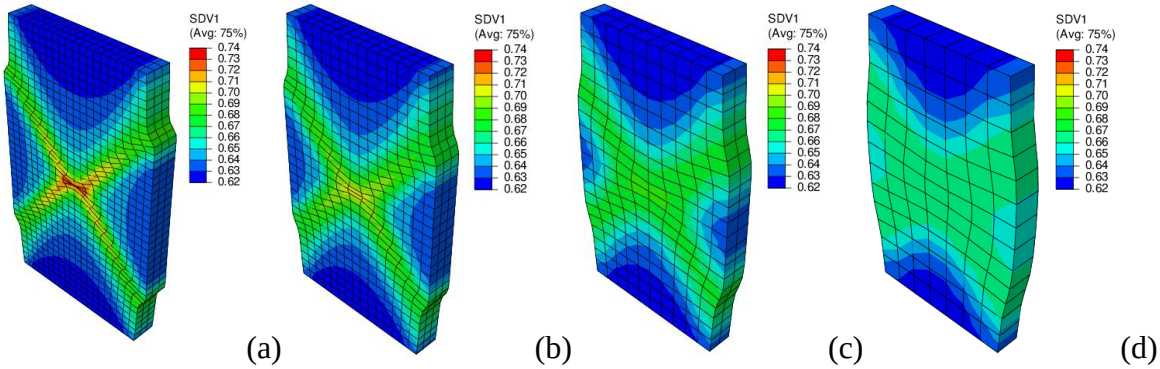

Figure 6.54 Void ratio e contour for the local model under undrained condition at $s/H =$ 9% for different mesh size: (a) 0.003 m; (b) 0.004 m; (c) 0.006 m; (d) 0.009 m

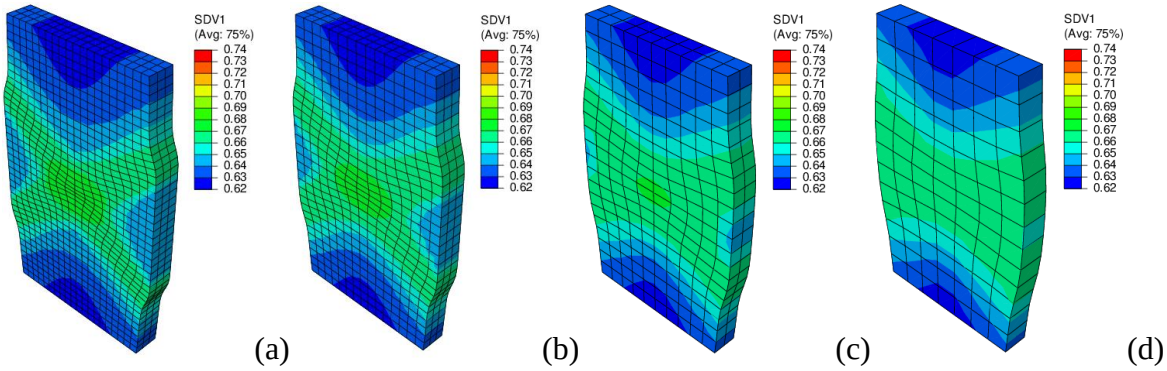

Figure 6.55 Void ratio e contour for the nonlocal model under drained condition at $s/H =$ 9% for different mesh size: (a) 0.003 m; (b) 0.004 m; (c) 0.006 m; (d) 0.009 m

6.8 Summary

The Chapter shows the validation of the nonlocal method in both drained and undrained plane strain compression tests under rough boundary conditions. Moreover, the evolution of state variables, the effect of initial density and confining pressure, and the effect of anisotropy on strain localisation of both local and nonlocal models under smooth boundary conditions were further compared.

(1) The force-displacement curves demonstrate that the nonlocal method can alleviate mesh dependency for both smooth and rough boundary conditions. The peak value of reaction force is reached at a lower vertical displacement under the rough boundary conditions.

(2) Similar to the smooth boundary condition, in the rough boundary conditions, the shear band orientation decreases with increasing mesh size, while the shear band thickness increases with mesh size. Notably, the local models exhibit a significant disparity in shear band orientation and thickness between coarse and fine meshes. In contrast, the nonlocal model, employing the G&S function, shows only minor variations.

(3) According to the evolution of state variables along the cross-section, the local model also exhibits a mesh-dependent width of state variables concentration. In contrast, the

nonlocal model displays only slight variations in the width of state variables concentration for different mesh sizes. For both smooth and rough boundary conditions, the results obtained from the G&S function indicate a significantly larger shear band thickness compared to the local model.

(4) After nonlocal regularisation, for the evolution of state variables in selected elements both inside and outside the shear band, not only does the fluctuation in the change of the state variables decrease, but the differences in peak values of the state variables between various mesh sizes observed in the local model are also significantly reduced. The values of the state variables within the shear band are significantly greater than those outside, primarily due to shear strain concentration. Regarding the impact of confining pressure and initial density on the nonlocal method, the effectiveness of reducing mesh dependency in the nonlocal method increases when the e is higher or when the confining pressure increases.

(5) The nonlocal method is unaffected by various positive bedding plane orientations. However, when considering negative bedding plane orientations, it does have an impact on the nonlocal method. In the local model, the peak reaction force for negative bedding plane orientation is greater than that for positive bedding plane orientation. Conversely, in the nonlocal model, the situation is reversed.

Chapter 7: Conclusions

Nonlocal regularisation is commonly employed to address the problem of mesh dependency arising from strain softening in finite element analysis. Nonlocal methods are developed based on the hypothesis that material response is influenced by both the deformation field of a local material point and a weighted average of its neighbouring points. This approach has primarily found application in soil models with simple strain-softening rules. In such cases, the models can be readily regularised by assuming that the strain-softening variable depends on the nonlocal plastic shear strain. However, sand exhibits strain softening influenced by several variables. Hence, the nonlocal regularisation of an anisotropic critical state sand model is presented in this thesis, and the void ratio in this model is assumed nonlocal.

The research presented in the thesis can be divided into four major parts.

In the first part (Chapter 3), the introduction and derivation of the anisotropic sand constitutive model used in this thesis were presented. Anisotropy refers to the different mechanical properties of materials in different directions. From the micro perspective, the anisotropic characteristics are due to the preferred orientation of particles and void and/or crack (Oda et al., 1985; Duveau et al., 1998; Li and Dafalias, 2012; Gao et al., 2013). The anisotropic sand model used in this thesis is developed based on the anisotropic critical state theory (Li and Dafalias, 2012). The main feature of the anisotropic critical state theory is that sand fabric at the critical state has a unique magnitude and is codirectional with the loading direction. The model to be used here was proposed by Gao et al. (2020).

In the second part (Chapter 4), three different nonlocal models were developed based on different weight functions: Gaussian (GD), Galavi and Schweiger (G&S), and over-nonlocal (ON) functions. The distributions of these weight functions were outlined. The GD function exhibited the highest contribution to the computed nonlocal variable at the centre. However, it led to the nonlocal variable being concentrated predominantly at the local point, hindering its spread to surrounding points and thereby reducing the effectiveness of the nonlocal method. The G&S and ON functions represented an improvement, dispersing the nonlocal variable away from the local point and forming two similar peaks near it. The ON function required the determination of an appropriate nonlocal parameter m, which significantly influenced this method.

In the third part (Chapter 5), a comprehensive comparison of three different weight functions was carried out by various BVPs, including drained and undrained plane strain compression tests, the strip footings problems on level ground and near a slope, and retaining wall problems under both passive and active conditions. The load-displacement curves, shear band thicknesses and shear band orientations predicted by different nonlocal models were compared, respectively.

In the final part of the work (Chapter 6), a more in-depth discussion and analysis of the G&S method were presented, since a comparison of three different nonlocal methods demonstrated that the G&S method is the most effective in mitigating mesh dependency issues. In this Chapter, plane strain compression tests with rough boundary conditions under both drained and undrained analysis are simulated. The efficiency of the G&S method is justified through force-displacement relationship curves and shear strain contours (shear band orientation and thickness). The effect of initial density and confining pressure on the nonlocal regularisation method is also discussed. Furthermore, the evolution of state variables within the shear band under smooth boundary conditions is investigated by cross-sections and selected elements (inside and outside the shear band). These state variables include void ratio e, anisotropic variable A, degree of anisotropy F and shear strain. The effect of anisotropy on strain localisation is investigated using soil samples with various bedding plane orientations (α=15°, α=30°, and α=45°). Finally, the performance of the nonlocal method under 3D loading conditions is presented.

The main conclusions of this thesis are summarised below.

7.1 Comparison of three weight functions in BVPs

In biaxial compression tests, the local and three diffident nonlocal models were compared under both drained and undrained conditions.

(1) The force-displacement curves show that G&S and ON functions display more insensitive results than GD under drained conditions. This is because the local value contributes most to the nonlocal variable for the GD method. As for the undrained case, there is no distinct difference between different nonlocal models.

(2) The orientation of shear bands increases with mesh size under both drained and

undrained conditions. The difference in shear band orientation due to mesh size is smaller under undrained conditions than drained conditions for both local and nonlocal analyses. Nonlocal methods help circumvent mesh dependency. Moreover, the G&S and ON functions demonstrate more consistent results than the GD function under both drained and undrained conditions.

(3) Based on the contour plots and the cross-section profiles, the local model exhibits mesh-dependent shear band thickness. In contrast, nonlocal models utilising the G&S and ON functions demonstrate slight variations in shear band thickness among different mesh sizes. Additionally, the maximum shear strain within the shear band is lower for the undrained case than the drained case in both local and nonlocal models.

(4) The regularisation techniques only work when the mesh size $h < l_c$. The shear band thickness simulated by the local model significantly increases with mesh size, and the shear band thickness predicted by G&S and ON functions is more stable with mesh size than GD function. Furthermore, the shear band predicted by the nonlocal models increases with l_c.

Three nonlocal models were also compared and implemented in real-world boundary value problems (BVPs) under drained conditions. These problems included strip footing problems on the ground sand level and near a slope, as well as retaining wall problems considering active and passive failure conditions respectively. Nonlocal models display consistent results than the local model in all simulations.

(1) The G&S function predicts better results in the problem of strip footing on level sand ground. However, the ON model gives a speedy reduction of Q after reaching the peak, which does not match the experimental observations. This is caused by the excessive volume expansion predicted by this model. It is found that a bigger m value gives an even steeper strain-softening curve for the ON function. Therefore, the ON function is unsuitable for this problem, even though it works well in the plane strain compression tests.

(2) In the results of the strip footing on the slope, as the mesh size becomes finer, the peak value of bearing capacity decreases. Nonlocal regularisation effectively mitigates the mesh-dependent issue and decreases the ratio of strain softening. Nonetheless, the nonlocal functions still indicate a minor variation in the mesh size.

(3) In the retaining wall problems, nonlocal models alleviate the mesh sensitivity, resulting in a consistent $\sigma_h - u/h_w$ curves. The nonlocal regularisation delays the peak state in the passive failure condition case. The angle of the shear band decreases with increasing mesh size under active earth pressure, whereas it increases under passive earth pressure. The nonlocal methods reduce the disparity between the largest and smallest measured angles obtained from contour plots, particularly with the G&S function, where the angle remains nearly constant under active earth pressure. Additionally, under passive earth pressure, the angle measured from the G&S function is slightly larger than that from the GD and ON functions.

7.2 Strain localisation in plane strain compression

The nonlocal method with G&S weight function was simulated by both drained and undrained plane strain compression tests under rough boundary conditions. Moreover, the evolution of state variables, the effect of initial density and confining pressure, and the effect of anisotropy on strain localisation of both local and nonlocal models under smooth boundary conditions were further investigated.

(1) Under rough boundary conditions, the nonlocal method demonstrates mesh-independent force-displacement curves, and the peak value is reached earlier compared to smooth boundary conditions. Minor variations were observed in both shear band orientation and thickness between coarse and fine meshes. The shear band orientation decreases with increasing mesh size, while the shear band thickness increases with mesh size.

(2) The local model also demonstrates a mesh-dependent width of state variable concentration in cross-sections. In contrast, the nonlocal model shows only slight variations in the width of state variable concentration for different mesh sizes. For both smooth and rough boundary conditions, the results obtained from the G&S function indicate a significantly larger shear band thickness compared to the local model.

(3) Not only does the fluctuation in the change of the state variables decrease, but also the differences in peak values of the state variables between various mesh sizes observed in the local model are significantly reduced after nonlocal regularisation. The values of the state variables within the shear band are significantly greater than those outside, primarily due to shear strain concentration. Regarding the impact of confining pressure

and initial density on the nonlocal method, the effectiveness of reducing mesh dependency in the nonlocal method increases when the void ratio is higher or when the confining pressure increases.

Regarding the impact of anisotropy on the nonlocal method, the results indicate that the nonlocal method remains unaffected by various positive bedding plane orientations. However, negative bedding plane orientations do have an impact on the nonlocal method. In the local model, the peak reaction force for negative bedding plane orientation is greater than that for positive bedding plane orientation. Conversely, in the nonlocal model, the situation is reversed.

7.3 Future work

(1) Treat More State Variables as Nonlocal

The strain softening of the anisotropic sand model used in this research is affected by the stress state, void ratio, and fabric tensor. The void ratio increment is only affected by the volumetric strain increment, making it convenient to assume the void ratio increment is nonlocal(Mallikarachchi and Soga, 2020; Gao et al., 2021). Other state variables remain local due to the difficulty in implementing nonlocal regularisation. When not all state variables affecting strain softening are nonlocal, it negatively impacts the effectiveness of nonlocal regularisation (Li and Gao, 2024). For example, there is still a slight variation in the nonlocal predictions of shear band thickness and shear band orientation with different mesh sizes, regardless of which nonlocal function is employed. All the nonlocal functions can reduce but not eliminate the mesh dependency (Summersgill et al., 2017). Thus, future work will mainly focus on trying to make more state variables nonlocal.

(2) Comparison and Combination of Nonlocal Method with Other Regularisation Methodologies

In the literature review, four regularisation methodologies were introduced: the viscosity regularisation method, the strain-gradient enhanced approach, the micro-polar continuum approach, and the nonlocal method. Each of these methodologies has its own advantages and disadvantages. Therefore, in future work, each regularisation method will be thoroughly compared in practical cases. For example, the micro-polar continuum approach will be

combined with the critical sand model from this research and compared with the nonlocal critical sand model. Additionally, the nonlocal method will be combined with other regularisation methodologies, as there is no single regularisation method that is perfectly effective in all scenarios. In cases where a single regularisation method may not suffice to address mesh-dependency issues, combining multiple regularisation approaches can be a viable solution. To date, some combinations of regularisation methods have already been applied. For instance, the combination of viscosity regularisation with the strain-gradient enhanced method (Wang et al., 1998; de Borst and Pamin, 1996; Oka et al., 2002; Zhang et al., 2004). Subsequently, Tang and Li (2007) proposed a combination of viscosity regularisation with the micro-polar continuum approach. However, there is currently no study on the combination of the nonlocal method with other regularisation methods, so this will also be part of future plans.

(3) Implementation of Explicit, Dynamic Analysis Method with Nonlocal Method

In this research, when simulating boundary value problems, calculations often halt due to convergence issues. This is primarily because the Standard, General – implicit algorithm is used for analysis in step options of Abaqus. The Standard, General – implicit algorithm uses the Newton method for iteration, which incurs a high cost for each time increment but allows for larger time increments (Hughes, 2012). Convergence can be an issue in this case. It can be efficient for linear and some nonlinear problems. More materials, elements, and procedures are available in the standard method. In future work, attempting to combine the explicit, dynamic analysis method in Abaqus with the nonlocal method. This approach eliminates the need to consider convergence issues. The Explicit, Dynamic – explicit algorithm uses a direct iterative method, which incurs a small cost for each time increment but requires relatively small increments. Abaqus pre-determines the time increment based on wave propagation speed and the minimum mesh size. This method can be efficient for highly nonlinear and contact problems. For quasi-static problems, it is important to properly adjust model parameters such as density and total time to achieve good computation efficiency (Abaqus Documentation, 2016; Wang and Yang, 2017).

(4) Implementation of Nonlocal Method under Cyclic Loading

In this research, only monotonic loading is considered for all simulations (where the load continuously increases or decreases throughout the process without reversing). However, cyclic loading is also common in many practical engineering applications (Gao et al. 2023). For instance, in the context of bridge engineering, structures often face cyclic loading due to

traffic loads, wind forces, and thermal variations (Smith et al. 2017; Johnson et al. 2018). Similarly, buildings experience cyclic loading from environmental factors like wind and seismic activities (Lee and Kim 2020; Zhang et al. 2021). While the nonlocal method has demonstrated its effectiveness under monotonic loading conditions, its application under cyclic loading still requires further exploration.

Appendix A: Evolution of state variable along the cross-section under rough boundary

(1) Void ratio *e*

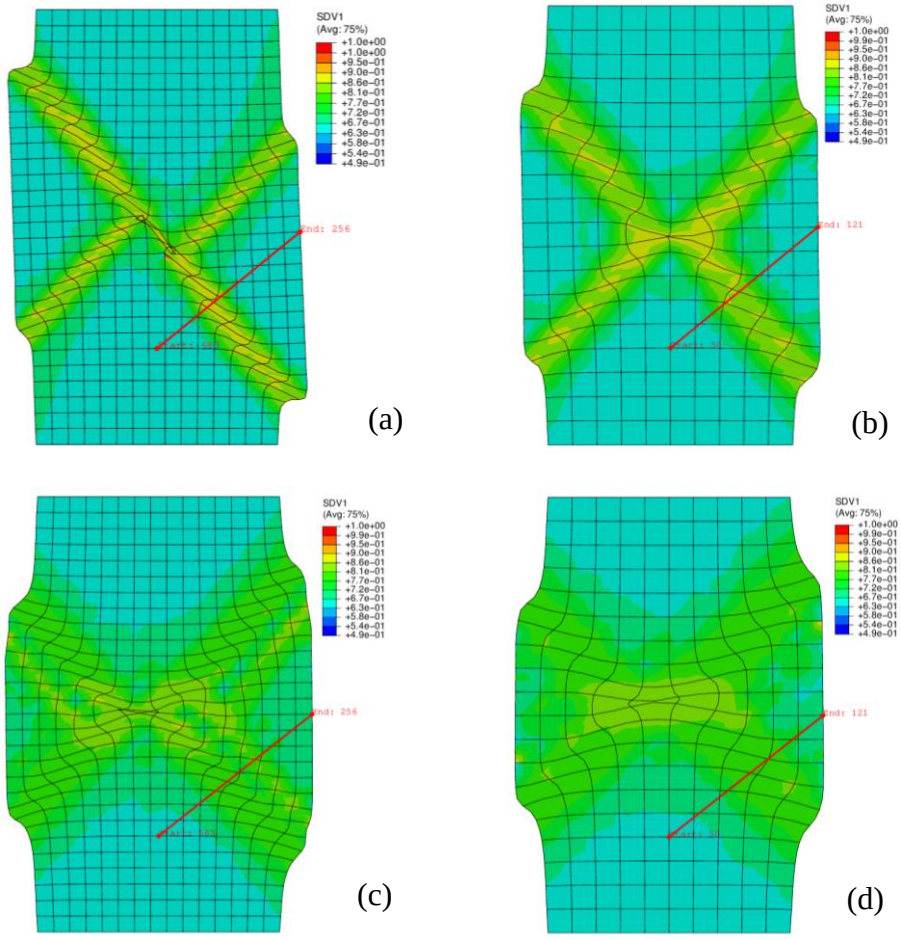

Figure A-1 Contours of the void ratio *e* from local and nonlocal models: (a) Local (0.004 m); (b) Local (0.006 m); (c) G&S function (0.004 m); (d) G&S function (0.006 m)

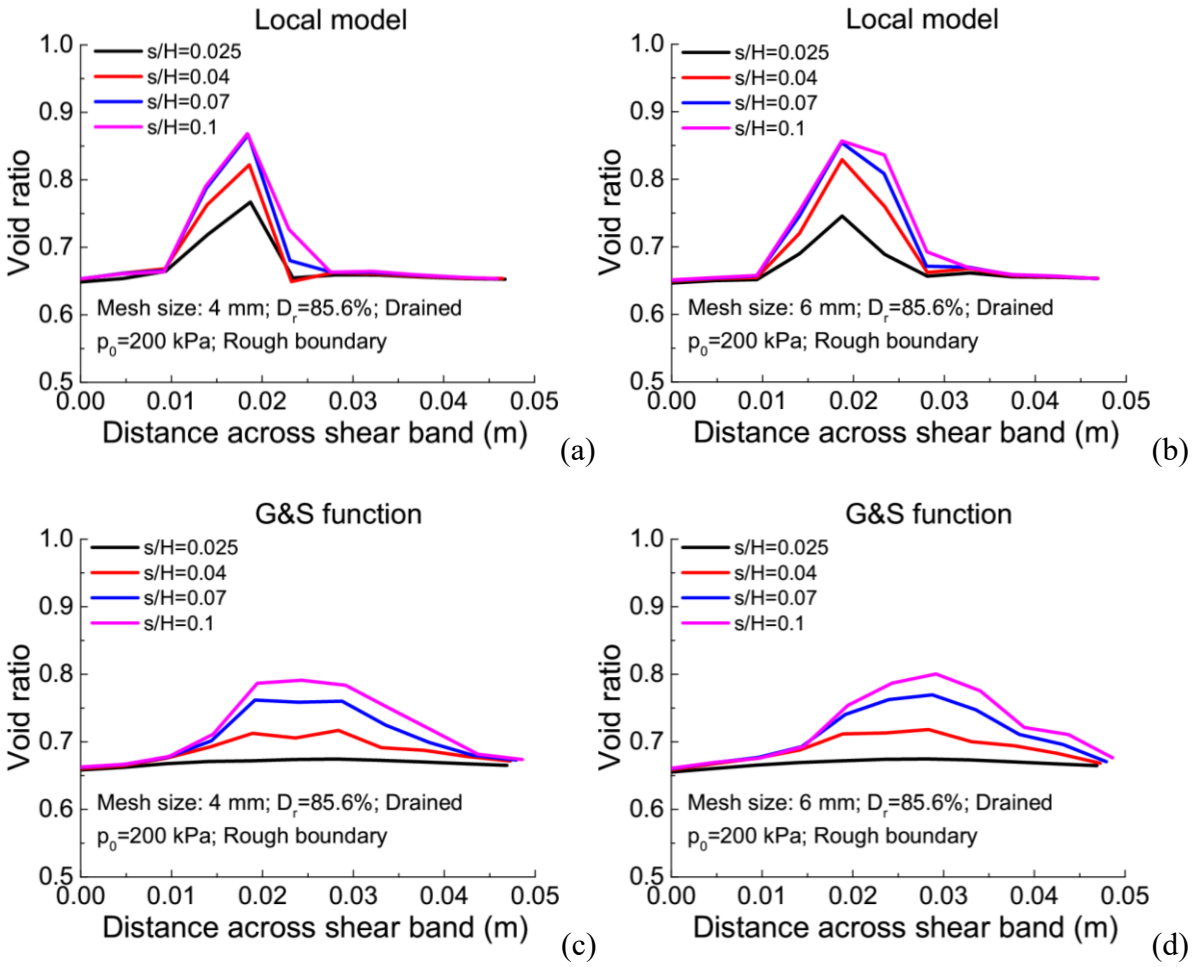

Figure A-2 Cross-sectional profiles of the void ratio *e* from local and nonlocal models: (a) Local (0.004 m); (b) Local (0.006 m); (c) G&S function (0.004 m); (d) G&S function (0.006 m)

(2) Anisotropic variable *A*

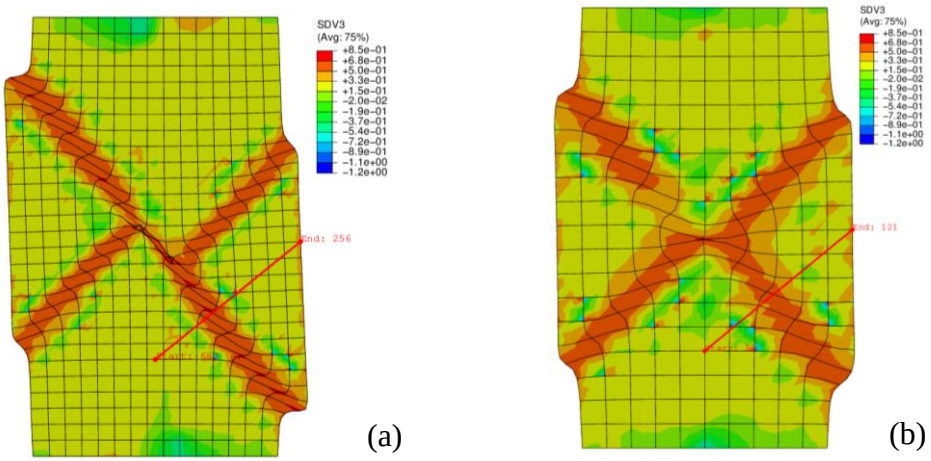

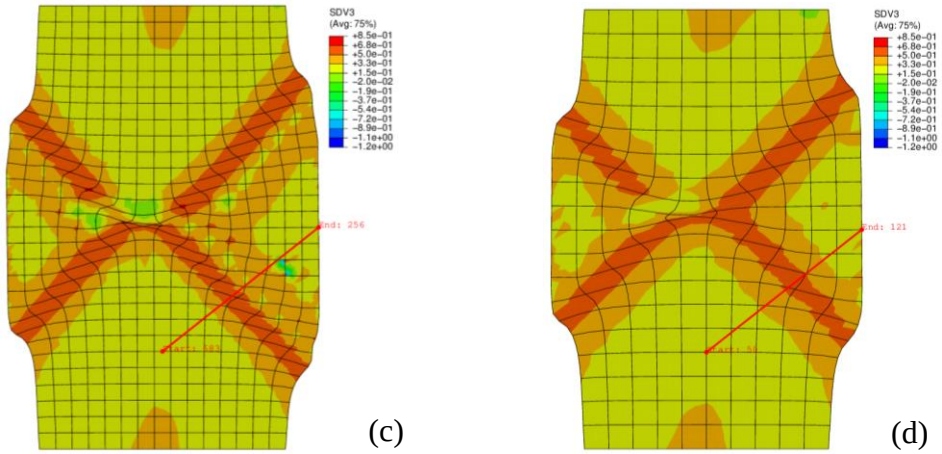

Figure A-3 Contours of the anisotropic variable *A* from local and nonlocal models: (a) Local (0.004 m); (b) Local (0.006 m); (c) G&S function (0.004 m); (d) G&S function (0.006 m)

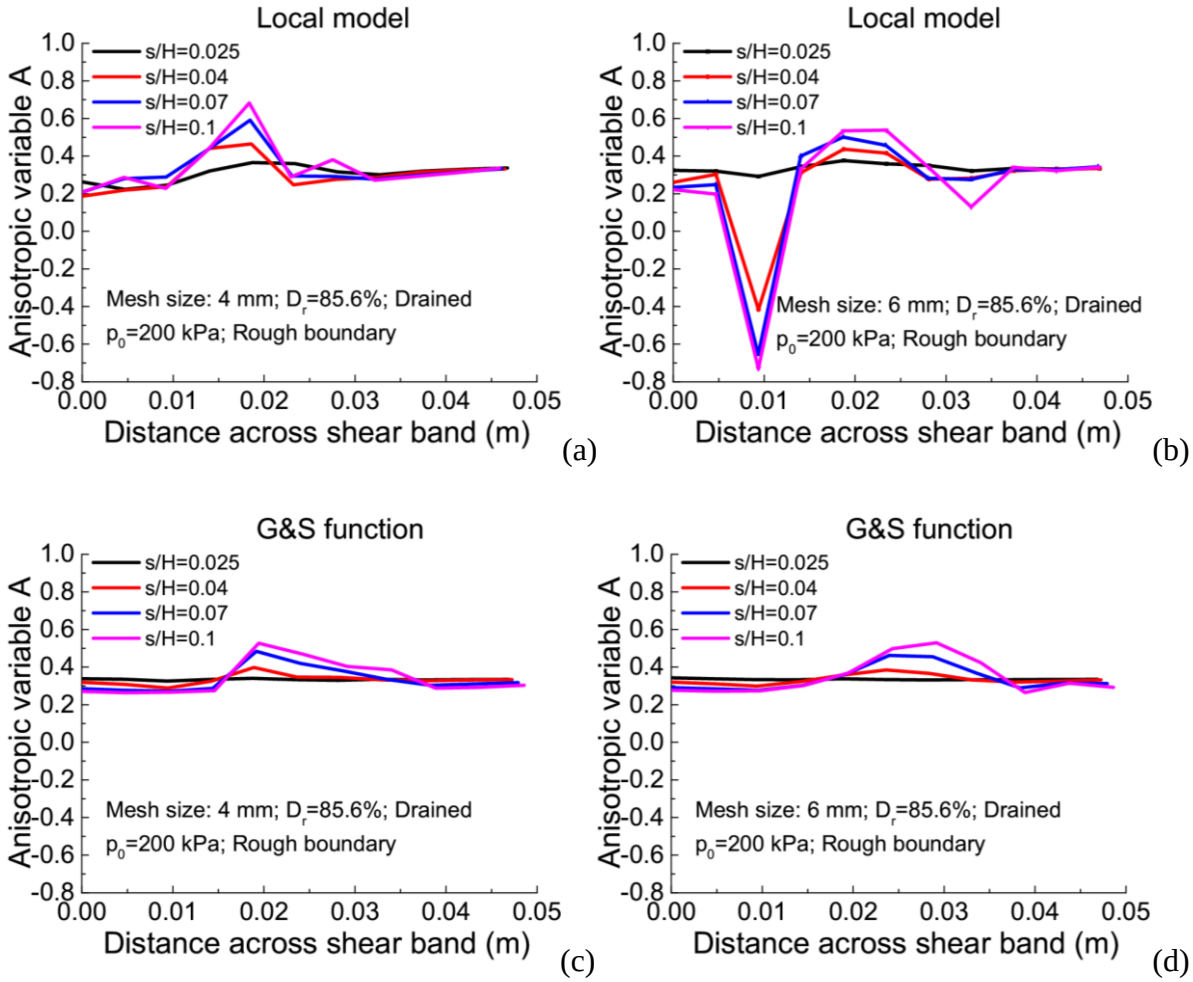

Figure A-4 Cross-sectional profiles of the anisotropic variable A from local and nonlocal models: (a) Local (0.004 m); (b) Local (0.006 m); (c) G&S function (0.004 m); (d) G&S function (0.006 m)

(3) Degree of anisotropy F

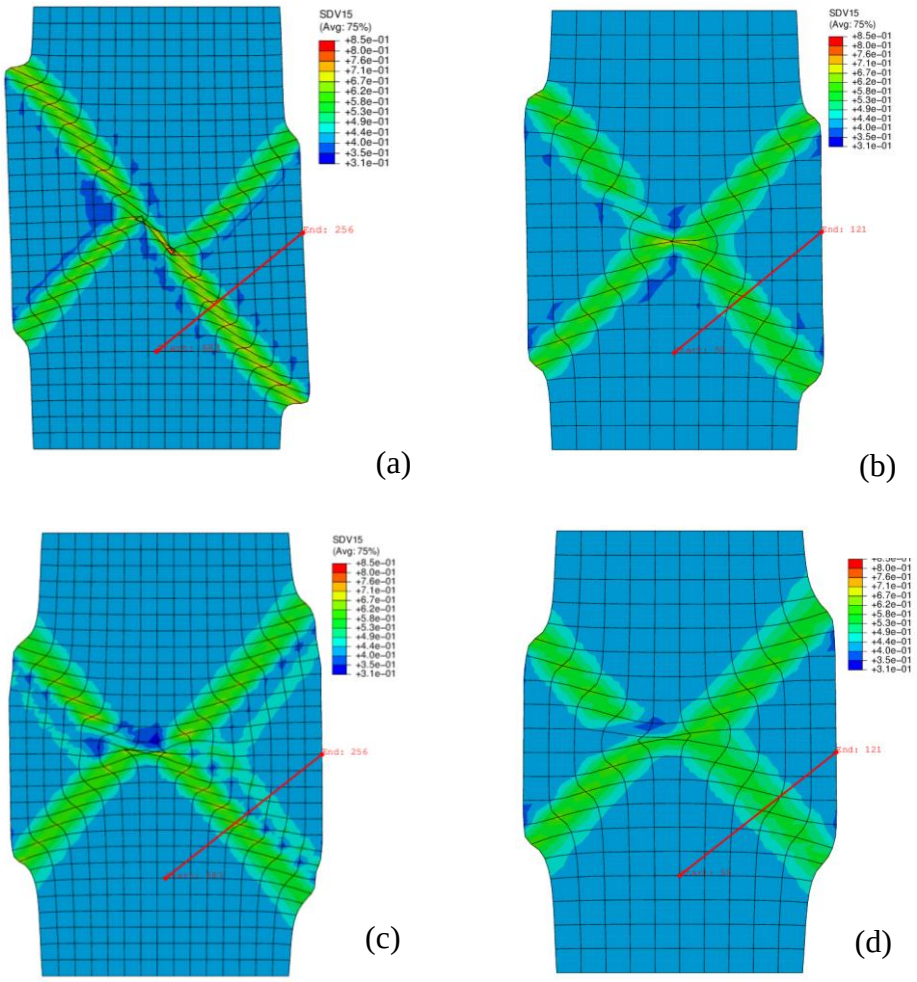

Figure A-5 Contours of the degree of anisotropy F from local and nonlocal models: (a) Local (0.004 m); (b) Local (0.006 m); (c) G&S function (0.004 m); (d) G&S function (0.006 m)

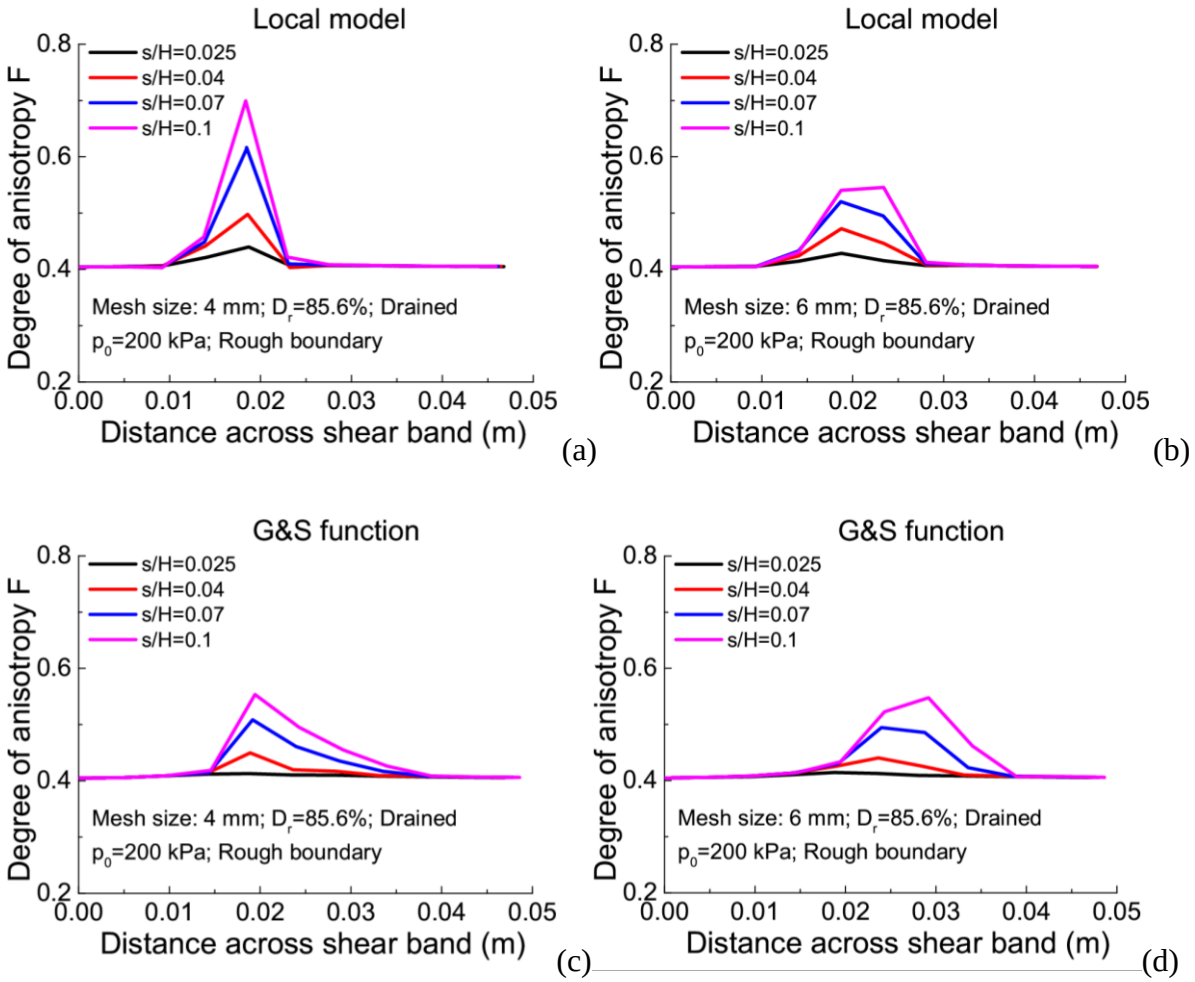

Figure A-6 Cross-sectional profiles of the degree of anisotropy F from local and nonlocal models: (a) Local (0.004 m); (b) Local (0.006 m); (c) G&S function (0.004 m); (d) G&S function (0.006 m)

(4) Shear strain

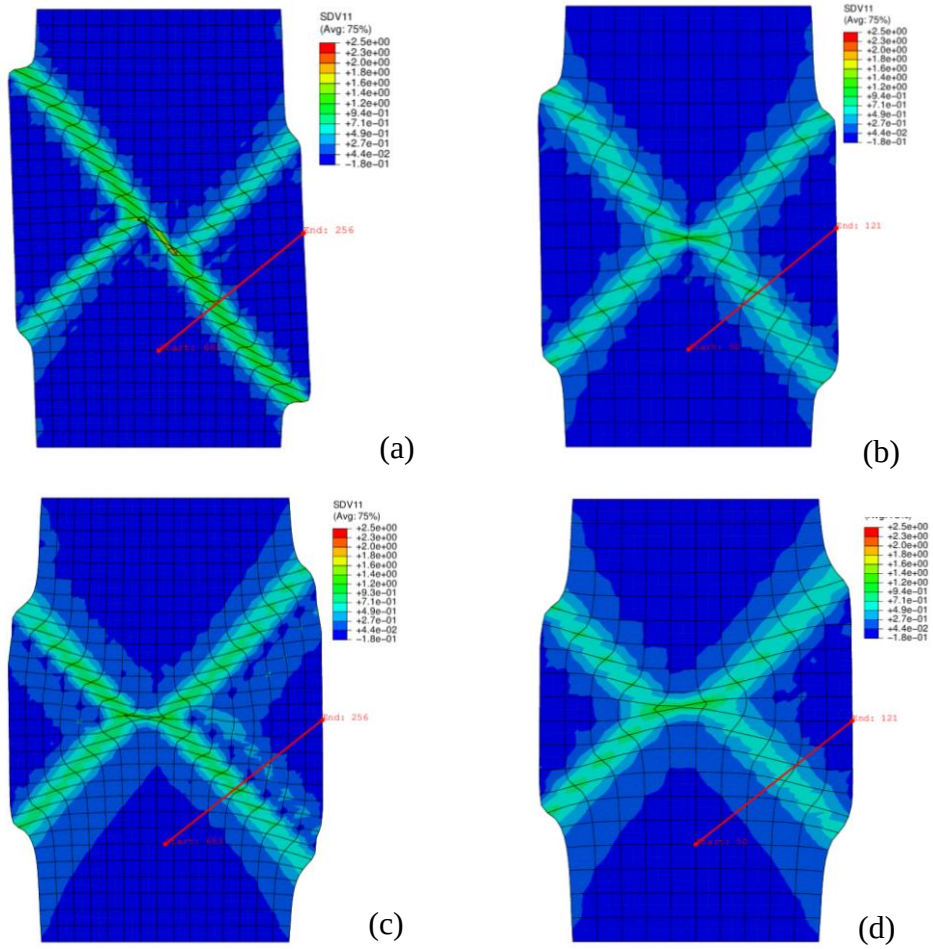

Figure A-7 Contours of the shear strain from local and nonlocal models: (a) Local (0.004 m); (b) Local (0.006 m); (c) G&S function (0.004 m); (d) G&S function (0.006 m)

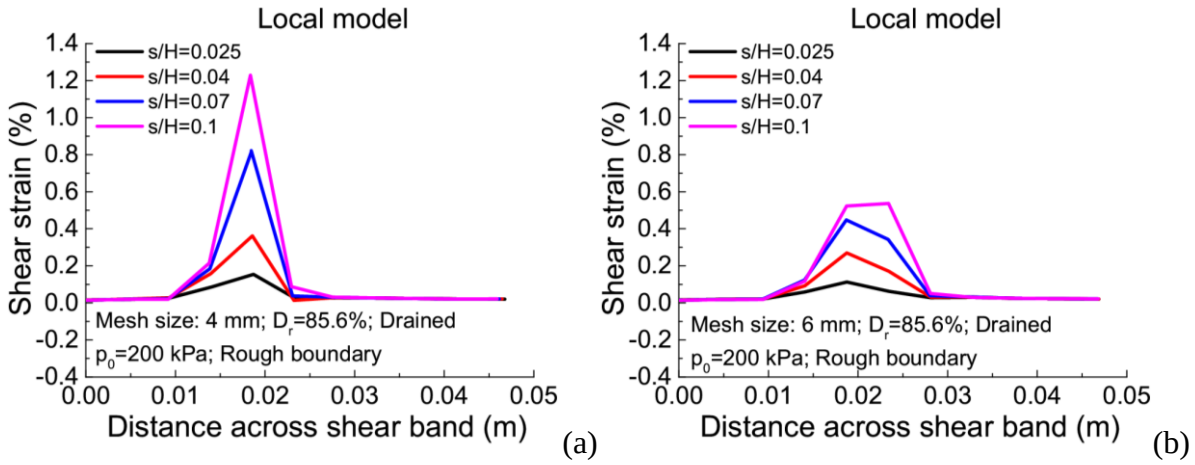

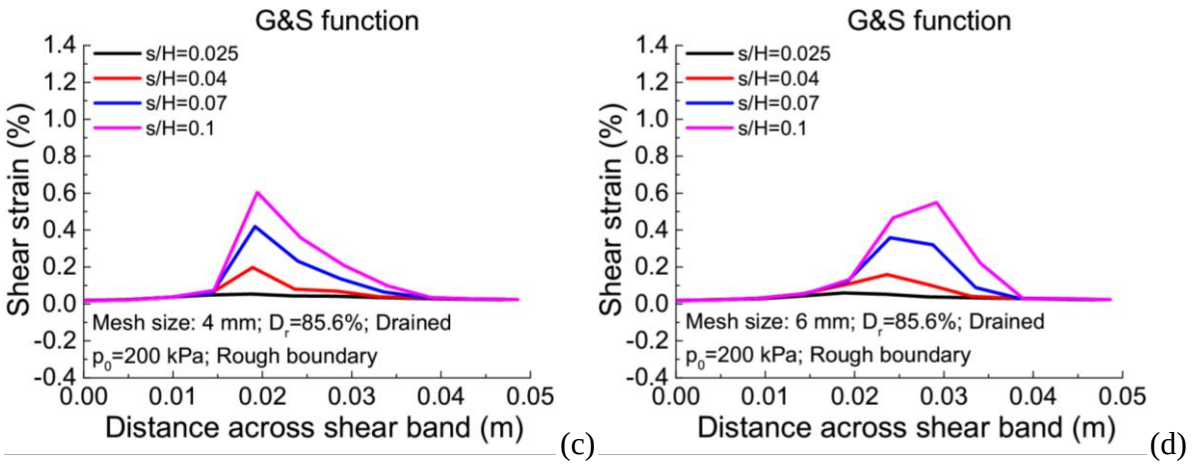

Figure A-8 Cross-sectional profiles of the shear strain from local and nonlocal models: (a) Local (0.004 m); (b) Local (0.006 m); (c) G&S function (0.004 m); (d) G&S function (0.006 m)

Appendix B: Evolution of the shear band from selected elements under rough boundary

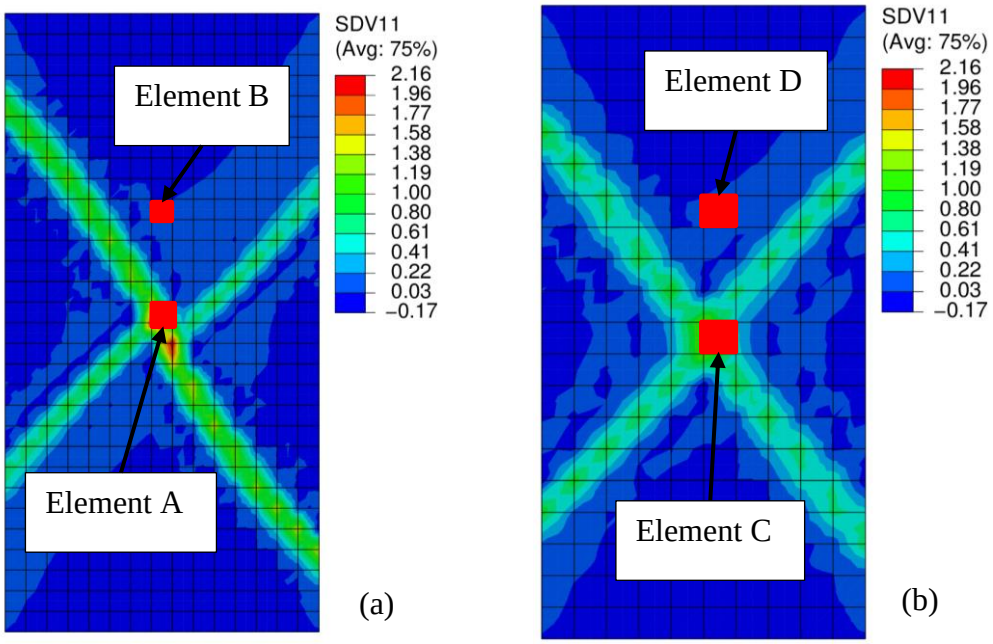

Figure B-1 Location of the selected elements for the cross shear band: (a) Fine mesh; (b) Coarse mesh

(1) Evolution of void ratio

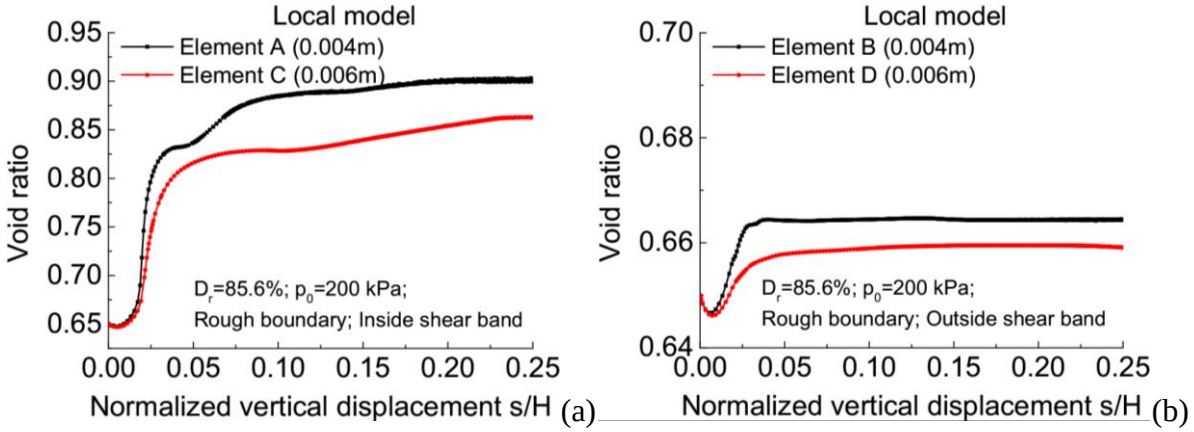

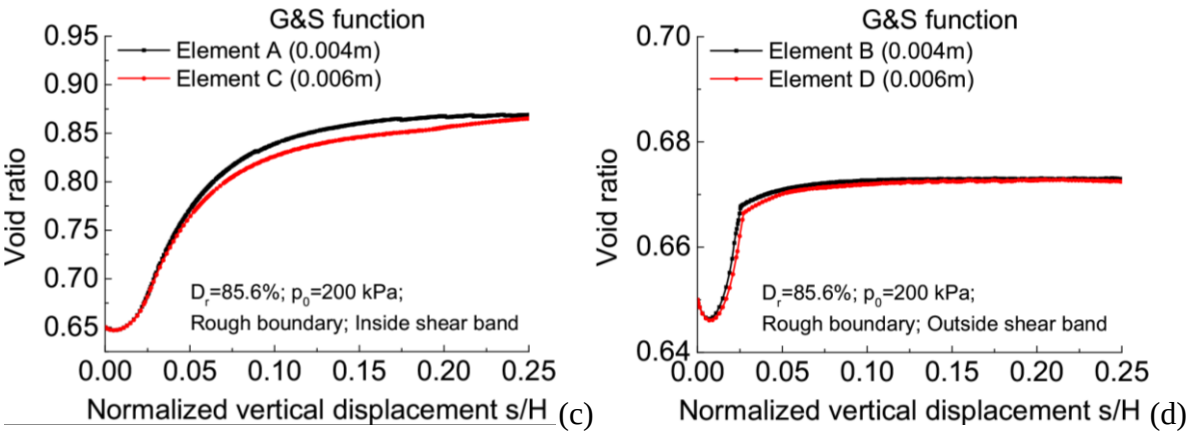

Figure B-2 The local evolution of the void ratio for the elements inside and outside the shear band under rough boundary conditions

(2) Local fabric evolution

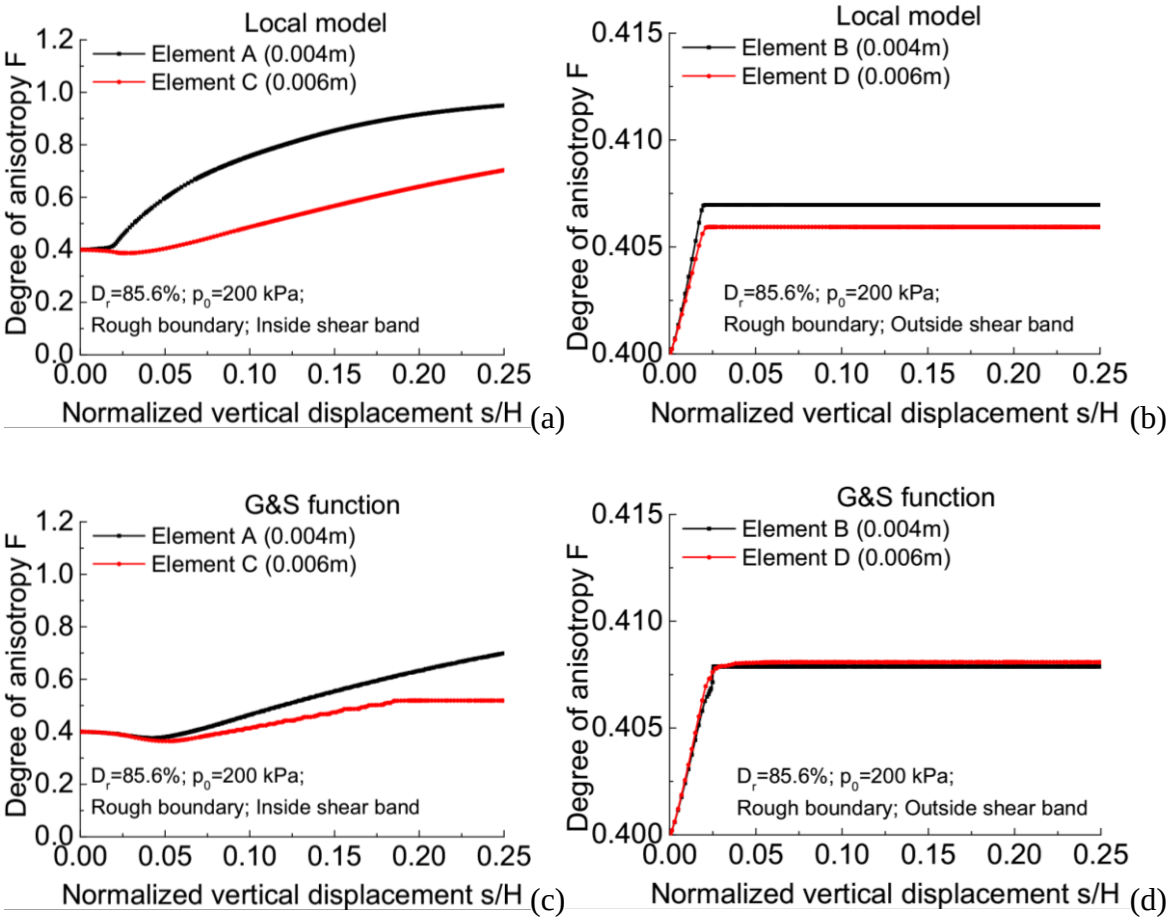

Figure B-3 The local evolution of the fabric for the elements inside and outside the shear band under rough boundary conditions

(3) Local evolution of *A*

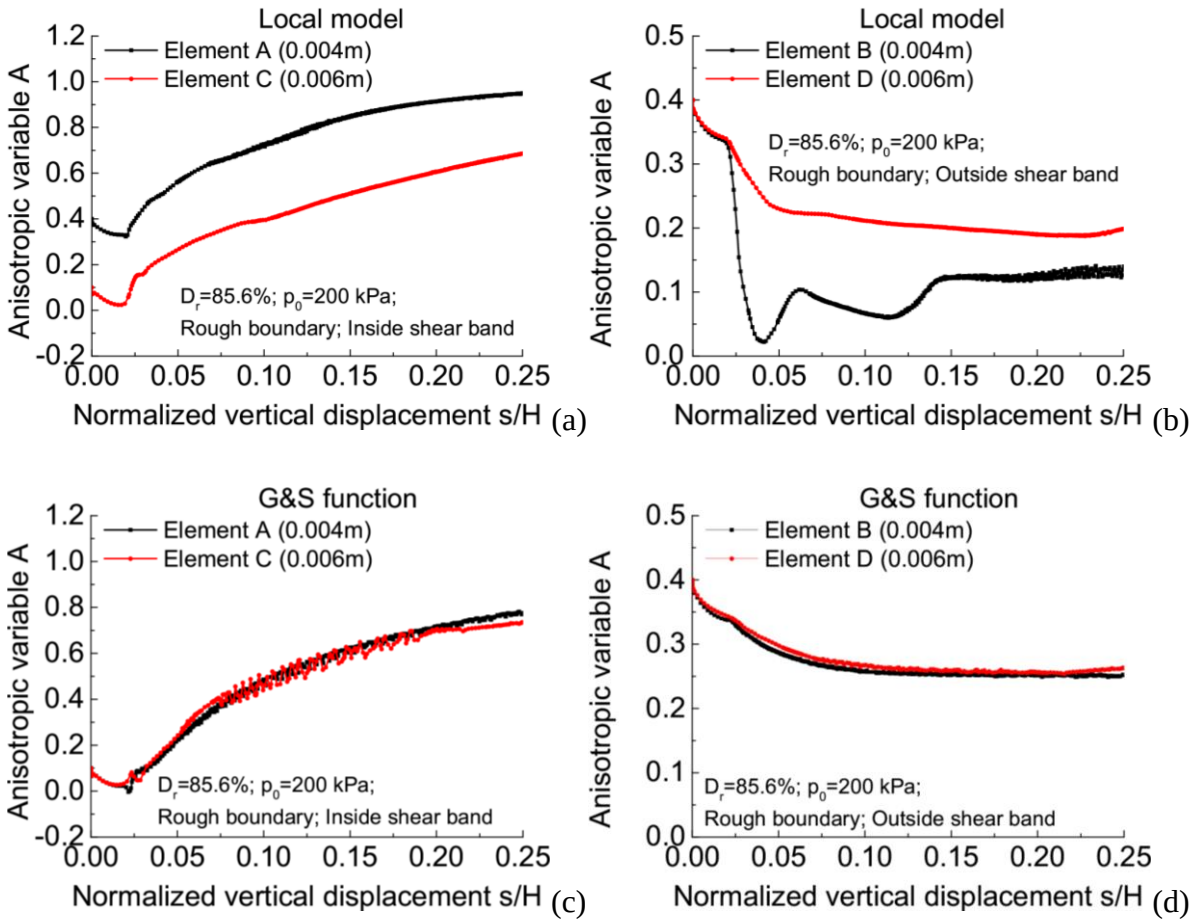

Figure B-4 The local evolution of the anisotropic variable *A* for the elements inside and outside the shear band under rough boundary conditions

Appendix C: Evolution of state variable along the cross-section under undrained condition with rough boundary

(1) Magnitude of displacement

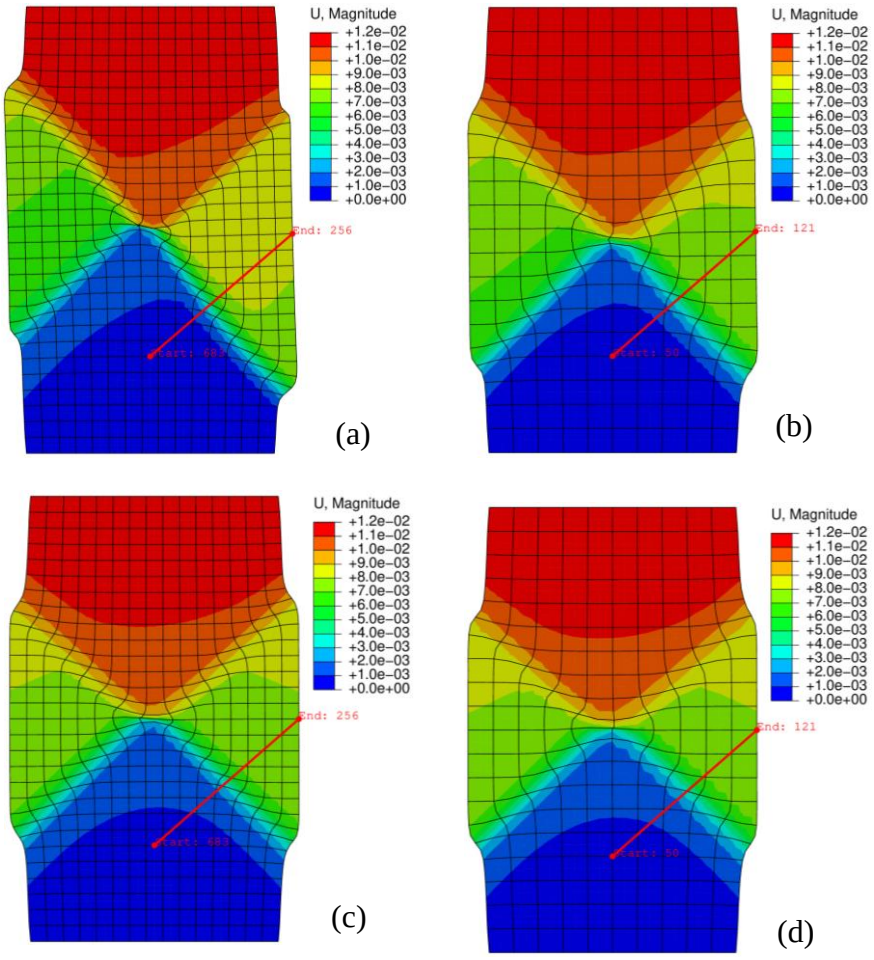

Figure C-1 Contours of magnitude of the displacement from local and nonlocal models: (a) Local (0.004 m); (b) Local (0.006 m); (c) G&S function (0.004 m); (d) G&S function (0.006m)

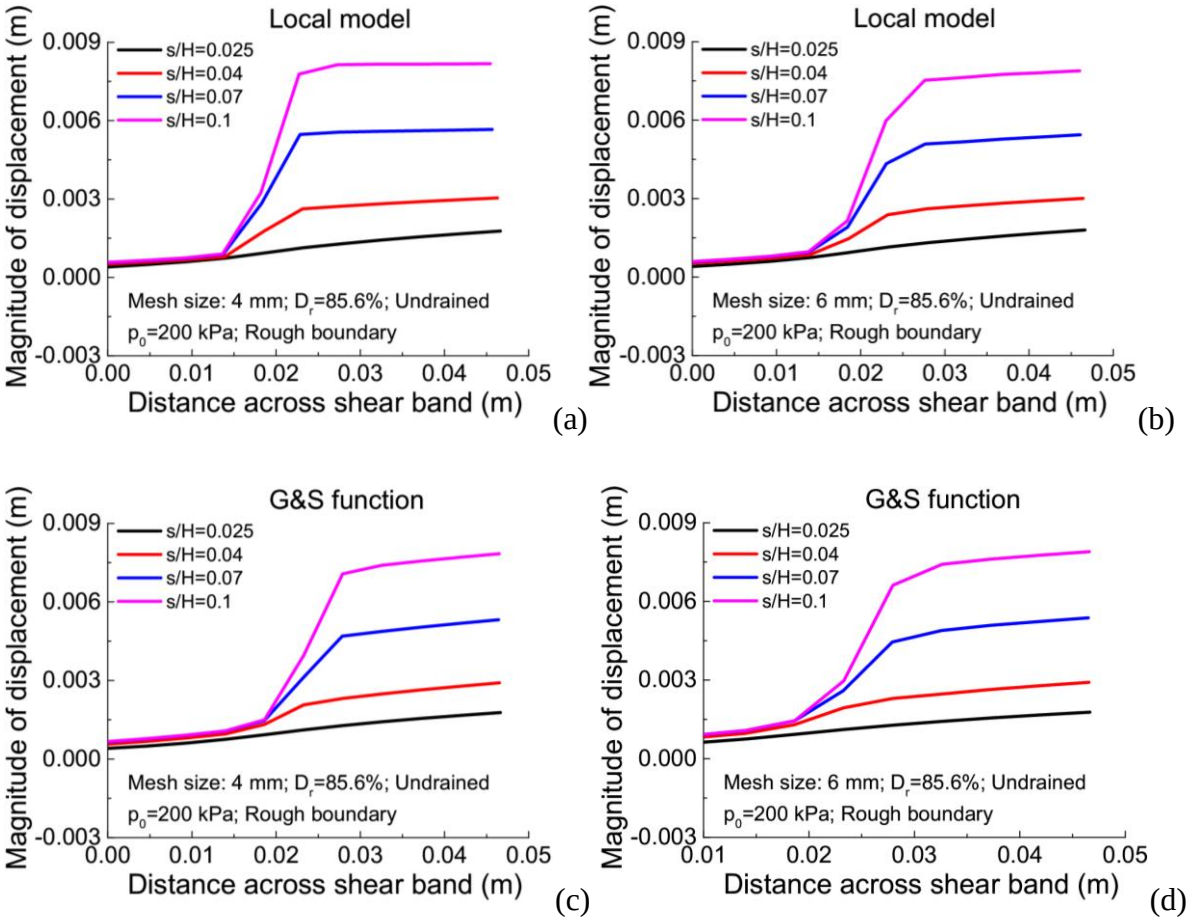

Figure C-2 Cross-sectional profiles of the magnitude of displacement from local and nonlocal models: (a) Local (0.004 m); (b) Local (0.006 m); (c) G&S function (0.004 m); (d) G&S function (0.006 m)

(2) Void ratio

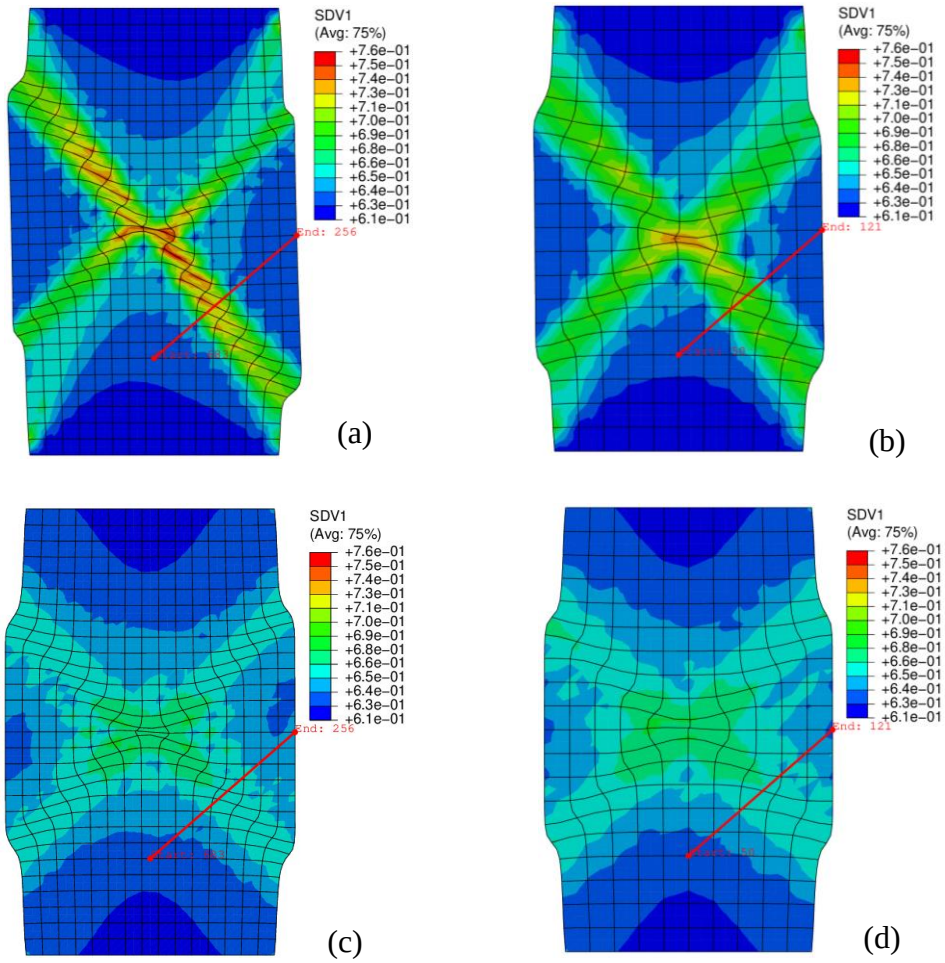

Figure C-3 Contours of the void ratio e from local and nonlocal models: (a) Local (0.004 m); (b) Local (0.006 m); (c) G&S function (0.004 m); (d) G&S function (0.006 m)

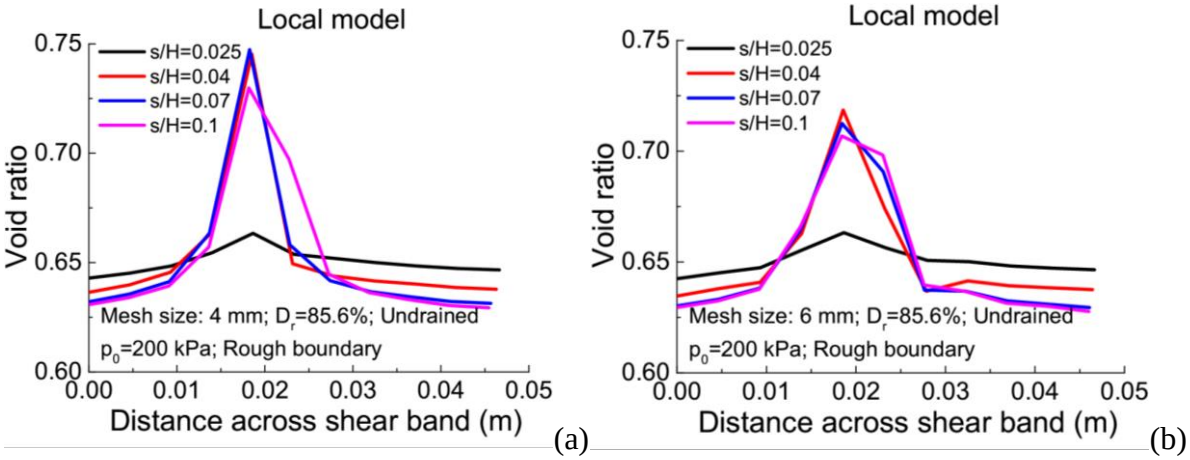

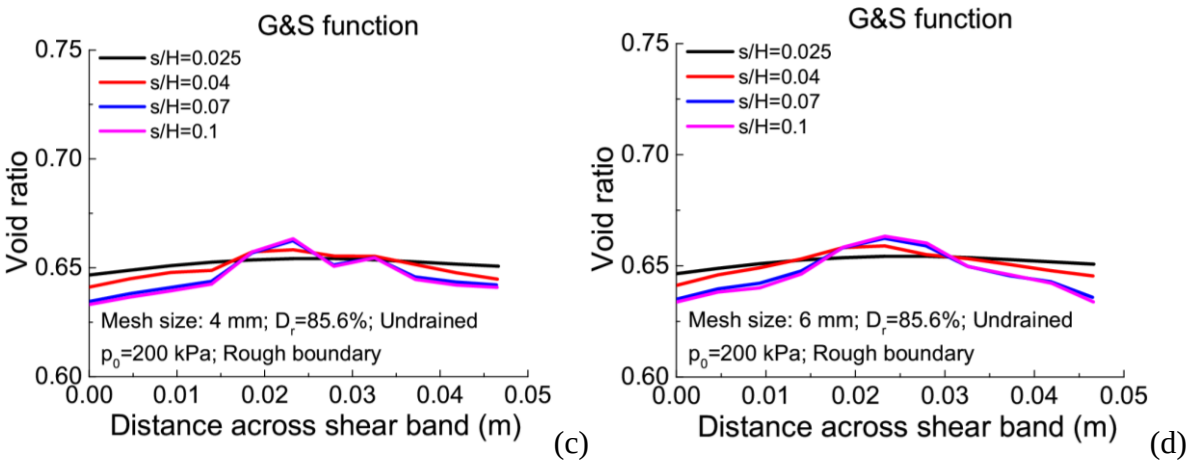

Figure C-4 Cross-sectional profiles of the void ratio *e* from local and nonlocal models: (a) Local (0.004 m); (b) Local (0.006 m); (c) G&S function (0.004 m); (d) G&S function (0.006 m)

List of References

Abaqus Documentation. (2016). *Abaqus Analysis User's Guide*.

Aifantis, E. C. (1984). On the microstructural origin of certain inelastic models. *Journal of Engineering Materials and Technology*, **106**(4), 326–330. https://doi.org/10.1115/1.3225725

Aifantis, E.C. (1984). Microscopic processes and macroscopic response. *Mechanics of engineering materials*, C. S. Desai and R. H. Gallagher, eds., Wiley, New York, 1–22.

Aifantis, E.C. (1987). The physics of plastic deformation. *International journal of plasticity*, **3**(3), 211-247. https://doi.org/10.1016/0749-6419(87)90021-0

Alsaleh, M. I., Voyiadjis, G.Z., Alshibli, K.A. (2006). Modelling strain localization in granular materials using micropolar theory: Mathematical formulations. *International Journal for Numerical and Analytical Methods in Geomechanics*, **30**(15), 1501-1524. https://doi.org/10.1002/nag.533

Alshibli, K. A., Alsaleh, M. I., Voyiadjis, G. Z. (2006). Modelling strain localization in granular materials using micropolar theory: Numerical implementation and verification. *International Journal for Numerical and Analytical Methods in Geomechanics*, **30**(15), 1525–1544. https://doi.org/10.1002/nag.534

Alshibli, K. A., Batiste, S. N., Sture, S. (2003). Strain localisation in sand: Plane strain versus triaxial compression, *Journal of Geotechnical and Geoenvironmental Engineering*, **129**(6), pp. 483–494. doi:10.1061/(asce)1090-0241(2003)129:6(483).

Alshibli, K. A., Roussel, L. M. (2006). Experimental investigation of strain localization in sand using digital image correlation. *International Journal of Geomechanics*, **6**(5), 354-366. https://doi.org/10.1061/(ASCE)1532-3641(2006)6:5(354)

Alshibli, K.A., Sture, S. (2000). Shear band formation in plane strain experiments of Sand, *Journal of Geotechnical and Geoenvironmental Engineering*, **126**(6), pp. 495–503. doi:10.1061/(asce)1090-0241(2000)126:6(495).

Anand, L., Aslan, O., Chester, S. A. (2012). A large-deformation gradient theory for elastic–plastic materials: Strain softening and regularization of shear bands. *International Journal of Plasticity*, **30–31**, 116–143. https://doi.org/10.1016/j.ijplas.2011.10.002

Antolovich, S. D., Armstrong, R. W. (2014). Plastic strain localisation in metals: Origins and consequences, *Progress in Materials Science*, **59**, pp. 1–160. doi:10.1016/j.pmatsci.2013.06.001.

Antonellini, M. A., Aydin, A., Pollard, D. D. (1994). Microstructure of deformation bands in porous sandstones at Arches National Park, Utah. *Journal of Structural Geology*, **16**(7), 941–959. https://doi.org/10.1016/0191-8141(94)90077-9

Antonellini, M., Aydin, A. (1994). Effect of faulting on fluid flow in porous sandstones: Geometry and spatial distribution. *American Association of Petroleum Geologists Bulletin*, **78**, 355–377. https://doi.org/10.1306/BDFF905D-1718-11D7-8645000102C1865D

Aydin, A. (1978). Small faults formed as deformation bands in Sandstone. *Rock Friction and Earthquake Prediction*, **116**, 913–930. https://doi.org/10.1007/978-3-0348-7182-2_22

Aydin, A., Borja, R. I., Eichhubl, P. (2006). Geological and mathematical framework for failure modes in granular rock. *Journal of Structural Geology*, **28**(1), 83–98. https://doi.org/10.1016/j.jsg.2005.07.008

Bardet, J.P., Proubet, J. (1992). Shear‐band analysis in idealized granular material, *Journal of Engineering Mechanics*, **118**(2), pp. 397–415. doi:10.1061/(asce)0733-9399(1992)118:2(397).

Bazant, Z. P., & Jirasek, M. (2002). Nonlocal integral formulations of plasticity and damage: Survey of progress. *Journal of Engineering Mechanics*, **128**(11), 1119-1149. https://doi.org/10.1061/(ASCE)0733-9399(2002)128:11(1119)

Bazant, Z. P., and Jirasek, M. (2002). Nonlocal integral formulations of plasticity and damage: Survey of progress. *Journal of Engineering Mechanics*, **128**(11), 1119-1149. https://doi.org/10.1061/(asce)0733-9399(2002)128:11(1119)

Bažant, Z. P., Chang, T. (1984). Instability of nonlocal continuum and strain averaging. *Journal of Engineering Mechanics*, **110**(10), 1441–1450. https://doi.org/10.1061/(asce)0733-9399(1984)110:10(1441)

Bažant, Z. P., Gambarova, P. G. (1984). Crack shear in concrete: Crack band Microflane Model. *Journal of Structural Engineering*, **110**(9), 2015–2035. https://doi.org/10.1061/(asce)0733-9445(1984)110:9(2015)

Bažant, Z. P., Jirásek, M. (2002). Nonlocal integral formulations of plasticity and damage: Survey of progress. *Journal of Engineering Mechanics*, **128**(11), 1119–1149. https://doi.org/10.1061/(asce)0733-9399(2002)128:11(1119)

Bažant, Z. P., Lin, F. (1988). Non‐local yield limit degradation. *International Journal for Numerical Methods in Engineering*, **26**(8), 1805–1823. https://doi.org/10.1002/nme.1620260809

Bažant, Z. P., Pijaudier-Cabot, G. (1988). Nonlocal continuum damage, localization instability and convergence. *Journal of Applied Mechanics*, **55**(2), 287–293. https://doi.org/10.1115/1.3173674

Been, K., Jefferies, M. G. (1985). A state parameter for sands. *Géotechnique*, **35**(2), 99–112. https://doi.org/10.1680/geot.1985.35.2.99.

Borja, R. I. (2004). Cam-Clay plasticity. Part V: A mathematical framework for three-phase deformation and strain localization analyses of partially saturated porous media. *Computer Methods in Applied Mechanics and Engineering*, **193**(48–51), 5301–5338. https://doi.org/10.1016/j.cma.2003.12.067

Borja, R. I., Aydin, A. (2004). Computational modeling of deformation bands in granular media. I. Geological and mathematical framework. *Computer Methods in Applied Mechanics and Engineering*, **193**(27–29), 2667–2698. https://doi.org/10.1016/j.cma.2003.09.019

Brandes, C., Tanner, D. C. (2012). Three-dimensional geometry and fabric of shear deformation-bands in unconsolidated Pleistocene sediments. *Tectonophysics*, 518–521, 84–92. https://doi.org/10.1016/j.tecto.2011.11.008

Brandl, H. (2006). Energy foundations and other thermo-active ground structures. *Géotechnique*, **56**(2), 81–122. https://doi.org/10.1680/geot.2006.56.2.81

Brinkgreve, R. (1994). *Geomaterial Models and Numerical Analysis of Softening*. PhD thesis, University of Delft, Delft.

Chandrasekhar, S. (1950). *Radiation transfer*, Oxford University Press, London

Chikazawa, Y., Koshizuka, S., Oka, Y. (2001). A particle method for elastic and visco-plastic structures and fluid-structure interactions. *Computational Mechanics*, **27**(2), 97–106. https://doi.org/10.1007/s004660000216

Chu, J., Leroueil, S., Leong, W. K. (2003). Unstable behaviour of sand and its implication for slope instability. *Canadian Geotechnical Journal*, **40**(5), 873–885. https://doi.org/10.1139/t03- 039.

Chu, J., Lo, S.-C. R., Lee, I. K. (1996). Strain softening and shear band formation of sand in multi-axial testing. *Geotechnique*, **46**(1), 63-82.

Coduto, D. P., Yeung, M. C. R., Kitch, W. A. (2018). *Geotechnical Engineering: Principles and practices*. Upper Saddle River, NJ: Pearson Education.

Coleman, B. D., Hodgdon, M. L. (1985). On shear bands in Ductile Materials. *Archive for Rational Mechanics and Analysis*, **90**(3), 219–247. https://doi.org/10.1007/bf00251732

Conte, E., Silvestri, F., Troncone, A. (2010). Stability analysis of slopes in soils with strain-softening behaviour. *Computers and Geotechnics*, **37**(5), 710–722. https://doi.org/10.1016/j.compgeo.2010.04.010

Cosserat, E., Cosserat, F. (1909). *Théorie des corps déformables*. A. Hermann et Fils, Paris, France, https://doi.org/10.1038/081067a0

Cui, W., Wu, X., Potts, D. M., Zdravković, L. (2023). Nonlocal strain regularisation for critical state models with volumetric hardening. *Computers and Geotechnics*, **157**, 105350. https://doi.org/10.1016/j.compgeo.2023.105350

Dafalias, Y. F. (1986). An anisotropic critical state soil plasticity model. *Mechanics Research Communications*, **13**(6), 341–347. https://doi.org/10.1016/0093-6413(86)90047-9

Davis, R. O., Selvadurai, A. P. S. (2002). *Plasticity and Geomechanics*. Cambridge University Press, New York.

de Borst, R. (1993). A generalisation of theory for Polar Continua. *Computer Methods in Applied Mechanics and Engineering*, **103**(3), 347–362. https://doi.org/10.1016/0045-7825(93)90127-j

de Borst, R., Mühlhaus, H. (1991). Continuum models for discontinuous media, Fracture processes in concrete, rock and ceramics. *Proceedings of the international rilem/esis conference*, Noordwijk, the Netherlands, June 19-21, **2**, 601-618.

de Borst, R., Mühlhaus, H. (1992). Gradient ‐ dependent plasticity: Formulation and algorithmic aspects. *International Journal for Numerical Methods in Engineering*, **35**(3), 521–539. https://doi.org/10.1002/nme.1620350307

de Borst, R., Pamin, J., (1996). Some novel developments in finite element procedures for gradient-dependent plasticity. *International Journal for Numerical Methods in Engineering*, **39**(14), 2477–2505. https://doi.org/10.1002/(sici)1097-0207(19960730)39:14<2477::aid-nme962>3.3.co;2-5

de Borst, R., Sluys, L. J., Muhlhaus, H., Pamin, J., (1993). Fundamental issues in finite element analyses of localization of deformation. *Engineering computations*, **10**(2), 99–121. https://doi.org/10.1108/eb023897

Descries, J., Chambon, R., Mokni, M., Mazerolle, F., (1996). Void ratio evolution inside shear bands in triaxial sand specimens studied by computed tomography, *Géotechnique*, **46**(3), pp. 529–546. doi:10.1680/geot.1996.46.3.529.

Desrues, J., Viggiani, G. (2004). Strain localization in sand: An overview of the experimental results obtained in Grenoble using stereophotogrammetry, *International Journal for Numerical and Analytical Methods in Geomechanics*, **28**(4), pp. 279–321. doi:10.1002/nag.338.

Dias da Silva, V. (2004). A simple model for viscous regularization of Elasto-plastic constitutive laws with softening, *Communications in Numerical Methods in Engineering*, **20**(7), pp. 547–568. doi:10.1002/cnm.700.

Dorgan, R. J., Voyiadjis, G. Z. (2003). Nonlocal dislocation-based plasticity incorporating gradients of hardening. *Mechanics of Materials*, **35**(8), 721–732. https://doi.org/10.1016/s0167-6636(02)00202-8

Duvaut, G., Lions, J. L. (1972). Inéquations en thermoélasticité et magneto-hydrodynamique, *Archive for Rational Mechanics and Analysis*, **46**(4), pp. 241–279. Available at: https://doi.org/10.1007/bf00250512.

Duveau, G., Shao, J. F., Henry, J. P. (1998). Assessment of some failure criteria for strongly anisotropic geomaterials. *Mechanics of Cohesive-Frictional Materials*, **3**(1), 1–26. https://doi.org/10.1002/(sici)1099-1484(199801)3:1<1::aid-cfm38>3.0.co;2-7

Ebrahimian, B., Noorzad, A., Alsaleh, M. I. (2012). Modeling shear localization along granular soil–structure interfaces using elasto-plastic cosserat continuum. *International Journal of Solids and Structures*, **49**(2), 257–278. https://doi.org/10.1016/j.ijsolstr.2011.09.005

Eringen, A. C. (1966). *Mechanics of micromorphic materials*. In: Goertler, H., Sorger, P. (Eds.), Applied Mechanics. Proc. 11th Int. Congress, Springer, Berlin, pp. 131–138

Eringen, A. C. (1972). Nonlocal Polar Elastic Continua. *International Journal of Engineering Science*, **10**(1), 1–16. https://doi.org/10.1016/0020-7225(72)90070-5

Eringen, A. C. (1981). On nonlocal plasticity. *International Journal of Engineering Science*, **19**(12), 1461–1474. https://doi.org/10.1016/0020-7225(81)90072-0

Eringen, A. C. (1983). Theories of nonlocal plasticity. *International Journal of Engineering Science*, **21**(7), 741–751. https://doi.org/10.1016/0020-7225(83)90058-7

Eringen, A. C., Edelen, D. G. B. (1972). On nonlocal elasticity. *International Journal of Engineering Science*, **10**(3), pp.233-248. https://doi.org/10.1016/0020-7225(72)90039-0

Eringen, A. C., Kim, B. S. (1974). Stress concentration at the tip of a crack. *Mechanics Research Communications*, **1**(4), 233–237. https://doi.org/10.1016/0093-6413(74)90070-6

Exner, U., Grassemann, B. (2010). Deformation bands in gravels: Displacement gradients and heterogeneous strain. *Journal of the Geological Society*, **167**, 905–913. https://doi.org/10.1144/0016-76492009-146

Exner, U., Kaiser, J., Gier, S. (2013). Deformation bands evolving from dilation to cementation bands in a hydrocarbon reservoir (Vienna Basin, Austria). *Marine and Petroleum Geology*, **43,** 504–515. https://doi.org/10.1016/j.marpetgeo.2013.03.005

Forest, S. (2009). Micromorphic approach for gradient elasticity, visco-plasticity, and damage. *Journal of Engineering Mechanics*, **135**(3), 117–131. https://doi.org/10.1061/(asce)0733-9399(2009)135:3(117)

Fossen, H., Bale, A. (2007). Deformation bands and their influence on fluid flow. *American Association of Petroleum Geologists Bulletin*, **91**, 1685–1700. https://doi.org/10.1306/06200706132

Fossen, H., Schultz, R. A., Shipton, Z. K., Mair, K. (2007). Deformation bands in Sandstone: A Review. *Journal of the Geological Society*, **164**(4), 755–769. https://doi.org/10.1144/0016-76492006-036

Fossen, H., Schultz, R. A., Torabi, A. (2011). Conditions and implications for compaction band formation in Navajo Sandstone, Utah. Journal of Structural Geology, **33**, 1477–1490. https://doi.org/10.1016/j.jsg.2011.08.008

Fukushima, S., Tatsuoka, F. (1984). Strength and deformation characteristics of saturated sand at extremely low pressures. *Soils and Foundations*, **24**(4), 30–48. https://doi.org/10.3208/sandf1972.24.4_30

Galavi, V., Schweiger, H. F. (2010). Nonlocal multilaminate model for strain softening analysis. *International Journal of Geomechanics*, **10**(1), 30–44. https://doi.org/10.1061/(asce)1532-3641(2010)10:1(30)

Gao, Z. W., Li, X., Lu, D. C. (2021). Nonlocal regularization of an anisotropic critical state model for Sand. *Acta Geotechnica*, **17**(2), 427–439. https://doi.org/10.1007/s11440-021-01236-3

Gao, Z. W., Lu, D. C., Du, X. (2020). Bearing capacity and failure mechanism of strip footings on Anisotropic Sand. *Journal of Engineering Mechanics*, **146**(8). https://doi.org/10.1061/(asce)em.1943-7889.0001814

Gao, Z. W., Zhao, J. D. (2013). Strain localization and fabric evolution in Sand, *International Journal of Solids and Structures*, **50**(22–23), pp. 3634–3648. doi:10.1016/j.ijsolstr.2013.07.005.

Gao, Z. W., Zhao, J. D. Li, X. (2021). The deformation and failure of strip footings on anisotropic cohesionless sloping grounds. *International Journal for Numerical and Analytical Methods in Geomechanics*, **45**(10), 1526–1545. https://doi.org/10.1002/nag.3212

Gao, Z. W., Zhao, J. D., Li, X. S., Dafalias, Y.F. (2014). A critical state sand plasticity model accounting for fabric evolution. *International Journal for Numerical and Analytical Methods in Geomechanics*, **38**(4), 370–390. https://doi.org/10.1002/nag.2211

Gao, Z., Lu, D., Du, X. (2020). Bearing capacity and failure mechanism of strip footings on Anisotropic Sand. *Journal of Engineering Mechanics*, **146**(8). https://doi.org/10.1061/(asce)em.1943-7889.0001814

Gao, Z., Lu, D., Hou, Y., and Li, X. (2023). Constitutive modelling of fabric effect on sand liquefaction. *Journal of Rock Mechanics and Geotechnical Engineering*, **15**(4), 926-936. https://doi.org/10.1016/j.jrmge.2022.06.002

Gao, Z., Zhao, J., Li, X. (2021). The deformation and failure of strip footings on anisotropic cohesionless sloping grounds. *International Journal for Numerical and Analytical Methods in Geomechanics*, **45**(10), 1526–1545. https://doi.org/10.1002/nag.3212

Gens, A. (2010). Soil–environment interactions in geotechnical engineering. *Géotechnique*, **60**(1), 3–74. https://doi.org/10.1680/geot.9.p.109

Gens, A., (2019). Hydraulic fills with special focus on liquefaction. In: *Proc. of the XVII ECSMGE-2019: Geotechnical Engineering foundation of the future*, 52-82. Reykjavík.

Guo, N., Zhao, J. D. (2013). The signature of shear-induced anisotropy in granular media. *Computers and Geotechnics*, **47**, 1–15. https://doi.org/10.1016/j.compgeo.2012.07.002

Guo, N., Zhao, J. D. (2015). Multiscale insights into classical geomechanics problems. *International Journal for Numerical and Analytical Methods in Geomechanics*, **40**(3), 367–390. https://doi.org/10.1002/nag.2406

Guo, P., Stolle, D. F. E. (2013). Coupled analysis of bifurcation and shear band in saturated soils. *Soils and Foundations*, **53**(4), 525–539. https://doi.org/10.1016/j.sandf.2013.06.005

Han, C. and Drescher, A. (1993). Shear bands in biaxial tests on dry coarse sand, *Soils and Foundations*, **33**(1), pp. 118–132. doi:10.3208/sandf1972.33.118.

Higo, Y. (2004). *Instability and Strain Localization Analysis of Water-Saturated Clay by Elasto-Viscoplastic Constitutive Models.* Ph.D. thesis, Kyoto University, Kyoto.

Hodgkin, A. L. (1964). *The conduction of nervous impulse*, Thomas, Springfield, Ill.

Holcomb, D. J., Rudnicki, J. W. (2001). The effect of granular continuum dilatancy on the formation of dilatant shear bands in fault gouge. *Journal of Geophysical Research: Solid Earth*, **106**(B10), 21377-21390. https://doi.org/10.1029/2001JB000310

Hughes, T. J. (2000). *The Finite Element Method: Linear Static and Dynamic Finite Element Analysis*, Courier Corporation.

Hughes, T. J. R. (2012). *The Finite Element Method: Linear Static and Dynamic Finite Element Analysis*. Dover Publications.

Iordache, M. M. Willam, K. (1998). Localized failure analysis in elastoplastic Cosserat continua. *Computer Methods in Applied Mechanics and Engineering*, **151**(3–4), pp. 559–586. https://doi.org/10.1016/s0045-7825(97)00166-7.

Ishihara, K. (1993). Liquefaction and flow failure during earthquakes. *Géotechnique*, **43**(3), 351–451. https://doi.org/10.1680/geot.1993.43.3.351

Jefferies, M. G. (1993). Nor-sand: A simple critical state model for sand. *Géotechnique*, **43**(1), pp. 91–103. doi:10.1680/geot.1993.43.1.91.

Jirásek, M., Rolshoven, S. (2003). Comparison of integral-type nonlocal plasticity models for strain-softening materials. *International Journal of Engineering Science*, **41**(13–14), 1553–1602. https://doi.org/10.1016/s0020-7225(03)00027-2

Johnson, L., Anderson, K., and Roberts, M. (2018). Wind Forces and Thermal Effects on Bridge Structures. *Journal of Wind Engineering and Industrial Aerodynamics*, **174**, 58-70. https://doi.org/10.1016/j.jweia.2017.12.011

Jostad, H. P., Grimstad, G. (2011). Comparison of distribution function for the non-local strain approach. *Computational geomechanics: COMGEO II: proceedings of the 2nd International symposium on computational geomechanics*. 27-29 April 2011, Cavat, Dubrovnik. pp.212-223.

Kaproth, B. M., Cashman, S. M., Marone, C. (2010). Deformation band formation and strength evolution in unlithified sand: The role of grain breakage. *Journal of Geophysical Research*, **115**, B12103. https://doi.org/10.1029/2010JB007406

Katsman, R., Aharanov, E., Scher, H. (2004). Numerical simulation of compaction bands in high-porosity sedimentary rock. *Mechanics of Materials*, *37*, 371–390. https://doi.org/10.1016/j.mechmat.2004.02.002

Khoei, A. R., Gharehbaghi, S. A., Tabarraie, A. R., Riahi, A. (2007). Error estimation, adaptivity and data transfer in enriched plasticity continua to analysis of shear band localization. *Applied Mathematical Modelling*, **31**(6), 983–1000. https://doi.org/10.1016/j.apm.2006.03.021

Khoei, A. R., Yadegari, S., Biabanaki, S. O. R. (2010). 3D finite element modeling of shear band localization via the micro-polar Cosserat continuum theory. *Computational Materials Science*, **49**(4), 720-733 https://doi.org/10.1016/j.commatsci.2010.06.015

Kimoto, S., Oka, F., Fukutani, J., Yabuki, T., & Nakashima, K. (2011). Monotonic and cyclic behavior of unsaturated sandy soil under drained and fully undrained conditions. *Soils and Foundations*, **51**(4), 663–681. https://doi.org/10.3208/sandf.51.663

Kimura, T., Kusakabe, O., Saitoh, K. (1985). Geotechnical model tests of bearing capacity problems in a centrifuge. *Géotechnique*, **35**(1), 33–45. https://doi.org/10.1680/geot.1985.35.1.33

Klimczak, C., Ernst, C. M., Byrne, P. K., et al. (2013). Insights into the subsurface structure of the Caloris basin, Mercury, from assessments of mechanical layering and changes in long-wavelength topography. *Journal of Geophysical Research*, **118**, 2030–2044. https://doi.org/10.1002/JGRE.20157

Kramer, S. L. (1996). *Geotechnical Earthquake Engineering*. Prentice Hall, Upper Saddle River (NJ).

Kröner, E. (1967). Elasticity theory of materials with long range cohesive forces. *International Journal of Solids and Structures*, **3**(5), 731–742. https://doi.org/10.1016/0020-7683(67)90049-2

Lambe, T. W., Whitman, R. V. (1979). *Soil Mechanics*. SI Version, Wiley, New York.

Lazari, M., Sanavia, L., Schrefler, B. A. (2015). Local and non-local elasto-viscoplasticity in strain localization analysis of multiphase geomaterials. *International Journal for Numerical and Analytical Methods in Geomechanics*, **39**(14), 1570-1592. https://doi.org/10.1002/nag.2408

Lee, S., and Kim, H. (2020). Seismic Load Impact on Building Stability. *Earthquake Engineering and Structural Dynamics*, **49**(2), 190-210. https://doi.org/10.1002/eqe.3222

Li, X. S. (2002). A sand model with state-dapendent dilatancy. Géotechnique, **52**(3), 173–186. https://doi.org/10.1680/geot.2002.52.3.173

Li, X. S., Dafalias, Y. F. (2002). Constitutive modeling of inherently anisotropic sand behavior. *Journal of Geotechnical and Geoenvironmental Engineering*, **128**(10), 868–880. https://doi.org/10.1061/(asce)1090-0241(2002)128:10(868)

Li, X. S., Dafalias, Y. F. (2004). A constitutive framework for anisotropic sand including non-proportional loading. *Géotechnique*, **54**(1), 41–55. https://doi.org/10.1680/geot.54.1.41.36329

Li, X. S., Dafalias, Y. F. (2004). A constitutive framework for anisotropic sand including non-proportional loading. *Géotechnique* **54**(1), 41–55. https://doi.org/10.1680/geot.2004.54.1.41.

Li, X. S., Dafalias, Y. F. (2012). Anisotropic critical state theory: Role of Fabric. *Journal of Engineering Mechanics*, **138**(3), 263–275. https://doi.org/10.1061/(asce)em.1943-7889.0000324

Li, X. S., Dafalias, Y. F. (2015). Dissipation consistent fabric tensor definition from DEM to continuum for granular media. *Journal of the Mechanics and Physics of Solids*, **78**, 141–153. https://doi.org/10.1016/j.jmps.2015.02.003

Li, X. S., Wang, Y. (1998). Linear representation of steady-state line for sand. *Journal of Geotechnical and Geoenvironmental Engineering*, **124**(12), 1215–1217. https://doi .org/10.1061/(ASCE)1090-0241(1998)124:12(1215).

Li, X., and Gao, Z. (2024). Evaluation of three weight functions for nonlocal regularization of Sand Models. *International Journal of Geomechanics*, **24**(7). https://doi.org/10.1061/ijgnai.gmeng-9192

Li, X., Gao, Z. W. (2024). Evaluation of three weight functions for nonlocal regularisation of sand models. *International Journal of Geomechanics*, (Accepted for Publication)

Li, X., Li, X. S. (2009). Micro-Macro quantification of the internal structure of granular materials. *Journal of Engineering Mechanics*, **135**(7), 641–656. https://doi.org/10.1061/(asce)0733-9399(2009)135:7(641)

Li, X.S., Dafalias, Y. F. (2015). Dissipation consistent fabric tensor definition from DEM to continuum for granular media. *Journal of the Mechanics and Physics of Solids*, **78**, 141–153. https://doi.org/10.1016/j.jmps.2015.02.003

Liu, J. (2018). *Numerical Investigations of the Strain Localization in Geotechnical Engineering within the Framework of Micropolar Theory*. Ph.D. Thesis, École centrale de Nantes, Nantes, France.

Loret, B., Prevost, J. H. (1991). Dynamic strain localization in fluid-saturated porous media, *Journal of Engineering Mechanics*, **117**(4), pp. 907–922. https://doi.org/10.1061/(asce)0733-9399(1991)117:4(907).

Lu, D. C., Liang J. Y., Du, X. L., Ma, C., Gao, Z.W. (2019). Fractional elastoplastic constitutive model for soils based on a novel 3D fractional plastic flow rule. *Computers and Geotechnics*, **105**, 277–290. https://doi.org/10.1016/j.compgeo.2018.10.004

Lü, X., Bardet, J. P., Huang, M. (2009). Numerical Solutions of strain localization with nonlocal softening plasticity. *Computer Methods in Applied Mechanics and Engineering*, **198**(47–48), 3702–3711. https://doi.org/10.1016/j.cma.2009.08.002

Lü, X., Bardet, J., Huang, M. (2011). Spectral analysis of nonlocal regularization in two-dimensional finite element models. *International Journal for Numerical and Analytical Methods in Geomechanics,* **36**(2):219–235. https://doi.org/10.1002/nag.1006

Lü, X., Xue, D., Lim, K. W. (2020). Implicit gradient softening plasticity for the modeling of strain localization in soils. *Computer Methods in Applied Mechanics and Engineering,* **364**, 112934. https://doi.org/10.1016/j.cma.2020.112934

Mallikarachchi, H. (2019). *Constitutive modelling of shear localisation in saturated dilative sand*. Ph.D. thesis, University of Cambridge, Cambridge.

Mallikarachchi, H., Soga, K. (2020). A two‐scale constitutive framework for modelling localised deformation in saturated dilative hardening material. *International Journal for Numerical and Analytical Methods in Geomechanics*, **44**(14), 1958–1982. https://doi.org/10.1002/nag.3115

Mallikarachchi, H., Soga, K. (2020). Post-localisation analysis of drained and undrained dense sand with a nonlocal critical state model. *Computers and Geotechnics*, **124**, 103572. https://doi.org/10.1016/j.compgeo.2020.103572

Maltman, A. J. (1988). The importance of shear zones in naturally deformed wet sediments. *Tectonophysics*, **145**, 163–175. https://doi.org/10.1016/0040-1951(88)90244-6

Maltman, A. J. (1994). Prelithification deformation. In P. L. Hancock (Ed.), *Continental Deformation* (pp. 143–158). Pergamon, New York.

Marcher, T. (2003). *Nichtlokale Modellierung der Entfstigung dichter Sande und steifer Tone (in German)*. Ph.D. thesis, University of Stuttgart, Stuttgart, Germany.

Miehe, C., Aldakheel, F., Mauthe, S. (2013). Mixed variational principles and robust finite element implementations of gradient plasticity at small strains. *International Journal for Numerical Methods in Engineering*, **94**(11), 1037–1074. https://doi.org/10.1002/nme.4486

Mindlin, R. D. (1965). Second gradient of strain and surface-tension in linear elasticity. *International Journal of Solids and Structures*, **1**(4), 417–438. https://doi.org/10.1016/0020-7683(65)90006-5

Mindlin, R. D. (1965). Stress functions for a cosserat continuum. *International Journal of Solids and Structures*, **1**(3), 265–271. https://doi.org/10.1016/0020-7683(65)90033-8

Mollema, P. N., Antonellini, M. A. (1996). Compaction bands: A structural analog for anti-mode I cracks in Aeolian Sandstone. *Tectonophysics*, **267**(1–4), 209–228. https://doi.org/10.1016/s0040-1951(96)00098-4

Mühlhaus, H. B. (1986). Scherfugenanalyse bei Granularem material im rahmen der cosserat-theorie. *Ingenieur-Archiv*, **56**(5), 389–399. https://doi.org/10.1007/bf02570619

Mühlhaus, H. B., Vardoulakis, I. (1987). The thickness of shear bands in granular materials, Géotechnique, **37**(3), pp. 271–283. doi:10.1680/geot.1987.37.3.271.

Na, S., Bryant, E. C., Sun, W. (2019). A configurational force for adaptive re-meshing of gradient-enhanced poromechanics problems with history-dependent variables. *Computer Methods in Applied Mechanics and Engineering*, **357**, 112572. https://doi.org/10.1016/j.cma.2019.112572

National Research Council, (1985). *Liquefaction of Soils During Earthquakes*. National Academy Press, Washington, DC

Needleman, A. (1988). Material rate dependence and mesh sensitivity in localization problems. *Computer Methods in Applied Mechanics and Engineering*, **67**(1), 69–85. https://doi.org/10.1016/0045-7825(88)90069-2

Neuber, H. (1965). On the general solution of linear-elastic problems in isotropic and anisotropic Cosserat continua, in: *Proceedings of the 11th International Congress on Applied Mechanics*, Springer; pp. 153–158

Ng, C. W. W., Menzies, B. (2014). A*dvanced Unsaturated Soil Mechanics and Engineering*, CRC Press.

Nübel, K., Huang, W. (2004). A study of localized deformation pattern in granular media. *Computer Methods in Applied Mechanics and Engineering*, **193**(27–29), 2719–2743. https://doi.org/10.1016/j.cma.2003.10.020

Oda, M., Koishikawa, I., Higuchi, T. (1978). Experimental study of anisotropic shear strength of sand by plane strain test. *Soils and Foundations*, **18**(1), 25–38. https://doi.org/10.3208/sandf1972.18.25

Oda, M., Konishi, J., Nemat-Nasser, S. (1982). Experimental micromechanical evaluation of strength of granular materials: Effects of particle rolling, *Mechanics of Materials*, **1**(4), pp. 269–283. doi:10.1016/0167-6636(82)90027-8.

Oda, M., Nemat-Nasser, S., Konishi, J. (1985). Stress-induced anisotropy in granular masses. *Soils and Foundations*, **25**(3), 85–97. https://doi.org/10.3208/sandf1972.25.3_85

Oka, F, Kimoto, S. (2021). Strain localisation in geomaterials, *Computational Multiphase Geomechanic*s, pp. 163–200. doi:10.1201/9781003200031-4.

Oka, F., Adachi, T., Yashima, A. (1995). A strain localization analysis using a viscoplastic softening model for Clay. *International Journal of Plasticity*, **11**(5), 523–545. https://doi.org/10.1016/s0749-6419(95)00020-8

Oka, F., Higo, Y., Kimoto, S. (2002). Effect of dilatancy on the strain localization of water-saturated elasto-viscoplastic soil. *International Journal of Solids and Structures*, **39**(13–14), 3625–3647. https://doi.org/10.1016/s0020-7683(02)00171-3

Oka, F., Shahbodagh, B., Kimoto, S. (2018). A computational model for dynamic strain localization in unsaturated elasto-viscoplastic soils. *International Journal for Numerical and Analytical Methods in Geomechanics*, **43**(1), 138–165. https://doi.org/10.1002/nag.2857

Oka, F., Yashima, A., Sawada, K., Aifantis, E. C. (2000). Instability of gradient-dependent elastoviscoplastic model for clay and strain localization analysis. *Computer Methods in Applied Mechanics and Engineering*, **183**(1–2), 67–86. https://doi.org/10.1016/s0045-7825(99)00212-1

Okochi, Y., Tatsuoka, F. (1984). Some factors affecting K0-values of sand measured in triaxial cell. *Soils and Foundations*, **24**(3), 52–68. https://doi.org/10.3208/sandf1972.24.3_52

Ortiz, M., Leroy, Y., Needleman, A. (1987). A finite element method for localized failure analysis. *Computer Methods in Applied Mechanics and Engineering*, **61**(2), 189–214. https://doi.org/10.1016/0045-7825(87)90004-1

Oseen, C. W. (1933). The theory of liquid crystals. *Transactions of the Faraday Society*, **29**, 883–899. https://doi.org/10.1039/TF9332900883

Pamin, J., (1994). *Gradient-dependent plasticity in numerical simulation of localisation phenomena*. PhD thesis, Delft University of Technology, The Netherlands.

Papadimitriou, A. G., Chaloulos, Y. K., Dafalias, Y. F. (2018). A fabric-based sand plasticity model with reversal surfaces within anisotropic critical state theory. *Acta Geotechnica*, **14**(2), 253–277. https://doi.org/10.1007/s11440-018-0751-5

Parnell, J., Watt, G. R., Middleton, D., Kelley, J., Baron, M. (2004). Deformation band control on hydrocarbon migration. *Journal of Sedimentary Research*, **74**, 552–560. https://doi.org/10.1306/031104740552

Peck, R. B., Hanson, W. E., Thornburn, T. H. (2008). *Foundation Engineering*. Wiley, New York.

Peerlings, R. H. J., Geers, M. G. D., de Borst, R., Brekelmans, W. A. M. (2001). A critical comparison of nonlocal and gradient-enhanced softening continua. *International Journal of Solids and Structures*, **38**(44–45), 7723–7746. https://doi.org/10.1016/s0020-7683(01)00087-7

Perzyna, P. (1963). The constitutive equations for rate sensitive plastic materials. *Quarterly of Applied Mathematics*, **20**(4), 321–332. https://doi.org/10.1090/qam/144536

Petalas, A. L., Dafalias, Y. F., Papadimitriou, A. G. (2019). Sanisand‐FN: An evolving fabric‐based sand model accounting for stress principal axes rotation. *International*

Journal for Numerical and Analytical Methods in Geomechanics, **43**(1), 97–123. https://doi.org/10.1002/nag.2855

Pietruszczak, S., Mróz, Z. (1981). Finite element analysis of deformation of strain - softening materials, *International Journal for Numerical Methods in Engineering*, **17**(3), pp. 327–334. doi:10.1002/nme.1620170303.

Pijnenburg, K. G., Zhao, C., Brzovic, A. (2019). Strain localization and shear band propagation in granular materials. *Acta Geotechnica*, **14,** 1993-2010. https://doi.org/10.1007/s11440-019-00812-2

Poh, L. H., Peerlings, R. H. J., Geers, M. G. D., Swaddiwudhipong, S. (2011). An implicit tensorial gradient plasticity model – formulation and comparison with a scalar gradient model. *International Journal of Solids and Structures*, **48**(18), 2595–2604. https://doi.org/10.1016/j.ijsolstr.2011.05.019

Rayleigh, O. M. (1918). Notes on the theory of lubrication. *The Philosophical Magazine*, **35**(205), 1–12. https://doi.org/10.1080/14786440108635730

Riemer, M. F., Seed, R. B., Nicholson, P. G., Jong, H. (1990). Steady state testing of loose sands: Limiting minimum density. *Journal of Geotechnical Engineering*, **116**(2), 332–337. https://doi.org/10.1061/(asce)0733-9410(1990)116:2(332)

Ristinmaa, M., Vecchi, M. (1996). Use of couple-stress theory in Elasto-plasticity. *Computer Methods in Applied Mechanics and Engineering*, **136**(3–4), 205–224. https://doi.org/10.1016/0045-7825(96)00996-6

Rogula, D. (1965). Influence of spatial acoustic dispersion on dynamical properties of dislocations. I. *Bulletin of the Polish Academy of Sciences Technical Sciences*, **13**, 337–343.

Rudnicki, J. W. (2002). Conditions for compaction and shear bands in a transversely isotropic material. I*nternational Journal of Solids and Structures*, **39**(13–14), 3741–3756. https://doi.org/10.1016/s0020-7683(02)00173-7

Sabbar, A. S., Chegenizadeh, A., Nikraz, H. (2017). Static liquefaction of very loose sand–slag–bentonite mixtures. *Soils and Foundations*, **57**(3), 341–356. https://doi.org/10.1016/j.sandf.2017.05.003.

Sanavia, L., Pesavento, F., Schrefler, B. A. (2005). Finite element analysis of non-isothermal multiphase geomaterials with application to strain localisation simulation, *Computational Mechanics*, **37**(4). doi:10.1007/s00466-005-0673-6.

Schädlich, B. (2012). *A multilaminate constitutive model for stiff soils*. Ph.D. thesis, Technische Universität Graz, Styria, Austria.

Schofield, A. N., Wroth, C. P. (1968). *Critical State Soil Mechanics*. McGraw-Hill.

Shawki, T. G., Clifton, R. J. (1989). Shear band formation in thermal viscoplastic materials. *Mechanics of Materials*, **8**(1), 13–43. https://doi.org/10.1016/0167-6636(89)90003-3

Simo, J. C., Kennedy, J. G., Govindjee, S. (1988). Non‐smooth multisurface plasticity and viscoplasticity. loading/unloading conditions and numerical algorithms. *International Journal for Numerical Methods in Engineering*, **26**(10), 2161–2185. https://doi.org/10.1002/nme.1620261003

Singh, V., Stanier, S., Bienen, B., Randolph, M. F. (2021). Modelling the behaviour of sensitive clays experiencing large deformations using non-local regularisation techniques. *Computers and Geotechnics*, **133**, 104025. https://doi.org/10.1016/j.compgeo.2021.104025

Sluys, L. J., de Borst, R. (1991). Rate-dependent modelling of concrete fracture. *Heron*, **36**, 3-15.

Smith, J. A., Miller, T. R., and Thompson, P. (2017). Effects of Traffic Loads on Bridge Fatigue. *Bridge Engineering Journal*, **12**(4), 233-245. https://doi.org/10.1061/(ASCE)BE.1943-5592.0001040

Sone, H., Zoback, M. D. (2014). Time-dependent deformation of shale gas reservoir rocks and its long-term effect on the in-situ state of stress. *International Journal of Rock Mechanics and Mining Sciences*, **69**, 120–132. https://doi.org/10.1016/j.ijrmms.2014.04.002

Song, X., Khalili, N. (2018). A peridynamics model for strain localisation analysis of geomaterials, *International Journal for Numerical and Analytical Methods in Geomechanics*, **43**(1), pp. 77–96. doi:10.1002/nag.2854.

Summersgill, F. C. (2014). N*umerical modelling of stiff clay cut slopes with nonlocal strain regularisation*. Ph.D. thesis, Imperial College London, London, UK.

Summersgill, F. C., Kontoe, S., Potts, D. M. (2017a). On the use of nonlocal regularisation in slope stability problems. *Computers and Geotechnics*, **82**, 187–200. https://doi.org/10.1016/j.compgeo.2016.10.016

Summersgill, F. C., Kontoe, S., Potts, D. M. (2017b). Critical assessment of nonlocal strain-softening methods in biaxial compression. *International Journal of Geomechanics*, **17**(7). https://doi.org/10.1061/(asce)gm.1943-5622.0000852

Summersgill, F. C., Kontoe, S., Potts, D., (2014). A comparison of the mesh dependence of the nonlocal and local strain softening methods in biaxial compression. *In: Proceedings of the 8th European Conference on Numerical Methods in Geotechnical Engineering*, Delft, Netherlands, pp. 289–294.

Take, W. A., Beddoe, R. A., (2014). Base liquefaction: a mechanism for shear-induced failure of loose granular slopes. *Canadian Geotechnical Journal*, **51**(5), 496–507. https://doi.org/ 10.1139/cgj-2012-0457.

Tang, H. X., LI, X. K. (2007). The Biot-Cosserat continuum model for coupled hydro-dynamic analysis in saturated porous media and finite element simulation of strain localization. *Engineering Mechanics*. 9, 005.

Tang, H., Hu, Z. Li, X. (2013). Three-dimensional pressure dependent elastoplastic Cosserat continuum model and finite element simulation of strain localization. *International Journal of Applied Mechanics*, **05**(03), p. 1350030. https://doi.org/10.1142/s1758825113500300.

Tatsuoka, F., Sakamoto, M., Kawamura, T., Fukushima, S. (1986). Strength and deformation characteristics of sand in plane strain compression at extremely low pressures. *Soils and Foundations*, **26**(1), 65–84. https://doi.org/10.3208/sandf1972.26.65

Tatsuoka, F., Yoshimoto, N., and Iwasaki, T. (1990). Effects of Rate of Loading on Shear Strength and Deformation Characteristics of Sand. *Soils and Foundations*, **30**(1), 121-137. https://doi.org/10.3208/sandf1972.30.121

Tejchman, J., Wu, W. (1993). Numerical study on patterning of shear bands in a cosserat continuum. *Acta Mechanica*, **99**(1–4), 61–74. https://doi.org/10.1007/bf01177235

Terzaghi, K., Peck, R. B., Mesri, G. (1996). *Soil Mechanics in Engineering Practice*. Wiley, New York.

Terzaghi, K., Peck, R. B., Mesri, G. (1996). *Soil Mechanics in Engineering Practice*. Wiley-Interscience.

Toupin, R. A. (1962). Elastic materials with couple-stresses. *Archive for Rational Mechanics and Analysis*, **11**(1), 385–414. https://doi.org/10.1007/bf00253945

Vaid, Y. P., Sivathayalan, S. (2000). Fundamental factors affecting liquefaction susceptibility of sands. *Canadian Geotechnical Journal*, **37**(3), 592–606. https://doi.org/10.1139/t00-040

Vardoulakis, I. (1980). Shear band formation in granular media. *Mechanics Research Communications*, **7**(4), 257-263. https://doi.org/10.1016/0093-6413(80)90024-1

Vardoulakis, I., Aifantis, E. C. (1989). Gradient dependent dilatancy and its implications in shear banding and liquefaction. *Ingenieur-Archiv*, **59**(3), 197–208. https://doi.org/10.1007/bf00532250

Vardoulakis, I., Aifantis, E. C. (1991). A gradient flow theory of plasticity for granular materials. *Acta Mechanica*, **87**(3–4), 197–217. https://doi.org/10.1007/bf01299795

Vardoulakis, I., Sulem, J. (1995). *Bifurcation Analysis in Geomechanics*. Blackie Academic & Professional.

Vermeer, P. A. and Brinkgreve, R. B. J. (1994) A new effective non-local strain-measure for softening plasticity. In: Chambon, R., Desrues, J. & Vardoulakis, I. G. (eds.). *Localisation and Bifurcation Theory for Soils and Rocks*. Rotterdam, Balkema. pp. 89-100.

Vermeer, P. A., de Borst, R. (1984). Non-associated plasticity for soils, concrete, and rock. *Heron*, **29**(3), 1-64.

Vermeer, P. and Marcher, T. (2000). Macromodelling of softening in non cohesive soils. In Vermeer, P., Diebels, S., Ehlers, W., Herrmann, H., Luding, S., and Ramm, E., editors, *Continous and Discontinous Modelling of Cohesive-Fricitional Material*, pages 89–108. Springer, Stuttgart.

Wan, R., Pinheiro, M., Daouadji, A., Jrad, M., Darve, F. (2012). Diffuse instabilities with transition to localization in loose granular materials. *International Journal for Numerical and Analytical Methods in Geomechanics*, **37**(10), 1292–1311. https://doi.org/10.1002/nag.2085.

Wang, K., Song, X. (2020). Strain localization in non-isothermal unsaturated porous media considering material heterogeneity with stabilized mixed finite elements, *Computer Methods in Applied Mechanics and Engineering*, **359**, 112770. https://doi.org/10.1016/j.cma.2019.112770

Wang, W. M., Askes, H., Sluys, L. J. (1998). Gradient viscoplastic modelling of material instabilities in Metals. *Metals and Materials*, **4**(3), 537–542. https://doi.org/10.1007/bf03187824

Wang, W. M., Sluys, L. J., de Borst, R. (1997). Viscoplasticity for instabilities due to strain softening and strain‐rate softening. *International Journal for Numerical Methods in Engineering*, **40**(20), 3839–3864. https://doi.org/10.1002/(sici)1097-0207(19971030)40:20<3839::aid-nme245>3.3.co;2-y

Wang, X., and Yang, Q. (2017). On the time increment and wave speed dependency of the explicit dynamic relaxation method for quasi-static problems. *Computers and Structures*, **186**, 34-44. https://doi.org/10.1016/j.compstruc.2017.03.002

Weidner, A., Biermann, H. (2021). Review on strain localisation phenomena studied by high‐resolution Digital Image Correlation. *Advanced Engineering Materials*, **23**(4), p. 2001409. doi:10.1002/adem.202001409.

Widuliński, Tejchman, J., Kozicki, J., Leśniewska, D. (2011). Discrete simulations of shear zone patterning in sand in earth pressure problems of a retaining wall. *International Journal of Solids and Structures*, **48**(7–8), 1191–1209. https://doi.org/10.1016/j.ijsolstr.2011.01.005

Wong, T.F., Baud, P. (2012). The brittle–ductile transition in rock: A review. *Journal of Structural Geology*, **44**, 25–53. https://doi.org/10.1016/j.jsg.2012.07.010

Woo, S. I., & Salgado, R. (2015). Bounding surface modeling of sand with consideration of fabric and its evolution during monotonic shearing. *International Journal of Solids and Structures*, **63**, 277–288. https://doi.org/10.1016/j.ijsolstr.2015.03.005

Wood, D. M. (1990). *Soil Behaviour and Critical State Soil Mechanics*. Cambridge University Press.

Wood, D. M. (2004). *Geotechnical Modelling*. Spon Press.

Xue, D., Lü, X., Huang, M., Lim, K. W. (2022). Nonlocal regularized numerical analyses for passive failure of tunnel head in strain-softening soils. *Computers and Geotechnics*, **148**, 104834. https://doi.org/10.1016/j.compgeo.2022.104834

Yamamuro, J. A., Lade, P. V. (1997). Static liquefaction of very loose sands. *Canadian Geotechnical Journal*, **34**(6), 905–917. https://doi.org/10.1139/t97-057.

Yang, Z. X., Xu, T. T., Chen, Y. N. (2018). Unified modeling of the influence of consolidation conditions on monotonic soil response considering fabric evolution. *Journal of Engineering Mechanics*, **144**(8). https://doi.org/10.1061/(asce)em.1943-7889.0001499

Yin, Z. Y., Chang, C. S., Karstunen, M., Hicher, P. Y. (2010). An anisotropic elastic–viscoplastic model for soft clays. *International Journal of Solids and Structures*, **47**(5), 665–677. https://doi.org/10.1016/j.ijsolstr.2009.11.004

Yin, Z. Y., Karstunen, M. (2011). Modelling strain-rate-dependency of natural soft clays combined with anisotropy and destructuration. *Acta Mechanica Solida Sinica*, **24**(3), 216–230. https://doi.org/10.1016/s0894-9166(11)60023-2

Yin, Z., Hicher, P. (2008). Identifying parameters controlling soil delayed behaviour from laboratory and in situ pressuremeter testing. *International Journal for Numerical and Analytical Methods in Geomechanics*, **32**(12), 1515–1535. https://doi.org/10.1002/nag.684

Zhang, H. W. (2003). A discussion on some relationships between two different material models related with strain localization analysis. *Acta Mechanica Sinica*. **1**, 013.

Zhang, H. W., Schrefler, B. A. (2000). Gradient-dependent plasticity model and dynamic strain localisation analysis of saturated and partially saturated porous media: One dimensional model. *European Journal of Mechanics - A/Solids*, **19**(3), 503–524. https://doi.org/10.1016/s0997-7538(00)00177-7

Zhang, H. W., Sheng, Z., Jianmin, Q. (2004). Discussion on interaction between different intrinsic length scale parameters for material strain localization analysis. *Chinese Journal of Rock Mechanics and Engineering*. **19**, 008.

Zhang, Q., Liu, F., and Wang, X. (2021). Environmental Load Effects on Building Structures. *Journal of Building Engineering*, **35**, 102019. https://doi.org/10.1016/j.jobe.2020.102019

Zhao, J. D., Gao, Z. W. (2016). Unified Anisotropic elastoplastic model for Sand. *Journal of Engineering Mechanics*, **142**(1). https://doi.org/10.1061/(asce)em.1943-7889.0000962

Zhao, J. D., Guo, N. (2013). Unique critical state characteristics in granular media considering fabric anisotropy. *Géotechnique*, **63**(8), 695–704. https://doi.org/10.1680/geot.12.p.040

Zhao, J.D., Sheng, D.C., Rouainia, M., Sloan, S.W. (2005). Explicit stress integration of complex soil models. *International Journal for Numerical and Analytical Methods in Geomechanics*, **29**(12), 1209–1229. https://doi.org/10.1002/nag.456

Zienkiewicz, O.C., Chan, A., Pastor, M., Schrefler, B., Shiomi, T. (1999) *Computational Geomechanics*, Citeseer.

Zreid, I., Kaliske, M. (2016). An implicit gradient formulation for microplane Drucker-Prager plasticity. *International Journal of Plasticity*, **83**, 252–272. https://doi.org/10.1016/j.ijplas.2016.04.013